



HAL
open science

Vibroacoustics of periodic structures : model order reduction, characterization, optimization

Régis Boukadia

► **To cite this version:**

Régis Boukadia. Vibroacoustics of periodic structures: model order reduction, characterization, optimization. Other. Université de Lyon, 2021. English. NNT : 2021LYSEC018 . tel-03506294

HAL Id: tel-03506294

<https://theses.hal.science/tel-03506294v1>

Submitted on 2 Jan 2022

HAL is a multi-disciplinary open access archive for the deposit and dissemination of scientific research documents, whether they are published or not. The documents may come from teaching and research institutions in France or abroad, or from public or private research centers.

L'archive ouverte pluridisciplinaire **HAL**, est destinée au dépôt et à la diffusion de documents scientifiques de niveau recherche, publiés ou non, émanant des établissements d'enseignement et de recherche français ou étrangers, des laboratoires publics ou privés.



Vibroacoustics of periodic structures

Model Order Reduction, Characterization, Optimization

Régis Fabien Boukadia

Supervisors:

Prof. dr. ir. W. Desmet

Prof. dr. ir. M. Ichchou

Prof. dr. ir. E. Deckers

Dissertation presented in partial fulfillment of the requirements for the degree of Doctor of Engineering Science (PhD): Mechanical Engineering

May 2021

Vibroacoustics of periodic structures

Model Order Reduction, Characterization, Optimization

Régis Fabien BOUKADIA

Examination committee:

Prof. dr. ir. H. Neuckermans , chair

Prof. dr. ir. W. Desmet, supervisor

Prof. dr. ir. M. Ichchou, supervisor

Prof. dr. ir. E. Deckers, co-supervisor

Prof. dr. ir. G. Lombaert

Dr. ir. C. Claeys

Prof. dr. A. Zine

(École Centrale de Lyon)

Prof. dr. ir. E. Manconi

(Università di Parma)

Prof. dr. ir. M. I. Hussein

(University of Colorado Boulder)

Dissertation presented in partial fulfillment of the requirements for the degree of Doctor of Engineering Science (PhD): Mechanical Engineering

May 2021

© 2021 KU Leuven – Faculty of Engineering Science
Uitgegeven in eigen beheer, Régis Fabien Boukadia, Celestijnenlaan 300 box 2420, B-3001 Leuven (Belgium)

Alle rechten voorbehouden. Niets uit deze uitgave mag worden vermenigvuldigd en/of openbaar gemaakt worden door middel van druk, fotokopie, microfilm, elektronisch of op welke andere wijze ook zonder voorafgaande schriftelijke toestemming van de uitgever.

All rights reserved. No part of the publication may be reproduced in any form by print, photoprint, microfilm, electronic or any other means without written permission from the publisher.

Preface

Here I am, days away from the end of a path I walked for about four years. There were good days, there were bad days, but overall, the journey was definitely worthwhile. I learned many things along the way, some about science and the academic world, some about history, politics and culture and others about myself. I got acquainted with many amazing people from all four corners of the world and was lucky enough to get a peek at life in different places and within different cultures. I am thankful for all these opportunities and encounters. While this PhD is not truly over, I am already feeling nostalgic. I am still unsure what all these experiences and interactions meant and it will take me time to fully integrate and process them. There is one thing however, that I am certain of. I would not have reached this point without the help and kindness of many people. You all have my heartfelt thanks and gratitude. This one section is dedicated to you!

I would like to start by thanking my KU Leuven supervisor, prof. Desmet, for believing in my abilities and giving me the academic freedom to explore and modify my initial research topic. Thank you also for always answering present when it mattered despite your innumerable responsibilities.

Secondly, I need to thank my supervisor on the ECL side, prof. Ichchou for helping me at the lowest point in my life, introducing me to the academic world and strongly recommending that I start I embark on this journey. I am not sure what my life would be like without these blessings.

I have to thank my co-supervisor, Elke, for the daily interactions and supervision, the scientific and personal discussions and the thorough review of my work. Thank you also for helping me keep track of administrative matters (something I am notably bad at) and for helping me connect with many great minds.

Then, I want to thank my assessors Claus and Geert. Claus for the close interactions, the mentoring and collaborations in and outside of the UCM meetings. Geert for the benevolent interest in my work and the various

suggestions and constructive remarks that helped me improve this thesis.

Special thanks are addressed to prof. Zine, who I have known since my first year at the ECL. He supervised my first student project on the development of an I.A. for the game of Go: IAGO. I have nothing but positive memories of this interesting project! The scope of my work has changed a lot since then, but prof. Zine's sharp mathematical analysis is still relevant and provides important insights for which I am thankful.

Finally, I would to thank the rest of my jury members. Prof. Neuckermans, prof. Manconi and prof. Hussein for the valuable and insightful comments and remarks during my preliminary defense. Due to the tight schedule, some of them could not be addressed in the manuscript but they definitely brought a new perspective to my work. Hopefully, you enjoyed reading my dissertation.

Outside of the jury members, there are many people and organizations I need to thank. First, the staff of the Arenberg and MEGA doctoral schools for making this joint degree possible and giving me some flexibility with regard to administrative matters. In addition, I would like to thank Bert Pluymers for ensuring all practical matters related to this PhD went smoothly and for introducing me to the industrial side of research.

Also, this research would not have been possible without financial support. Firstly, the European Commission is gratefully acknowledged for their support of the VIPER research project (GA No. 675441). Furthermore, this research was partially supported by Flanders Make, the strategic research center for the manufacturing industry.

Here, I would like to acknowledge the staff and professors of the VIPER project as well as the fellows that went through this adventure with me: Fabrizio, Marc-Antoine, Nassardin, Dario, Simone, Taoufik, Rita, Ravi, Safiullah, Giovanni and Sepide. Thank you all, for making this project so much more interesting, for the lively dinners, scientific presentations and exchange of ideas. I also would like to address special thanks to Sepide, Taoufik and Ravi with whom I spent a lot of time due to shared main/secondary universities within the project. Sepide, thank you for always being present and ready to help. It was pleasure working and collaborating with you. Best of luck for your defense! Taoufik, thanks for the many conversations at Alma, the tour around Gent and the interesting conversations on economics. Ravi, thanks for your undying enthusiasm! Your ability to take a step back and approach difficult situations with humor is truly inspiring!

I would like to thanks the regulars and organizers of the Happy Hours: Dionysios, Matteo, Pavel, Philip, Nico, Sergio and Joschua. I drank more coke than beer but it doesn't mean I had less fun than any of you :) Also, Special thanks

to Laurens, Sander and the staff of the secretariat for organizing the MECH sandwiches on Friday lunches. These were definitely one of the “highlights of the week” and I am looking forward to ordering my favorite sandwich again once circumstances allow for it!

I would also like to acknowledge my comrades of the UCM: Alireza, Augusto, Felipe, Femke, Florian, Kristof, Lise, Luca, Lucas, Philip, Matias, Marcelo, Noé, Qu Fei, Sepide, Simon, Vanessa and Zhang Ze. Thank you for the productive meetings, the brainstormings and for all the help that I received along the years. Also, special thanks to Luca, Lucas, Noé and Vasileios for helping me with the experimental part of my thesis. It would have been so much harder without you guys!

I would like to thank my colleagues and friends from the ECL. Christophe for the fruitful collaborations, for helping me getting a foothold in Leuven and for the many interesting discussions about science and politics. Changwei for your brilliant manuscript, the personal advice and support and for being my guide in Nantes and its surroundings. Fan Yu, for the discussions about philosophy and the meaning of life, your generous hospitality during my visit in Beijing and the games of Go we played. Diane, for ensuring I stayed safe at the beginning of the pandemics and motivating me to study nonlinear dynamics. I would like to also acknowledge Hui Yi, Jean-Loup, Kaijun Omar, Pascal, Rita, Yifan, Xiangkun, Zakaria and others at the ECL whom I had the pleasure to work with.

I should not forget my past and present officemates: Alireza, Augusto, Axel, Elke, Felix, Kengo, Marcelo, Philip, Qu Fei, Sander, Sepide, Sjoerd, Taoufik, Thiago and Zhang Ze. I miss our lunches at ViaVia, the discussions about everything and nothing and the pie tradition for birthdays and papers. Special thanks to Sander for helping me moving in (I thought we were going to die carrying the washing machine upstairs !), Augusto for the board games and the help with the piano and Felix for the trip around Belgium and the chill weekend afternoons! I am looking forward to resuming these interactions once the pandemic is over!

There are others I would like to acknowledge here for their contributions to this work: Olivier Bareille, Stijn Jonckheere, Isabelle Tixier, Regine Vanswijgenhoven, Hanne Verhaegen, Nele Buytaert, Patrick Guézou, Christine Feuillet, Laurent Nouvelot, Marc Vianey and Placide Carava.

J'aimerais enfin remercier mes amis de longues dates, ainsi que ma famille. Henri, notre amitié date de 1996 ! Merci pour ta présence et ton soutien à travers toutes les étapes de ma vie. Guillaume (Robert) et Guillaume (Martinet) mes camarades des classes préparatoires ! Les mots me manquent et il est difficile de faire justice aux expériences que nous avons vécu ensemble. Malgré la pandémie

et le fait que nous vivions dans des pays différents, j'espère que nous aurons l'occasion de nous revoir pour se remémorer le bon vieux temps et discuter des récents changement dans nos vies respectives ! Un grand merci également à toute ma famille, en particulier à mon cousin Claire Mael pour son hospitalité lors de mon arrivé en Belgique et pour avoir été mon guide dans la capitale. À mes frères, Alexandre et William pour leur soutien constant et infaillible. Enfin, je tiens à remercier mes parents pour les soins, l'attention, les efforts et l'amour inconditionnel dont j'ai bénéficié tout au long de ma vie. Cette thèse n'aurait jamais été possible sans vous !

Lastly, I would like to thank you, my current reader, for your interest in this work. I hope you find it worth your while!

Abstract

Noise pollution has been identified as a physiological stressor that impacts both the physiological and psychological health of those exposed to it. This recognition has motivated the imposition of stricter noise regulations which justify the increasing importance of vibroacoustic performance in a broad range of industries that includes the automotive, aerospace, building, and home appliance industries. However, the need and demand for better acoustic comfort often conflict with other design imperatives such as compactness, cost, weight, or ecological targets. Notably, an easy way to increase the vibroacoustic performance of a structure is to increase its mass which, because it requires the use of more material, impacts all the aforementioned targets.

In the past decades, the technical challenges induced by higher vibroacoustics standards have been answered by combining stiff, lightweight materials such as aluminum with so-called “vibroacoustic packages” including viscoelastic and poroelastic materials known for their respective abilities to dissipate vibration and acoustic energy. Recently, periodic structures and metamaterials have emerged as a possible, complementary way to achieve better vibroacoustic performance as they often possess unconventional wave propagation properties caused by their multi-scale nature. As a result, they have been the focus of intensive research aimed at understanding their phenomenology and leveraging it in novel vibroacoustic designs.

Three challenges to the realization of the aforementioned research program are identified and constitute the main focus of this thesis. Firstly, the computational cost associated with the modeling of metamaterial solutions. Secondly, the absence of a well-established optimization framework for the optimization of metamaterials that accounts for the specificities of the multi-scale/spectral methods developed to model them. Lastly, the difficulty to compare experimental results with numerical models as multiscale methods predict indicators that are not easily measured or estimated (e.g. wavenumbers).

To reduce the computational cost associated with the modeling of metamaterials, two model order reduction schemes are developed. The first one concerns the free and forced wave propagation in periodic media and combines mode-based and wave-based reduction methods. The proposed scheme is compared to other techniques presented in the literature and is shown to perform favorably. The second method is based on a multiparameter moment matching technique and is developed to speed up sound transmission loss computations in the shift cell operator method. A reduction of CPU time by up to three orders of magnitude is observed.

Regarding optimization, a framework for the unit-cell modeling of periodic structures and metamaterials is developed. The proposed framework combines semi-analytical derivatives of objectives functions computed through unit-cell methods with a second-order optimization algorithm. The aforementioned algorithm is an instance of sequential quadratic programming that combines a line search method (used when the optimization function is locally convex) and an ellipsoidal trust-region method. The proposed framework is applied to model updating, sound transmission loss, and vibration-based problems and produces effective solutions in all cases.

Concerning the experimental characterization of periodic media, a novel wavenumber extraction method is developed. The proposed method requires periodic sampling of the signal of interest to produce a convolution kernel that describes its wavenumbers or k -space. In this work, the proposed method is compared to other wavenumber extraction techniques presented in the literature and outperforms them in terms of speed and accuracy.

Keywords:

Periodic structures, Metamaterials, Vibroacoustics, Model Order Reduction, Optimization, Wavenumber extraction

Beknopte samenvatting

Geluidsoverlast is geïdentificeerd als een fysiologische stressfactor die zowel de fysiologische als psychologische gezondheid van degenen die eraan worden blootgesteld, beïnvloedt. Deze erkenning heeft de ontwikkeling van strengere regelgeving en een toename van het belang van vibroakoestische prestaties in een breed scala van industrieën gemotiveerd, waaronder de automobiel-, lucht- en ruimtevaart-, bouw- en huishoudelijke apparaten. De behoefte aan en de vraag naar beter akoestisch comfort zijn echter vaak in strijd met andere ontwerpvereisten, zoals compactheid, kosten, gewicht of ecologische doelstellingen. De meest gemakkelijke manier om de vibro-akoestische prestatie van een constructie te verbeteren, is door de massa ervan te vergroten, wat, omdat er meer materiaal nodig is, invloed heeft op alle bovengenoemde vereisten.

In de afgelopen decennia zijn de technische uitdagingen die werden veroorzaakt door hogere vibroakoestische normen beantwoord door stijve, lichtgewicht materialen zoals aluminium te combineren met zogenaamde "vibro-akoestische addons", waaronder visco-elastische en poro-elastische materialen die bekend staan om hun respectievelijk vermogen om trillingen en akoestische energie af te voeren. Onlangs zijn periodieke structuren en metamaterialen naar voren gekomen als een mogelijke, complementaire manier om betere vibro-akoestische prestaties te bereiken, aangezien ze vaak onconventionele golfvoortplantingseigenschappen bezitten die worden veroorzaakt door hun multi-schaal karakter. Als gevolg hiervan zijn ze de focus geweest van intensief onderzoek gericht op het begrijpen van hun fenomenologie en het benutten ervan in nieuwe vibro-akoestische structuren.

Drie uitdagingen voor de realisatie van het bovengenoemde onderzoeksprogramma worden geïdentificeerd en vormen de belangrijkste focus van dit proefschrift. Ten eerste de computationele kosten die gepaard gaan met het modelleren van metamateriaaloplossingen. Ten tweede, het ontbreken van een goed ingeburgerd optimalisatiekader voor de optimalisatie van metamaterialen dat rekening houdt met de specificiteit van de multischaal / spectrale methoden

die zijn ontwikkeld om ze te modelleren. Ten slotte is het moeilijk om experimentele resultaten te vergelijken met numerieke modellen gebaseerd op deze multischallmethoden omdat de voorspelde grootheden niet gemakkelijk gemeten of afgeschat kunnen worden (bv. golfgetallen).

Om de computationele kosten die gepaard gaan met het modelleren van metamaterialen te verminderen, zijn twee modelreductieschema's ontwikkeld. De eerste beschouwt vrije en geforceerde golfvoortplanting in periodieke structuren en golfgeleiders. Het voorgestelde schema wordt vergeleken met andere technieken uit de literatuur en presteert erg goed. De tweede methode is ontwikkeld om de evaluatie van geluidstransmissieverlies via eenheidscelmodelleringstechnieken te versnellen en kan de vereiste CPU-tijd met drie ordes van grootte verminderen.

Met betrekking tot optimalisatie wordt een raamwerk ontwikkeld voor eenheidscelmodellering van periodieke structuren en metamaterialen. Het voorgestelde raamwerk combineert semi-analytische afgeleiden van doelfuncties berekend via eenheidscelmethoden met een tweede-orde optimalisatie-algoritme. Dit algoritme is een voorbeeld van sequentiële kwadratische programmering die een lijnzoekmethode combineert (gebruikt wanneer de optimalisatiefunctie lokaal convex is) en een ellipsoïdale trustregio-methode. Het voorgestelde raamwerk wordt toegepast op het identificeren van modelparameters, het optimaliseren van geluidstransmissie en trillingsniveaus en levert in alle gevallen effectieve oplossingen op.

Met betrekking tot de experimentele karakterisering van metamaterialen wordt een nieuwe golfgetalextractiemethode ontwikkeld. De voorgestelde methode vereist periodieke bemonstering van het signaal om een convolutiekern te produceren die de golfgetallen of k -ruimte beschrijft. In dit werk wordt de voorgestelde methode vergeleken met andere golfgetal-extractietechnieken uit de literatuur en overtreft deze in termen van snelheid en nauwkeurigheid.

Trefwoorden:

Periodieke structuren, Metamaterialen, Viabroakoestiek, Model Orde Reductie, Optimalisatie, Golfgetalextractie

Résumé

De nombreuses études identifient la pollution sonore comme une source de stress physiologique et psychologique impactant négativement la santé de ceux qui y sont exposés. Cette reconnaissance, relativement récente, de l'impact des nuisances sonores a conduit à l'introduction de normes et réglementations sonores de plus en plus strictes pour les industries aérospatiales, automobiles et électroménagères. Cependant, ces nouvelles exigences en matière de confort acoustique entrent souvent en conflit avec d'autres objectifs de conception industriels tels que la compacité, le poids, la minimisation des coûts et de l'impact écologique.

Traditionnellement, les défis techniques induits par les réglementations sonores sont résolus par l'usage joint de matériaux légers et résistants (comme l'aluminium) et de traitements vibroacoustiques s'appuyant sur les propriétés dissipatives des matériaux viscoélastiques (pour dissiper l'énergie vibratoire) et poroélastiques (pour la dissipation de l'énergie acoustique). Du fait de leur nature multi-échelles et de leurs propriétés non conventionnelles en matière de propagation des ondes, structures périodiques et métamatériaux sont depuis peu considérés comme de nouvelles solutions techniques permettant l'amélioration des performances vibroacoustiques sans trop impacter les autres objectifs de conception. En tant que tels, ils sont l'objet de maintes recherches avec pour objectifs la compréhension de leur phénoménologie et leur intégration dans le milieu industriel.

Les thématiques abordées dans ce manuscrit correspondent à trois obstacles majeurs à la réalisation du programme de recherche susmentionné. En premier lieu, les coûts de calcul associés à la modélisation de structures périodiques et de métamatériaux. Deuxièmement, l'absence d'un cadre conceptuel pour l'optimisation systématique des métamatériaux. Un tel cadre se devant de prendre en compte les spécificités des méthodes spectrales développées pour leur étude. En dernier lieu, les difficultés liées à la comparaison de résultats expérimentaux (e.g. champs de déplacement) à des résultats théoriques (e.g.

nombres d'ondes).

Deux méthodes de réduction sont développées en vue de réduire les coûts de calculs associés à la modélisation de structures périodiques. La première vise l'étude de la propagation des ondes dans lesdites structures. Elle combine des méthodes de réductions fondées sur l'analyse modale, l'analyse ondulatoire et la sous-structuration. La deuxième s'applique aux calculs de transmission acoustique. Elle se fonde sur une extension des méthodes de sous-espaces de Krylov à l'analyse multiparamétrique et permet de réduire la complexité du problème de plusieurs ordres de grandeur.

Concernant l'optimisation des métamatériaux, un cadre conceptuel permettant leur optimisation systématique via des méthodes numériques est développé. Ce cadre combine une approche permettant d'obtenir les dérivées premières et secondes des fonctions objectifs à un algorithme d'optimisation quadratique successive. L'algorithme susmentionné marie une méthode de recherche linéaire (utilisée quand la fonction objective est localement convexe) à un algorithme de région de confiance ellipsoïdale (utilisée en présence de courbure négative). Le cadre conceptuel décrit dans le présent manuscrit est appliqué à des problèmes de caractérisation, de transmission acoustique, et d'optimisation vibratoire et produit des solutions effectives dans chacun de ces cas.

Concernant la caractérisation expérimentale des milieux périodiques, une nouvelle méthode pour l'extraction de nombres d'onde est développée. Ladite méthode requiert un échantillonnage périodique des signaux considérés, qu'elle utilise pour produire un opérateur de convolution compacte qui décrit les nombres d'ondes et/ou le k -space. Cette nouvelle technique est comparée à d'autres méthodes de la littérature et les surpasse en termes de précision et de rapidité.

Mots Clés :

Structures périodiques, Métamatériaux, Vibroacoustique, Réduction de Modèles, Optimisation, Extraction de nombres d'onde

Contents

| | |
|--|-------------|
| Abstract | v |
| Beknopte samenvatting | vii |
| Résumé | ix |
| Contents | xiii |
| List of Figures | xvii |
| List of Tables | xxi |
| 1 Introduction | 1 |
| 1.1 General context | 1 |
| 1.2 Scientific context | 2 |
| 1.3 Identified Challenges and Research Objectives | 3 |
| 1.4 Outline of the manuscript | 5 |
| 2 Literature review and state of the art | 7 |
| 2.1 Introduction | 7 |
| 2.2 The 1D Wave Finite Element Method | 7 |
| 2.2.1 Discretization of an infinite 1D medium | 8 |
| 2.2.2 Free wave propagation in a 1D periodic medium | 10 |
| 2.2.3 Forced response of a finite 1D periodic waveguide | 11 |
| 2.2.4 Computation of transmission-reflection coefficients | 13 |
| 2.3 The 2D Wave Finite Element Method | 16 |
| 2.3.1 Direct formulation of the 2D WFEM | 17 |
| 2.3.2 Inverse formulation of the 2D WFEM | 19 |
| 2.4 The semi analytical finite element method and the shift-cell operator method | 20 |
| 2.4.1 A brief overview of the classical finite element method | 21 |

| | | |
|----------|--|-----------|
| 2.5 | Wavenumber extraction techniques | 24 |
| 2.5.1 | The Fourier transform | 25 |
| 2.5.2 | Mc Daniel's method | 26 |
| 2.5.3 | The ESPRIT algorithm | 27 |
| 2.5.4 | The Inhomogeneous Wave Correlation | 30 |
| 2.5.5 | The Inverse Wave Decomposition | 32 |
| 3 | Model Order Reduction for 1D Unit Cell Modeling | 33 |
| 3.1 | Reminder: Computing waveshapes and propagation constants via the direct 1D WFEM | 35 |
| 3.2 | Craig-Bampton Model Order Reduction for dynamic condensa- tion speed up | 36 |
| 3.3 | Wave Based Reduced Order Modeling | 37 |
| 3.4 | The proposed MOR strategy | 40 |
| 3.4.1 | Modifications brought to the sampling strategy | 40 |
| 3.4.2 | Construction of the reduced order model | 43 |
| 3.5 | Benchmarks and numerical examples | 44 |
| 3.5.1 | Sandwich beam | 45 |
| 3.5.2 | Locally Resonant Metamaterial | 48 |
| 3.5.3 | Doubly stiffened panel | 51 |
| 3.6 | Conclusions and perspectives | 54 |
| 4 | Wave Based Optimization | 56 |
| 4.1 | Derivatives for linear systems of equations | 57 |
| 4.2 | Derivatives of Simple Eigenvalues and Eigenvectors | 59 |
| 4.2.1 | First order derivatives | 61 |
| 4.2.2 | Second order derivatives | 61 |
| 4.3 | Derivatives for the direct 1D WFEM | 62 |
| 4.3.1 | Recaps | 63 |
| 4.3.2 | Derivatives of the condensed dynamic stiffness matrix | 64 |
| 4.3.3 | Derivatives of propagation constants and wave shapes | 66 |
| 4.4 | Derivatives in the 2D inverse WFEM framework | 67 |
| 4.4.1 | Recaps 2D inverse WFEM | 68 |
| 4.4.2 | Derivatives for eigenfrequencies, wave shapes and forced response | 69 |
| 4.5 | Second Order Optimization Algorithm | 71 |
| 4.6 | Numerical Examples | 74 |
| 4.6.1 | FRF based parameter identification | 74 |
| 4.6.2 | Optimization of a resonant metabeam | 78 |
| 4.6.3 | Optimization of a multi-resonant metabeam | 80 |
| 4.6.4 | Optimization of the diffuse field transmission loss of a resonant metapanel | 83 |
| 4.7 | Conclusions and perspectives | 86 |

| | | |
|----------|--|------------|
| 5 | Wavenumber Extraction | 89 |
| 5.1 | The 1D inverse convolution method | 91 |
| 5.1.1 | Main Principle | 92 |
| 5.1.2 | Reflected Wave | 94 |
| 5.1.3 | General 1D formulation | 96 |
| 5.1.4 | Palindromic transform | 97 |
| 5.1.5 | Number of waves | 98 |
| 5.2 | The 2D inverse convolution method | 98 |
| 5.2.1 | General version of the 2D case | 98 |
| 5.2.2 | Extracting wavenumbers and k-space | 100 |
| 5.3 | Experimental considerations | 101 |
| 5.3.1 | Weighted residuals and two step estimates | 102 |
| 5.3.2 | Alternative shapes for 2D convolution kernels | 104 |
| 5.3.3 | Using data from different origins | 106 |
| 5.4 | Numerical validation and benchmarks | 107 |
| 5.4.1 | Analytical Euler-Bernoulli Beam | 107 |
| 5.4.2 | Helmholtz Equation | 108 |
| 5.4.3 | Orthotropic Plate | 111 |
| 5.5 | Experimental applications | 113 |
| 5.5.1 | Beam with constrained viscoelastic layer | 114 |
| 5.5.2 | 2D Locally resonant metamaterial | 116 |
| 5.5.3 | Rubber Panel | 119 |
| 5.6 | Conclusions and perspectives | 120 |
| 6 | A rational Krylov subspace method for sound transmissions loss computation with the Shift Cell Method | 123 |
| 6.1 | Hybrid coupling with the shift cell operator method | 124 |
| 6.1.1 | Reminder: Basic properties of the shift-cell method | 124 |
| 6.1.2 | Sound transmission loss computation with shift cell method | 125 |
| 6.2 | Model Order Reduction Scheme | 127 |
| 6.2.1 | Multiparameter moment matching | 127 |
| 6.2.2 | MOR strategy | 129 |
| 6.3 | Numerical Results | 130 |
| 6.3.1 | Validation Case | 130 |
| 6.3.2 | Doubly stiffened plate | 131 |
| 6.4 | Conclusions and perspectives | 133 |
| 7 | Conclusions and perspectives | 135 |
| 7.1 | Main contributions of the thesis | 136 |
| 7.2 | Future work and perspectives | 138 |
| A | General Codes | 141 |
| A.1 | Normalizing all columns of a matrix | 141 |

| | | |
|----------|---|------------|
| A.2 | Create a sparse diagonal matrix from a vector | 141 |
| A.3 | QR-based Orthogonalization | 141 |
| A.4 | SVD-based Orthogonalization | 143 |
| A.5 | Solving a quadratic eigenvalue problem | 144 |
| A.6 | Solving a Hermitian quadratic eigenvalue problem | 144 |
| B | 1D WFEM Code Snippets | 145 |
| B.1 | Classical 1D WFEM implementation | 145 |
| B.2 | Zhong's formulation with an iterative solver | 146 |
| B.3 | An improved version of the MOR scheme of Droz et al | 149 |
| B.4 | Basic Craig-Bampton MOR scheme implementation for inner dofs reduction | 151 |
| C | Wavenumber extraction code snippets | 153 |
| C.1 | The 1D ESPRIT algorithm | 153 |
| C.2 | A modified 1D ESPRIT algorithm | 154 |
| C.3 | A basic implementation of the 1D IWC | 155 |
| C.4 | A basic implementation of the 2D IWC | 156 |
| C.5 | A basic implementation of the IWD | 156 |
| C.6 | A 1D INCOME code for 2 wavetypes | 158 |
| C.7 | The Mc Daniel method for Euler-Bernoulli beams | 159 |
| C.8 | A 2D INCOME code for quasi-isotropic wave propagation with 1 wavetype | 163 |
| C.9 | Palindromic Transform | 164 |
| C.10 | Comparison of the accuracy of different methods for an analytical Euler-Bernoulli beam | 165 |
| C.11 | Comparison of the accuracy of different methods for the Helmholtz equation | 168 |
| D | Some Proofs and analytical formulas | 171 |
| D.1 | Coherent system of derivatives for eigenvalues and eigenvectors | 171 |
| D.2 | Derivatives of the wave stiffness matrix | 174 |
| D.3 | Derivatives of the displacement field | 175 |
| | Bibliography | 177 |
| | Curriculum Vitae | 199 |
| | List of publications | 201 |

List of Figures

| | | |
|-----|--|----|
| 2.1 | Schematic representation and dofs partition of the k^{th} cell of an infinite 1D periodic medium. | 9 |
| 2.2 | An illustration of a periodic waveguide [145] | 12 |
| 2.3 | Illustration of the coupling of to semi-infinite periodic media coupled by a scatterer | 14 |
| 2.4 | Schematic representation of the UC of a 2D periodic media illustrating the corresponding dofs partition. | 17 |
| 2.5 | Displacement field of a composite plate and its 2D Fourier transform [160] | 26 |
| 2.6 | Comparison of the actual wavenumber values to one estimated with Mc Daniel’s method [138] | 27 |
| 2.7 | The real parts of the positive going (left) and negative going (right) free wave components identified from noise-free data (dashed lines) and noisy data (dot-dashed lines) and the exact free waves (solid lines); (a)–(c): wave pairs 1 to 3. [210] | 28 |
| 3.1 | Dofs’ partition for the UC of a 1D periodic structure | 35 |
| 3.2 | Illustration of the frequencies chosen to build the snapshot matrix | 38 |
| 3.3 | Illustration of the K-Space sampling strategy for the proposed scheme | 42 |
| 3.4 | Cross-section discretization for the sandwich structure of [60] | 46 |
| 3.5 | Comparison of the accuracy of the ROMs from Droz2014 and Boukadia2018 for the model of Droz2014 | 47 |
| 3.6 | Dispersion curves of the sandwich beam obtained with Droz2014’s reduction (Blue) and Boukadia2018’s reduction (Red) | 48 |
| 3.7 | Geometry and dimension of the UC from [170]. The dimensions are given in millimeters | 49 |
| 3.8 | Comparison of the accuracy of the ROMs from Droz2014 and Boukadia2018 for the model of [170] | 50 |

| | | |
|------|--|-----|
| 3.9 | Dispersion curves of the locally resonant metamaterial of [170] obtained with Droz2014's reduction (Blue) and Boukadia2018's reduction (Red) | 51 |
| 3.10 | Cross-section discretization of the UC of the doubly stiffened plate of [32] | 52 |
| 3.11 | Comparison of the accuracy of the ROMs from Droz2014 and Boukadia2018 for the model of [32] | 53 |
| 3.12 | Dispersion curves of the doubly stiffened panel of [32] obtained with Droz2014's reduction (Blue) and Boukadia2018's reduction (Red) | 53 |
| 4.1 | Dofs' partition for the UC of a 1D periodic structure | 63 |
| 4.2 | Dofs' partition of a 2D UC | 68 |
| 4.3 | Unit cell for the cross-section of the beam (1cm by 3cm by 0.556mm) | 75 |
| 4.4 | Comparison of the direct forced responses for the reference values and their initial estimates | 76 |
| 4.5 | Evolution of the material properties' estimates and of the objective function | 77 |
| 4.6 | Evolution of the direct forced response's shape through the iterations | 77 |
| 4.7 | Schematic representation of the metabeam and its parameters | 79 |
| 4.8 | Response of the bare structure (direct), starting point (direct and far field) and optimum (direct and far field). The vertical dashed lines indicate the frequency band of optimization | 80 |
| 4.9 | Evolution of the resonator's tuned frequency, mass, damping ratio and position | 81 |
| 4.10 | Evolution of the objective function | 81 |
| 4.11 | Response of the bare structure (direct), starting point (direct and far field) and optimum (direct and far field). The vertical dashed lines indicate the frequency band of optimization | 82 |
| 4.12 | Evolution of the objective function and all three resonators' properties | 83 |
| 4.13 | Unit Cell of the host structure | 86 |
| 4.14 | Comparison of the performance of the host structure and the optimum | 87 |
| 4.15 | Evolution of the objective function and of the TVA's properties | 87 |
| 5.1 | Illustration of the output of an ideal wavenumber extraction process in the 2D case | 90 |
| 5.2 | Comparison of the wavenumbers obtained with INCOME, the ESPRIT algorithm and the IWC for an Euler-Bernoulli beam | 109 |

| | | |
|------|---|-----|
| 5.3 | Comparison of the accuracy of wavenumbers retrieved with INCOME, the ESPRIT algorithm and the IWC for an Euler-Bernoulli beam | 109 |
| 5.4 | Randomly generated solution of the Helmholtz equation | 110 |
| 5.5 | Comparison of dispersion curves obtained via INCOME, the Shift Cell Operator method and the IWC | 112 |
| 5.6 | Comparison of the K-Spaces at 600 Hz obtained via INCOME and the Shift Cell Operator method | 113 |
| 5.7 | K-Space at 600 Hz computed with the IWC | 113 |
| 5.8 | Experimental setup for the aluminum beam with a constrained viscoelastic layer | 114 |
| 5.9 | Experimental dispersion curves of the aluminum beam retrieved with the ESPRIT algorithm (blue) INCOME (red), the Mc Daniel method(black) and the IWC (magenta). | 115 |
| 5.10 | Geometry of the locally resonant add-ons. Dimensions in mm . | 116 |
| 5.11 | Experimental setup for the locally resonant metamaterial . . . | 117 |
| 5.12 | Comparison of the experimental and theoretical dispersion curves in the x (top) and y (bottom) directions. | 118 |
| 5.13 | Comparison of the k-spaces at 1150 Hz obtained using INCOME on experimental data and the shift-cell operator method | 118 |
| 5.14 | Experimental setup for the rubber panel | 119 |
| 5.15 | Dispersion curves of the rubber panel retrieved with INCOME | 120 |
| 6.1 | Diffuse field transmission loss of the aluminum plate | 131 |
| 6.2 | Mesh of the unit cell of the doubly stiffened panel. Aluminum is purple and Perspex is green | 132 |
| 6.3 | Transmission loss and absorption of the doubly stiffened panel | 133 |

List of Tables

| | | |
|-----|--|-----|
| 3.1 | Material properties for the sandwich beam layer | 46 |
| 3.2 | CPU time performance of the five methods | 46 |
| 3.3 | Material properties of aluminum and PMMA in the model of [170] | 48 |
| 3.4 | CPU time performance of the five methods for the locally resonant metamaterial of [170] | 50 |
| 3.5 | CPU time performance of the five methods for the doubly stiffened panel of [32] | 52 |
| 4.1 | Reference material properties for the numerical model updating | 75 |
| 5.1 | Accuracy and CPU of wavenumber retrieval for INCOME, the IWD and the IWD | 111 |
| 5.2 | Density and Young Moduli of the studied plate | 111 |
| 5.3 | Shear Moduli of the studied plate | 112 |
| 5.4 | Poisson's ratios of the plate material | 112 |
| 5.5 | Material parameters for the host structure (aluminum) and the resonant add-ons (PMMA) | 116 |
| 6.1 | Material properties of aluminum and Perspex in the model of [33] | 131 |
| 6.2 | Performance of the proposed model order scheme | 132 |

Chapter 1

Introduction

1.1 General context

Noise pollution has been shown to impact both the physiological and psychological health [179, 84, 149, 171] of those exposed to it and is recognized as an important public health issue [35, 201]. This recognition is responsible for the inception of stricter noise regulations and an increase in the importance of vibroacoustic performance in a broad range of industries. This includes the automotive, aerospace, railway, building construction and home appliance industries. Unfortunately, the need for better vibroacoustic performance often conflicts with other design imperatives such as compactness (low volume), cost, weight (portability) which often impacts ecological targets via e.g. an increase in fuel consumption. Thus began the search for lightweight, high stiffness and high vibroacoustic performance solutions. Traditionally, these have been designed by combining stiff and light materials (e.g. aluminum) with vibroacoustic treatments including viscoelastic materials -that can convert vibration energy into heat- or poroelastic materials - which are able to absorb sound waves. In past decades, periodic structures and metamaterials have emerged as a potential third complementary way to design such solutions. The following section gives a brief overview of their scientific history and explains how/why they could achieve such performance.

1.2 Scientific context

This story starts with a result obtained in 1883 [76] by Gaston Floquet. The result concerns the fundamental properties of first order linear differential equations with periodic coefficients. These equations take the form:

$$\dot{x} = A(t)x \tag{1.1}$$

with $A(t)$ a periodic matrix function. At the time, the result was mostly used to determine the Lyapunov stability [120] of dynamical systems' limit cycles such as Earth's orbit around the Sun. Another breakthrough happened in 1929 [24]. Floquet's theory was extended by Bloch to the case of partial differential equations as the latter was interested in solutions of the Schrödinger equation for electrons in a periodic lattice of atoms (crystal). This led to the discovery of Bloch-waves and of the electronic band structures whose gaps govern the electric properties of the corresponding materials. These were crucial discoveries without which the semi-conductor industry as we know it and all its applications would have not been possible. As is often the case for physics and mathematics, concepts discovered in one branch can be reused in another [199]. And so, Floquet-Bloch theory spread from the study of electronic wavefunctions in periodic crystal lattices to the study of photonic crystals, phononic crystals and more recently, periodic structures and metamaterials. In all these domains, periodicity can be leveraged to produce unconventional wave propagation features that enable applications such as wave guiding [99, 182, 153], sound insulation [121, 56, 61], perfect absorption [70, 213, 114, 198], or vibration attenuation [43, 181, 172]. Apart from their unconventional properties, periodic media also present a significant advantage compared to other kinds of designs used in order to achieve similar performance level. Indeed, from a computational point of view, periodic media can be characterized, studied and designed via manipulation of one (and only one) of their irreducible periods called a unit cell (UC). While UCs with simple geometries and properties can be studied analytically/semi-analytically via asymptotic homogenization methods [77, 33] or with the plane wave expansion method [174], more complex cases require the use of numerical tools. In the fields of vibroacoustics, this has led to the development of several wave based methods that only require a single UC in order to study the corresponding medium. The Semi Analytical Finite Element Method (SAFE or SAFEM) is one of them and can be traced back to the early 1970's [196]. The method was further developed during the 80's [173, 53] and enables the computation of dispersion curves, K-Spaces, transmission-reflection coefficients and the forced response of homogeneous, layered and helical waveguides [50, 3, 18, 184]. Despite its success, the SAFE is limited to the study homogeneous waveguides and cannot deal with truly periodic media. The first method to do so is the Wave Finite Element Method (WFEM).

Developed by Mead in the 1970's [139, 140, 141], the WFEM combines, classical finite element modeling with Floquet-Bloch theory to model 1D and 2D periodic Media. In the 1D case, the method has a range of application similar to that of the SAFEM, though most of its many formulations suffer from numerical issues [197, 10]. In the 2D case, the WFEM achieved mixed success. On the one hand, the WFEM framework was extended by techniques enabling the computation of the sound transmission loss (STL) through 1D and 2D periodic media, on the other hand, the computation of dispersion curves is limited to the main directions of periodicity of the media when using the 2D WFEM. This last feature has prevented the computation of K-Spaces and lead to the development of the Shift-Cell Operator Method (SCOM) [47] an extension of the SAFEM to the case of periodic media. It is at that point, after decades of methodological progress and phenomenological investigations that the VIPER (VIbroacoustics of Periodic Media) project was launched. It was a Marie-Curie innovative training network project aiming at consolidating the research of previous decades while stimulating interactions and collaborations between European universities by awarding grants tied to joint/dual doctorates programs. There were to be 12 Early Stage Researchers (ESRs) spread among 5 European universities. Each ESR was assigned a topic corresponding, for the most part, to a specific investigative path, e.g. "Periodic inclusions in PU foams", "Periodic visco-elastic add-ons", "Industrial applications to aircrafts/launchers",... or "Vibroacoustics and structural dynamics of periodic structures" which was assigned to me. Given the massive ground covered by the topic I had to make choices and focus on areas where I perceived methodological gaps.

1.3 Identified Challenges and Research Objectives

In this section, the methodological gaps I identified at start of my PhD are highlighted and the corresponding research objectives formulated.

Speeding up computations within the WFEM framework.

The 1D WFEM enables the computation of the dispersion curves of periodic media and the forced response of finite periodic structures via manipulations of a single of their unit-cells. While there are not much alternatives for the computation of dispersion curves, the forced responses of finite periodic structures can in principle be computed by modeling such structures using classical finite elements (FE). The question obviously becomes, which is faster? For finite periodic structures containing a large number of UCs it is obvious that the WFEM is more advantageous than the FEM as it restricts computational operations to a single UCs (making it memory efficient) and its computational time is the same regardless of the number of cell (making it computationally

efficient). What about scenarios involving low to medium number of UCs then? For these, it does not hold that the WFEM is faster than classical FE models as the method requires two very computationally expensive steps. The first one is the dynamic condensation of the interior degrees of freedom (dofs) of the UC which may require as many "matrix-inversions" (per frequency) as the UC has interface dofs. The second one is the computation of all the eigenvalues of a matrix whose size is equal to the UC's interface dof count. This last operation is known to have a $o(n^3)$ complexity which is not very efficient. Meanwhile, FE models usually produce highly sparse matrices and the computation of their forced responses requires a single "matrix-inversion" (per frequency) which can be carried out efficiently using iterative methods. Similar issues arise when computing the diffuse field STL of periodic structures with the 2D spectral methods (e.g. the WFEM or SCOM). In the 1D case, some reduced order modeling strategies have been developed in the literature to address these issues. They are however not applicable to every case (e.g. damping models) and still had room for optimization. In the 2D case, it seems no method was developed in order to speed up 2D STL computations within the WFEM or SCOM frameworks. These observations led to the formulation of the first Research Objective (RO) of this thesis. **RO1: To develop efficient and widely applicable reduced order modeling strategies for computations in the 1D WFEM framework and STL evaluations via spectral methods.**

Optimized designs of periodic structures and metamaterials.

Many of the PhD thesis topics in the VIPER project dealt with phenomenological investigations -such as " Periodic inclusions in auxetic media", "Multilayer core topology - and once interesting concepts were to be found and partially understood, producing optimized designs maximizing specific manifestations of these concepts would be relevant for several reasons. Firstly they could help increasing our understanding of such phenomena. Secondly, optimized designs could be used either in demonstrators for scientific communication with the broad public or in practical industrial applications. However, while some papers can be found in the literature about the optimization of metamaterials and periodic structures, optimization itself is often treated as a second thought, the problems studied generally involve simplified 1D and 2D models, and the objective functions used often focus on partially predictive variables which do not tell a complete story. A good example of the last point is the spatial decay of flexural waves which can be caused by energy dissipation mechanisms or conservative Bragg/local resonance mechanisms which have different use cases and interpretations. As a results of these observations, the following research objective was formulated. **RO2: To develop an efficient unified framework for design and optimization via unit cell modeling techniques that exploits the full predictive power of this class of methods.**

Characterization and comparison between theoretical dispersion curves and experiments.

From a vibroacoustic standpoint, sensors are only able to measure displacements/accelerations/velocities and sound pressure fields. This is problematic for two reasons. Firstly, these fields are highly dependent on (possibly) hard to characterize boundary conditions such that observed mismatch may not be caused by a discrepancy between theoretical and the experimental media themselves but by differences in the environments they operate in. The second issue is related to the computational complexity of computing these fields values. Indeed, while efficient formulations for computing the forced response of 1D periodic media and waveguides exists there are none for 2D and higher dimensions which makes direct computations difficult. Notably, these problems can easily be bypassed by dispersion curves and k-space measurements as these properties are inherent to periodic media and do not depend on boundary condition. Moreover these can be efficiently computed using the previously mentioned spectral methods. An exploration of the literature on this topic showed that several accurate and robust "wavenumber extraction" methods enabling the measurement of experimental dispersion curves existed for 1D structures. In the 2D case however, existing methods suffered either from poor accuracy or had computational complexities so great that they could not be used in practical cases. From this vacuum, the following research objective was derived. **RO3: To develop efficient, accurate and robust wavenumber extraction methods for 2D homogeneous and periodic structures.**

1.4 Outline of the manuscript

The rest of this dissertation contains 6 chapters allowing to reach the aforementioned research objectives.

Chapter 2 - Literature review and state of the art: This chapter gives an overview of the numerical methods available for the modeling and study of periodic structures and metamaterials. Particular attention is given to the 1D WFEM framework as it plays a role in most of the following chapters. The most popular methods for wavenumber extraction in a vibroacoustic context are also described in details.

Chapter 3 - Model Order Reduction for 1D Unit Cell Modeling: In this chapter, a model order reduction scheme developed during this thesis is presented. The proposed scheme is benchmarked against previous reduced order modeling strategies in the literature which are also described.

Chapter 4 - Wave Based Optimization: In this chapter, a framework for the optimization of 1D and 2D periodic structures is presented. Closed formulas for first and second order derivatives of most quantities computed via the WFEM framework are derived. Additionally, a second order optimization algorithm combining line-search and an ellipsoidal trust-region methods is proposed in order to fully exploit the obtained second order information.

Chapter 5 - Wavenumber Extraction: In this chapter a novel method for 1D and 2D wavenumber extraction is presented. The proposed method exploits the 1D and 2D convolution frameworks in order to compute a kernel containing all the information about wavenumbers/k-space. It is benchmarked against other methods of the literature and validated on experimental cases.

Chapter 6 - A rational Krylov subspace method for sound transmissions loss computation with the Shift Cell Method: In this chapter, a method for sound transmission loss computations within the SCOM framework is developed. The subspace spanned by the columns of the obtained fluid-structure coupling matrices is shown to be independent of the wave's incidence angles and wavenumbers which enables the use of moment matching techniques to reduce the structural part of the problem. The proposed modeling technique and model order reduction schemes are validated by comparison to other methods of the literature and their efficiency is illustrated on a complex application case.

Chapter 7 - Conclusion The last chapter of this manuscript summarizes the main contributions of the thesis and gives recommendations for further research tracks and directions.

Chapter 2

Literature review and state of the art

2.1 Introduction

This chapter gives an overview of the numerical methods available for the modeling and study of periodic structures and metamaterials. Particular attention is given to the 1D WFEM framework as it plays a role in most of the following chapters. The most popular methods for wavenumber extraction in a vibroacoustic context are also described in details.

2.2 The 1D Wave Finite Element Method

The 1D wave finite element method (WFEM) is a numerical method that combines the flexibility of the finite element method (FEM) with Floquet-Bloch theory in order to compute the dispersion properties of a 1D periodic medium. By using the FEM in this manner, the WFEM enables the computation of the dispersion curves, waveshapes and forced response of periodic media of arbitrary geometric complexity with little additional implementation efforts for its practitioners. The method was first developed by Mead in the early 1970's [139, 140, 141, 142, 143], but other authors contributed to its formalization, dissemination [145, 64], and to the improvement of its numerical properties [197, 214, 89]. Along the years the 1D WFEM framework has been extended to include circular periodicity [135, 17], polar periodicity [129] and helical structures

[128, 178]. Stochastic extensions have also been derived [93, 27, 176]. In this section, the most popular applications of the 1D direct WFEM are presented using a unifying approach. The somewhat less popular inverse 1D WFEM is also quickly discussed. In the previous sentence, the adjective "direct" refers to the direct computation of the propagation constants when the driving frequency is known, while the adjective "inverse" refers to the opposite setting where the propagation constant is known and the corresponding frequencies remains to be determined. This terminology was introduced as early as 1993 [217, 214] and is likely a result of a transfer from optimal control theory as (numerical) wave propagation with the WFEM is analogous to the Riccati equation of optimal control [215] for which propagation constants are the natural unknowns. The rest of the section is organized as follows. In subsection 2.2.1 a formalism for the discretization of 1D infinite waveguides is presented. With the added assumption of periodicity, an eigenvalue problem yielding the characteristics of free waves propagating through the media is derived in subsection 2.2.2. Subsection 2.2.3 describes how the forced response of a finite 1D periodic waveguide may be derived from the knowledge of free waves propagating in the corresponding media while subsection 2.2.4 discusses how to derive the scattering properties of coupling elements connecting several periodic waveguides. Lastly in subsection 2.2.4 the inverse formulation of the 1D WFEM is presented.

2.2.1 Discretization of an infinite 1D medium

In this subsection, an explicit equation of motion is derived for an infinite one-dimensional waveguide comprised of an infinite number of cells $(X_k)_{k \in \mathbb{Z}}$ indexed on \mathbb{Z} , the set of all integers. Additionally, the assumption is made that a finite element model is available for each cell X_k and that interface meshes of successive UC are compatible such that direct assembly between them is possible i.e. the right interface of the k^{th} UC and the left interface of the $(k+1)^{\text{th}}$ have identical meshes and shape functions).

A partition of the degrees of freedom (dofs) is realized for each UC X_k according to its topology (see Figure 2.1):

- The dofs of the left interface: $U_L^{(k)}$,
- The inner dofs of the UC: $U_I^{(k)}$,
- The dofs of the right interface: $U_R^{(k)}$,
- The combined dofs of the left and right interfaces: $U_B^{(k)}$.

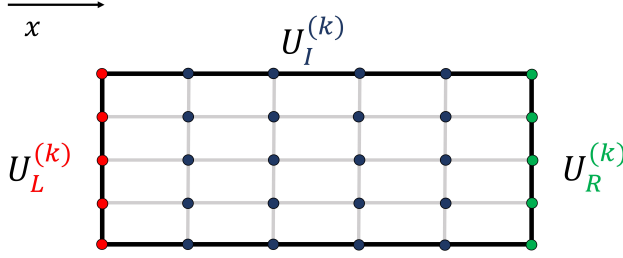


Figure 2.1: Schematic representation and dofs partition of the k^{th} cell of an infinite 1D periodic medium.

This partition is also used for the mass matrix $M^{(k)}$, and the stiffness matrix $K^{(k)}$ of each cell:

$$K^{(k)} = \begin{pmatrix} K_{LL}^{(k)} & K_{LI}^{(k)} & K_{LR}^{(k)} \\ K_{IL}^{(k)} & K_{II}^{(k)} & K_{IR}^{(k)} \\ K_{RL}^{(k)} & K_{RI}^{(k)} & K_{RR}^{(k)} \end{pmatrix}; \quad M^{(k)} = \begin{pmatrix} M_{LL}^{(k)} & M_{LI}^{(k)} & M_{LR}^{(k)} \\ M_{IL}^{(k)} & M_{II}^{(k)} & M_{IR}^{(k)} \\ M_{RL}^{(k)} & M_{RI}^{(k)} & M_{RR}^{(k)} \end{pmatrix} \quad (2.1)$$

In case damping is present in the UC it is accounted for by considering that the stiffness matrix is frequency-dependent, thus the equation of motion for the k^{th} cell takes the form:

$$\begin{pmatrix} G_{LL}^{(k)} & G_{LI}^{(k)} & G_{LR}^{(k)} \\ G_{IL}^{(k)} & G_{II}^{(k)} & G_{IR}^{(k)} \\ G_{RL}^{(k)} & G_{RI}^{(k)} & G_{RR}^{(k)} \end{pmatrix} \begin{bmatrix} U_L^{(k)} \\ U_I^{(k)} \\ U_R^{(k)} \end{bmatrix} = \begin{bmatrix} F_L^{(k)} \\ F_I^{(k)} \\ F_R^{(k)} \end{bmatrix} \quad (2.2)$$

in the frequency domain, with $G^{(k)} = K^{(k)} - \omega^2 M^{(k)}$ the dynamic stiffness matrix of the UC. The inner dofs of each cell can be condensed by rewriting the second line of equation (2.2):

$$U_I^{(k)} = \left(G_{II}^{(k)} \right)^{-1} \left(F_I^{(k)} - G_{IL}^{(k)} U_L^{(k)} - G_{IR}^{(k)} U_R^{(k)} \right) \quad (2.3)$$

This lead to the condensed equation of motion:

$$\begin{pmatrix} G_{LL}^{(k)} - G_{LI}^{(k)} \left(G_{II}^{(k)} \right)^{-1} G_{IL}^{(k)} & G_{LR}^{(k)} - G_{LI}^{(k)} \left(G_{II}^{(k)} \right)^{-1} G_{IR}^{(k)} \\ G_{RL}^{(k)} - G_{RI}^{(k)} \left(G_{II}^{(k)} \right)^{-1} G_{IL}^{(k)} & G_{RR}^{(k)} - G_{RI}^{(k)} \left(G_{II}^{(k)} \right)^{-1} G_{IR}^{(k)} \end{pmatrix} \begin{bmatrix} U_L^{(k)} \\ U_R^{(k)} \end{bmatrix} = \begin{bmatrix} F_L^{(k)} - G_{LI}^{(k)} \left(G_{II}^{(k)} \right)^{-1} F_I^{(k)} \\ F_R^{(k)} - G_{RI}^{(k)} \left(G_{II}^{(k)} \right)^{-1} F_I^{(k)} \end{bmatrix} \quad (2.4)$$

, which can be used to define the condensed dynamic stiffness matrix $D^{(k)}$ and the force delocalization operator $\Theta^{(k)}$ of the k^{th} , cell:

$$\begin{pmatrix} D_{LL}^{(k)} & D_{LR}^{(k)} \\ D_{RL}^{(k)} & D_{RR}^{(k)} \end{pmatrix} \begin{bmatrix} U_L^{(k)} \\ U_R^{(k)} \end{bmatrix} = \begin{bmatrix} F_L^{(k)} - \Theta_{LI}^{(k)} F_I^{(k)} \\ F_R^{(k)} - \Theta_{RI}^{(k)} F_I^{(k)} \end{bmatrix} \quad (2.5)$$

To form the 1D infinite medium, the cells can now be assembled which requires enforcing the relations:

$$\forall k \in \mathbb{Z}, U_R^{(k-1)} = U_L^{(k)} = V_k \quad (2.6)$$

Finally, the condensed equation of motion for the full infinite 1D waveguide can be written:

$$\forall k \in \mathbb{Z}, D_{RL}^{(k-1)} V_{k-1} + (D_{RR}^{(k-1)} + D_{LL}^{(k)}) V_k + D_{LR}^{(k)} V_{k+1} = F_k - \Theta_{RI}^{(k-1)} F_I^{(k-1)} - \Theta_{LI}^{(k)} F_I^{(k)} \quad (2.7)$$

2.2.2 Free wave propagation in a 1D periodic medium

It is now assumed that every cell of the wave guide is identical such that $D^{(k)} = D$ and $\Theta^{(k)} = \Theta$ for all values of k . Thus equation (2.7) is simplified to:

$$\forall k \in \mathbb{Z}, D_{RL} V_{k-1} + (D_{RR} + D_{LL}) V_k + D_{LR} V_{k+1} = F_k - \Theta_{RI} F_I^{(k-1)} - \Theta_{LI} F_I^{(k)} \quad (2.8)$$

To solve for free wave propagation, the assumption is made that no external forces are applied on the periodic medium. Moreover, the solutions sought should take the form of Bloch-waves with propagation constants λ and waveshape ψ .

$$\exists \psi \in \mathbb{C}^n, \exists \lambda \in \mathbb{C}^*, \forall k \in \mathbb{Z}, V_k = \lambda^k \psi \quad (2.9)$$

By substituting this expression of V_k in equation (2.8), the signature eigenvalue problem (EVP) of the 1D direct WFEM is derived [64, 143, 197, 10]:

$$\left(\frac{1}{\lambda_p} D_{RL} + (D_{RR} + D_{LL}) + \lambda_p D_{LR} \right) \psi_p = 0 \quad (2.10)$$

Because FEM matrices are symmetric in most cases, so is the dynamic stiffness matrix D such that $D_{RL} = D_{LR}^T$, $D_{LL} = D_{LL}^T$ and $D_{RR} = D_{RR}^T$. Thus, taking the transpose equation (2.10) leads to:

$$\psi_p^T \left(\lambda_p D_{RL} + (D_{RR} + D_{LL}) + \frac{1}{\lambda_p} D_{LR} \right) = 0 \quad (2.11)$$

Which shows that ψ_p^T is a left eigenvector of equation (2.10) for the eigenvalue $\frac{1}{\lambda_p}$. Therefore, the eigenvalues of (2.10) come in pairs $\left(\lambda_p, \frac{1}{\lambda_p} \right)$ corresponding to

waves propagating in the positive ($|\lambda_p| \leq 1$) and negative ($|\lambda_p| \geq 1$) directions. One way to solve the EVP (2.10) would be to change it into a quadratic EVP and then linearize it [64, 143, 10]. The most practical way to solve this EVP however, is to use a linearization that fully exploits its T-palindromic symmetry [214, 89, 126]:

$$\left[\begin{pmatrix} D_{RL} - D_{LR} & D_{LL} + D_{RR} \\ -D_{LL} - D_{RL} & D_{RL} - D_{LR} \end{pmatrix} - \mu_p \begin{pmatrix} 0 & -D_{LR} \\ D_{RL} & 0 \end{pmatrix} \right] \begin{bmatrix} X_p \\ Y_p \end{bmatrix} = 0 \quad (2.12)$$

The eigenvalues and eigenvectors of (2.10) are then obtained by applying the following transformations [89]:

$$\left\{ \begin{array}{l} \left(\lambda_p, \frac{1}{\lambda_p} \right) = \left(\frac{\mu_p + \sqrt{\mu_p^2 - 4}}{2}, \frac{\mu_p - \sqrt{\mu_p^2 - 4}}{2} \right) \\ \psi_p = X_p + \lambda_p Y_p \\ \phi_p = X_p + \frac{1}{\lambda_p} Y_p \end{array} \right. \quad (2.13)$$

with ψ_p and ϕ_p the right eigenvectors of (2.10) for the eigenvalues λ_p and $\frac{1}{\lambda_p}$ respectively.

2.2.3 Forced response of a finite 1D periodic waveguide

In this subsection, formulas enabling the computation of the Frequency Response Function (FRF) of a finite 1D periodic waveguide comprised of N UCS are presented. Alternative but equivalent formulas can also be found in the literature [64, 143, 144]. First some notations are introduced: From now on, we assume that the eigenvalues and eigenvectors are sorted so that $(\lambda_1, \dots, \lambda_n)$ are eigenvalues associated with waves propagating in the positive direction and $(\lambda_{n+1}, \dots, \lambda_{2n}) = \left(\frac{1}{\lambda_1}, \dots, \frac{1}{\lambda_n}\right)$ with waves propagating in the negative direction. Two pairs of eigenvalues and eigenvector matrices are defined:

$$\left\{ \begin{array}{l} \Lambda = \Lambda^+ = \begin{pmatrix} \lambda_1 & 0 & 0 \\ 0 & \ddots & 0 \\ 0 & 0 & \lambda_n \end{pmatrix}, \Psi^+ = [\psi_1, \dots, \psi_n] \\ \Lambda^- = (\Lambda^+)^{-1} = \begin{pmatrix} \lambda_{n+1} & 0 & 0 \\ 0 & \ddots & 0 \\ 0 & 0 & \lambda_{2n} \end{pmatrix}, \Psi^- = [\psi_{n+1}, \dots, \psi_{2n}] \end{array} \right. \quad (2.14)$$

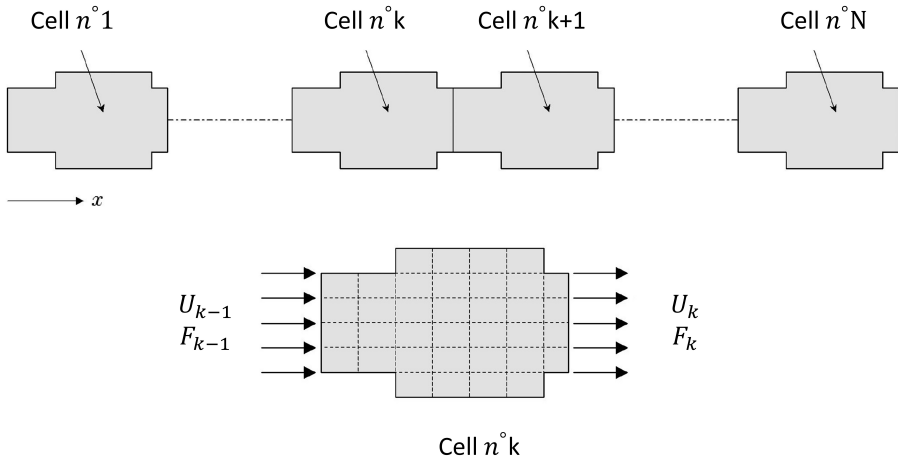


Figure 2.2: An illustration of a periodic waveguide [145]

They correspond to positive and negative going waves and satisfy the following relationships:

$$\begin{cases} D_{RL}\Psi^+\Lambda^{-1} + (D_{RR} + D_{LL})\Psi^+ + D_{LR}\Psi^+\Lambda = 0 \\ D_{RL}\Psi^-\Lambda + (D_{RR} + D_{LL})\Psi^- + D_{LR}\Psi^-\Lambda^{-1} = 0 \end{cases} \quad (2.15)$$

With these notations in place, the forced response of a finite waveguide can now be considered. It is assumed that forces on the waveguides are only applied at its extremities. The UCs are numbered from 1 to N . We note U_{k-1} the left interface displacement vector of the k^{th} unit cell and U_k its right interface displacement vector as indicated in Figure 2.2. First, the equation of motion of the full assembled waveguide is derived:

$$\begin{cases} \forall k \in \llbracket 1, N-1 \rrbracket, D_{RL}U_{k-1} + (D_{RR} + D_{LL})U_k + D_{LR}U_{k+1} = 0 \\ D_{LL}U_0 + D_{RL}U_1 = F_0 \\ D_{RL}U_{N-1} + D_{RR}U_N = F_N \end{cases} \quad (2.16)$$

The displacement of the waveguide can be developed as a superposition of positive (resp. negative) going waves originating at the left (resp. right) interface of the waveguide:

$$\forall k \in \llbracket 0, N \rrbracket, U_k = \Psi^+\Lambda^k q^+ + \Psi^-\Lambda^{N-k} q^- \quad (2.17)$$

With q^+ and q^- vectors containing the complex amplitudes of the positive and negative going waves respectively. Because the matrices Ψ^+ , Ψ^- and Λ

satisfy equation (2.15), the equation of motion is automatically verified inside the waveguide. Formulations for the forced response of the waveguide can then be derived for various boundary conditions. For free-free boundary conditions the following equation holds:

$$\begin{bmatrix} F_0 \\ F_N \end{bmatrix} = \begin{pmatrix} D_{LL}\Psi^+ + D_{LR}\Psi^+\Lambda & D_{LL}\Psi^-\Lambda^N + D_{RL}\Psi^-\Lambda^{N-1} \\ D_{RL}\Psi^+\Lambda^{N-1} + D_{RR}\Psi^+\Lambda^N & D_{RL}\Psi^-\Lambda + D_{RR}\Psi^- \end{pmatrix} \begin{bmatrix} q_+ \\ q_- \end{bmatrix} \quad (2.18)$$

For imposed displacements equation (2.19) holds:

$$\begin{bmatrix} U_0 \\ U_N \end{bmatrix} = \begin{pmatrix} \Psi^+ & \Psi^-\Lambda^N \\ \Psi^+\Lambda^N & \Psi^- \end{pmatrix} \begin{bmatrix} q_+ \\ q_- \end{bmatrix} \quad (2.19)$$

And for mixed boundary conditions:

$$\begin{bmatrix} F_0 \\ AU_N \end{bmatrix} = \begin{pmatrix} D_{LL}\Psi^+ + D_{LR}\Psi^+\Lambda & D_{LL}\Psi^-\Lambda^N + D_{RL}\Psi^-\Lambda^{N-1} \\ A\Psi^+\Lambda^N & A\Psi^- \end{pmatrix} \begin{bmatrix} q_+ \\ q_- \end{bmatrix} \quad (2.20)$$

where A is an invertible matrix chosen in order to mitigate the dimensional contrast between the displacement vector U_N and the force vector F_0 . $A = D_{LL} + D_{RR}$ is a good choice but it could also be chosen equal to the identity matrix without facing major numerical issues in most cases. In all three cases the values in any UC of the waveguide can be computed from the wave amplitudes using equation (2.17). The main advantage of computing the frequency forced response of a waveguide using the WFEM is that the computational cost is independent of the number of UCs which makes it computationally efficient when studying waveguides comprised of a large number of UCs.

2.2.4 Computation of transmission-reflection coefficients

In this section, formulas for the computation of the transmission-reflection of waves amplitude through a coupling element are presented. For this case we consider two different periodic waveguides and note D^1 the condensed dynamic stiffness matrix of the unit cell of the first periodic medium, D^2 that of the second periodic medium and D^c that of the coupling element. Moreover, Ψ^+ , Ψ^- and Λ are used for waves propagating in the first waveguide while Φ^+ , Φ^- and Γ are used for waves propagating in the second one. To compute the transmission and reflection coefficients, we use the formalism developed in subsection 2.2.1 for the discretization of an infinite waveguide with the assumption that all UCs of the waveguide with indexes strictly inferior to zero are unit cells of the first wave guide. The coupling element is the cell number 0 and all UCs with indexes strictly superior to zero are that of the second waveguide. Mathematically this

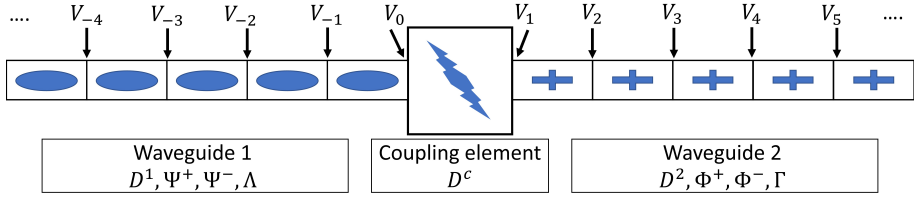


Figure 2.3: Illustration of the coupling of two semi-infinite periodic media coupled by a scatterer

is expressed as:

$$\begin{cases} \forall k, \in \mathbb{Z}, k < 0, D^{(k)} = D^1 \\ \forall k, \in \mathbb{Z}, k > 0, D^{(k)} = D^2 \\ D^{(0)} = D^c \end{cases} \quad (2.21)$$

and is represented in Figure 2.3. First, the assumption is made that no load is applied on the waveguide. Thus the equilibrium of the full infinite waveguide can be written as:

$$\begin{cases} \forall k \in \mathbb{Z}, k < 0, D_{RL}^1 V_{k-1} + (D_{RR}^1 + D_{LL}^1) V_k + D_{LR}^1 V_{k+1} = 0 \\ \forall k \in \mathbb{Z}, k < 1, D_{RL}^2 V_{k-1} + (D_{RR}^2 + D_{LL}^2) V_k + D_{LR}^2 V_{k+1} = 0 \\ D_{RL}^1 V_{-1} + (D_{RR}^1 + D_{LL}^c) V_0 + D_{LR}^c V_1 = 0 \\ D_{RL}^c V_0 + (D_{RR}^c + D_{LL}^2) V_1 + D_{LR}^2 V_2 = 0 \end{cases} \quad (2.22)$$

In order to compute the transmission-reflection coefficients of waves going through the coupling elements, kinematic assumptions need to be made. The first one corresponds to the case of waves coming from $k = -\infty$ getting reflected and partially transmitted by and through the coupling element. This is mathematically expressed as:

$$\begin{cases} \forall k, \in \mathbb{Z}, k \leq 0, V_k = \Psi^+ \Lambda^k q_1^+ + \Psi^- \Lambda^{-k} q_1^- \\ \forall k, \in \mathbb{Z}, k > 0, V_k = \Phi^+ \Gamma^{k-1} q_2^+ \\ q_1^- = R_{11} q_1^+ \\ q_2^+ = T_{21} q_1^+ \end{cases} \quad (2.23)$$

Conversely, the opposite assumption can be made where waves are coming from $k = +\infty$ and are scattered at the coupling elements' interfaces:

$$\begin{cases} \forall k, \in \mathbb{Z}, k \leq 0, V_k = \Psi^- \Lambda^{-k} q_1^- \\ \forall k, \in \mathbb{Z}, k > 0, V_k = \Phi^+ \Gamma^{k-1} q_2^+ + \Phi^- \Gamma^{1-k} q_2^- \\ q_2^+ = R_{22} q_2^- \\ q_1^- = T_{12} q_2^- \end{cases} \quad (2.24)$$

In equations (2.23) and (2.24) q_1^+ and q_1^- (resp. q_2^+ and q_2^-) are the wave amplitude vectors for the positive and negative going waves in the first waveguide (resp. second waveguide) while matrices R_{11} , T_{21} , R_{22} and T_{12} are reflection and transmission matrices to be determined. This is achieved by substituting the kinematic assumptions of equations (2.23) and (2.24) into the equation (2.22). Two systems of equations involving a matrix S are obtained:

$$S = \begin{pmatrix} S_{11} & S_{12} \\ S_{21} & S_{22} \end{pmatrix} = \begin{pmatrix} D_{RL}^1 \Psi^- \Lambda + (D_{RR}^1 + D_{LL}^c) \Psi^- & D_{LR}^c \Phi^+ \\ D_{RL}^c \Psi^- & (D_{RR}^c + D_{LL}^2) \Phi^+ + D_{LR}^2 \Phi^+ \Gamma \end{pmatrix} \quad (2.25)$$

$$\begin{pmatrix} S_{11} & S_{12} \\ S_{21} & S_{22} \end{pmatrix} \begin{bmatrix} R_{11} \\ T_{21} \end{bmatrix} = - \begin{bmatrix} D_{RL}^1 \Psi^+ \Lambda^{-1} + (D_{RR}^1 + D_{LL}^c) \Psi^+ \\ D_{RL}^c \Psi^+ \end{bmatrix} \quad (2.26)$$

$$\begin{pmatrix} S_{11} & S_{12} \\ S_{21} & S_{22} \end{pmatrix} \begin{bmatrix} T_{12} \\ R_{22} \end{bmatrix} = - \begin{bmatrix} D_{LR}^c \Phi^- \\ (D_{RR}^c + D_{LL}^2) \Phi^- + D_{LR}^2 \Phi^- \Gamma^{-1} \end{bmatrix} \quad (2.27)$$

The presented formulation is equivalent to that of [145] that was subsequently used in [58] to optimize damage detection in joints via a wave based methodology. Noteworthy, in order to interpret the computed transmission-reflection coefficient correctly attention should be paid to the way the eigenvector constituting the matrices Φ^+ , Φ^- , and Ψ^- , Ψ^+ are constantly normalized [145]. Additionally, it is recommended to track the different wavemodes across the frequency range of interest which can be done using a modal assurance criterion [124, 123, 117] on the fully developed waveshapes of these modes (they include both interface and the condensed inner dofs of the UC).

The inverse formulation of the 1D WFEM

In previous subsections, the considered waveguides were studied at a given frequency and their dispersion properties (propagation constants, wave shapes,

scattering) and forced response were computed at that specific frequency. This is usually called the direct (formulation of the) WFEM. By contrast, one can work at a fixed wavenumber, impose the corresponding Floquet-Bloch boundary conditions and compute the eigenfrequencies and waveshapes corresponding to this wavenumber [141]. This approach is not very popular in the 1D case because damping is accounted for in terms of temporal decay via the imaginary part of the eigenfrequencies instead of via spatial decay in the real part of the wavenumber. Nonetheless, the method proceeds as follows. One chooses a wavenumber k . The corresponding propagation constant λ is obtained using the length of the UC, L , via the formula $\lambda = e^{-ikL}$. The corresponding Floquet-Bloch boundary conditions are then applied to the UC:

$$\begin{cases} U_R = \lambda U_L \\ F_R = -\lambda F_L \end{cases} \quad (2.28)$$

These conditions can be enforced using right and left projection matrices:

$$\Lambda_R = \begin{pmatrix} I & 0 \\ 0 & I \\ \lambda & 0 \end{pmatrix} \text{ and } \Lambda_L = \begin{pmatrix} I & 0 & \frac{1}{\lambda} \\ 0 & I & 0 \end{pmatrix} \quad (2.29)$$

The mass, stiffness and damping matrices of the UC are then projected which leads to the wavenumber dependent mass, stiffness and damping matrices presented in equation (2.30).

$$K(\lambda) = \Lambda_L K \Lambda_R, \quad M(\lambda) = \Lambda_L M \Lambda_R, \quad C(\lambda) = \Lambda_L C \Lambda_R \quad (2.30)$$

Eigenfrequencies and waveshapes can then be retrieved by solving the generalized eigenvalue problem:

$$(K(\lambda) + s_j C(\lambda) + s_j^2 M(\lambda)) \psi_j = 0 \quad (2.31)$$

which is analogous to complex modal analysis.

2.3 The 2D Wave Finite Element Method

With the many applications of the 1D WFEM and subsequent adaptation to discrete symmetry groups, it wasn't long before extensions to higher dimensions were considered. A first formulation for the 2D WFEM was first published in 1973 [141] but it wasn't until the 2000's [125] that the method gained some popularity. Despite this, the 2D WFEM has not been as successful as its 1D counterpart. This mostly, because a wave based formulation enabling the

computation of the FRF of 2D finite periodic media from their dispersion properties has eluded WFEM practitioners for years. Additionally, the direct version of the method can only compute wave propagation features the main directions of periodicity of a 2D (periodic) medium [125, 175]. While numerical formulations have been derived to study the scattering and transmission reflection phenomena for 2D periodic waveguides [95, 75, 44, 45, 147], these do not have the same attention as their 1D equivalent [145] as they can only deal with plane waves in infinite domains. Surprisingly, the inverse formulation of the 2D WFEM has seen more use. It is the standard method for the computation of wave solutions along the irreducible Brillouin contour (IBC) [34, 134] which is a procedure followed to track band-gaps and determine their lower and upper frequencies. Additionally, the method has been used to numerically evaluate the sound transmission loss (STL) of infinite [155, 42, 203, 57, 156] 2D periodic media which by using wavenumber windowing techniques [161, 192] allow to obtain good estimates for finite structures [204, 66]. The rest of the section is structured as follows. Subsection 2.3.1 introduces some notations and quickly presents the 2D direct WFEM. In Subsection 2.3.2 the inverse 2D WFEM is presented and a brief overview on how it can be used in order to compute the the STL of periodic structures is presented.

2.3.1 Direct formulation of the 2D WFEM

We consider the discretized UC of a 2D periodic medium. We note U its displacement vector and M , K , C its mass, stiffness and damping matrices respectively. The dofs of the UC are partitioned according to its spatial structure as illustrated in Figure 2.4 and equation (2.32):

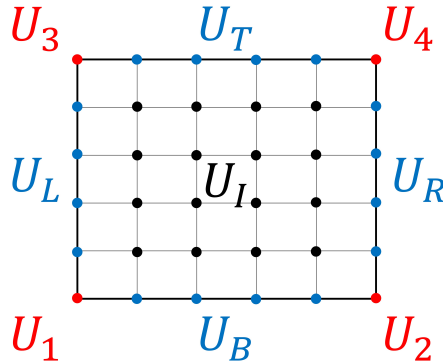


Figure 2.4: Schematic representation of the UC of a 2D periodic media illustrating the corresponding dofs partition.

$$U = [U_1 \ U_2 \ U_3 \ U_4 \ U_L \ U_R \ U_B \ U_T \ U_I]^T \quad (2.32)$$

The first step of the direct 2D WFEM consist in choosing a circular frequency ω and forming the dynamic stiffness matrix $G = K + i\omega C - \omega^2 M$ of the UC at that frequency. The inner degrees of freedom (dofs) of the UC are then condensed according to equation (2.33) which yields the condensed dynamic stiffness matrix \tilde{D} :

$$\tilde{D} = G_{HH} - G_{HI}G_{II}^{-1}G_{IH} \quad (2.33)$$

where the index H correspond to all the boundary dofs of the UC (indexes 1, 2, 3, 4, L, R, B and T). As in subsection 2.2.1 the explicit assembly of the 2D periodic structure can be realised. By rearranging the dynamic stiffness matrix according to a process described in [28] one obtains the following equation of motion for the full 2D periodic waveguide:

$$\begin{aligned} F_{r,s} = & (D_{11} + D_{22} + D_{33} + D_{44})V_{r,s} + (D_{13} + D_{24})V_{r,s+1} + (D_{12} + D_{34})V_{r+1,s} \\ & + (D_{31} + D_{42})V_{r,s-1} + (D_{21} + D_{43})V_{r-1,s} \\ & + D_{14}V_{r+1,s+1} + D_{23}V_{r-1,s+1} + D_{32}V_{r+1,s-1} + D_{41}V_{r-1,s-1} \end{aligned} \quad (2.34)$$

In equation (2.34), the indexes r and s indicate the position of the unit cell inside the 2D periodic medium. The vectors V contain only the proper dofs of the UC when it is assembled into the infinite medium:

$$V_{r,s} = [U_1^{r,s}, U_L^{r,s}, U_B^{r,s}]^T \quad (2.35)$$

and the matrix D enlarging the condensed dynamic stiffness matrix \tilde{D} of the UC to include the proper displacement vectors of adjacent cells (the sub matrices corresponding to theses added dofs are filled with 0s). One can than then look for solutions of equations (2.34) corresponding to free Bloch-Waves. I.e.:

$$\begin{cases} \forall (r, s) \in \mathbb{Z}^2, F_{r,s} = 0 \\ \exists (\lambda_x, \lambda_y) \in \mathbb{C}^2, \exists V_0 \in \mathbb{C}^n, \forall (r, s) \in \mathbb{Z}^2, V_{r,s} = \lambda_x^r \lambda_y^s V_0 \end{cases} \quad (2.36)$$

Which leads to the classical 2D WFEM formulation [141, 4, 125]:

$$\begin{aligned} 0 = & \left[(D_{11} + D_{22} + D_{33} + D_{44}) + \lambda_y(D_{13} + D_{24}) + \lambda_x(D_{12} + D_{34}) \right. \\ & + \frac{1}{\lambda_x}(D_{31} + D_{42}) + \frac{1}{\lambda_y}(D_{21} + D_{43}) \\ & \left. + \lambda_x \lambda_y + D_{14} + \frac{\lambda_y}{\lambda_x} D_{23} + \frac{\lambda_x}{\lambda_y} D_{32} + \frac{1}{\lambda_x \lambda_y} D_{41} \right] \Psi \end{aligned} \quad (2.37)$$

A modified equation of motion whose validity is restrained to loads and displacements satisfying the Floquet-Bloch conditions associated to the wavenumber pair (k_x, k_y) is derived:

$$[\tilde{K}(k_x, k_y) + i\omega\tilde{C}(k_x, k_y) - \omega^2\tilde{M}(k_x, k_y)] U_r = \tilde{D}(k_x, k_y)U_r = P_F(k_x, k_y)F \quad (2.42)$$

Where for a generic matrix $A \in M_n(\mathbb{C})$, the matrix $\tilde{A}(k_x, k_y)$ is derived from matrix A according to equation (2.43).

$$\tilde{A}(k_x, k_y) = P_F(k_x, k_y)AP_U(k_x, k_y) \quad (2.43)$$

Equation (2.42) can be used to compute the response of an infinite periodic medium to a load with 2D Floquet-Bloch symmetry (such as a plane wave) or to compute its band diagram when there is no load [134]:

$$[\tilde{K}(k_x, k_y) + i\omega_r\tilde{C}(k_x, k_y) - \omega_r^2\tilde{M}(k_x, k_y)] \psi_r = 0 \quad (2.44)$$

2.4 The semi analytical finite element method and the shift-cell operator method

The Semi Analytical Finite Element Method (SAFE or SAFEM) can be traced back to the early 1970's [196] and was further developed during the 80's [173, 53] in order to compute the dispersion properties of homogeneous media. By including wavenumbers in a modified FEM formulation, the SAFE allows the modeling of dispersive phenomena with analytical (infinite) accuracy in their directions of propagation. Thus the numerical discretization effects are limited to the traverse modeling of the cross-section. Like the WFEM, The method enables the computation of dispersion curves, K-Spaces, the transmission-reflection coefficients of waves through scatterers and the forced response of homogeneous, layered and helical waveguides [50, 3, 18, 184]. Originally the SAFE was developed for structures that are homogeneous in their direction of propagation as in this particular case it has better numerical properties than the WFEM. More recently, the method was used to study wave propagation through periodic media [47, 8, 7, 127]. In that setting, it is known as the shift-cell operator method or shift-cell method (SCOM) and its main advantage over the WFEM lies in the fact it enables the computation of dispersion curves in any direction of propagation by solving a well behaved quadratic eigenvalue problem [47] instead of the difficult to solve transcendental problem that would be required to solve with the WFEM [125, 175]. Despite its complementary with the WFEM, the SCOM is a far less popular method because it requires extra non standard FEM-like matrices that are not included in most commercial

FEM packages. Therefore, the only ways to use it are to enter the corresponding weak form equation in software like COMSOL or FreeFem++ or to implement the whole formulation by hand in ones preferred programming language. Those interested in the latter option should give a look to the FEM tutorial on "What-When-How" (link). The rest of the section is organized as follows. In subsection 2.4.1 the classical weak form for FEM corresponding to 3D linear elasticity [152, 112, 218] is derived. Notations and concepts are introduced that allow to easily show how the SAFE and the SCOM diverge from the classical discretization techniques. Finally, the weak form for the SAFE/SCOM is derived in Subsection 2.4.1.

2.4.1 A brief overview of the classical finite element method

We first consider the problem of linear elasticity for a displacement field u , a volume load f and density ρ on a domain Ω with Neumann boundary conditions at its boundary $\partial\Omega$:

$$\begin{cases} \operatorname{div}(\sigma) + f = \rho \ddot{u} \text{ on } \Omega \\ \sigma \cdot \vec{n} = t_0 \text{ on } \partial\Omega \end{cases} \quad (2.45)$$

The stress tensor σ is linked to the linear strain tensor ϵ by a fourth order symmetric tensor C representing Hooke's law of elasticity as per equation (2.46) in which Einstein's notation is used:

$$\sigma_{ij} = C_{ijkl} \epsilon_{kl} \quad (2.46)$$

Equation (2.46) is put in vector form by focusing on the 6 independent components of the strain and stress tensors. The following notations are introduced:

$$\begin{cases} \epsilon_v = [\epsilon_{11}, \epsilon_{22}, \epsilon_{33}, 2\epsilon_{23}, 2\epsilon_{13}, 2\epsilon_{12}]^T \\ \sigma_v = [\sigma_{11}, \sigma_{22}, \sigma_{33}, \sigma_{23}, \sigma_{13}, \sigma_{12}]^T \end{cases} \quad (2.47)$$

Leading to the vector form of equation (2.46):

$$\sigma_v = C_m \epsilon_v \quad (2.48)$$

, with C_m a 6 by 6 symmetric matrix representing Hooke's law. In order to completely rewrite equation (2.45) in a FEM friendly way, two differential

operators are introduced:

$$D = \begin{bmatrix} \frac{\partial}{\partial x} & 0 & 0 \\ 0 & \frac{\partial}{\partial y} & 0 \\ 0 & 0 & \frac{\partial}{\partial z} \\ 0 & \frac{\partial}{\partial z} & \frac{\partial}{\partial y} \\ \frac{\partial}{\partial z} & 0 & \frac{\partial}{\partial x} \\ \frac{\partial}{\partial y} & \frac{\partial}{\partial x} & 0 \end{bmatrix} \quad \text{and} \quad D^T = \begin{bmatrix} \frac{\partial}{\partial x} & 0 & 0 & 0 & \frac{\partial}{\partial z} & \frac{\partial}{\partial y} \\ 0 & \frac{\partial}{\partial y} & 0 & \frac{\partial}{\partial z} & 0 & \frac{\partial}{\partial x} \\ 0 & 0 & \frac{\partial}{\partial z} & \frac{\partial}{\partial y} & \frac{\partial}{\partial x} & 0 \end{bmatrix} \quad (2.49)$$

Because of their differential nature, these operators can only be used to left multiply when doing matrix operations. It should also be noticed that:

$$\begin{cases} \epsilon_v = Du \\ \text{div}(\sigma) = D^T \sigma_v \end{cases} \quad (2.50)$$

The first part of equation (2.45) is then rewritten as:

$$D^T C_m D u + f = \rho \ddot{u} \quad (2.51)$$

Introducing a vector test function w belonging to the relevant space S , the weak form of equation (2.51) is derived:

$$\forall w \in S, \iint\iint w^T D^T C_m D u + \iint\iint w^T f = \iint\iint w^T \rho \ddot{u} \quad (2.52)$$

Integrating by part and using the boundary conditions, equation (2.53) is derived:

$$\forall w \in S, \iint\iint w^T f + \iint\iint w^T t_0 = \iint\iint (Dw)^T C_m D u + \iint\iint w^T \rho \ddot{u}, \quad (2.53)$$

with t_0 defined in equation (2.45). Appropriate shape functions can then be chosen for w and u leading to a FEM discretization. In most cases the same shape functions are used for w and u which leads to symmetric mass and stiffness matrices. This is known as the Ritz–Galerkin method.

The SAFE and the SCOM

The Shift Cell Operator Method [47] was invented to compute the dispersion curves of 2D periodic media in any direction, which was not possible using the WFEM. The method works mostly like FEM with a simple difference: a change of variables is operated in the displacement variable u and the equation

of motion is rewritten for functions v and g such that:

$$\begin{cases} u(x, y, z, t) = v(x, y, z, t)e^{-i(k_x x + k_y y)} \\ f(x, y, z, t) = g(x, y, z, t)e^{-i(k_x x + k_y y)}. \end{cases} \quad (2.54)$$

Equation (2.51) is then rewritten using v and g :

$$\begin{cases} (D_{xy}^T C_m D_{xy} v + g)e^{-i(k_x x + k_y y)} = \rho v e^{-i(k_x x + k_y y)} \\ D_{xy} = D - ik_x D_x - ik_y D_y, \end{cases} \quad (2.55)$$

,with D_x and D_y matrices, and not differential operators, defined in equation (2.56):

$$D_x = \begin{bmatrix} 1 & 0 & 0 \\ 0 & 0 & 0 \\ 0 & 0 & 0 \\ 0 & 0 & 0 \\ 0 & 0 & 1 \\ 0 & 1 & 0 \end{bmatrix} \quad \text{and} \quad D_y = \begin{bmatrix} 0 & 0 & 0 \\ 0 & 1 & 0 \\ 0 & 0 & 0 \\ 0 & 0 & 1 \\ 0 & 0 & 0 \\ 1 & 0 & 0 \end{bmatrix} \quad (2.56)$$

They account for the fact that derivatives of the product of a function with an exponential follow the pattern of equation (2.57):

$$\forall q \in C^1(\mathbb{R}), \quad \frac{\partial}{\partial x}(q(x)e^{-ik_x x}) = \left(\frac{\partial}{\partial x}q(x) - ik_x q(x) \right) e^{-ik_x x} \quad (2.57)$$

Taking the weak form of equation (2.55), and integrating by part, equation (2.58) is derived:

$$\begin{aligned} \iiint w^T g + \iint w^T t_0 e^{i(k_x x + k_y y)} &= \iiint (Dw)^T C_m Dv + \iiint w^T \rho \ddot{v} \\ &+ k_x^2 \iiint (D_x w)^T C_m D_x v \\ &+ k_y^2 \iiint (D_y w)^T C_m D_y v \\ &+ k_x k_y \iiint (D_x w)^T C_m D_y v + (D_y w)^T C_m D_x v \\ &- ik_x \iiint (Dw)^T C_m D_x v - (D_x w)^T C_m Dv \\ &- ik_y \iiint (Dw)^T C_m D_y v - (D_y w)^T C_m Dv, \end{aligned} \quad (2.58)$$

which leads to the discretization described in equation (2.59).

$$(K + sC + s^2M - ik_xL_x - ik_yL_y + k_x^2H_{xx} + k_y^2H_{yy} + k_xk_yH_{xy})U = F, \quad (2.59)$$

where K , M , and C are the classical mass, stiffness and damping matrices. The additional H and L matrices are respectively symmetric and antisymmetric and account for modulation in equation (2.54). In order to compute the dispersion characteristics of a medium using the SAFE/SCOM one must apply periodicity boundary conditions to the corresponding UC. One could then choose a circular frequency ω and a direction of propagation θ . By substituting k_x and k_y by $k \cos \theta$ and $k \sin \theta$ the wave propagation properties of the medium in that direction can then be computed. Another possibility is to fix the wavenumbers k_x and k_y and solve for eigenfrequencies at which these wavenumbers are reached. This is usually not done as the WFEM already allows for such computation without requiring the extra L and H matrices.

2.5 Wavenumber extraction techniques

Wavenumber extraction, also known as wavenumber identification, has many applications in various scientific fields such as magnetic resonance imaging, Raman spectroscopy [110, 111] or the protection of power lines [91]. In the context of structural dynamics and vibroacoustics, wavenumber extraction is being used in imaging techniques for damage detection [162, 105, 205], to gain insight into the wave propagation features of homogeneous and periodic media [160, 187], or for the characterization [186] and model updating of structures [210]. Herein, wavenumber extraction is defined as the determination of the complex wavenumbers (1D case) or k-space (2D, 3D and N-D cases) that characterize wave propagation inside a physical medium at a given frequency from the displacement field of such a medium at the frequency of interest. It is an inverse problem that has given raise to various methods in different fields. This section discusses the most popular methods for wavenumber extraction in a vibroacoustics context and is structured as follows. In subsection 2.5.1, the Fourier transform is discussed as it is the easiest method to implement. subsection 2.5.2 is dedicated to Mc Daniels method, a 1D wavenumber extraction that relies on a nonlinear fit based on a general analytical expression for 1D displacements fields. In subsections 2.5.4 and 2.5.5, the Inhomogenous Wave Correlation (IWC) and the Inverse Wave Decomposition are presented.

2.5.1 The Fourier transform

The Fourier transform (FT) is an integral transform that maps a function of time (resp. space) into another function of frequency (resp. wavenumber). In the 1D case, the Fourier transform is natively defined on $L^1(\mathbb{R})$ for the 1D case (the space of Lebesgue summable functions from \mathbb{R} to \mathbb{C}) and the Fourier transform \hat{f} of a function $f \in L^1(\mathbb{R})$ is obtained as follows:

$$\forall k \in \mathbb{R}, \hat{f}(k) = \int_{-\infty}^{+\infty} e^{-ikx} f(x) dx \quad (2.60)$$

While it is only natively defined on L^1 , the Fourier transform can be extended to L^2 and beyond e.g. by continuity or duality. Equation (2.60) can be interpreted as the decomposition of the function f in the continuous orthogonal basis formed by complex exponential functions (function of the form $f : x \mapsto e^{ikx}$), thus, $\hat{f}(k)$ can be interpreted as the contribution of a plane wave of wavenumber k to the function f . On paper, the FT seems perfect for wavenumber extraction but there are three issues that hinder its application to practical cases.

The first issue is related to orthogonality and signal length. Indeed, as can be seen in equation (2.60) the FT only deals with functions defined on the full real axis and thus is only defined for signals of infinite lengths as complex exponential functions do not form an orthogonal basis on finite intervals. Attempts to deal with finite signals introduce windowing which by convolution leads to leakage.

The second issue is related to sampling (a.k.a discrete signals). With the advent of the digital era, signals are no longer processed in analog forms but in digital ones. I.e. available signals are discrete and not continuous as they are obtained by periodic sampling of continuous variables/functions. To account for this one must use the Discrete Fourier Transform instead and the Fourier transform which introduces aliasing (the inability to distinguish between certain wavenumbers) by Nyquist–Shannon sampling theorem. The impact of sampling can also be understood from a continuous framework by using Dirac Combs which leads to the same conclusions.

The last issue is related to the very definition of the FT. Indeed, the FT only involves real wavenumbers and thus does not (in itself) provides the means to estimate the imaginary parts of wavenumbers that come e.g. with the introduction of energy dissipation mechanisms in vibroacoustics.

Nonetheless, the FT can be an appropriate wavenumber extraction method when all three of its downsides are properly mitigated. That is, (1) the signal length contains a high number of wavelengths for the considered wavenumbers in order to mitigate leakage. (2) The sampling period is small compared to the

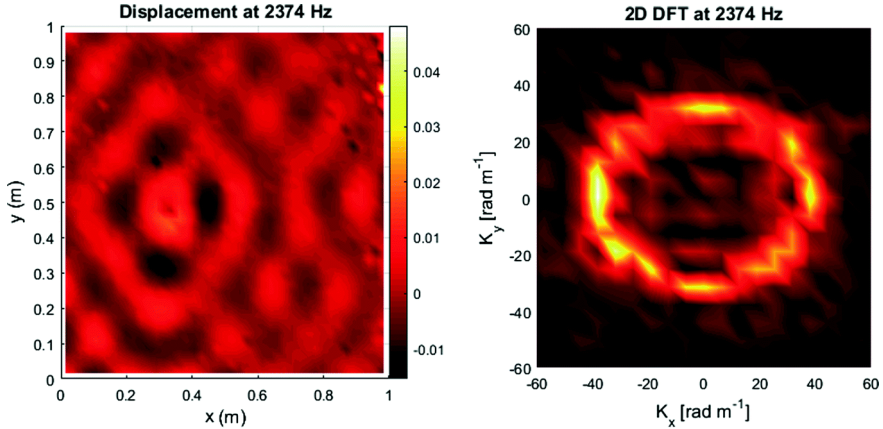


Figure 2.5: Displacement field of a composite plate and its 2D Fourier transform [160]

considered wavelengths and an appropriate low-pass filter is used in order to prevent issues related to aliasing. (3) The considered phenomena/signal involve mostly-real wavenumbers such that the imaginary parts of wavenumbers can be neglected. In such cases the Fourier transform can be used in order to gain insight as is demonstrated in Figure 2.5 taken from the paper [160] by Ramzi et al. in which the K-space of a composited plate is identified using the 2D Fourier transform.

2.5.2 Mc Daniel's method

Mc Daniel's method [138] is a method for wavenumber extraction for 1D homogeneous media that extracts the wavenumbers from a 1D displacement by creating a nonlinear fit based on an analytical formula. Indeed, in the absence of sources within the measurement zone, the displacement field f can be developed into a sum of forward and backward going waves as described in equation (2.61):

$$f(x) = \sum_{n=1}^{\infty} (a_n e^{-ik_n x} + b_n e^{ik_n x}) \quad (2.61)$$

In equation (2.61), k_n is the n^{th} wavenumber, a_n the complex amplitude of the n^{th} forward going wave and b_n the complex amplitude of the n^{th} backward going wave. Though f is theoretically the sum of an infinite series, this series can be truncated in all practical cases. In the original paper, Euler-Bernoulli and Timoshenko beam theories are used in order to justify a truncation at

$n = 2$ when dealing with beams. Good numerical results are obtained as demonstrated in Figure 2.6 taken from the article. An implementation of this

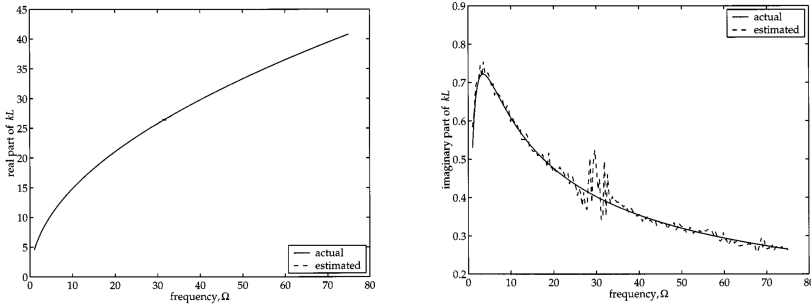


Figure 2.6: Comparison of the actual wavenumber values to one estimated with Mc Daniel's method [138]

method limited to the Euler-Bernoulli assumption is given in Appendix C. Recently, Mc Daniels method was extended by Zhang et al. [210] in order to deal with periodic structures. Based on Floquet-Bloch theory, the new expansion uses the propagation constants $\lambda = e^{-ikL_x}$ instead of the wavenumber k and uses vector displacements for each UC:

$$V_j = \sum_{n=1}^{n_c} \alpha_n \psi_n^+ \lambda_n^j + \beta_n \psi_n^- \lambda_n^{N-j} \quad (2.62)$$

In equation (2.62) V_j is the vector of measurements carried out on the j^{th} UC, λ_n is the n^{th} propagation constant, N is the total number of cells in the structure, ψ^+ and ψ^- the projection of the n^{th} forward and backward going waveshapes at the measurements location. Lastly, α_n and β_n are the complex amplitudes of the forward and backward going waves. This method has been used to retrieve the propagation constants and waveshapes of periodic structures both in numerical and experimental cases. An example of 3D waveshapes retrieved via this method is presented in Figure 2.7 taken from [210].

2.5.3 The ESPRIT algorithm

ESPRIT, or Estimation of Signal Parameters via Rotational Invariance Techniques is a method that was originally created for high resolution Direction Of Arrival (DOA) and frequency estimations [163, 166, 165]. This is achieved by decomposing the process signal f into a finite sum of plane waves for which the wavenumbers k_n are retrieved. The method has 1D and 2D versions which

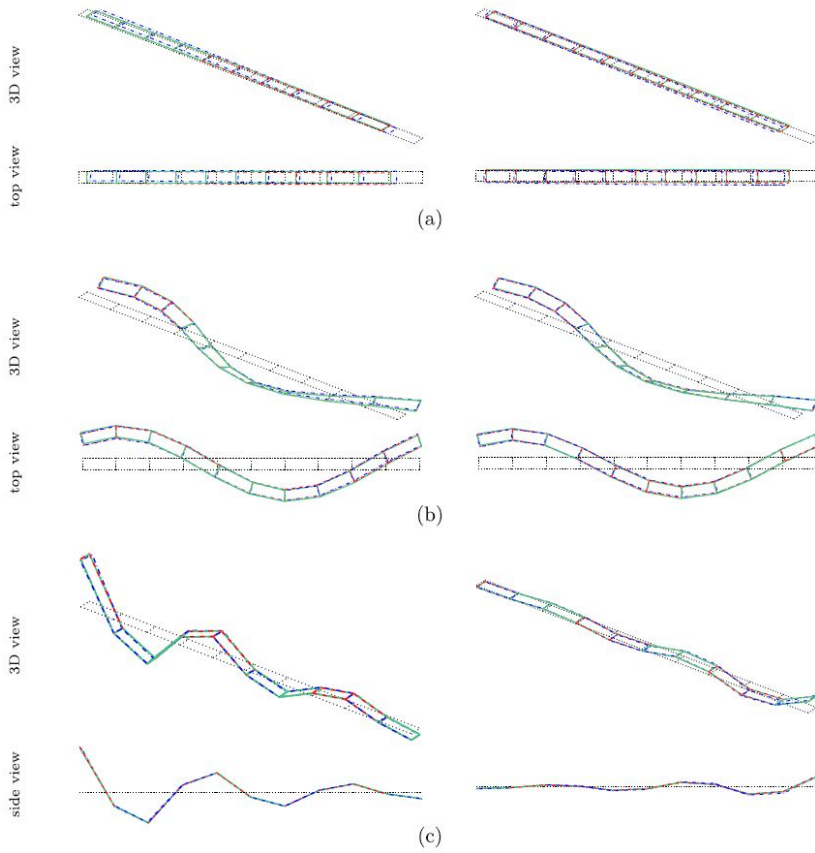


Figure 2.7: The real parts of the positive going (left) and negative going (right) free wave components identified from noise-free data (dashed lines) and noisy data (dot-dashed lines) and the exact free waves (solid lines); (a)–(c): wave pairs 1 to 3. [210]

have been used in vibroacoustics under the respective names High Resolution Wavenumber Analysis [131] (1D) and High Resolution Wavevector Analysis [132] (2D) (HRWA for both). In the 1D case ESPRIT assumes the signals takes the form:

$$f(x) = \sum_{n=1}^{n_c} a_n e^{-ik_n x} \quad (2.63)$$

and seeks to identify the value of the wavenumbers k_n from the values f takes. It achieves this by exploiting important algebraic properties of exponential

functions and translation operators.

For all translation lengths $L \in \mathbb{R}$, a corresponding operator \mathcal{O}_L is defined on $\mathbb{C}^{\mathbb{R}}$, the space of functions from \mathbb{R} to \mathbb{C} .

$$\begin{aligned} \mathcal{O}_L : \mathbb{C}^{\mathbb{R}} &\rightarrow \mathbb{C}^{\mathbb{R}} \\ f &\mapsto g, \forall x \in \mathbb{R}, g(x) = f(x + L) \end{aligned} \quad (2.64)$$

As it happens, exponential functions g of the form $g(x) = e^{-ikx}$ are eigenvectors for all operators \mathcal{O}_L for the eigenvalues $\lambda = e^{-ikL}$ which stems from the multiplicative property of exponential functions. By choosing a length L such that $\lambda_n = e^{-ik_n L}$ and $\lambda_m = e^{-ik_m L}$ are different if $n \neq m$, one can estimate all the wavenumbers k_n of equation (2.63) in two key steps.

First, we introduce the Krylov subspace [104] $E = \text{span}\{\mathcal{O}_L^n(f), n \in \mathbb{N}\}$ which by construction is stable by \mathcal{O}_L . Using the aforementioned algebraic property of exponential functions and the analytical expression of f , it can be shown that E is spanned by the first n_c (independent) Krylov vectors such that it is of finite dimension (n_c): $E = \text{span}\{\mathcal{O}_L^n(f), n \in \llbracket 0, n_c - 1 \rrbracket\}$. Since E is both of finite dimension and stable by \mathcal{O}_L the restriction of \mathcal{O}_L to E is an endomorphism of finite dimension and can be represented on matrix form in any basis \mathcal{B} of E . The resulting matrix, M can be diagonalised and its eigenvalues are the propagation constants $\lambda_n = e^{-k_n L}$. The wavenumbers k_n are then retrieved by taking the logarithm of these eigenvalues. This process can be generalized to 2D and more by simultaneously diagonalising translation operators in each direction of the underlying space.

While the method described above works well, it does not account for the fact that most signals are finite, discrete and usually contain some noise. Thus the function f takes the form of a vector of length N corresponding to a periodic sampling of period L . We also refer to this vector as f :

$$f = [f_1, f_2, \dots, f_N]^T = [f(x_0 + L), f(x_0 + 2L), \dots, f(x_0 + NL)]^T \quad (2.65)$$

To build a representation of the Krylov subspace E , the Hankel matrix H of the vector f is built.

$$\begin{bmatrix} f_1 & f_2 & \dots & f_{N-K} \\ f_2 & f_3 & \dots & f_{N-K+1} \\ \vdots & \dots & \ddots & \vdots \\ f_K & f_{K+1} & \dots & f_N \end{bmatrix} \quad (2.66)$$

with the integer K usually chosen as $\lfloor \frac{N}{2} \rfloor$. In order to build a robust representation of E a singular value decomposition (SVD) of H is carried

out in order to separate the signal space from the noise space:

$$H = WDV^* \quad (2.67)$$

with W and D orthogonal matrices and D a diagonal matrix with only positive elements ordered by decreasing values. The columns of W are called the left singular vectors and span the same subspace as the columns of H . To separate the signal space from the noise space, one needs to only keep the first n_c columns of W thus creating the matrix W_s . Having built a robust representation of E in the matrix W_s , the only task left is to build a representation of the translation operator \mathcal{O}_L . This achieved by partitioning lines of W_s in three parts:

$$W_s = \begin{bmatrix} W_- \\ W_m \\ W_+ \end{bmatrix} \quad (2.68)$$

with W_- and W_+ 1 by n_c matrices and W_m a $K - 2$ by n_c matrix. A matrix representation M of the operator \mathcal{O}_L is then obtained by solving the the following problem in the least square sense:

$$\begin{bmatrix} W_m \\ W_+ \end{bmatrix} = M \begin{bmatrix} W_- \\ W_m \end{bmatrix} \quad (2.69)$$

The propagation constants λ_n are then obtained by computing the eigenvalues of M .

Finally, when the number of observable waves n_c present in the signal is not known in advance, an automatic estimation criterion called ESTER (ESTimation or ERror) [12] was used in [132]. The idea is to build the W_s matrix for different values of n_c the final number of waves is obtained by finding the value of n_c that minimizes the norm of the residual:

$$\left\| \begin{bmatrix} W_m(n_c) \\ W_+(n_c) \end{bmatrix} - M(n_c) \begin{bmatrix} W_-(n_c) \\ W_m(n_c) \end{bmatrix} \right\|_2 \quad (2.70)$$

corresponding to the representation M of \mathcal{O}_L .

The presented methodology easily extends to the 2D cases by diagonalizing translation operators in both directions of sampling. Additionally, a basic implementation of the ESPRIT algorithm for wavenumber extraction in beams can be found in Appendix C and its performance is compared with the wavenumber extraction method developed within this thesis in Chapter 5.

2.5.4 The Inhomogeneous Wave Correlation

The Inhomogenous Wave Correlation (IWC) is a wavenumber extraction techniques that is based on a correlation criterion. It was first developed

by Berthault et al [21]. The idea is as follows. Let S be a subset of \mathbb{R}^n of finite measure $|S|$. The standard Hermitian scalar product for two functions f and g from S to \mathbb{C} is defined as follows:

$$(f|g) = \frac{1}{|S|} \int_S f^*(x)g(x)dx \quad (2.71)$$

Accordingly, the norm of f (or any other function) is defined as:

$$\|f\|_2 = (f|f) \quad (2.72)$$

And the correlation between f and g is defined as:

$$corr(f, g) = \frac{|(f|g)|}{\|f\|_2 \|g\|_2} \quad (2.73)$$

The set of wavevectors K is then defined as follows:

$$K = \{k_r d, (d, k_r) \in \mathbb{S}^n \times \mathbb{C}\} \quad (2.74)$$

with \mathbb{S}^n being the unit sphere of \mathbb{R}^n . For all wavevectors $k \in K$ the associated plane wave function f_k on S is then defined as follows:

$$f_k(x) = e^{-i(x|k)} \quad (2.75)$$

with $(\cdot|\cdot)$ the standard Hermitian product on \mathbb{C}^n . The *IWC* function can then be defined for a direction d , a wavenumber k_r and a function f :

$$IWC(f, d, k_r) = corr(f, f_{k_r d}) \quad (2.76)$$

For a given function f , and direction d , the *IWC* carries out wavenumber extraction by looking for the wavenumber k_r that maximizes the *IWC* function. The corresponding wavevector, $k_r d$ is considered to be part of the k -space of the function f .

Like the Fourier transform, the *IWC* suffers from the fact that for two wavevectors $(k_1, k_2) \in K^2$ such that $k_1 \neq k_2$, the correlation function $corr(f_{k_1}, f_{k_2})$ is not necessarily equal to 0 due to both the finiteness of the set S and the fact that the *IWC* accepts complex wavevectors. This lack of orthogonality can lead to strong distortions in the estimates of the wavenumbers/wavevector of the function f if the domain S is not big enough compared to the characteristics wavelengths of f .

To try and tackle this issue variantes of the *IWC* that modify the family of function f_k have been developed [187, 185]. In [187] Van Belle et al, used a new family of functions g_k defined as follows

$$g_k(x) = e^{-i(|d|x-x_0)|k_r} \quad (2.77)$$

with $k = k_r d$, $(d, k_r) \in \mathbb{S}^n \times \mathbb{C}$ and $x_0 \in \mathbb{R}^n$ the position of the excitation source. In [185], G. Tufano proposed a similar method for 2D flat structures that is based on the Green function of an infinite isotropic Kirchhoff-Love plate. Because isotropy is assumed, the method only retrieves one wavenumber k_r instead of a collection of wavevectors k . Consequently, the corresponding family of functions is

$$h_{k_r}(x) = H_0^{(1)}(k_r \|x - x_0\|) - H_0^{(1)}(ik_r \|x - x_0\|) \quad (2.78)$$

with $H_0^{(1)}$ being a Hankel function of the first kind.

Overall, the strength of IWC class of methods is its resistance to noise which is practical when dealing with experimental data and its relative accuracy when the characteristic wavelength of the function f is small compared to the characteristic length of the domain S . On the other hand, because the method is not exact (e.g. like Mc Daniel's methods) it is unable to retrieve the extract wavenumbers/k-space even when dealing with noiseless numerical data.

2.5.5 The Inverse Wave Decomposition

The Inverse Wave Decomposition [169] (IWD) is a 2D wavenumber extraction method that was initially developed by Chardon et al. [40]. The method relies on a fit of the displacement field by a sum of plane waves coming from different directions:

$$f(x) = \sum_{n=0}^{N-1} \alpha_n e^{-i(d_n|x)k_n} + \beta_n e^{i(d_n|x)k_n}. \quad (2.79)$$

In equation (2.79), $d_n = (\cos(\frac{n\pi}{N}), \sin(\frac{n\pi}{N}))$ is the unit vector indicating the direction of the n^{th} pair of forward and backward going waves, k_n is the wavenumber of that pair of waves and α_n and β_n their respective complex amplitudes. Asymptotically, when $N \rightarrow \infty$ the IWD becomes close to (but is not actually) exact for the Helmholtz equation and it remains a good approximation for the dynamics of 2D plate-like structures. In spirit, it can be considered as the 2D successor of Mc Daniel's method [138] though the formulation would need some modifications in order to fully deserve the title. The main limitation of the IWD is related to the fact that high values of N are required to obtain a good estimates of the wavenumbers k_n when the considered wavefield f correspond to mid-high frequencies. Under such conditions, a nonlinear fit based on equation (2.79) becomes practically infeasible.

Chapter 3

Model Order Reduction for 1D Unit Cell Modeling

Part of this Chapter has already been published as [32]: "R. Boukadia, C. Droz, M. Ichchou, W. Desmet. A Bloch wave reduction scheme for ultrafast band diagram and dynamic response computation in periodic structures, *Finite Elements In Analysis And Design*, 148, 1-12, September 2018."

In this Chapter, a novel model order reduction scheme for the unit-cell modeling of 1D wave propagation in periodic structures is presented. The proposed method is developed to reduce the time required to compute the 1D dispersion characteristics of periodic media or the forced response of finite periodic structures and coupled waveguides. The proposed MOR scheme targets the two most computationally expensive operations of the direct 1D WFEM: The dynamic condensation of the inner degrees of freedom and the resolution of the WFEM's palindromic eigenvalue problem. For the former, an efficient approach inspired by substructuring techniques is proposed. It uses the Craig-Bampton MOR [49] to reduce the inner degrees of freedom of the UC. This technique was first developed By Cotoni et al. in [48] where 2D wave propagation features computed with the WFEM were used in order to feed Statistical Energy Analysis (SEA) based models of complex structures and waveguides for which analytical expressions of the modal density are not available. The method was later rediscovered by Zhou et. al in [216] and another step was taken by Krattiger et. al in [102] with the addition of an interface reduction (IR) in the context of band diagram computations. That second reduction, however, had to be carried out at every point of the irreducible Brillouin contour. In the author's words: "*this means that IR must be applied at every \mathbf{k} point, which limits the*

ability of IR to speed up band structure computations. For this reason, IR is only recommended for situations where a reduced model size is desirable for reasons other than directly speeding up band-structure computations". This issue was finally addressed by the same authors in [103] in which the IR was made wavenumber independent by forcing the mode-based projection basis to respects the topological structure of the UC. In all these cases, the Craig-Bampton MOR scheme was shown to have little impact on the model accuracy while massively increasing its computational efficiency. Hence this scheme serves as a foundation of the MOR strategy proposed in this chapter. In order to speed up the resolutions of the WFEM's palindromic eigenvalue problem, a novel interface reduction technique is developed. The proposed method takes inspiration from the work of Droz et al. [60, 62] where a sample of solutions computed at the waves' cut-on frequencies is used in order to project the WFEM's signature eigenvalue problem. While this interface reduction strategy typically requires more time to produce a ROM than those presented in [102] and [103] the reduced order models (ROMs) it produces are usually more compact and more accurate than those generated with these methods as each added dof corresponds to an exact solutions of the eigenvalue problem of interest. However, the sampling strategy proposed in [60] uses an inefficient formulation of the direct 1D WFEM and is not guaranteed the capture all wave-related phenomena in periodic structures as it was developed for homogeneous waveguides. The MOR scheme proposed in this chapter overcome the limitations of previous methods in the following ways. The Craig-Bampton MOR used in [48, 102, 216, 103] is extended to the case of generalized and viscoelastic damping models which were not addressed in previous studies. Additionally, a new sampling strategy relying on the inverse formulation of the 1D WFEM is used in order to improve the scheme of [60] and ensure complex wave phenomena in periodic waveguides are captured.

The rest of the Chapter is organized as follows. In Section 3.1 a quick reminder of the 1D WFEM workflow is given. The method of [216] is then presented in Section 3.2 along with the proposed generalization of the method. In Section 3.3 the interface reduction scheme of [60] is detailed while the method developed during this thesis is presented in Section 3.4. Numerical benchmarks are proposed in Section 3.5 and Section 3.6 summarizes the main conclusions. Lastly, basic Matlab codes for some of the methods presented can be found in Appendix B.

3.1 Reminder: Computing wavelshapes and propagation constants via the direct 1D WFEM

In this Chapter, we assume a discretized representation of the UC has been obtained using e.g. the finite element method. The mass, stiffness and damping matrices of the UC are referred to as K , M and C respectively. Additionally, a partition of the UC's dofs vector, U , is established according to the UC's spatial structure presented in Figure 3.1:

$$U = \begin{bmatrix} U_L \\ U_R \\ U_I \end{bmatrix}. \quad (3.1)$$

The subscripts R , L and I are used for variables associated with the right, left

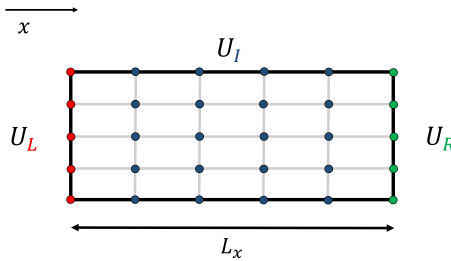


Figure 3.1: Dofs' partition for the UC of a 1D periodic structure

and internal dofs of the UC, respectively. Additionally, the subscript B will be used for quantities associated to all interface dofs i.e.:

$$U_B = \begin{bmatrix} U_L \\ U_R \end{bmatrix}. \quad (3.2)$$

The dynamic stiffness matrix D of the UC at the circular frequency ω is then formed: $G = K + i\omega C - \omega^2 M$. In order to compute the propagation constants and wavelshapes of waves propagating at that frequency, the inner dofs of the UC are condensed according to equation (3.3):

$$D = G_{BB} - G_{BI}G_{II}^{-1}G_{IB}, \quad (3.3)$$

which requires the inversion of the matrix G_{II} . This operation can be extremely computationally expensive when the number of inner dofs n_I of the UC is large. Conversely, its computational time could be lowered greatly assuming n_I can

be reduced without degrading the model's accuracy. This is the focus of Section 3.2.

Once the condensed dynamic stiffness matrix has been computed the eigenvalue problem (EVP) [64]:

$$\left(\frac{1}{\lambda_p} D_{RL} + (D_{RR} + D_{LL}) + \lambda_p D_{LR} \right) \psi_p = 0 \quad (3.4)$$

yielding the propagation constants λ_p and waveshapes ψ_p must be solved. Again, this can be computationally expensive depending on both the linearization chosen to solve the EVP and the number of interface dofs n_B as computational complexity of solving this EVP scales with n_B^3 . Therefore, reducing the number of interface dofs n_B in a way such that all the "important" propagation constants and waveshape can be retrieved would also enable high gains in computational efficiency. Methods developed to reach this goal are presented in Sections 3.3 and 3.4.

3.2 Craig-Bampton Model Order Reduction for dynamic condensation speed up

This Section details the method of [216] that uses the Craig-Bampton MOR in order to speed up dynamic condensation computations in 1D UCM. To achieve this, the UC's boundary dofs are used as master degrees of freedom while the internal dofs are targeted for reduction. The MOR scheme has two parameters: A frequency f_{max} that describes the maximal frequency at which the ROM should be valid and a frequency multiplier n_f that controls the modal truncation in the MOR process. As such, the structure of the projection basis P is the following:

$$U = \begin{bmatrix} U_B \\ U_I \end{bmatrix} = \begin{pmatrix} I_B & 0 \\ \Phi_C & \Phi_D \end{pmatrix} \begin{bmatrix} U_B \\ U_I^r \end{bmatrix} = P U^r. \quad (3.5)$$

In equation (3.5), Φ_C represents the static constraint modes of the Guyan condensation [83] and is given by the equation:

$$\Phi_C = -K_{II}^{-1} K_{IB}. \quad (3.6)$$

The matrix Φ_D is a real matrix whose columns span the subspace of the clamped interface modes of the UC's whose frequency f is inferior to the product $n_f f_{max}$. We assume that there are p such modes. In the original paper [216], it is recommended to choose $n_f \geq 3$. Several cases are considered. When there is no damping in the UC, or that it is represented via a Caughey damping

matrix (i.e. a matrix that is diagonalized by the conservative modes of the system) Φ_D is obtained by computing the first few solutions of the eigenvalue problem (3.7):

$$\begin{cases} (K_{II} - \omega_k^2 M_{II})\phi_k = 0 \\ \Phi_D = [\phi_1, \dots, \phi_p] \end{cases}. \quad (3.7)$$

Dealing with hysteretic damping is similar. If the structure is only slightly damped, is comprised of only one material, or that all materials share the same damping coefficient, the procedure of equation (3.7) still holds but $\Re(K_{II})$ and $\Re(K_{IB})$ should be used instead of K_{II} and K_{IB} in equations (3.6) and (3.7). When that is not the case, e.g. if the structure is comprised of two materials with very different damping coefficients, the clamped interface modes should be computed according to equation (3.8):

$$\begin{cases} (K_{II} - \omega_k^2 M_{II})\phi_k = 0 \\ \Phi_D = orth(\Re[\phi_1, \dots, \phi_p], \Im[\phi_1, \dots, \phi_p]) \end{cases}. \quad (3.8)$$

Similarly, when dissipation is modeled using a generic C matrix, a quadratic eigenvalue problem needs to be solved instead:

$$\begin{cases} (K_{II} + s_k C + s_k^2 M_{II})\phi_k = 0 \\ \Phi_D = orth(\Re[\phi_1, \dots, \phi_p], \Im[\phi_1, \dots, \phi_p]) \end{cases}. \quad (3.9)$$

Lastly, in case a complex viscoelastic model is used, the nonlinear eigenvalue problem of equation (3.10) must be solved:

$$\begin{cases} (K_{II}(s_k) + s_k^2 M_{II})\phi_k = 0 \\ \Phi_D = orth(\Re[\phi_1, \dots, \phi_p], \Im[\phi_1, \dots, \phi_p]) \end{cases}, \quad (3.10)$$

which can be done using an iterative method [116].

3.3 Wave Based Reduced Order Modeling

This section details the reduced order modeling strategy of [60] that was developed in order to speed up the resolution of the frequency-dependent palindromic eigenvalue problem of the 1D WFEM. This is achieved by projecting that eigenvalue problem on a smaller subspace spanned by solutions of that eigenvalue problem in a subset of well chosen frequencies. The real and imaginary parts of the obtained eigenvectors are separated and the resulting collection of

vectors is orthogonalized using a Gram–Schmidt orthogonalization process. We start by considering the eigenvalue problem used by Droz et al. [60]:

$$\left(\lambda_k D_{LR}(\omega) + (D_{LL}(\omega) + D_{RR}(\omega)) + \frac{1}{\lambda_k} D_{RL}(\omega) \right) \psi_k(\omega) = S(\lambda_k, \omega) \psi_k = 0 \quad (3.11)$$

In equation (3.11), D is the dynamic stiffness matrix of the UC at the circular frequency ω . The equation describes a family of eigenvalue problems with a C_∞ dependence in ω . Noteworthy, only a few n_ω ($n_\omega \ll n_L$) solutions corresponding to propagating and slowly decaying waves, i.e. $|\lambda_k| \approx 1$, are of interest at a given frequency. Hence one can expect all solutions of interest for a frequency band $[0, f_{max}]$ to approximately lie in a subspace of dimension $n_{red} \ll n_L$ spanned by the columns of a real orthogonal matrix Ψ . This justifies the reduced modeling approach taken in [60]. Practically, the main question become: "How to quickly determine a small but representative subset of frequencies that will be used to build the snapshot matrix leading to Ψ ?". In the original paper, Droz et al. make the assumption that wave-shapes remain relatively stable as the frequency increases with most variations arising around the cut-on frequencies where new wave types become propagative. Thus equation (3.11) only needs to be solved at these cut-on frequencies in order to obtain a representative sample of waveshapes. This idea is illustrated in Figure 3.2 taken form the original article. Noteworthy, the base assumption of this sampling strategy comes from empirical

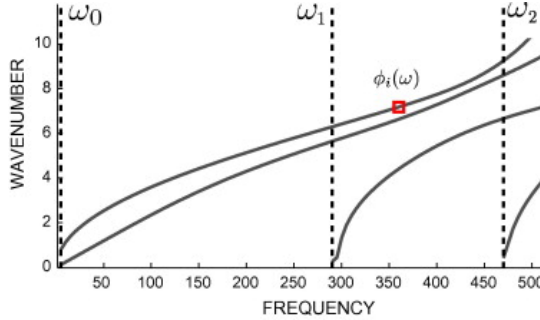


Figure 3.2: Illustration of the frequencies chosen to build the snapshot matrix

observations and mostly holds true for homogeneous waveguides -which were the target of the paper- but could be problematic for periodic waveguides as cut-off frequencies caused e.g. by band gaps and veering effects are possible without the appearance of any new propagating wave. In the original paper, Droz et al. compute all the cut-on frequencies ω_l in the interval $[0, \omega_{max}]$ using the inverse formulation of the 1D WFEM with the value $k = 0$, i.e. $\lambda = 1$.

$$(K(\lambda) - \omega_l^2 M(\lambda)) X_l. \quad (3.12)$$

Because only models with hysteretic damping are studied in [60], it is unclear what strategy would be used if a damping matrix or frequency dependent material properties were involved. Once the sampling frequencies have been determined, their real parts are used to obtain $\psi_{k,l}$ the snapshots (vectors) that verify equation (3.13) used to build the matrix Ψ :

$$\begin{cases} S(\lambda_{k,l}, \Re(\omega_l))\psi_{k,l} = 0 \\ \lambda_{min} \leq |\lambda_{k,l}| \leq 1 \end{cases}. \quad (3.13)$$

The snapshot matrix Ψ_0 is then formed:

$$\Psi_0 = [\psi_{1,1}, \dots, \psi_{1,q}, \dots, \psi_{p,q}], \quad (3.14)$$

and the projection matrix Ψ is obtained by using the QR algorithm on the vector collection $[\Re(\Psi_0), \Im(\Psi_0)]$. Once Ψ has been obtained, it is used to reduce the eigenvalue problem (3.11). First, a Galerkin projection is carried out on the sub-parts of the (condensed) dynamic stiffness matrix D_{LL} , D_{LR} , D_{RL} and D_{RR} resulting in their reduced counterparts.

$$\begin{cases} D_{LL}^{red} = \Psi^T D_{LL} \Psi \\ D_{LR}^{red} = \Psi^T D_{LR} \Psi \\ D_{RR}^{red} = \Psi^T D_{RR} \Psi \\ D_{RL}^{red} = \Psi^T D_{RL} \Psi \end{cases}. \quad (3.15)$$

Equation (3.11) is then rewritten in (3.16) using the reduced matrices and yields reduced eigenvectors:

$$S^{red}(\tilde{\lambda}_k, \omega)\tilde{\psi}_k = 0. \quad (3.16)$$

Finally, the link between the reduced eigenvalue pairs $(\tilde{\lambda}_k, \tilde{\psi}_k)$ and the solutions of the original problem (λ_k, ψ_k) is given in equation (3.17):

$$\begin{cases} \tilde{\lambda}_k \approx \lambda_k \\ \Psi\tilde{\psi}_k \approx \psi_k \end{cases}. \quad (3.17)$$

While ingenious, the approach proposed in [60] has a number of flaws and blind-spots. The proposed sampling strategy may fail once applied to periodic structures or complex homogeneous waveguides as variation of waveshapes may occur far from any cut-on frequency though this is usually unlikely. Additionally, the chosen linearization of (3.11) is problematic as it requires working with full matrices and obtaining all the eigenvalue-eigenvector pairs while only a

small subset is of interest. Another issue has to do with the QR scheme used in order to build the projection matrix from the snapshot matrix as it leads to projection basis of sizes almost as big as the snapshot collection. Lastly, the proposed projection of the eigenvalue problem happens at each frequency when the (condensed) dynamic stiffness matrix is formed. This is unnecessary and could be avoided by using Ψ to build the projection matrix for the interface degrees of freedom. These issues are addressed in our proposed MOR strategy presented in Section 3.4.

3.4 The proposed MOR strategy

In this Section, we describe a MOR scheme that combines ideas from [216] and [60] and improves upon them. A first version of the resulting scheme was published in [32]. The following modifications are brought to both methods. First, the Craig-Bampton MOR is enhanced as described in section 3.2 in order to deal with damping models of arbitrary complexities. Secondly, a different sampling strategy and eigenvalue problem are used when building the snapshot matrix. These changes ensure a more thorough sampling of the k-space but do not result in a higher computation time. The orthogonalization algorithm used to compute the projection matrix is changed from QR-based to SVD-based as the latter enables finer control of the accuracy-dofs ratio. Lastly, the computed projection matrix is used to reduce the UCs matrices instead of the WFEM's eigenvalue problem. This avoids performing a projection at each frequency. Because the first step of this reduction process was already described in Section 3.2 this Section focuses on the interface reduction scheme and is structured as follows. In Subsection 3.4.1 the modifications brought to the sampling strategy of [60] are detailed while the construction of the reduced order model is described in Subsection 3.4.2.

3.4.1 Modifications brought to the sampling strategy

The following targets are set for the new sampling strategy and resulting projection basis. (1) As in [60], the basis should capture the propagative waves accurately and (2) allow fast dispersion analysis of the 1D medium. (3) When needed, a mechanism allowing to sample the least evanescent waves should be available as these waves are needed in order to describe the dynamics of waveguides near inputs/sources and edges.

To achieve (1) and (2), we estimate it is better to sample the K-Space using the inverse approach instead of the direct one. This preference can be justified by

the algebraic properties of the EVPs of both formulations. Indeed, the inverse approach EVPs have real-symmetric or complex-Hermitian symmetries while the direct approach's EVPs have no symmetry to exploit from a practical point of view. The inverse approach's symmetries ensure eigenvectors are computed accurately and efficiently. Moreover, because the inverse approach estimates frequencies instead of propagation constants, iterative solvers can be used to compute only the few eigenvalues and wave shapes of interest. In contrast, all of the direct WFEM formulations suffer from numerical issues (see [197]) and only Zhong's formulation [214, 89] is compatible with the use of iterative solvers that enable the computation of a subset of eigenvalues. However, that formulation leads to an EVP where eigenvalues tend to be clustered (and they have multiplicity of at least 2) which typically results in poor accuracy/convergence for iterative eigenvalue solvers [136]. It is thus often necessary to increase the number of Lanczos basis vectors used in order to ensure the convergence of eigenvalue-eigenvector pairs which results in higher computation time and implementation complexity compared to the inverse approach. Lastly, target (3) can also be achieved using the inverse approach. Indeed, because its EVP estimates wavemodes and their corresponding frequencies, a frequency truncation criterion can be put in place to keep waves with eigenfrequencies up to n_f times the maximal frequency as is often done in mode-based MOR schemes.

Having decided to use the inverse approach to sample the k -space, it remains to decide at what values of k (resp. λ) the k -space should be sampled. In order to make this decision, preliminary information about the k -space's topology is necessary. It is therefore needed to evaluate: (1) The number of propagating waves appearing in the bandwidth of interest and their cut-on frequencies. (2) If waves reach aliasing, what their cut-off frequencies are in case band gaps or Bragg aliasing are occurring. (3) The wavenumbers values at the maximal frequency of interest. An illustration is shown in Figure 3.3 to describe the combination of inverse and direct methods for retrieving these solutions. To determine values of k for which the inverse approach will be used a sampling set S_0 is introduced and initialized with the value $k_0 = 0$. In the first step of the method the direct approach is used with Zhong's formulation [214, 89] and an iterative eigenvalue solver to retrieve the propagating values of k (resp. λ) at the maximal frequency of interest f_{max} . The corresponding eigenvalue problem is recalled in equation (3.18) and the corresponding values of k are depicted by square markers on the vertical dashed line at f_{max} in Figure 3.3.

$$\left[\begin{pmatrix} D_{RL} - D_{LR} & D_{LL} + D_{RR} \\ -D_{LL} - D_{RL} & D_{RL} - D_{LR} \end{pmatrix} - \left(\lambda_j + \frac{1}{\lambda_j} \right) \begin{pmatrix} 0 & -D_{LR} \\ D_{RL} & 0 \end{pmatrix} \right] \begin{bmatrix} X_T^j \\ X_B^j \end{bmatrix} \quad (3.18)$$

These values of k (in the Figure, k_1, k_2 and k_3) are then added to the sampling set S_0 . To determine whether aliasing is reached in the frequency band of interest, the inverse approach is used with $\lambda = -1$ and the smallest

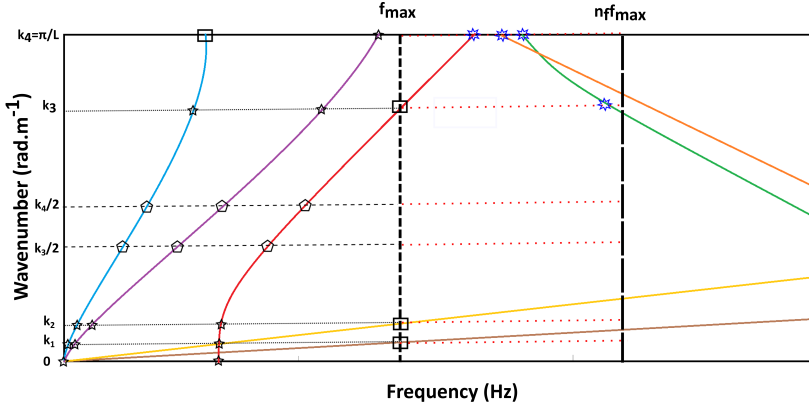


Figure 3.3: Illustration of the K-Space sampling strategy for the proposed scheme

eigenvalue ω_0 is computed according to equation (3.19):

$$\left[\begin{pmatrix} K_{LL}(\lambda, \omega_0) & K_{LI}(\lambda, \omega_0) \\ K_{IL}(\lambda, \omega_0) & K_{II}(\lambda, \omega_0) \end{pmatrix} - \omega_0^2 \begin{pmatrix} M_{LL}(\lambda, \omega_0) & M_{LI}(\lambda, \omega_0) \\ M_{IL}(\lambda, \omega_0) & M_{II}(\lambda, \omega_0) \end{pmatrix} \right] \begin{bmatrix} \psi_I \\ \psi_L \end{bmatrix} = 0 \quad (3.19)$$

If it is within the frequency band of interest, i.e. if $\omega_0 \leq 2\pi f_{max}$, the value $k = \frac{\pi}{L}$ is added to S_0 . This corresponds to the square markers on the horizontal line in Figure 3.3. The parameter $n_k \in \mathbb{N}^*$ that governs the level of fineness of the sampling is then used. The final sampling set S is then defined in equation (3.20):

$$S = \left\{ p \frac{k_i}{n_k}, k_i \in S_0, p \in \llbracket 1; n_k \rrbracket \right\}. \quad (3.20)$$

This new parameter n_k ensures that each wave is sampled at least $n_k + 1$ times and minimizes the chance that wave conversion and veering phenomena are missed. In Figure 3.3 this is illustrated for $n_k = 2$ for k_3 and k_4 with the horizontal dashed lines and pentagon markers are used for the corresponding sampled solutions. Lastly, in case $n_f > 1$ is chosen additional solutions beyond f_{max} are retained. These are marked with blue stars in Figure 3.3.

3.4.2 Construction of the reduced order model

The sampling set S being defined, the inverse approach is used with the corresponding values of k (resp. λ) as in equation (3.21):

$$\left[\begin{pmatrix} K_{LL}(\lambda, \omega_j) & K_{LI}(\lambda, \omega_j) \\ K_{IL}(\lambda, \omega_j) & K_{II}(\lambda, \omega_j) \end{pmatrix} - \omega_j^2 \begin{pmatrix} M_{LL}(\lambda, \omega_j) & M_{LI}(\lambda, \omega_j) \\ M_{IL}(\lambda, \omega_j) & M_{II}(\lambda, \omega_j) \end{pmatrix} \right] \begin{bmatrix} \psi_I^j(\lambda) \\ \psi_L^j(\lambda) \end{bmatrix} = 0 \quad (3.21)$$

The parameter n_f that determines the frequency truncation criterion is introduced. All partial eigenvectors $\psi_I^j(\lambda)$ associated to eigenfrequencies ω_j within the $[0, 2\pi n_f f_{max}]$ range are normalized and put in the snapshot matrix Q :

$$\begin{cases} Q_0 = [\psi_I^1(\lambda_1), \psi_I^2(\lambda_1), \dots, \psi_I^p(\lambda_q)] \\ Q = [\Re(Q_0), \Im(Q_0)] \end{cases} \quad (3.22)$$

The local interface projection matrix P_{LR} is obtained by performing a singular value decomposition of Q :

$$Q = VAW^H. \quad (3.23)$$

With V and W complex unitary matrices whose columns are the left (resp. right) singular vectors of Q and A a real positive diagonal matrix with singular values σ_i ordered in decreasing order. Lets note $\sigma = \sum_i \sigma_i$ the sum of all the singular values of Q . The projection basis is then obtained by taking the first few singular vectors of V . To define the absolute minimal number of vectors that should be retained, the effective rank [164] of Q is computed:

$$\begin{cases} \forall i \in \llbracket 1, n_L \rrbracket, p_i = \frac{\sigma_i}{\sigma} \\ H_Q = - \sum_{i=1}^{n_L} p_i \log(p_i) \cdot \\ \text{erank}(Q) = e^{H_Q} \end{cases} \quad (3.24)$$

It is obtained by taking the exponential of the entropy of the distribution of the singular values of Q as defined in equation (3.24). We also introduce a precision criterion $\epsilon < 1$ to be set by the user and we keep at least the n_ϵ first left singular vectors of Q . The integer number n_ϵ is defined as the smallest integer satisfying equation (3.25):

$$\frac{(\sigma - \sum_{i=1}^{n_\epsilon} \sigma_i)}{\sigma} \leq \epsilon. \quad (3.25)$$

The final number of vectors kept is $m = \max(\lceil \text{erank}(Q) \rceil, n_\epsilon)$. In practice, a choice of ϵ between 10^{-4} and 10^{-6} is recommended in order to obtain a good ratio between accuracy and the number of vectors kept. At last, the local interface projection matrix P_{LR} is obtained by only keeping the first m columns of V :

$$\begin{cases} V = [V_1, V_2, \dots, V_{n_L}] \\ P_{LR} = [V_1, V_2, \dots, V_m] \end{cases} \quad (3.26)$$

And the global projection matrix P is as follows in order to preserve the structure of the UC dofs:

$$\begin{bmatrix} U_L \\ U_R \\ U_I \end{bmatrix} = P \begin{bmatrix} U_L^{red} \\ U_R^{red} \\ U_I \end{bmatrix} = \begin{pmatrix} P_{LR} & 0 & 0 \\ 0 & P_{LR} & 0 \\ 0 & 0 & I_{n_I} \end{pmatrix} \begin{bmatrix} U_L^{red} \\ U_R^{red} \\ U_I \end{bmatrix} \quad (3.27)$$

The reduced order UC matrices are the obtained via Galerkin projection, e.g. $K_{red} = P^T K P$, $M_{red} = P^T M P$, etc.

3.5 Benchmarks and numerical examples

In this Section the efficiency of the proposed MOR scheme is assessed in term of interface reduction by comparison with:

- A simple implementation of the WFEM using a quadratic linearization thereby computing all waves. It is referred to as QWFEM.
- An iterative implementation of the standard WFEM using Zhong's formulation [214, 89] which will be noted as ZWFEM.
- A first version of the method of Droz et al. [60] referred to as Dro2014a that received a small improvement with respect to the original formulation. Specifically, Droz2014a is identical to the method of the original article but the produced projection basis is used in order to reduce the UC matrices thereby removing the need to project the eigenvalue problem at each frequency.
- A second implementation of [60] referred to as Droz2014b where Zhong's formulation is used in order to carry out the sampling of the k-space.

Three classical criteria are used for the comparison. First, the time required in order to produce a ROM. This indicator can be important when trying

to speed up computation e.g. in order to optimize some design or negligible in applications such as virtual sensing and digital twins in which the ROM is only produced once and can be used until the end of life of its physical counterpart. Another important factor when considering a reduction method is its accuracy. Because many MOR techniques have parameters, the comparisons should be done with parameters values within the range prescribed in the literature. In case no "canonical settings" exists, the fine-tuning of the ROM should be included in its computation time. The last metric of comparison, is the speed of the derived ROMs whose relevance is obvious in the context of reduced order modeling. Practically, the comparison of the aforementioned modeling strategies is carried out on three structures from the literature. The first one is a sandwich structure with aluminum skins and a rubber core that was introduced in [60]. The second one is a locally resonant metamaterial taken from [170] made of an aluminum beam with resonant PMMA add-ons. The last one is a stiffened plate that was introduced in [32]. All computations are performed on a Intel(R) Core(TM) i9-10980XE CPU at 3.00 GHz functioning at stock settings.

3.5.1 Sandwich beam

In this subsection the first example from [60] is used in order to benchmark the different modeling strategies. The model is comprised of three layers. The top and bottom layers are 2 and 3 millimeters thick respectively, and are made of steel. The middle layer is 20 millimeters thick and is made of rubber. The cross-section of the sandwich is 40 millimeters. A global hysteretic damping of one percent is applied to the structure. The cross-section of the sandwich is modeled with Lagrange Q_1 elements coded on Matlab. The mesh, however, was generated using ANSYS APDL 2020 with elements 0.5 millimeters length in the direction of propagation. The resulting model has 3744 dofs with 1872 dofs on each interface. Its mesh is displayed in Figure 3.4 and the characteristics of all layers of the cross-section are summed up in Table 3.1. The maximal frequency of interest is $f_{max} = 1000$ Hz. The cut-off imaginary part for the methods Droz2014a and Droz2014b is set to $k_c = 30 \text{ rad.m}^{-1}$ which is the criterion used for the post-processing of the dispersion curves. For the proposed method, referred to as Boukadia2018, the settings are the following. The frequency factor is set to $n_f = 1$ such that only propagating waves are sampled and the wavenumber sampling factor is set to $n_k = 3$ which ensures each wave is sampled at least 4 times. Finally, the SVD truncation criterion is set $\epsilon = 10^{-5}$. The performance of each method is displayed in Table 3.2. The column "Reduction time" indicates the time it takes to produce a reduced order model with a given method while the column "WFEM time" indicates the time required to compute

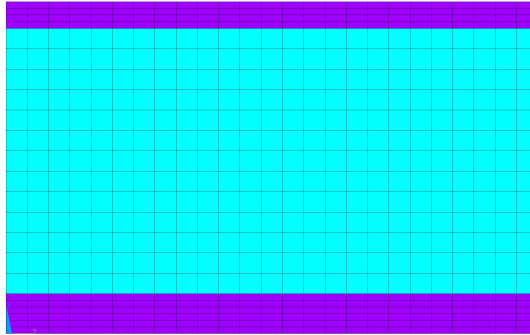


Figure 3.4: Cross-section discretization for the sandwich structure of [60]

| Layer - Material | Thickness (<i>mm</i>) | Density (<i>kg.m⁻³</i>) | Young Modulus (<i>Pa</i>) | Poisson coefficient | Damping ratio |
|------------------|----------------------------|---|--------------------------------|------------------------|------------------|
| Top - Steel | 2 | 7850 | 210×10^9 | 0.3 | 0.01 |
| Middle - Rubber | 20 | 950 | 1.5×10^6 | 0.48 | 0.01 |
| Bottom - Steel | 3 | 7850 | 210×10^9 | 0.3 | 0.01 |

Table 3.1: Material properties for the sandwich beam layer

the propagation constants and wavenumbers at one frequency using that method. Computations for the ZWFEM were made computing the first 60 eigenvalue-eigenvector pairs i.e. 30 wave types. The first thing that stands out is the gap between the QWFEM and the ZWFEM as no reduction process is involved here. The first one takes about 6 minutes to return a result while the other only needs 18 seconds. This showcases the importance of mastering Zhong's formulation for serious WFEM practitioners. This difference in performance is also reflected in the gap between Droz2014a and Droz2014b as it takes them about 50 and 3 minutes respectively in order to produce the same ROM. When it comes to comparing the different MOR schemes, our proposed method outperforms all other implementations. It takes less than a minute to produce a ROM and the produced ROM is also more compact leading to a lower computation time than

| Method | Reduction time (s) | Model size | WFEM time (s) |
|--------------|--------------------|------------|------------------------|
| QWFEM | NA | 3744 | 3.451×10^2 |
| ZWFEM | NA | 3744 | 1.859×10^1 |
| Droz2014a | 3107.43 | 298 | 2.134×10^{-1} |
| Droz2014b | 168.96 | 298 | 2.134×10^{-1} |
| Boukadia2018 | 44.35 | 166 | 3.890×10^{-2} |

Table 3.2: CPU time performance of the five methods

the ROM produced by Droz2014.

Another important point of comparison for the two ROMs is accuracy. We test this by computing the relative error between propagation constants and waveshapes obtained via the ZWFEM and the those obtained with the Droz2014 and Boukadia2018 ROMs. The comparison is carried out for the first 12 most propagative waves and the formulae used are the following:

$$err(\lambda_i) = \left| \frac{\lambda_i - \tilde{\lambda}_i}{\lambda_i} \right|, \quad (3.28)$$

with λ_i the i^{th} propagation constant computed with the ZWFEM and $\tilde{\lambda}_i$ the i^{th} with a ROM. Similarly, the error for waveshapes is defined in equation (3.29):

$$err(\psi_i) = 1 - \left| \frac{(\psi_i | \tilde{\psi}_i)}{\|\psi_i\| \|\tilde{\psi}_i\|} \right|. \quad (3.29)$$

The results are displayed in Figure 3.5 As can be seen, both ROMs are very

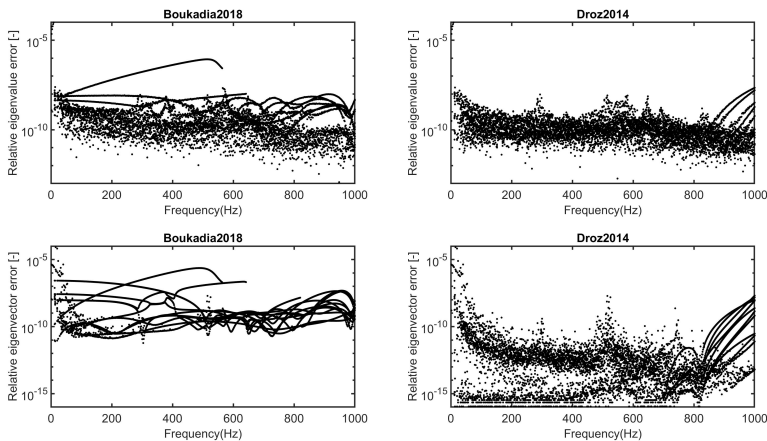


Figure 3.5: Comparison of the accuracy of the ROMs from Droz2014 and Boukadia2018 for the model of Droz2014

accurate but the ROM from Droz2014 performs better in that regard owing to its bigger size and higher computation time. For practical applications however, the extra accuracy from the Droz2014 ROM does not bring much added value while the computation time is multiplied by 5. This illustrates the benefit of an SVD based orthogonalization with a well chosen truncation criteria over a basic QR based orthogonalization scheme.

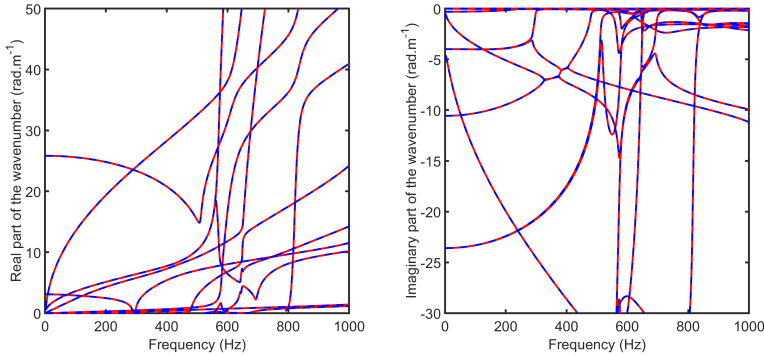


Figure 3.6: Dispersion curves of the sandwich beam obtained with Droz2014's reduction (Blue) and Boukadia2018's reduction (Red)

| Material | Density ($kg.m^{-3}$) | Young Modulus (GPa) | Poisson coefficient | Damping ratio |
|----------|----------------------------|----------------------------|------------------------|------------------|
| Aluminum | 2690.2 | 68.07 | 0.325 | 0.0025 |
| PMMA | 1188.4 | 4.8 | 0.31 | 0.05 |

Table 3.3: Material properties of aluminum and PMMA in the model of [170]

The dispersion curves computed by both methods are given in Figure 3.6 to emphasize this point.

3.5.2 Locally Resonant Metamaterial

In this subsection the locally resonant metamaterial UC studied in [170] is used as a numerical example to assess the performance of the proposed model order reduction scheme. The metamaterial is an aluminum beam with locally resonant add-ons in PMMA. Hysteretic damping is used to model dissipation in both materials. The cross-section of the beam is 2 millimeters thick and 3 centimeters wide and the dimensions of the locally resonant add-on are given in Figure 3.7 taken from the original article. The material properties of aluminum and PMMA are given in Table 3.3. The UC is modeled using quadratic Serendipity \mathcal{S}_2 elements coded in Matlab though the mesh was generated using ANSYS APDL 2020. There is total of 51570 dofs, 1878 of which are on the UC's (left and right)

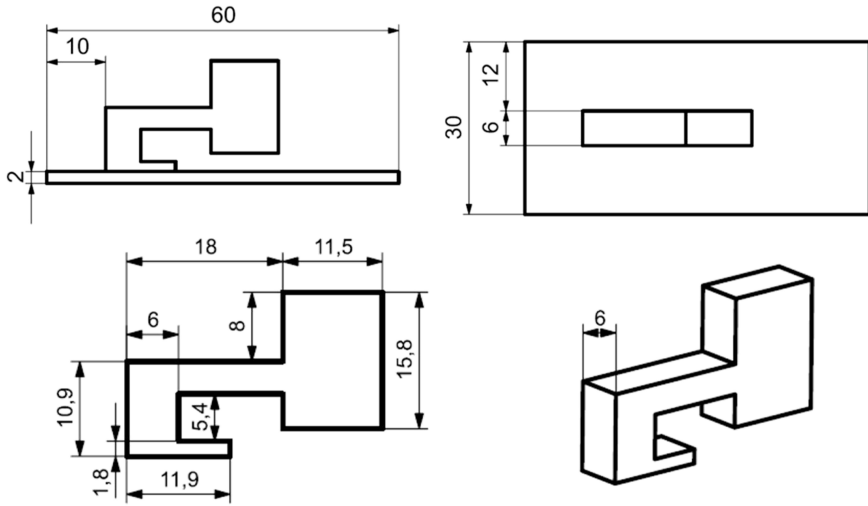


Figure 3.7: Geometry and dimension of the UC from [170]. The dimensions are given in millimeters

interfaces. The maximal frequency of interest is $f_{max} = 1600 \text{ Hz}$. Because of the many internal dofs of the model, the inner dof reduction presented in Section 3.2 is applied with $n_f = 4$. The resulting ROM, ROM1, serves as reference to evaluate the accuracy and performance of the other methods. As with the previous example, ROM1 is ran with the QWFEM for a few frequencies in order to form a good estimate of the average time it takes to obtain the propagation constants and wave shapes at one frequency. ROM1 is then used with the ZWFEM to compute 60 eigenvalue-eigenvector pairs (i.e., 30 wave types) and the resulting waveshapes and propagation constants are used in order to evaluate the accuracy of the following MOR schemes. ROM1 is further reduced using the methods Droz2014a, Droz2014b with $k_c = 30 \text{ rad.m}^{-1}$ and the method Boukadia2018 with $n_f = 1$, and $n_k = 3$ and $\epsilon = 10^{-5}$. The results in terms of CPU performance are presented in Table 3.4. The first thing to notice is the efficiency of the inner dof reduction as these went from 49692 in the full order model to 14 in the reduced order model. Moreover, creating this ROM took only about a minute (67.16 seconds). As in the previous example, the efficiency of Zhong's formulation is also highlighted as the computation time is divided by 40 when compared to the classical WFEM formulation. In terms of reduction time, the methods Droz2014b and Boukadia2018 are both pretty close as it takes them respectively 8 and 5 additional seconds to further reduce (ROM1). The first method ends up with 50 interface dofs and the latter with 38 due to the SVD-based orthogonalization which is why it is 1.6 time

| Method | Reduction time (s) | Model size | WFEM time (s) |
|--------------|--------------------|------------|------------------------|
| QWFEM (ROM1) | 67.16 | 1892 | 3.867×10^1 |
| ZWFEM (ROM1) | 67.16 | 1892 | 0.8794×10^0 |
| Droz2014a | 67.16 + 124,28 | 64 | 2.069×10^{-3} |
| Droz2014b | 67.16 + 8.39 | 64 | 2.069×10^{-3} |
| Boukadia2018 | 67.16 + 5.36 | 52 | 1.325×10^{-3} |

Table 3.4: CPU time performance of the five methods for the locally resonant metamaterial of [170]

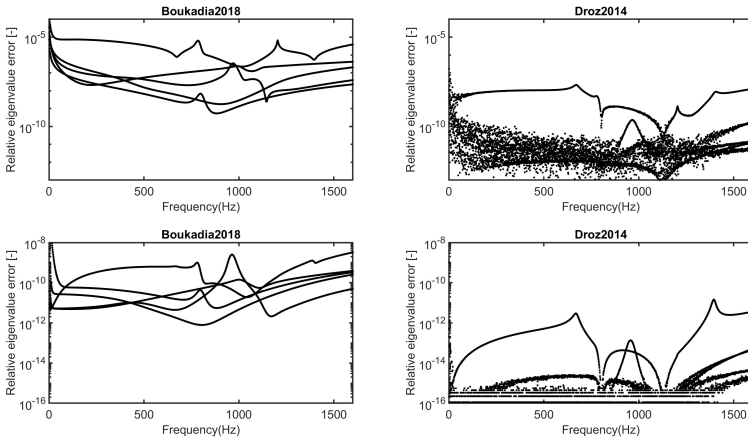


Figure 3.8: Comparison of the accuracy of the ROMs from Droz2014 and Boukadia2018 for the model of [170]

faster. Naturally, this gain in dofs and computation time is compensated by a slight loss in accuracy as is demonstrated in Figure 3.8. The maximal relative error for eigenvalues is around 10^{-5} for Boukadia2018 and 10^{-8} for Droz2014. For eigenvectors, these values are around 10^{-8} and 10^{-11} . Again, the extra accuracy from Droz2014 is not relevant for most applications. This shows that $\epsilon = 10^{-5}$ is a good truncation criterion to strike a balance between accuracy and number of dofs. Finally, the dispersion curves obtained via both methods are displayed in Figure 3.9. As expected, both the real and imaginary parts of the wavenumber matches even inside Bragg and locally resonant bandgaps.

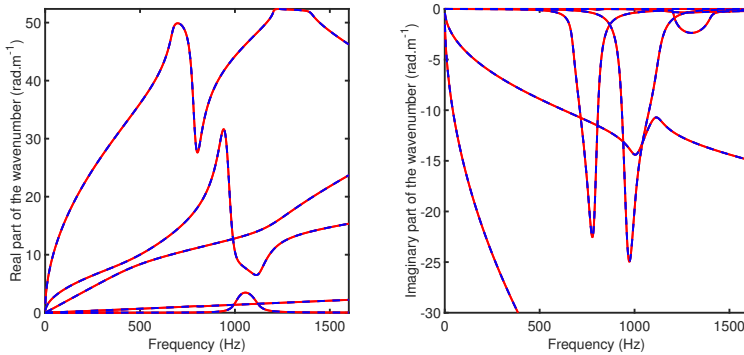


Figure 3.9: Dispersion curves of the locally resonant metamaterial of [170] obtained with Droz2014's reduction (Blue) and Boukadia2018's reduction (Red)

3.5.3 Doubly stiffened panel

In this subsection, the doubly stiffened panel studied in [32] is used as a numerical example in order to assess the performance and accuracy of the proposed MOR scheme. The considered waveguide is an aluminum plate of thickness $e = 2\text{mm}$ and width 40cm stiffened using rectangular beams of height $h = 10\text{mm}$ and width $l_s = 5\text{mm}$. The spacing between the stiffeners is 10cm along the width and 5cm along the propagation direction. An hysteretic damping of $\eta = 10^{-4}$ is introduced. The mesh of the finite element model of a periodic UC of the structure is shown in Fig 3.10 and was obtained using ANSYS APDL 2020. The elements however, were coded in Matlab and are Lagrange \mathcal{Q}_1 linear elements. The original model has 47928 dofs 5154 of which are on its left and right interfaces. Because of its high number of dofs, this model is first reduced using the method presented in Section 3.2 with a frequency factor n_f of 4. The resulting ROM, ROM1, serves as a reference in order to evaluate the accuracy and performance of the other methods. As with the other examples, ROM1 is ran with the QWFEM for a few frequencies in order to form a good estimate of the time it takes to compute the propagation constants and wave shapes at one frequency. It is then used with the ZWFEM, computing 60 eigenvalue-eigenvector pairs (i.e., 30 wave types) and the resulting waveshapes and propagation constants are used in order to evaluate the accuracy of the following MOR schemes. ROM1 is further reduced using the methods Droz2014a, Droz2014b with $k_c = 30\text{rad.m}^{-1}$ and the method Boukadia2018 with $n_f = 1$, and $n_k = 3$ and $\epsilon = 10^{-5}$. The

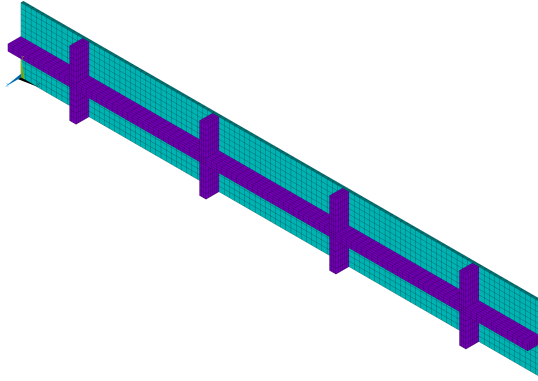


Figure 3.10: Cross-section discretization of the UC of the doubly stiffened plate of [32]

| Method | Reduction time (s) | Model size | WFEM time (s) |
|--------------|--------------------|------------|------------------------|
| QWFEM (ROM1) | 69.15 | 5185 | 3.867×10^1 |
| ZWFEM (ROM1) | 69.15 | 5185 | 4.167×10^0 |
| Droz2014a | 69.15 + 523,28 | 419 | 2.470×10^{-1} |
| Droz2014b | 69.15 + 82.14 | 419 | 2.470×10^{-1} |
| Boukadia2018 | 69.15 + 73.91 | 219 | 3.341×10^{-2} |

Table 3.5: CPU time performance of the five methods for the doubly stiffened panel of [32]

results in terms of CPU performance are presented in Table 3.5. Again, the efficiency of the inner dofs strategy is remarkable. These went from 42774 in the FOM to just 31 in ROM1. Without this reduction, it would not be feasible to use the WFEM on this type of well meshed structures as the dynamic condensation would be too time consuming. As in the previous examples our proposed method produces a ROM much faster than the original formulation of [60] and still slightly faster than the improved implementations benchmarked in this Section. Similarly, the ROM produced is smaller with the proposed method and a speed-up factor around 10 is observed compared to the other ROMs. This because the WFEM's computation time scales with the third power of the number of interface dofs once the inner dofs have been reduced. An evaluation of the accuracy for the eigenvalue-eigenvector pairs produced by both methods is given in Figure 3.11. The maximal error for eigenvalues and eigenvectors are around 10^{-4} and 10^{-5} for proposed strategy while the ROM of Dro2014 achieves near machine precision accuracy. Again, the extra accuracy does not impact practical purposes as the dispersion curves obtained via both methods

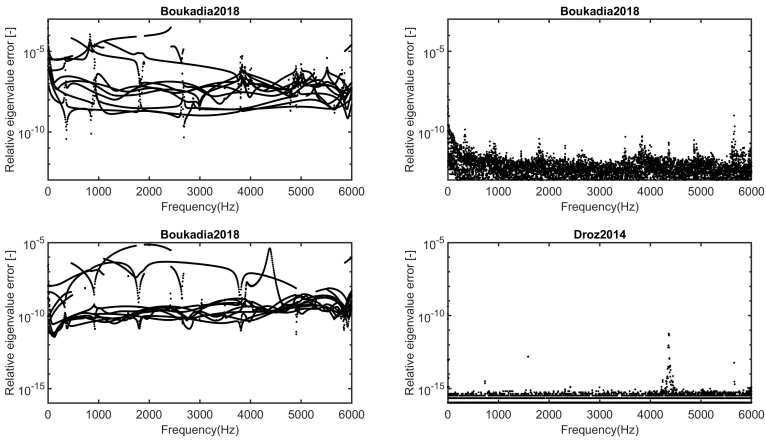


Figure 3.11: Comparison of the accuracy of the ROMs from Droz2014 and Boukadia2018 for the model of [32]

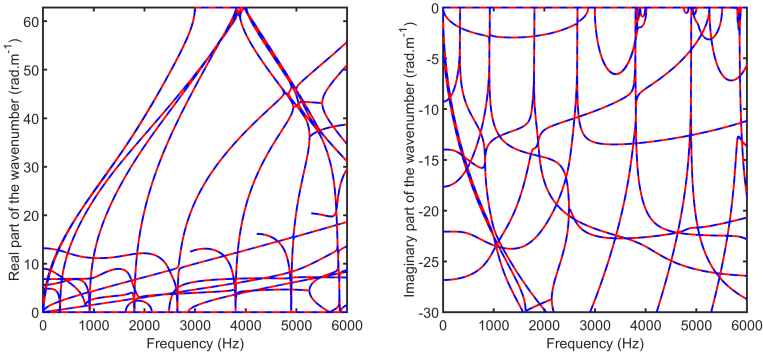


Figure 3.12: Dispersion curves of the doubly stiffened panel of [32] obtained with Droz2014's reduction (Blue) and Boukadia2018's reduction (Red)

are virtually indistinguishable (See Figure 3.12).

3.6 Conclusions and perspectives

In this Chapter a novel model order reduction strategy for the unit cell modeling of 1D periodic structures in the WFEM framework was presented. The proposed strategy builds upon the inner dof reduction of [48, 102, 216] and the interface reduction of [60, 62]. The main contributions of the Chapter can be summarized as follows:

- The Craig-Bampton model order reduction scheme used in [216] was expanded to tackle models including hysteretic and generalized damping as well as frequency dependent material properties.
- A faster and more complete sampling strategy has been developed to replace the one used in [60]. These simultaneous gains are achieved by relying on the inverse WFEM formulation instead of the direct one as the former is usually faster than the latter.
- A better control of the dofs/accuracy trade off is achieved in the proposed interface reduction strategy by the use of an SVD based orthogonalization scheme instead of QR-based one. This can result in much faster ROMs as the complexity of the WFEM eigenvalue problem scales with the third power of the number of interface dofs.

Further work on the topic of reduced order modeling should consider parametric model order reduction (PMOR) which consists in reducing parameter dependent models in such a way that they are accurate over a predefined range of parameters values. A good review of the topic can be found in [20] where 3 families of methods are considered to extend projection-based MOR techniques to the parametric case:

- A global projection basis for the whole parameters space. Early tests indicate that this method may be suitable for inner dofs reduction but may be undesirable for interface reduction. This is because the WFEM's complexity scales with the third power of the number of interface dofs. A double in size increase would translate in a eight fold increase of in CPU time as was observed in [29]. This issue could be mitigated by applying a second reduction to the models generated by the PMOR scheme.
- Interpolating the projection basis [5]. Though the method produces efficient ROMs, this method can be memory intensive, the interpolation process itself can also computationally expensive and the projection operation as to be realized a the model is evaluated with at a new parameter value. To mitigate the second drawback, a method that seeds

up the interpolation of the projection matrix in the tangential manifold for proposed in [194, 195].

- Another possibility is to interpolate both the reduced order models and their projection matrices [6]. Which avoids performing the projection operation every time new parameter values are considered but adds a second interpolation process. The trade-off between both operations usually depends on both the dimension of the original model and that of the projection basis.

Chapter 4

Wave Based Optimization

Part of this Chapter has already been published as [31]: "R.F. Boukadia, E. Deckers, C. Claeys, M. Ichchou, W. Desmet. A wave-based optimization framework for 1D and 2D periodic structures. *Mechanical Systems And Signal Processing*, 139:106603, May 2020."

This Chapter presents an optimization framework for 1D and 2D periodic media and waveguides that was developed during this thesis and published in [31]. The proposed framework builds on top of the existing WFEM framework and provides expressions for the first and second order derivatives of most quantities that can be computed with the WFEM. In order to complement these derivatives, a second order algorithm that combines a line search method and an ellipsoidal trust-region approach [151] is developed. The former method usually performs better in regions where the optimized function is convex while the latter allows to quickly escape saddle-points and works better in regions where negative curvature is present. The aforementioned developments and choices are motivated in part by the noise levels [197] of the WFEM which make it unsuitable for fast numerical differentiation techniques. The shortfalls of first order optimization algorithms when dealing with saddle points [157, 54] and their scaling issues caused by the lack of a natural metric in the optimization space were also motivating factors. The latter issue in particular, is more serious than may appear and is responsible for the development of numerous adaptive learning rate strategies [118, 55] in the field of machine learning where second order optimization techniques are rarely used [26]. Another motivating factor is language specific and relates to the design of Matlab's "fmincon" function (general optimization function). Of the many algorithms it implements, only the "interior-point" and "trust-region reflective" algorithms enable the use of

second order information supplied by the user. As of now, the former algorithm is not suitable for the proposed framework as it requires that the hessian is passed via a separate function. In the WFEM framework, this leads to a loss of efficiency because computing the hessian requires (at minima) the computation of the objective function and its gradient. While the "trust-region-reflective" algorithm does not suffer from this issue, it tends to perform poorly in regions where the objective function is convex. This is likely due to a shrinking of the trust-region radius in previous steps of the optimization process where negative curvature was present. This issue is addressed by the algorithm developed during this thesis which switches to a line search based on Newton's method when the objective function is locally convex. Another important issue justifying the developments of this chapter is the quasi-exclusive focus of the unit cell based optimization literature (e.g.[85, 7, 86]) on wavenumbers (associated to bandgap depth) and eigenfrequencies (related with bandgap width). While these dispersion characteristics are relatively easy to compute and interpret, they do not give a complete picture as they neglect the effects that loads, (finite) size and boundary conditions [202, 182, 153, 207] have on practical applications. The possible results of such oversights are showcased in [170] where the naive application of a metamaterial solutions leads to the appearance of edge modes which decrease the effectiveness of the metamaterial design. The optimization framework presented in this Chapter accounts for these potential issues at the design stage as loads and boundary conditions can be included in the optimization process. The rest of the Chapter is organized as follows. First, Sections 4.1 and 4.2 present general and computationally efficient formulae for the first and second order derivatives of generalized eigenvalue-eigenvector pairs and for the solutions of linear systems. These formulae are then applied to the 1D direct WFEM and the 2D inverse WFEM in Sections 4.3 and 4.4. Numerical examples illustrating the potential of the proposed framework are presented in Section 4.6 while Section 4.7 summarizes the findings and conclusions of the Chapter.

4.1 Derivatives for linear systems of equations

This section details the computation of first and second order derivatives for solutions of parametric linear systems of equations. A parametric linear system of the form of equation (4.1) is considered:

$$A(p)U(p) = F. \tag{4.1}$$

In equation (4.1), $p \in \mathbb{R}^n$ is the vector of parameters. The solution of the system, $U(p)$, is obtained by inverting the matrix $A(p)$ resulting in the simple

expression is given in equation (4.2) where the dependency in p is dropped:

$$U = A^{-1}F \quad (4.2)$$

Most numerical algorithms used to compute U however, never directly form the matrix A^{-1} , rather, an appropriate decomposition of A (QR, LDL, etc.) is performed according to its algebraic properties and the solutions of equation (4.1) are computed on a vector by vector basis. In order to maximize the efficiency of what follows, it is crucial to perform that decomposition only once and store it in memory for all computations that follow. The first order derivatives of U are obtained via simple differentiation:

$$\frac{\partial A}{\partial p_i}U + A \frac{\partial U}{\partial p_i} = 0. \quad (4.3)$$

Thus:

$$\frac{\partial U}{\partial p_i} = -A^{-1} \frac{\partial A}{\partial p_i}U. \quad (4.4)$$

The same can be done for the second order derivatives of U leading to the expression of equation (4.5):

$$\frac{\partial^2 U}{\partial p_i \partial p_j} = -A^{-1} \left(\frac{\partial^2 A}{\partial p_i \partial p_j}U + \frac{\partial A}{\partial p_i} \frac{\partial U}{\partial p_j} + \frac{\partial A}{\partial p_j} \frac{\partial U}{\partial p_i} \right). \quad (4.5)$$

Since A^{-1} is used in equations (4.2), (4.4) and (4.5), storing the matrix decomposition of A enables the computation of the first or second order derivatives of U at low extra cost. This is especially true when A is a large FEM matrix. Apart from sensitivity analysis and some stochastic methods, however, it is rare that vector derivatives are used directly. Rather one tends to consider systems of the form of equation (4.6) where the vector U is used to define a real scalar objective function f :

$$\begin{cases} A(p)U(p) = F \\ f(p) = U^*BU \end{cases} \quad (4.6)$$

Here, we focus on the case where f is quadratic as most objective functions are either directly quadratic or are obtained by performing a sum, product or some composition involving quadratic functions. Hence this is viewed as the most useful case. In (4.6) the matrix B can be chosen Hermitian without loss of generality thus this assumption will be made in the following developments. First, the first order derivatives of f are introduced:

$$\frac{\partial f}{\partial p_i} = 2\Re \left(U^* B \frac{\partial U}{\partial p_i} \right). \quad (4.7)$$

In equation (4.7), the derivatives of U can be replaced using equation (4.4):

$$\frac{\partial f}{\partial p_i} = 2\Re \left(-U^* B A^{-1} \frac{\partial A}{\partial p_i} U \right) = 2\Re \left((-U^* B A^{-1}) \left(\frac{\partial A}{\partial p_i} U \right) \right). \quad (4.8)$$

Equation (4.8) introduces the adjoint:

$$Adj = -U^* B A^{-1} = -(U^* B) A^{-1}. \quad (4.9)$$

It needs only to be computed once at the cost of one relatively cheap matrix-vector inversion given the decomposition of A should be stored in memory. Once this is done, all first order derivatives of f can be computed at the cost of one matrix-vector multiplication and one vector-vector scalar product which significantly lowers the computational cost of evaluating f 's gradient. Similarly, the second order derivatives of f are given by the expression of equation (4.10):

$$\frac{\partial^2 f}{\partial p_i \partial p_j} = 2\Re \left(U^* B \frac{\partial^2 U}{\partial p_i \partial p_j} + \frac{\partial U^*}{\partial p_i} B \frac{\partial U}{\partial p_j} \right). \quad (4.10)$$

Using equations (4.5) and (4.9) this can be rewritten as:

$$\frac{\partial^2 f}{\partial p_i \partial p_j} = 2\Re \left(Adj \left(\frac{\partial^2 A}{\partial p_i \partial p_j} U + \frac{\partial A}{\partial p_i} \frac{\partial U}{\partial p_j} + \frac{\partial A}{\partial p_j} \frac{\partial U}{\partial p_i} \right) + \frac{\partial U^*}{\partial p_i} B \frac{\partial U}{\partial p_j} \right). \quad (4.11)$$

Unlike equation (4.10), equation (4.11) does not involve $\frac{\partial^2 U}{\partial p_i \partial p_j}$: This means that the full hessian matrix of f can be computed at the cost of only $(n+1)$ matrix inversions instead of $\frac{n(n+3)}{2} + 1$. However, since both equation (4.10) and (4.11) require the first order derivatives of U it is not necessary to use equations (4.8) and (4.9) to compute f 's gradient as equation (4.7) is equally fast under these conditions. That being said, using equation (4.8) never result in a loss of computation time.

4.2 Derivatives of Simple Eigenvalues and Eigenvectors

This section is dedicated to the evaluation of the first and second order derivatives of simple eigenvalues and eigenvectors (multiplicity of 1) of general nonlinear eigenvalue problems. It generalizes and extends the works of Nelson et al. [150], Tang et al. [183] and Friswell et al. [80] where formulae for the first order derivatives of linear and quadratic eigenvalue problems were presented. In the context of this Chapter, knowing how to efficiently derive first and second order

derivatives of eigenvalue problems is necessary as the direct and inverse WFEM formulations rely on the solutions of such problems in all of their applications. We start by introducing a few notations that will be used throughout this section.

- U/U_i : Right eigenvector.
- V/V_i : Left eigenvector.
- λ/λ_i : Eigenvalue, propagation constant.
- $p \in \mathbb{R}^m$: vector of parameters.
- p_i : The i^{th} component of p .
- X^+ : Moore-Penrose inverse of the matrix X .

Let n be a positive integer superior or equal to 1. We define a generalized eigenvalue problem of order n in equation (4.12):

$$\left\{ \begin{array}{l} X : \mathbb{C} \rightarrow M_n(\mathbb{C}) \\ \lambda \mapsto X(\lambda) \\ Sol = \{\lambda \in \mathbb{C}, \det(X(\lambda)) = 0\} \end{array} \right. . \quad (4.12)$$

For each λ in Sol left and right eigenvectors can be defined. They are non-trivial solutions of equation (4.13):

$$X(\lambda)U = 0 = V^T X(\lambda). \quad (4.13)$$

For a given λ in Sol , the dimension of $Ker(X(\lambda))$ is at least one. Herein, the assumption that $Ker(X(\lambda))$ (the kernel of $X(\lambda)$) is always of dimension 1 is made. In this case left and right eigenvectors can be simply chosen as all possible choices differ only by a scalar multiplication. Having defined a generalized eigenvalue problem, a parametric generalized eigenvalue problem can now be introduced. The difference is that the matrix function X now also depends on a parameter vector $p \in \mathbb{R}^m$ hence the eigenvalues λ and eigenvectors U and V become function of p . Assuming the matrix X is an analytic function of (λ, p) , derivatives of eigenvalues and eigenvectors with respect to the parameters p_i can be computed.

In order to simplify expressions we define the total derivative with respect to the scalar parameter p_k in equation (4.14):

$$\frac{dX}{dp_k} = \frac{\partial X}{\partial p_k} + \frac{\partial \lambda}{\partial p_k} \frac{\partial X}{\partial \lambda}. \quad (4.14)$$

4.2.1 First order derivatives

The first order derivative of an eigenvalue λ_i and its eigenvectors U_i and V_i can now be defined. First we notice that the following relationships hold:

$$\forall p \in \mathbb{R}^m, X(\lambda_i(p), p)U_i(p) = 0 = V_i^T(p)X(\lambda_i(p), p). \quad (4.15)$$

Differentiating equation (4.15) with respect to p_k we get:

$$\frac{dX}{dp_k}U_i + X \frac{\partial U_i}{\partial p_k} = 0. \quad (4.16)$$

Taking advantage of the fact that $V_i^T X = 0$, premultiplying equation (4.15) by V_i^T yields:

$$V_i^T \frac{dX}{dp_k}U_i = 0. \quad (4.17)$$

This scalar equation can be developed using equation (4.14) leading to equation (4.18):

$$\frac{\partial \lambda_i}{\partial p_k} \left(V_i^T \frac{\partial X}{\partial \lambda} U_i \right) = - \left(V_i^T \frac{\partial X}{\partial p_k} U_i \right). \quad (4.18)$$

thus obtaining an expression for the first order derivatives of the eigenvalue λ_i . Now that $\frac{\partial \lambda_i}{\partial p_k}$ is known, all the terms of equation (4.14) can be evaluated enabling the computation of the eigenvectors derivatives:

$$\frac{\partial U_i}{\partial p_k} = -X^+ \frac{dX}{dp_k} U_i. \quad (4.19)$$

Since the matrix X is singular, there would be infinitely many solutions to equation (4.19) if the Moore-Penrose inverse was not used. This corresponds to a choice of normalized rectified eigenvectors satisfying $\left(\frac{dU_i}{dp_k} \Big| U_i \right) = 0$. This condition can be enforced without making any particular hypothesis (see Appendix D for more details). In practice, equation (4.19) is solved by computing the Complete Orthogonal Decomposition [88] (COD) of the matrix X and storing it for the computation of all eigenvector derivatives.

4.2.2 Second order derivatives

It is assumed that the first order derivatives of eigenvalues and eigenvectors have been computed and stored in memory as well as the relevant matrix decompositions. In order to find expressions for the second order derivatives of

eigenvalues and eigenvectors, equation (4.13) is differentiated two times which leads to:

$$\frac{d^2 X}{dp_k dp_l} U + \frac{dX}{dp_k} \frac{\partial U}{\partial p_l} + \frac{dX}{dp_l} \frac{\partial U}{\partial p_k} + X \frac{\partial^2 U}{\partial p_k \partial p_l} = 0. \quad (4.20)$$

Since $V^T X = 0$, premultiplying by V^T yields:

$$V^T \left(\frac{d^2 X}{dp_k dp_l} U + \frac{dX}{dp_k} \frac{\partial U}{\partial p_l} + \frac{dX}{dp_l} \frac{\partial U}{\partial p_k} \right) = 0. \quad (4.21)$$

The term $\frac{d^2 X}{dp_k dp_l}$ can be developed leading to the expression for the second order derivatives of λ :

$$\begin{aligned} \frac{d^2 \lambda}{dp_k dp_l} \left(V^T \frac{\partial X}{\partial \lambda} U \right) = & -V^T \left[\left(\frac{\partial^2 X}{\partial p_l \partial p_k} + \frac{\partial \lambda}{\partial p_l} \frac{\partial^2 X}{\partial \lambda \partial p_k} + \frac{\partial \lambda}{\partial p_k} \frac{\partial^2 X}{\partial \lambda \partial p_l} + \frac{\partial \lambda}{\partial p_k} \frac{\partial \lambda}{\partial p_l} \frac{\partial^2 X}{\partial \lambda^2} \right) U \right. \\ & \left. + \left(\frac{dX}{dp_k} \frac{dU}{dp_l} + \frac{dX}{dp_l} \frac{dU}{dp_k} \right) \right] \end{aligned} \quad (4.22)$$

The value of $\frac{d^2 \lambda}{\partial p_k \partial p_l}$ being known, the matrix $\frac{d^2 X}{dp_k dp_l}$ can be evaluated such that the second order derivatives of the eigenvector is obtained:

$$\frac{\partial^2 U}{\partial p_l \partial p_k} = -X^+ \left(\frac{d^2 X}{dp_k dp_l} U + \frac{dX}{dp_k} \frac{\partial U}{\partial p_l} + \frac{dX}{dp_l} \frac{\partial U}{\partial p_k} \right) - \Re \left(\frac{\partial U}{\partial p_l} \middle| \frac{\partial U}{\partial p_k} \right) U. \quad (4.23)$$

More details about the origins of equation (4.23) are provided in Appendix D.

4.3 Derivatives for the direct 1D WFEM

In this Section, expressions for the derivatives of propagation constants, waveshapes and forced responses computed using the 1D WFEM are derived. The proposed formulae enable the computation of the gradient and hessian matrix of most objective functions at relatively low computational cost. These derivatives can then be used with first or second order algorithms in order to perform optimization in a unit cell modeling framework. The Section is organized in order to mirror the workflow of the 1D WFEM. Notations and a quick recap of the 1D WFEM framework are introduced in Subsection 4.3.1. The expression for the derivatives of the condensed dynamic stiffness matrix are then developed in Subsection 4.3.2. Finally, by applying the results of Section 4.2 to the WFEM framework, the derivatives of the propagation constants and waveshapes are derived in Subsection 4.3.3.

4.3.1 Recaps

The mass matrix M , stiffness matrix K and damping matrix C of a periodic structure's UC are considered. A partition of its degrees of freedom U is established according to the UC's spatial structure (see Figure 4.1):

$$U = \begin{bmatrix} U_L \\ U_I \\ U_R \end{bmatrix}. \quad (4.24)$$

The subscripts R , L and I are used for variables associated with the right, left

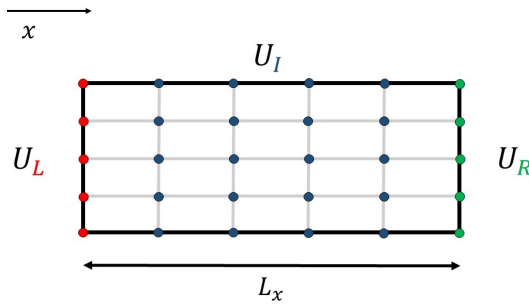


Figure 4.1: Dofs' partition for the UC of a 1D periodic structure

and internal dofs of the UC, respectively. Additionally, the subscript B will be used for quantities associated to all interface dofs. The first step in the direct formulation of the 1D WFEM is to compute the dynamic stiffness matrix G for a given circular frequency ω :

$$G = K + i\omega C - \omega^2 M. \quad (4.25)$$

The internal dofs of the UC are then condensed out in order to form the condensed dynamic stiffness matrix D :

$$D = G_{BB} - G_{BI}G_{II}^{-1}G_{IB}. \quad (4.26)$$

Applying Floquet-Bloch boundary conditions $U_R = \lambda U_L$ (displacement), $F_R = -\lambda F_L$ (load) leads to the eigenvalue problem [197]:

$$\left(\lambda D_{LR} + (D_{LL} + D_{RR}) + \frac{1}{\lambda} D_{RL} \right) \psi = 0. \quad (4.27)$$

The propagation constant λ is related to the wavenumber k_x via the relation $\lambda = e^{-ik_x L_x}$, L_x being the length of the UC in the direction of propagation. The

eigenvalue problem (4.27) yields the waveshapes ψ_k and propagation constants λ_k of free waves in the periodic medium at the circular frequency ω . It should be noted that the propagation constants come in pairs $(\lambda_k, \frac{1}{\lambda_k})$ with eigenvectors (ψ_k^+, ψ_k^-) that correspond to waves traveling in the positive and negative direction. For passive structures, direction of propagation and direction of decay coincide, therefore, positive going waves correspond to $|\lambda| \leq 1$ and negative going waves to $|\lambda| \geq 1$. In case $\lambda \approx 1$, positive going wave have a positive powerflow and negative going waves a negative one [92]. For active structures, waves should be sorted according to their direction of decay to solve equation (4.28) hence the proposed sorting method may still be used. Once propagation constants and waveshapes are properly sorted, it is possible to compute the forced response of a finite waveguide comprised of N UCs by relating the waves' amplitudes to the excitations and boundary conditions. The specific case of Clamped-Free boundary conditions is detailed in equation (4.28) as it is used in Section 4.6 but similar formulae are available for other types of boundary conditions [145, 143, 64]:

$$\begin{pmatrix} \Psi^+ & \Psi^- \Lambda^N \\ D_{RL} \Psi^+ \Lambda^{N-1} + D_{RR} \Psi^+ \Lambda^N & D_{RL} \Psi^- \Lambda + D_{RR} \Psi^- \end{pmatrix} \begin{bmatrix} q^+ \\ q^- \end{bmatrix} = \begin{bmatrix} V_0 \\ F_N \end{bmatrix}. \quad (4.28)$$

In equation (4.28), q^+ and q^- are the vectors of the positive and negative going waves' amplitudes. V_0 is the imposed displacement at the left side of the waveguide while F_N is the force applied at its right side. Ψ^+ is an n by n matrix whose columns are the eigenvectors Ψ_k^+ corresponding to positive going waves. Likewise, Ψ^- is formed with the eigenvectors Ψ_k^- of the negative going waves. Λ is a diagonal matrix with the positive propagation constants λ_k on the diagonal. The displacement of the i^{th} section of the waveguide is given by equation (4.29):

$$V_i = \Psi^+ \Lambda^i q^+ + \Psi^- \Lambda^{N-i} q^-. \quad (4.29)$$

4.3.2 Derivatives of the condensed dynamic stiffness matrix

In order to optimize a UC to obtain a desired behavior, some properties of the UC are parametrized. The vector of these m parameters is noted $p = (p_1, \dots, p_m) \in \mathbb{R}^m$. It follows that the mass, stiffness and damping matrix, $M(p)$, $K(p)$, $C(p)$ are functions of the parameter vector p . Assuming the first and second order derivatives of the matrices with respect to p are available, the derivatives of all the quantities derived in Subsection 4.3.1 can be computed. For a given circular frequency ω the first order derivatives of the dynamic stiffness matrix are:

$$\frac{\partial G}{\partial p_k} = \frac{\partial K}{\partial p_k} + i\omega \frac{\partial C}{\partial p_k} - \omega^2 \frac{\partial M}{\partial p_k}. \quad (4.30)$$

Likewise, the second order derivatives of the dynamic stiffness matrix are:

$$\frac{\partial^2 G}{\partial p_k \partial p_l} = \frac{\partial^2 K}{\partial p_k \partial p_l} + i\omega \frac{\partial^2 C}{\partial p_k \partial p_l} - \omega^2 \frac{\partial^2 M}{\partial p_k \partial p_l}. \quad (4.31)$$

Using equation (4.26), the derivatives of the condensed dynamic stiffness matrix are derived:

$$\begin{aligned} \frac{\partial D}{\partial p_k} = & \frac{\partial G_{BB}}{\partial p_k} + G_{BI} G_{II}^{-1} \frac{\partial G_{II}}{\partial p_k} G_{II}^{-1} G_{IB} \\ & - \frac{\partial G_{BI}}{\partial p_k} G_{II}^{-1} G_{IB} - G_{BI} G_{II}^{-1} \frac{\partial G_{IB}}{\partial p_k}. \end{aligned} \quad (4.32)$$

Taking advantage of the fact that G and D are symmetric matrices this can be rewritten as:

$$\frac{\partial D}{\partial p_k} = \frac{\partial G_{BB}}{\partial p_k} + \Theta_{IB}^T \frac{\partial G_{II}}{\partial p_k} \Theta_{IB} - 2sym \left(\Theta_{IB}^T \frac{\partial G_{IB}}{\partial p_k} \right). \quad (4.33)$$

With:

$$\begin{cases} \Theta_{IB} = G_{II}^{-1} G_{IB} \\ sym(A) = \frac{1}{2} (A + A^T) \end{cases} \quad (4.34)$$

Equation (4.33) is much more compact than equation (4.32). It also highlights an efficient way to compute all the first order derivatives of D . Indeed, one only needs to compute Θ_{IB} once during the dynamic condensation such that all first order derivatives of D are evaluated without further matrix inversion or decomposition.

Closed expressions for the second order derivatives of D are now derived:

$$\begin{aligned} \frac{\partial^2 D}{\partial p_k \partial p_l} = & \frac{\partial^2 G_{BB}}{\partial p_k \partial p_l} - 2sym \left[\frac{\partial \Theta_{IB}^T}{\partial p_l} \left(\frac{\partial G_{II}}{\partial p_k} \Theta_{IB} - \frac{\partial G_{IB}}{\partial p_k} \right) - \Theta_{IB}^T \frac{\partial^2 G_{IB}}{\partial p_k \partial p_l} \right] \\ & + \Theta_{IB}^T \frac{\partial^2 G_{II}}{\partial p_k \partial p_l} \Theta_{IB} \end{aligned} \quad (4.35)$$

With:

$$\frac{\partial \Theta_{IB}}{\partial p_l} = G_{II}^{-1} \left(-\frac{\partial G_{II}}{\partial p_l} \Theta_{IB} + \frac{\partial G_{IB}}{\partial p_l} \right). \quad (4.36)$$

Using equations (4.35) and (4.36), one needs to "invert" G_{II} m times in order to compute all second order derivatives of D . Consequently, keeping the LU decomposition of G_{II} the first time it is computed can further reduce the computation time of the derivatives' evaluation.

4.3.3 Derivatives of propagation constants and wave shapes

The hardest part of this Subsection was already taken care of in Section 4.2. As such we only need to adapt the results presented there to the case of one of the WFEM formulation. Here, the palindromic version is chosen which leads to equation (4.37):

$$X(\lambda, p) = \lambda D_{LR}(p) + (D_{LL}(p) + D_{RR}(p)) + \frac{1}{\lambda} D_{RL}(p). \quad (4.37)$$

Consequently the formulae of Section 4.2 can be applied by filling in the corresponding matrices in the expressions:

$$\left\{ \begin{array}{l} \frac{\partial X(\lambda, p)}{\partial p_k} = \lambda \frac{\partial D_{LR}}{\partial p_k} + \left(\frac{\partial D_{RR}}{\partial p_k} + \frac{\partial D_{LL}}{\partial p_k} \right) + \frac{1}{\lambda} \frac{\partial D_{RL}}{\partial p_k} \\ \frac{\partial X(\lambda, p)}{\partial \lambda} = D_{LR} - \frac{1}{\lambda^2} D_{RL} \\ \frac{dX(\lambda, p)}{dp_k} = \frac{\partial X(\lambda, p)}{\partial p_k} + \frac{\partial \lambda}{\partial p_k} \frac{\partial X(\lambda, p)}{\partial \lambda} \\ \frac{\partial^2 X(\lambda, p)}{\partial \lambda^2} = \frac{2}{\lambda^3} D_{RL} \\ \frac{\partial^2 X(\lambda, p)}{\partial \lambda \partial p_k} = \frac{\partial D_{LR}}{\partial p_k} - \frac{1}{\lambda^2} \frac{\partial D_{RL}}{\partial p_k} \\ \frac{\partial^2 X(\lambda, p)}{\partial p_k \partial p_l} = \lambda \frac{\partial D_{LR}}{\partial p_k \partial p_l} + \left(\frac{\partial D_{RR}}{\partial p_k \partial p_l} + \frac{\partial D_{LL}}{\partial p_k \partial p_l} \right) + \frac{1}{\lambda} \frac{\partial^2 D_{RL}}{\partial p_k \partial p_l} \\ \frac{d^2 X(\lambda, p)}{dp_k dp_l} = \frac{\partial^2 X(\lambda, p)}{\partial p_k \partial p_l} + \frac{\partial \lambda}{\partial p_l} \frac{\partial^2 X(\lambda, p)}{\partial \lambda \partial p_k} + \frac{\partial \lambda}{\partial p_k} \frac{\partial^2 X(\lambda, p)}{\partial \lambda \partial p_l} \\ \quad + \frac{\partial^2 \lambda}{\partial p_k \partial p_l} \frac{\partial X(\lambda, p)}{\partial \lambda} + \frac{\partial \lambda}{\partial p_k} \frac{\partial \lambda}{\partial p_l} \frac{\partial^2 X(\lambda, p)}{\partial \lambda^2} \end{array} \right. \quad (4.38)$$

It should also be noted that the parametric eigenvalue problem (4.37) is T-palindromic [36]. This means the eigenvalues come in pairs $(\lambda_i, \frac{1}{\lambda_i})$ and that the right eigenvector for λ_i , ψ_i , is the left eigenvector for $\frac{1}{\lambda_i}$. Conversely, the right eigenvector for $\frac{1}{\lambda_i}$, ϕ_i , is the left eigenvector for λ_i . Thanks to this feature, computing the left eigenvectors of (4.37) is not required to evaluate the derivatives. Taking this into account and using the formulae of section 4.2 expressions for the first order derivatives of the propagation constants and wave

shapes are given in equations (4.39) and (4.40):

$$\frac{\partial \lambda_i}{\partial p_k} = - \frac{\phi_i^T \left[\lambda_i \frac{\partial D_{LR}}{\partial p_k} + \left(\frac{\partial D_{RR}}{\partial p_k} + \frac{\partial D_{LL}}{\partial p_k} \right) + \frac{1}{\lambda_i} \frac{\partial D_{RL}}{\partial p_k} \right] \psi_i}{\phi_i^T \left(D_{LR} - \frac{1}{\lambda_i^2} D_{RL} \right) \psi_i}. \quad (4.39)$$

$$\begin{aligned} \frac{\partial \psi_i}{\partial p_k} = -X^+(\lambda_i, p) & \left[\left(\frac{\partial \lambda_i}{\partial p_k} D_{LR} + \lambda_i \frac{\partial D_{LR}}{\partial p_k} \right) + \left(\frac{\partial D_{RR}}{\partial p_k} + \frac{\partial D_{LL}}{\partial p_k} \right) \dots \right. \\ & \left. + \left(-\frac{\partial \lambda_i}{\partial p_k} \frac{1}{\lambda_i^2} D_{RL} + \frac{1}{\lambda_i} \frac{\partial D_{RL}}{\partial p_k} \right) \right] \psi_i \end{aligned} \quad (4.40)$$

Similarly, for the second order derivatives, equations (4.22) and (4.23) are used with the expressions given in equation (4.38):

$$\begin{aligned} \frac{d^2 \lambda_i}{\partial p_k \partial p_l} \left(\phi_i^T \frac{\partial X}{\partial \lambda} \psi_i \right) = -\phi_i^T & \left[\left(\frac{\partial^2 X}{\partial p_l \partial p_k} + \frac{\partial \lambda}{\partial p_l} \frac{\partial^2 X}{\partial \lambda \partial p_k} + \frac{\partial \lambda}{\partial p_k} \frac{\partial^2 X}{\partial \lambda \partial p_l} + \frac{\partial \lambda}{\partial p_k} \frac{\partial \lambda}{\partial p_l} \frac{\partial^2 X}{\partial \lambda^2} \right) \psi_i \right. \\ & \left. + \left(\frac{dX}{dp_k} \frac{\partial \psi_i}{\partial p_l} + \frac{dX}{dp_l} \frac{\partial \psi_i}{\partial p_k} \right) \right] \end{aligned} \quad (4.41)$$

$$\begin{aligned} \frac{\partial^2 \psi_i}{\partial p_l \partial p_k} = -X^+ & \left(\frac{d^2 X}{dp_k dp_l} \psi_i + \frac{dX}{dp_k} \frac{\partial \psi_i}{\partial p_l} + \frac{dX}{dp_l} \frac{\partial \psi_i}{\partial p_k} \right) \\ & - \Re \left(\frac{\partial \Psi_i}{\partial p_l} \middle| \frac{\partial \psi_i}{\partial p_k} \right) \psi_i \end{aligned} \quad (4.42)$$

4.4 Derivatives in the 2D inverse WFEM framework

In this section formulae for the derivatives of quantities computed through the 2D inverse WFEM are made explicit. The direct 2D WFEM is not considered for two reasons. Firstly, the derived equations would be almost identical to those of section 4.3. Secondly, the general formalism for any type of eigenvalue problem was already covered in 4.2. Lastly, the direct 2D WFEM formulation is not very popular as it cannot compute K-Spaces. For this last application, the shift-cell operator method [47] is usually preferred. The rest of the section is structured as follows.

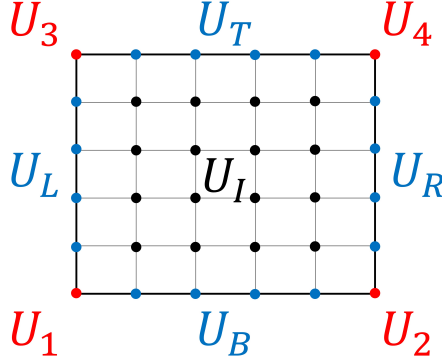


Figure 4.2: Dofs' partition of a 2D UC

4.4.1 Recaps 2D inverse WFEM

We now consider a 2D unit-cell. Its stiffness, mass and damping matrix respectively referred to as K , M and C . The UC's displacement vector is referred to as U . The dofs of the UC are partitioned according to its spatial structure as illustrated in Figure 4.2 and equation (4.43).

$$U = [U_1 \ U_2 \ U_3 \ U_4 \ U_L \ U_R \ U_B \ U_T \ U_I]^T. \quad (4.43)$$

The numbers of dofs in U_1, U_2, U_3 and U_4 are identical and noted n_1 . Likewise, the number of dofs in U_L and U_R is noted n_L . For U_B and U_T n_B is used while n_I is used for U_I . The inverse form of the 2D WFEM proceeds by choosing two wavenumbers (k_x, k_y) and enforcing the corresponding Floquet-Bloch boundary conditions on the UC:

$$U_2 = \lambda_x U_1, \ U_3 = \lambda_y U_1, \ U_4 = \lambda_x \lambda_y q_1, \ U_R = \lambda_x U_L, \ U_T = \lambda_y U_B \quad (4.44)$$

$$\begin{cases} f_1 + \frac{f_2}{\lambda_x} + \frac{f_3}{\lambda_y} + \frac{f_4}{\lambda_x \lambda_y} = 0 \\ f_L + \frac{f_R}{\lambda_x} = 0 \\ f_B + \frac{f_T}{\lambda_y} = 0 \end{cases} \quad (4.45)$$

With λ_x and λ_y the propagation constants in the x and y direction. They are related to the wavenumbers (k_x, k_y) in the periodic medium via the side lengths of the UC, L_x and L_y , by equation (4.46):

$$\lambda_x = e^{-ik_x L_x}, \ \lambda_y = e^{-ik_y L_y}. \quad (4.46)$$

The Floquet-Bloch boundary conditions are enforced using two projection matrices P_U and P_F (see [62]):

$$U = P_U(k_x, k_y)U_r = \begin{pmatrix} I_{n_1} & 0 & 0 & 0 \\ \lambda_x I_{n_1} & 0 & 0 & 0 \\ \lambda_y I_{n_1} & 0 & 0 & 0 \\ \lambda_x \lambda_y I_{n_1} & 0 & 0 & 0 \\ 0 & I_{n_L} & 0 & 0 \\ 0 & \lambda_x I_{n_L} & 0 & 0 \\ 0 & 0 & I_{n_B} & 0 \\ 0 & 0 & \lambda_y I_{n_B} & 0 \\ 0 & 0 & 0 & I_{n_I} \end{pmatrix} \begin{bmatrix} U_1 \\ U_L \\ U_B \\ U_I \end{bmatrix}. \quad (4.47)$$

$$P_F(k_x, k_y) = \begin{pmatrix} I & \frac{1}{\lambda_x} I_{n_1} & \frac{1}{\lambda_y} I_{n_1} & \frac{1}{\lambda_x \lambda_y} I_{n_1} & 0 & 0 & 0 & 0 & 0 \\ 0 & 0 & 0 & 0 & I_{n_L} & \frac{1}{\lambda_x} I_{n_L} & 0 & 0 & 0 \\ 0 & 0 & 0 & 0 & 0 & 0 & I_{n_B} & \frac{1}{\lambda_y} I_{n_B} & 0 \\ 0 & 0 & 0 & 0 & 0 & 0 & 0 & 0 & I_{n_I} \end{pmatrix}. \quad (4.48)$$

By enforcing these relations a modified equation of the dynamics whose validity is restrained to loads and displacements satisfying the Floquet-Bloch conditions associated to the wavenumber pair (k_x, k_y) is derived:

$$[K(k_x, k_y) + i\omega C(k_x, k_y) - \omega^2 M(k_x, k_y)] U_r = D(k_x, k_y)U_r = F_r. \quad (4.49)$$

For a generic matrix $A \in M_n(\mathbb{C})$, the matrix $A(k_x, k_y)$ is derived from matrix A according to equation (4.50).

$$A(k_x, k_y) = P_F(k_x, k_y)AP_U(k_x, k_y). \quad (4.50)$$

Equation (4.49) can be used to compute the response of an infinite periodic medium to a load with 2D Floquet-Bloch symmetry (such as a plane wave) or to compute its band diagram when there is no load [134]:

$$[K(k_x, k_y) + i\omega_r C(k_x, k_y) - \omega_r^2 M(k_x, k_y)] \psi_r = 0. \quad (4.51)$$

4.4.2 Derivatives for eigenfrequencies, wave shapes and forced response

We now assume that a parametric UC model is available. The vector of these m parameters is noted $p = (p_1, \dots, p_m) \in \mathbb{R}^m$. It follows that the mass, stiffness and damping matrix, respectively $M(p)$, $K(p)$ and $C(p)$, are functions of the parameter vector p . It is also assumed that the first and second order derivatives

of these matrices with respect to p are available. Under these assumptions, the derivatives for equations (4.49) and (4.51) can be computed.

Starting with equation (4.49) the first and second order derivatives of the modified dynamic stiffness matrix are given in equation (4.52):

$$\begin{cases} \frac{\partial D(k_x, k_y)}{\partial p_k} = P_F(k_x, k_y) \left(\frac{\partial K}{\partial p_k} + i\omega \frac{\partial C}{\partial p_k} - \omega^2 \frac{\partial M}{\partial p_k} \right) P_U(k_x, k_y) \\ \frac{\partial^2 D(k_x, k_y)}{\partial p_k \partial p_l} = P_F(k_x, k_y) \left(\frac{\partial^2 K}{\partial p_k \partial p_l} + i\omega \frac{\partial^2 C}{\partial p_k \partial p_l} - \omega^2 \frac{\partial^2 M}{\partial p_k \partial p_l} \right) P_U(k_x, k_y) \end{cases} \quad (4.52)$$

These expressions can be straightforwardly substituted in the equations of Section 4.1 in order to compute the derivatives of the dynamic response U_r or that of an objective function based on it.

The same can be done of the derivatives of eigenfrequencies and waveshapes working with k_x and k_y as fixed we have:

$$X(\omega, p) = K(k_x, k_y, p) + i\omega C(k_x, k_y, p) - \omega^2 M(k_x, k_y, p). \quad (4.53)$$

The relevant expressions for matrix derivatives as then defined in equation (4.54) where the dependence in p is omitted for the matrices $K(k_x, k_y)$, $M(k_x, k_y)$ and

$C(k_x, k_y)$ in order to keep the expressions shorter.

$$\left\{ \begin{array}{l}
 \frac{\partial X(\omega, p)}{\partial p_k} = \frac{\partial K(k_x, k_y)}{\partial p_k} + i\omega_r \frac{\partial C(k_x, k_y)}{\partial p_k} - \omega_r^2 \frac{\partial M(k_x, k_y)}{\partial p_k} \\
 \frac{\partial X(\omega, p)}{\partial \omega} = iC(k_x, k_y) - 2\omega M(k_x, k_y) \\
 \frac{dX(\omega, p)}{dp_k} = \frac{\partial D(k_x, k_y, \omega)}{\partial p_k} + \frac{\partial \omega}{\partial p_k} \frac{\partial D(k_x, k_y, \omega)}{\partial \omega} \\
 \frac{\partial^2 X(\omega, p)}{\partial \omega^2} = -2M(k_x, k_y) \\
 \frac{\partial^2 X(\omega, p)}{\partial \omega \partial p_k} = i \frac{\partial C(k_x, k_y)}{\partial p_k} - 2\omega \frac{M(k_x, k_y)}{\partial p_k} \\
 \frac{\partial^2 X(\omega, p)}{\partial p_k \partial p_l} = \frac{\partial^2 K(k_x, k_y)}{\partial p_k \partial p_l} + i\omega \frac{\partial^2 C(k_x, k_y)}{\partial p_k \partial p_l} - \omega^2 \frac{\partial^2 M(k_x, k_y)}{\partial p_k \partial p_l} \\
 \frac{d^2 X(\omega, p)}{dp_k dp_l} = \frac{\partial^2 X(\omega, p)}{\partial p_k \partial p_l} + \frac{\partial \omega}{\partial p_l} \frac{\partial X(\omega, p)}{\partial \omega \partial p_k} + \frac{\partial \omega}{\partial p_k} \frac{\partial X(\omega, p)}{\partial \omega \partial p_l} + \frac{\partial^2 \omega}{\partial p_k \partial p_l} \frac{\partial X(\omega, p)}{\partial \omega} \\
 \quad + \frac{\partial \omega}{\partial p_k} \frac{\partial \omega}{\partial p_l} \frac{\partial^2 X(\omega, p)}{\partial \omega^2}
 \end{array} \right. \quad (4.54)$$

The expressions of equation (4.54) can be directly substituted in the formulae derived in Section 4.2 in order to evaluate the derivatives of eigenfrequencies and wave-shapes. Noteworthy, it is usually the case that the eigenvalue problem (4.51) is solved with both wavenumbers k_x and k_y being real. In that case, $\frac{1}{\lambda_x} = \overline{\lambda_x}$, $\frac{1}{\lambda_y} = \overline{\lambda_y}$ thus $P_F = P_U^*$ thus, all matrices of the eigenvalue problem are Hermitian. The eigenvalues come in pairs $(\omega_r, -\overline{\omega_r})$ with eigenvectors (ψ_r, ϕ_r) . Additionally, $\overline{\psi_r}$ is the left eigenvector for $-\overline{\omega_r}$, therefore only the right eigenvectors of need to be computed.

4.5 Second Order Optimization Algorithm

This Section describes the second order optimization strategy used in the examples of Section 4.6. The proposed strategy is developed to account for two characteristics of the direct 1D WFEM and some properties of Matlab's "fmincon" function (general purpose optimization function). Firstly, obtaining accurate derivatives by numerical differentiation is difficult due to the low

numerical accuracy of the WFEM as compared to usual FEM modeling [197]. Secondly, computing the response of a waveguide is relatively cheap because all computations are done based on a single UC. It follows that semi-analytical gradients and Hessians of C^2 objective functions can be computed at an acceptable cost. Regarding "fmincon", only two of its algorithms accept user supplied Hessians, the "interior-point" algorithm and "trust-region-reflective" algorithm. In order to use the former, a function computing the Hessian matrix must be passed as an additional argument. This is problematic because in the WFEM framework, the computation of derivatives requires the computation of the objective function thus separating the two leads to redundant computations. The "trust-region-reflective" algorithm does not suffer from this issue as gradient and Hessian can be passed as auxiliary outputs of the objective function. However, it suffered from poor convergence speed in regions of positive curvature when performing tests on the example of 4.6.1. For these reasons, an algorithm that combines both line search and trust region methods was developed. The ellipsoidal trust-region approach [54, 157] is based on a transformation of the local Hessian matrix of the objective function and ensures that the algorithm quickly escapes saddle points in regions of negative curvature. The line search method, on the other hand, performs better in neighborhoods where the optimized function is convex. Because of these exotic features, the proposed algorithm had to be implemented in Matlab. It is an instance of sequential quadratic programming (SQP) [151, Chapter 18] thus possesses all the convergence properties of that class of algorithms.

An objective function f and the vector of optimization variables $p \in \mathbb{R}^m$ are introduced. The variables may be subject to n_e linear equality constraints:

$$\forall i \in \llbracket 1, n_e \rrbracket, E_i(p) = 0. \quad (4.55)$$

And n_c convex inequality constraints:

$$\forall j \in \llbracket 1, n_c \rrbracket, C_j(p) \leq 0. \quad (4.56)$$

For a starting point p_0 , the function's value $f(p_0)$, the gradient $\nabla f(p_0)$ and the Hessian $\nabla^2 f(p_0)$ are computed. A surrogate function \tilde{f} approximating f around p_0 is introduced:

$$f(p) \approx \tilde{f}(p) = f(p_0) + \nabla f(p_0) (p - p_0) + \frac{1}{2} (p - p_0)^T \nabla^2 f(p_0) (p - p_0). \quad (4.57)$$

If the Hessian is positive definite, a line search method is used [151, Chapter 3]. First, the search direction ν is computed:

$$\nu = \operatorname{argmin} \{ \tilde{f}(p_0 + \nu), E_i(p) = 0, C_j(p) \leq 0 \}. \quad (4.58)$$

Equation (4.58) can be solved using the interior point method [151, Chapter 19] or analytically when there are no constraints. Once the search ν is computed, f is minimized in the corresponding direction:

$$\alpha_m = \operatorname{argmin} \{f(p_0 + \alpha\nu), \alpha \in [0, 1]\}. \tag{4.59}$$

Defining the next iteration:

$$p_1 = p_0 + \alpha_m\nu \tag{4.60}$$

When the Hessian is not positive definite, a trust region method [151, 54, 157, 115] is used. First, the matrix $|\nabla^2 f(p_0)|$ is defined. This matrix is obtained by keeping the eigenvectors of $\nabla^2 f(p_0)$ and taking the absolute value of all its eigenvalues. A supplementary constraint is then introduced:

$$T(p) = (p - p_0)^T |\nabla^2 f(p_0)| (p - p_0) - R_0^2 \leq 0. \tag{4.61}$$

The next iteration is defined as:

$$p_1 = \operatorname{argmin} \{ \tilde{f}(p), T(p) \leq 0, E_i(p) = 0, C_j(p) \leq 0 \}. \tag{4.62}$$

The trust region's radius R_i is updated at each iteration to make sure that the surrogate function can be trusted. In practice it is adjusted so that decreases or increases in the objective function are correctly predicted by the surrogate model:

$$\forall p \in \mathbb{R}^n, T(p) \leq 0, \frac{f(p) - f(p_0)}{\tilde{f}(p) - \tilde{f}(p_0)} > \frac{1}{4}. \tag{4.63}$$

Guidelines and algorithms about how to update the trust region radius R_i at each iteration can be found in [151, Chapter 4]. Summarized, the optimization algorithm consists of the following steps:

1. Select an initial point p_0 .
2. Compute: $f(p_0)$, $\nabla f(p_0)$ and $\nabla^2 f(p_0)$.
3. Assume:

$$f(p) \approx \tilde{f}(p) = f(p_0) + \nabla f(p_0) (p - p_0) + \frac{1}{2} (p - p_0)^T \nabla^2 f(p_0) (p - p_0)$$
- 4.a. If $\nabla^2 f(p_0) > 0$ use line search with Newton-like direction ν :
 - Find an approximate minimizer α_m of: $\{f(p_0 + \alpha\nu), \alpha \in [0, 1]\}$.
 - Define $p_1 = p_0 + \alpha_m\nu$.
- 4.b. Else, a trust region method is used to take the step:
 - Define $p_1 = \operatorname{argmin} \{ \tilde{f}(p), T(p) \leq 0, E_i(p) = 0, C_j(p) \leq 0 \}$.

5. Iterate steps 2 to 4 until convergence.

A mixed criterion combining change in function value and 1st order optimality, is used to defined convergence. At least one of the conditions of equation (4.64) needs to be fulfilled for convergence to be achieved:

$$\begin{cases} \|\hat{\nabla} f(p_0)\| \leq \epsilon_1 \\ |p_k - p_{k+1}| \leq \epsilon_2 \end{cases} \quad (4.64)$$

In equation (4.64), $\hat{\nabla}$ is the effective gradient that accounts for equality constraints and active inequality constraint. ϵ_1 is the first order optimality tolerance and ϵ_2 is the step size tolerance. These two parameters should be set by the user. Lastly, it should be noted that the proposed algorithm can still be used when the equality constraints E_i are not linear or the inequality constraints C_j non-convex. In that case, step 4.b. should be used whether the matrix $\nabla^2 f(p_0)$ is positive or not as line search methods are not valid for this type of optimization problems.

4.6 Numerical Examples

In this Section, the algorithm of Section 4.5 is used in the WFEM framework with derivatives computed according to Section 4.3 and 4.4. Additionally, the complexity of the proposed examples is limited to avoid introducing (parametric) reduced order modeling considerations or shape optimization formalism. First, the proposed method is used in an FRF-based parameter identification procedure. This serves as a proof of concept and a validation of the implementation. The method is subsequently used to optimize the vibro-acoustic performance of a resonant metabeam. Finally, the optimization of the transmission loss of a metapanel in the coincidence region is considered.

4.6.1 FRF based parameter identification

In this Subsection, the optimization algorithm and analytical derivatives formulation developed in the previous sections are used in a parameter identification scheme to validate their implementation. A 0.5 meter long beam with a 1cm by 3cm rectangular cross-section and unknown material properties is considered. Assuming a Poisson's ratio of 0.3, the cross section of a beam with unitary density ρ and unitary Young's modulus E is modeled with 108 SOLID 185 elements in ANSYS APDL 17.0 to serve as the basis for a parametric

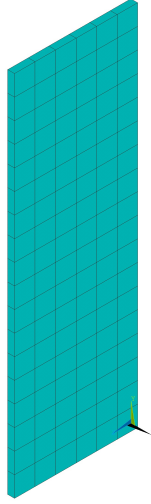


Figure 4.3: Unit cell for the cross-section of the beam (1cm by 3cm by 0.556mm)

model. The corresponding UC is shown in Figure 4.3. The mass matrix M_0 and stiffness matrix K_0 are used in a model for which the density, the real part and the imaginary part of the Young’s modulus are the parameters as specified in equation (4.65).

$$\left\{ \begin{array}{l} K(p) = (E_r + iE_i)K_0 \\ M(p) = \rho M_0 \\ p = \begin{bmatrix} E_r \\ E_i \\ \rho \end{bmatrix} \end{array} \right. \quad (4.65)$$

Clamped-Free boundary conditions are used and a unit force of 1N is applied at the free end of the beam. The direct forced response is computed on the 10Hz-1000Hz frequency range for material parameters values corresponding roughly to those of aluminum and given in Table 4.1.

| Material | Density ($kg.m^{-3}$) | Young Modulus (GPa) | Poisson coefficient | Damping ratio |
|----------|----------------------------|----------------------------|------------------------|------------------|
| Aluminum | 2700 | 69 | 0.3 | 0.03 |

Table 4.1: Reference material properties for the numerical model updating

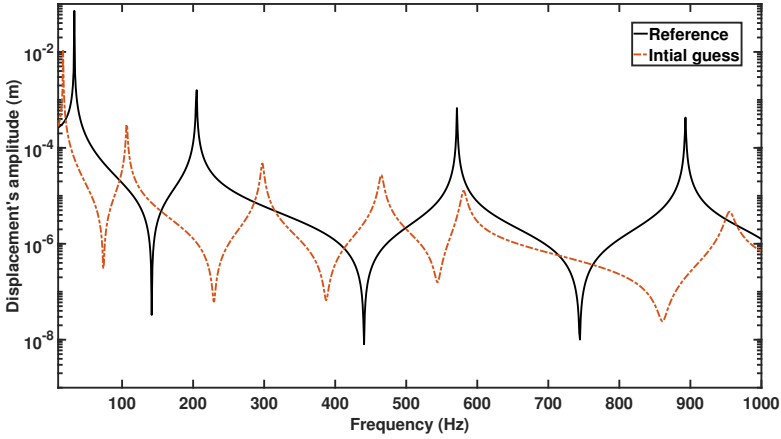


Figure 4.4: Comparison of the direct forced responses for the reference values and their initial estimates

The response, $X_0(\omega)$, is used to build an error function f that evaluates the difference between the reference and a response obtained using a material property vector p .

$$f(p) = \int_{\omega_-}^{\omega_+} (\log(|X_0(\omega)|) - \log(|X(\omega, p)|))^2 d\omega \quad (4.66)$$

In equation (4.66) the logarithm ensures that the objective function is sensitive to the information available on the full frequency range. Without this precaution, modal frequencies would dominate the error evaluation as these are where most of the signal's energy is located. The optimization process is started with material properties $\rho = 13000 \text{ kg.m}^{-3}$, $E_r = 90.10^9 \text{ Pa}$ and $E_i = 1,08.10^9 \text{ Pa}$. The first order optimality tolerance, ϵ_1 , is set to 10^{-3} and the step size tolerance, ϵ_2 , to 10^{-6} . Additionally, all material properties are constrained to be positive during the optimization process. The difference between the reference forced response and that obtained with the initial guess of the material properties is showcased in Figure 4.4 while Figure 4.5 shows the parameter values at each step of the optimization along with the value of the objective function. Looking at the optimization path of the real part of the Young's modulus, iterations 1 and 7 particularly stand out as the value of the real part of the Young's modulus becomes very low. To investigate this, the forced responses for iterations 1, 7, 9 and 11 are displayed in Figure 4.6. From iterations 1 to 10 the values of the material properties are adjusted so that the average logarithmic values of the forced response match that of the reference case. This explains the very high

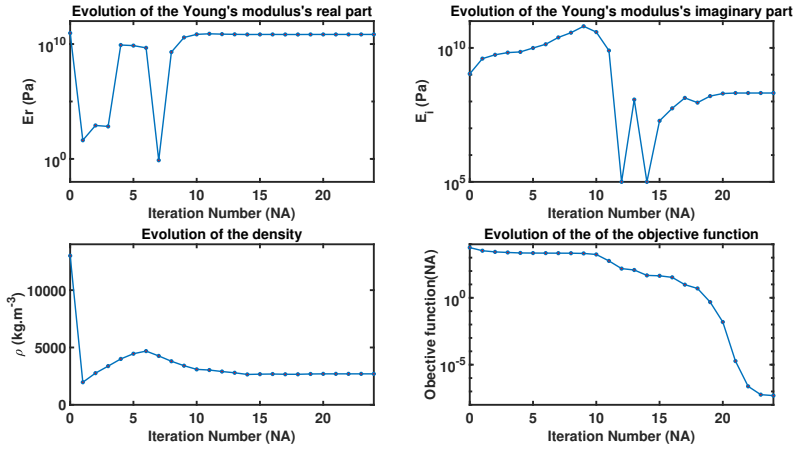


Figure 4.5: Evolution of the material properties' estimates and of the objective function

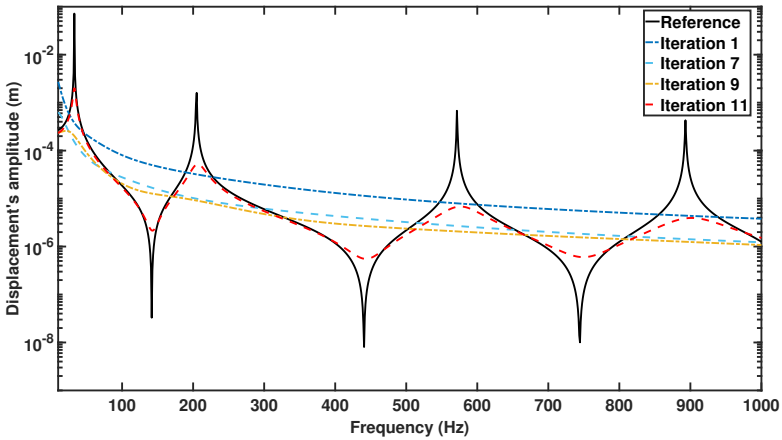


Figure 4.6: Evolution of the direct forced response's shape through the iterations

values for the imaginary part of the Young's modulus and the low values for its real part. Once the mean values approximately correspond, the estimated material properties evolve so that the modal features of the parametric model start matching that of the reference as evidenced from the forced response for iteration 11. Ultimately, the optimization algorithm converges to the reference values of the material properties with a relative error of 3.7×10^{-8} for the Young's modulus, 8.1×10^{-4} for the hysteretic loss factor and 8.5×10^{-8} for the density despite the initial guess being quite off. Incidentally, this example motivated the development of optimization algorithm presented in Section 4.5.

4.6.2 Optimization of a resonant metabeam

In this subsection, the wave-based methodology is applied to the optimization of the mean square velocity of a 1m long aluminum beam with a square section of side length 1cm and Clamped-Free boundary conditions. The beam is modeled using Euler-Bernoulli elements and is subjected to a 1N force applied on its free side. The resonant add-on is modeled by introducing an additional degree of freedom corresponding to the mass and linked to the corresponding out of plane dof of the bare structure via a spring element. The optimization variables are the mass, stiffness and damping parameters of the periodic resonant add-ons used to treat the host structure. The length of the UC is decided beforehand and fixed to 5cm, hence the beam contains 20 UCs. The variables of the vector of parameters are subsequently introduced:

- The added mass to the UC m (cannot be negative and shall not exceed 20% of the host structure's).
- The stiffness of the spring k (cannot be negative).
- The hystertic damping loss facor of the spring $\eta \in [0, 0.1]$.
- The position of the resonator in the UC (should be between 5mm and 4.5cm). The corresponding optimization variable β is normalized to be in the $[0, 1]$ interval.

Thus the vector of parameters is given in equation (4.67) while Figure 4.7 provides a schematic representation of the beam and its parameters:

$$p = [k \quad \eta \quad m \quad \beta]^T \quad (4.67)$$

The objective function takes the form:

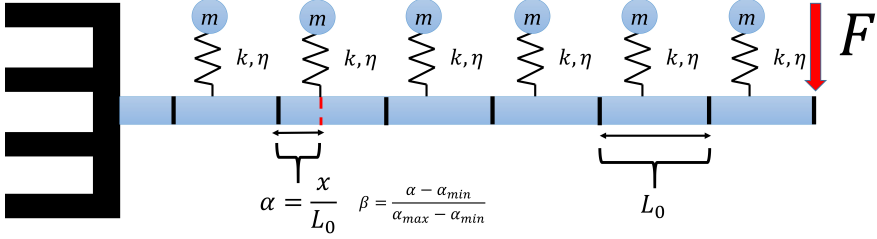


Figure 4.7: Schematic representation of the metabeam and its parameters

$$f(p) = \int_{\omega^-}^{\omega^+} \frac{1}{N} \sum_{i=1}^N \omega^2 |X_i(p, \omega)|^2 d\omega \tag{4.68}$$

Where $X_i(p, \omega)$ is the frequency forced response of the i^{th} section of the waveguide for a unitary load on the free side and N is the number of UCs. From a geometric point of view, moving the resonator e.g. to the right can be accomplished by lengthening the elements to its left and shortening the elements to its right by an equal amount. Therefore, the computation of derivatives with respect to β involves the matrix derivatives of Euler-Bernoulli elements with respect to their length. However, when evaluating models with different resonator positions, elements are not lengthened resp. shortened as it would lead to high length ratios between elements when the resonator approaches one of the UC's end. Instead, for a given resonator position, a mesh size is decided according to the shortest distance between the resonator and the UC's ends and re-meshing occurs at each iteration. For the optimization, the 5^{th} mode of the bare structure around 712Hz is targeted as shown in Figure 4.8. The frequency band of optimization, 648Hz-919Hz, is defined by the two anti-resonances surrounding the 5^{th} mode in the direct forced response of the bare structure. The second order optimization algorithm described in Section 4.5 is applied for a random starting point p_0 . The first order optimality tolerance ϵ_1 and the step size tolerance ϵ_2 are set respectively to 10^{-5} and 10^{-6} . In Figure 4.8, the direct forced response for the bare structure, the starting point of the

optimization, and the optimum are shown. Additionally, the response at section 1 (near the clamped side) is presented for the starting point and the optimum so that the stopband behavior can be evaluated in both cases. The value of the optimization variables at each iteration can be observed in Figure 4.9 while Figure 4.10 shows the evolution of the objective function. Unsurprisingly,

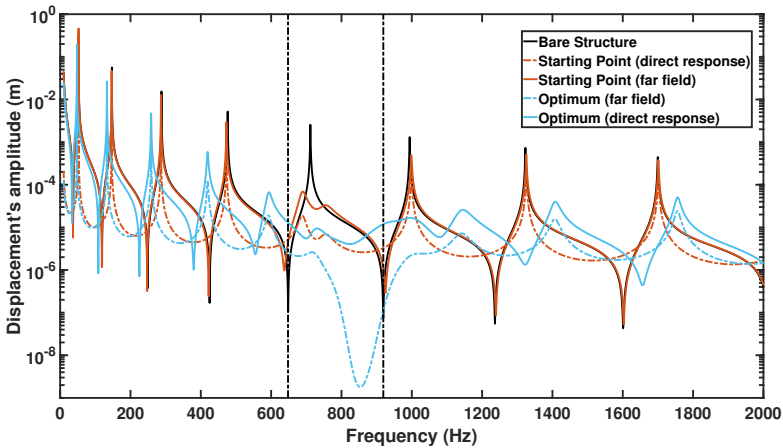


Figure 4.8: Response of the bare structure (direct), starting point (direct and far field) and optimum (direct and far field). The vertical dashed lines indicate the frequency band of optimization

maximizing the added mass and loss factor results in optimal performances. However, having the tuned resonance frequency on the targeted mode or at the center of the targeted frequency band does not. Similarly, the resonator's position in the UC is not a neutral parameter. These observations cannot be predicted from simple dispersion analysis and highlight the need to account for boundary conditions, finiteness and source location properties during the design phase.

4.6.3 Optimization of a multi-resonant metabeam

Given the vibration attenuation obtained in subsection 4.6.2 the case of multi resonant systems is investigated to see if it is possible to target several modes simultaneously without increasing the percentage of added mass. A 15 cm long UC with 3 resonators is considered. The resonator's positions are fixed at 4.5 cm of their respective 5 cm long sub-UCs. The length of the beam is also extended to 1.5 m as to be a multiple of the 15 cm long triple UC and Clamped-Free

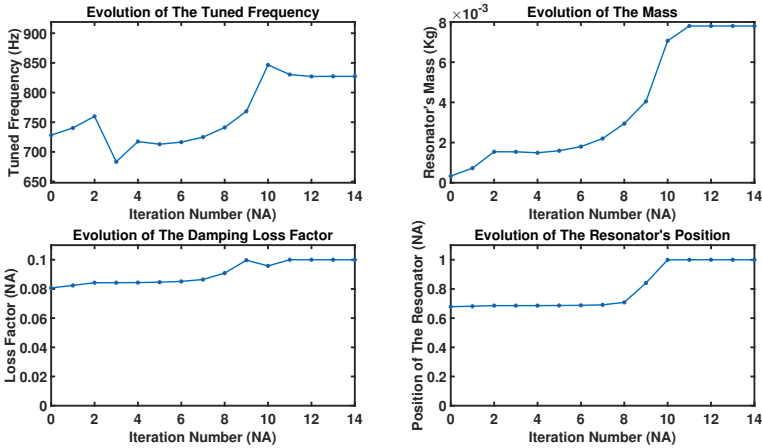


Figure 4.9: Evolution of the resonator’s tuned frequency, mass, damping ratio and position

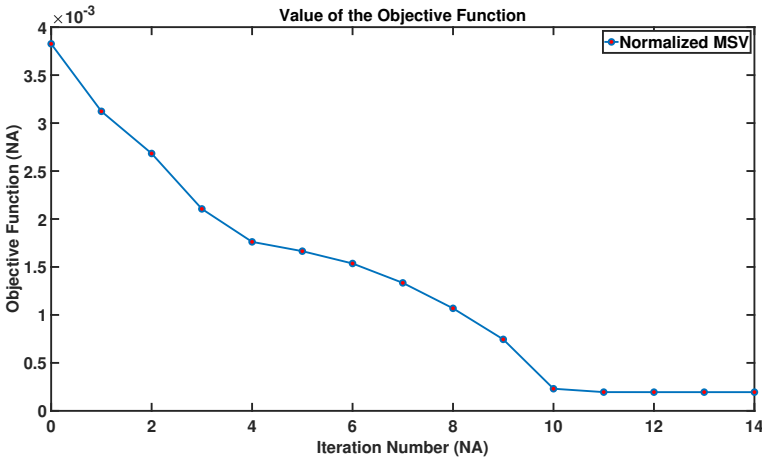


Figure 4.10: Evolution of the objective function

boundary conditions are used. The targeted frequency band, 188Hz-408Hz is defined by the anti-resonances surrounding the 4th and 5th modes of the host structure. As in the previous case, the added mass of each resonator is limited to 20% of that of the host structure in its sub UC. The damping loss factors are also limited to 10%. The vector of material properties is given in equation

(4.69):

$$p = [k_1 \quad \eta_1 \quad m_1 \quad k_2 \quad \eta_2 \quad m_2 \quad k_3 \quad \eta_3 \quad m_3]^T \quad (4.69)$$

Likewise, the objective function is still that of equation (4.68):

$$f(p) = \int_{\omega^-}^{\omega^+} \frac{1}{N} \sum_{i=1}^N \omega^2 |X_i(p, \omega)|^2 d\omega$$

The starting point of the optimization is chosen randomly with the additional constraint that all three resonators have identical material properties to see if this still holds for the optimum and during the optimization process. The values of the convergence criteria are set to 10^{-4} for the first order optimality tolerance and 10^{-7} for the step size tolerance. In Figure 4.11, the direct forced

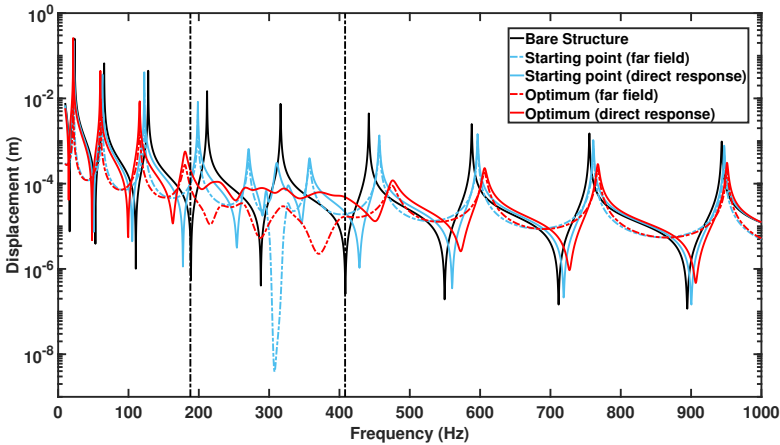


Figure 4.11: Response of the bare structure (direct), starting point (direct and far field) and optimum (direct and far field). The vertical dashed lines indicate the frequency band of optimization

response for the bare structure, the starting point of the optimization, and the optimum are shown. Additionally, the response at section 1 (near the clamped side) is presented for the starting point and the optimum so that the stopband behavior can be evaluated in both cases. The values of the resonators' attributes at each iteration can be observed in Figure 4.12 along with that of the objective function. The optimum is not really surprising. The added mass and damping loss factor of all resonators reached the maximal allowed values and the tuned resonance frequencies are spread over the optimization zone in order to cover the maximum area.

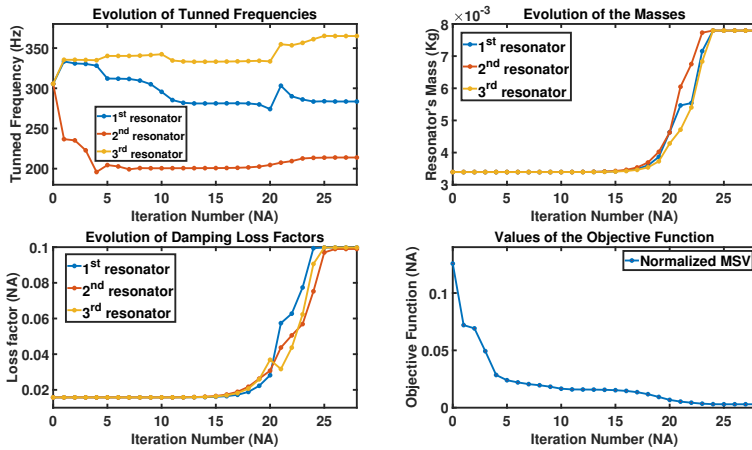


Figure 4.12: Evolution of the objective function and all three resonators' properties

4.6.4 Optimization of the diffuse field transmission loss of a resonant metapanel

In this subsection, the 2D WFEM framework is used in conjunction with the method developed by Christen et al. [42] to evaluate and optimize the transmission loss through a metapanel. The general lines of the transmission loss computation are discussed in subsection 4.6.4 in order to introduce the objective function. Then, the modeling of the panel, its parameters and the optimization results are subsequently discussed in subsection 4.6.4.

Transmission loss through a weakly periodic structure

Two semi-infinite acoustic domains separated by a periodic structure filling the space region $-h \leq z \leq 0$ are considered. An incident acoustic field is present in the half space $z \leq -h$ which, by fluid structure coupling, leads to a structural response X , a reflected acoustic field and a transmitted acoustic field. The transmission loss is defined as the ratio between the intensity of the incident field and that of the transmitted one. In 2016, Christen et al. introduced a method based on the 2D WFEM to compute the transmission loss through homogeneous multi-layer panels [42]. The method can be extended to periodic structures assuming that the dimensions of the UC are smaller than all acoustic wavelengths considered and that the structural response to a spatially

harmonic load is approximately spatially harmonic. That is, the UC must be subwavelength and the structure weakly periodic. First, the transmission loss for an incident acoustic plane wave at circular frequency ω , acoustic wavenumber k_0 and incidence angles (θ, ϕ) is considered. Using the complex notation, the plane wave has the form:

$$\begin{cases} P_{inc} = P_i e^{-ik_z z} e^{-ik_y y} e^{-ik_x x} \\ k_z = k_0 \cos \phi, \quad k_y = k_0 \sin \theta \sin \phi, \quad k_x = k_0 \cos \theta \sin \phi \end{cases} \quad (4.70)$$

Its transmission loss, $\tau(\omega, \theta, \phi)$, can be computed by linking the structural displacement to the transmitted and reflected acoustic pressures. Indeed, the continuity of the normal velocity should hold at the two fluid-structure interfaces:

$$\frac{\partial v}{\partial t} = -\frac{\nabla P}{\rho_{air}} \quad (4.71)$$

In equation (4.71) P is the pressure on the fluid domain, v is the particle velocity and ρ_{air} is the density of the air. Taking both the spatial and temporal Fourier transforms this equation can be written on both fluid-structure interfaces:

$$P_r = P_i - \frac{i\rho_{air}\omega^2}{k_z} X_- \quad (4.72)$$

$$P_t = \frac{i\rho_{air}\omega^2}{k_z} X_+ \quad (4.73)$$

with X_- the out of plane structural displacement at the incident side and X_+ the out of plane displacement at the transmission side. The reflected and transmitted pressure fields take the form:

$$\begin{cases} P_{ref} = P_r e^{ik_z z} e^{-ik_y y} e^{-ik_x x} \\ P_{tra} = P_t e^{-ik_z z} e^{-ik_y y} e^{-ik_x x} \end{cases} \quad (4.74)$$

Following the logic of subsection 4.4.1, the complete structural response X can be evaluated by solving:

$$(D(k_x, k_y) + A^+(k_z) + A^-(k_z)) X = 2F_i \quad (4.75)$$

In equation (4.75), F_i is the force vector associated to the incident pressure field while $A^+(k_z)$ and $A^-(k_z)$ integrate the parts of the reflected and transmitted pressure fields that scale linearly with the structural displacement. The factor 2 comes from the fact that the reflected pressure is derived from both the displacement and the incident pressure. Once the structural displacement is known, the quadratic amplitude of transmitted pressure field can be evaluated:

$$|P_t|^2 = \frac{\rho_{air}\omega^2}{Nk_z} X_+^* X_+ \quad (4.76)$$

With X_+ the structural displacement at the interface and N the dimension of X_+ . The transmission loss $\tau(\omega, \theta, \phi)$ is then defined as:

$$\tau(\omega, \theta, \phi) = \frac{|P_t|^2}{|P_i|^2} \quad (4.77)$$

The diffuse transmission loss at the circular frequency ω can then be obtained as:

$$\tau_d(\omega) = \frac{\int_0^{2\pi} \int_0^{\frac{\pi}{2}} \tau(\omega, \theta, \phi) \sin \theta \cos \theta \, d\theta \, d\phi}{\int_0^{2\pi} \int_0^{\frac{\pi}{2}} \sin \theta \cos \theta \, d\theta \, d\phi} \quad (4.78)$$

while the global diffuse field transmission loss on the frequency range $[\omega_-, \omega_+]$ is defined by:

$$\tau_g(\omega^-, \omega^+) = \frac{\int_0^{2\pi} \int_0^{\frac{\pi}{2}} \int_{\omega_-}^{\omega_+} \tau(\omega, \theta, \phi) \sin \theta \cos \theta \, d\theta \, d\phi \, d\omega}{\int_0^{2\pi} \int_0^{\frac{\pi}{2}} \int_{\omega_-}^{\omega_+} \sin \theta \cos \theta \, d\theta \, d\phi \, d\omega} \quad (4.79)$$

Finally, while the present section maintained the distinction between X_+ and X_- (in accordance to [42]) these vectors are equal in subsection 4.6.4 because shell elements are used to model the metapanel.

Numerical modeling and results

The method described in subsection 4.6.4 is applied to a metapanel. The bare panel is 4 mm thick and mass spring systems are added to it periodically. The UC is chosen to be 1cm by 1cm which guarantees that the subwavelength condition is respected. The host structure's UC is modeled in Ansys APDL 17.0 with elements SHELL181. Its mesh is shown in Figure 4.13. The additional dof of the mass is connected to the central node of the UC and the parameters of the model are the added mass, the stiffness of the spring and the hysteretic damping. The mass is constrained so that it does not exceed 10% of the host structure's mass while the damping is limited to 10%. The parameter vector is:

$$p = \begin{bmatrix} k \\ \eta \\ m \end{bmatrix} \quad (4.80)$$

The aim of the optimization is to mitigate the decrease of transmission loss in the 1900-6000 Hz frequency range caused by the structural-acoustic coincidence (see Figure 4.14) hence the objective function is:

$$f(p) = \frac{\int_0^{2\pi} \int_0^{\frac{\pi}{2}} \int_{\omega_-}^{\omega_+} \tau(\omega, \theta, \phi, p) \sin \theta \cos \theta \, d\theta \, d\phi \, d\omega}{\int_0^{2\pi} \int_0^{\frac{\pi}{2}} \int_{\omega_-}^{\omega_+} \sin \theta \cos \theta \, d\theta \, d\phi \, d\omega} \quad (4.81)$$

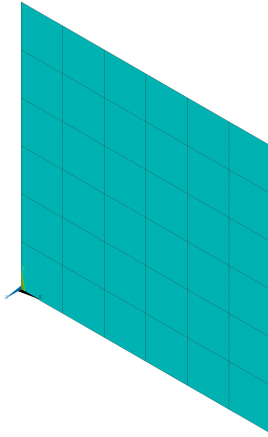


Figure 4.13: Unit Cell of the host structure

where $\tau(\omega, \theta, \phi, p)$ is the transmission loss for an incident acoustic wave at circular frequency ω and angles (θ, ϕ) and parameter vector p . This function satisfies the conditions of Section 4.1 (see equation (4.77)), therefore the additional cost of computing its derivatives is low. The optimization is carried out starting from a random point in the design space with stopping criteria values set to 10^{-16} for the first order optimality tolerance and 10^{-7} for the minimal step size. A comparison between the TL of the bare structure and that of the optimal design is given in Figure 4.14. Additionally, Figure 4.15 shows the optimization path of the resonators attributes as well as the value of the objective function. As expected, maximizing the TL requires to maximize both the mass and damping of the resonator and the optimal tuned frequency is close to that of the minimal TL for the bare structure. The optimum is reached in a few iterations despite the starting point being far from the optimal values, proving the efficiency of the optimization methodology.

4.7 Conclusions and perspectives

In this chapter, first and second order derivatives were derived for the 1D and 2D WFEM via an intrusive methodology. Additionally, a second order optimization algorithm based on the sequential quadratic programming paradigm [25] was proposed to exploit the derivatives to their fullest. The proposed algorithm combines an ellipsoidal trust-region method [157, 54, 115] with a line search

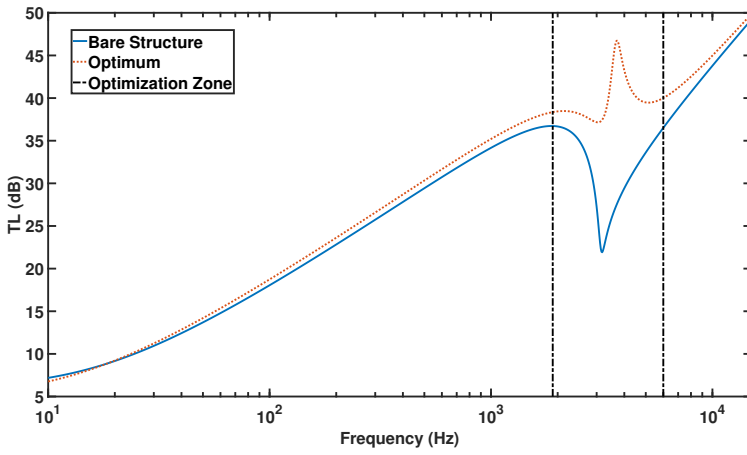


Figure 4.14: Comparison of the performance of the host structure and the optimum

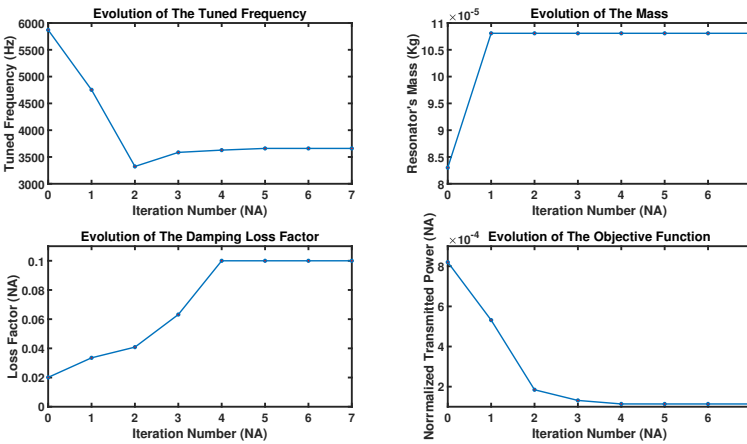


Figure 4.15: Evolution of the objective function and of the TVA's properties

method when appropriate. When it is not, the algorithm reduces to the ellipsoidal trust-region method. Combined, both contributions form a framework for the optimization of 1D and 2D periodic structures. In the 1D case, the size of the waveguide, the boundary conditions and eventual loads can all be taken into account during the optimization process. In the 2D case, only infinite structures are considered but the load's characteristics can still be accounted for. This is demonstrated in the numerical examples in which the proposed methodology is used to successfully optimize the vibro-acoustic performances of metabeams under clamped-free boundary conditions and the diffuse field transmission loss of a metapanel. The proposed methodology accounts for both strong and weak points of the WFEM. Namely, the decoupling of the computation cost from the size of the waveguide and the lower accuracy of the WFEM as compared to FEM modeling. It is versatile and can be used in a wide range of applications including parameter identification, homogenization, model updating, design optimization and potentially damage detection. Further technical developments will focus on the incorporation of model order reduction in the proposed framework and its extension to other UCM techniques such as the shift cell operator method. The former could prove challenging because rigorously, the derivatives of all projection matrices are required to ensure the accuracy of the gradient and Hessian matrix of objective functions [11]. Applications with complex cases including 3D geometric parameters and topology optimization [191, 71] will also be considered, they may require to recast some of proposed formula for eigenvalue and eigenvector derivatives within adjoint and adjoint-adjoint frameworks [81, 94] in order to quickly provide low dimensional approximation of the hessian matrix that could be used with conjugate gradient methods [180, 46]. Similar ideas were proposed in [193, 158] for deep learning and aerodynamic shape optimization respectively.

Chapter 5

Wavenumber Extraction

Part of this chapter has been submitted as: "R.F. Boukadia, C. Claeys, C. Droz, M. Ichchou, W. Desmet, E. Deckers. An INverse CONvolution MEthod for wavenumber extraction (INCOME): formulations and applications. *Journal of Sound and Vibration*, Manuscript in revision, 2021."

Wavenumber extraction is a process by which a displacement field in a N -dimensional medium is converted to a finite collection of $(N-1)$ dimensional manifolds that contains information about plane wave propagation in that media. It is an inverse problem. This chapter deals with the cases $N = 1$ and $N = 2$. For $N = 1$ one seeks to extract a finite set of wavenumbers that characterize wave propagation inside the medium which in essence boils down to performing an inverse WFEM. In the case $N = 2$ one wants to know a finite collection of continuous wavenumbers functions parametrized by their direction of propagation given by the angle θ . That is, $k = f_i(\theta)$. An ideal outcome of this process is illustrated in Figure 5.1. Obviously, wavenumber extraction shares links with both the Fourier and Laplace transforms but differs from them in a crucial way. That is both the aforementioned transformations produce a single N -dimensional output (in either \mathbb{R} or \mathbb{C}) when fed an N -dimensional input while wavenumber extraction leads to several $(N-1)$ -dimensional outputs giving the "sharpness" observed in Figure 5.1 with contrast to the blur usually obtained when using the Laplace or Fourier transforms (see e.g. Figure 2.5). In practice this blur is problematic because it prevents a precise evaluation of both the phase velocity and spatial attenuation of waves traveling in a given direction inside the media.

In order to tackle this issue many wave extraction methods have been developed and the most important were presented in the state of the art (Chapter 2.5). In

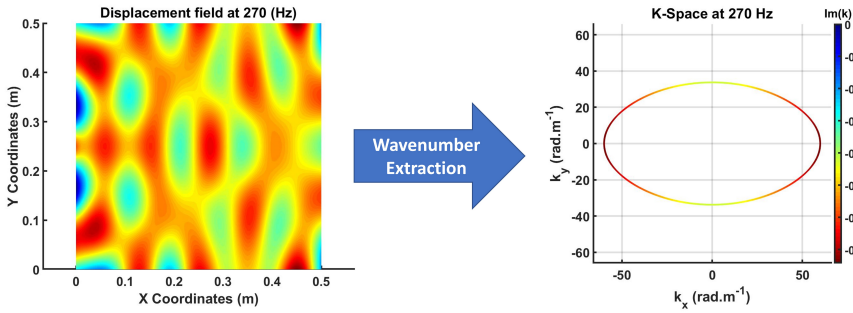


Figure 5.1: Illustration of the output of an ideal wavenumber extraction process in the 2D case

the one-dimensional case, Mc Daniel type of methods have been quite successful [137, 138, 210]. These methods leverage the general analytical expression that describes the displacement field in a 1D homogeneous or periodic medium to perform a nonlinear fit of the measured displacement field. The downside of this class of methods is that they rely on nonlinear non-convex optimization problems, thus issues regarding the presence of multiple local minima can arise. On the other hand, these methods typically have a very low sensitivity to noise and are able to deal with scattered measurements. Another interesting category of methods for 1D wavenumber extraction is the class of 'linear methods', namely, the Prony series method [108, 97, 38, 96] and the ESPRIT algorithm [163, 131, 132]. Both methods need periodic sampling of the input data and only require the solving of well posed linear systems in order to correctly estimate the wavenumbers. The advantage of this class of methods is that it relies on solving linear problems and thus avoid issues related to non-convex optimization. On the other hand, periodic sampling of the wave-field is required and the Prony series method in particular is very noise sensitive. Though attempts to extend these methods to the 2D case were made [96, 132], they produce a finite, scattered set of wavenumbers pairs and thus do not meet the proposed definition of the wavenumber extraction process.

At this point, two class of methods have been proposed in the literature to properly deal with 2D wavenumber extraction: (1) The Inhomogenous Wave Correlation [21, 187, 186, 130] (IWC) that works by maximizing the correlation function between a measured displacement field and a parametric function that depends on a wavenumber and (2) the Inverse Wave Decomposition [40] (IWD) that generalizes Mc Daniel's method to the 2D case by proposing a fit for the displacement field. Both methods however have issues. Because it is based on a correlation function, the IWC only works well when many wavelengths

are present in the measured displacement field making it unsuitable at low frequencies. Also, it never returns an exact value for the wavenumber even when given noiseless data. The IWD on the other suffers from the opposite problem. Because it fits the displacement field with a continuous (integral) sum of plane waves it has to retrieve a high number of wave amplitudes and wavenumbers (when the structure studied is not isotropic) such that the associated optimization problem becomes practically unsolvable at higher frequencies outside of the modal regime where few plane waves are needed in order to obtain a good fit.

Inspired by the success of the linear class of methods in the 1D case and the gaps present regarding the methods available for 2D wavenumber extraction we propose a method belonging to the former category that works in the 2D case and manages to encode the full k -space in a single convolution kernel determined by solving a linear problem system formed using a periodic sampling of the displacement field. The proposed method is named INCOME (INverse CONvolution METHod) and is presented in details in Sections 5.1, 5.2 and 5.3. Its performance is assessed and compared to other methods of the literature in Section 5.4. In Section 5.5, INCOME is used on experimental test cases while Section 5.6 summarizes the main conclusions and perspectives for INCOME.

5.1 The 1D inverse convolution method

In this section, the 1D version of the proposed method is presented. First, the case of a single exponential function is studied in subsection 5.1.1: the associated recurrence relationship and its associated convolution equivalent are derived. In subsection 5.1.2 the signal studied is the sum of an exponential function and another one with the opposite wavenumber. This central symmetry in the wavenumber domain induces a palindromic symmetry in the convolution operator the proposed method seeks to estimate. The number of effective parameters estimated is thus brought back to one. The general case with many waves and their reflections is considered in subsection 5.1.3 and a regularization technique taking advantage of the palindromic symmetry is derived in subsection 5.1.4. That technique improves the accuracy of the propagation constant's estimates and enforces the relevant wavenumber symmetries. Lastly, a method to predetermine the number of independent exponential functions present in the signal is described in subsection 5.1.5.

5.1.1 Main Principle

In this subsection the principle behind the proposed methodology is presented by considering the propagation of a single plane wave on a finite 1D domain. The size of the domain is L_{max} and it is assumed to occupy the space region $x \in [0, L_{max}]$. The displacement field is represented by a function U of the form:

$$U(x) = Ae^{-ikx}. \quad (5.1)$$

In equation (5.1), k is a complex wavenumber and A is the complex wave amplitude. Both are unknown but the aim is only to retrieve k . To that end, the wavefield U is sampled at N points x_n periodically spaced with distance L as per equation (5.2):

$$\begin{cases} x_n = x_0 + nL \\ U_n = U(x_n) + \epsilon_n \end{cases}. \quad (5.2)$$

In equation (5.2), x_n is the abscissa of the n^{th} measurement point while ϵ_n is the measurement error on the n^{th} point. In case there is no error, the sequence $(U_n)_{n \in \llbracket 1, N \rrbracket}$ is a geometric sequence with common ratio $\lambda = e^{-ikL}$ also called propagation constant. The propagation constant can be computed by taking the ratio of any two successive measurements as in equation (5.3):

$$\lambda = \frac{U_{n+1}}{U_n}. \quad (5.3)$$

The wavenumber k can then be retrieved:

$$k = \frac{i}{L} \ln(\lambda). \quad (5.4)$$

In most cases however, the measurements are not perfect, hence only an estimate of the propagation constant can be computed. The most intuitive way to do so is to average the ratios of consecutive terms of the sequence as in equation (5.5):

$$\hat{\lambda}_1 = \frac{1}{N-1} \left(\sum_{n=1}^{N-1} \frac{U_{n+1}}{U_n} \right). \quad (5.5)$$

Equation (5.5) leverages all the measurements to form a robust estimate of the propagation constant. However, it cannot be generalized in case several propagation constants must be retrieved from one set of measurements. Consequently, an estimate using a method easier to generalize is derived. When no error is present in the measurements, the sequence $(U_n)_{n \in \llbracket 1, N \rrbracket}$ satisfies:

$$\forall n \in \llbracket 1, N-1 \rrbracket, \quad U_{n+1} - \lambda U_n = 0. \quad (5.6)$$

To form an estimate using this relationship it is helpful to see it as a convolution product between two sequences. First, the convolution product of two infinite sequences is defined. For two infinite sequences $(g_n)_{n \in \mathbb{Z}}$ and $(h_n)_{n \in \mathbb{Z}}$ their convolution product $(e_n)_{n \in \mathbb{Z}}$ is defined in equation (5.7):

$$\begin{cases} e = g * h = h * g \\ e_n = \sum_{l=-\infty}^{\infty} g_{n-l} h_l \end{cases} \quad (5.7)$$

This paradigm can be extended to finite sequences. Considering two finite sequences $(g_n)_{n \in \llbracket 1, N \rrbracket}$ and $(h_n)_{n \in \llbracket 1, M \rrbracket}$ such that $M \leq N$ their convolution product $(e_n)_{n \in \llbracket 1, N+1-M \rrbracket}$ is defined by:

$$\begin{cases} e = g * h = h * g \\ e_n = \sum_{l=1}^M g_{n+M-l} h_l \end{cases} \quad (5.8)$$

In this context, equation (5.6) can be rewritten as $U * (1, -\lambda) = 0$, therefore a good estimate of λ can be found by least square optimization:

$$\begin{cases} (\alpha, \beta) = \operatorname{argmin} \{ \| U * (a, b) \|_2, \| (a, b) \|_2 = 1 \} \\ \hat{\lambda} = -\frac{\beta}{\alpha} \end{cases} \quad (5.9)$$

The first part of equation (5.9) seeks to find a two term sequence that produces a new sequence of minimal norm when convoluted with the discretized displacement field. The constraint $\| (a, b) \|_2 = 1$ is imposed because the norm of the product scales linearly with that of each sequence involved. Therefore, making comparisons at equal norms is necessary. This means α cannot be chosen equal to 1 hence $\hat{\lambda}$ is defined by the ratio of β and α .

Finally, a practical implementation of equation (5.9) is proposed. By identifying a finite sequence of n terms with the corresponding vector in \mathbb{C}^N the convolution product can be put in matrix form. For a sequence $(U_n)_{n \in \llbracket 1, N \rrbracket}$ the matrix $C_i(U)$ is defined as per equation (5.10):

$$C_i(U) = \begin{pmatrix} U_i & U_{i-1} & \dots & U_1 \\ U_{i+1} & U_i & \dots & U_2 \\ \vdots & \vdots & \vdots & \vdots \\ U_N & U_{N-1} & \dots & U_{N+1-i} \end{pmatrix} \quad (5.10)$$

With this notation the convolution product of equation (5.9) can be rewritten:

$$U * (a, b) = C_2(U) \begin{bmatrix} a \\ b \end{bmatrix} = \begin{pmatrix} U_2 & U_1 \\ U_3 & U_2 \\ \vdots & \vdots \\ U_{N-1} & U_{N-2} \\ U_N & U_{N-1} \end{pmatrix} \begin{bmatrix} a \\ b \end{bmatrix} \quad (5.11)$$

The system of equation (5.9) can be rewritten as:

$$\begin{cases} \begin{bmatrix} \alpha \\ \beta \end{bmatrix} = \operatorname{argmin} \{ x^* C_2^*(U) C_2(U) x, \|x\|_2^2 = 1 \} \\ \hat{\lambda} = -\frac{\beta}{\alpha} \end{cases} \quad (5.12)$$

This can be solved by computing the eigenvalues and eigenvectors of a Hermitian positive matrix. α and β are the first and second components of the eigenvector of $D_2(U) = C_2^*(U) C_2(U)$ associated to its smallest eigenvalue (see Courant–Fischer–Weyl min-max theorem).

5.1.2 Reflected Wave

In most cases, the wave field is not as simple as a single plane wave propagating in one direction. Due to the boundaries of the finite domain a reflected wave field with the opposite wavenumber should also be present. In that case, the displacement field takes the form:

$$U(x) = Ae^{-ikx} + Be^{ikx} \quad (5.13)$$

Consequently, the general form for $(U_n)_{n \in \llbracket 1, N \rrbracket}$ the sequence of measurements is:

$$\begin{cases} U_n = A\lambda^n + B\lambda^{-n} + \epsilon_n \\ \lambda = e^{-ikL} \end{cases} \quad (5.14)$$

Because the sequence is the sum of two geometric sequences, its characteristic polynomial is:

$$P_U = (X - \lambda) \left(X - \frac{1}{\lambda} \right) = X^2 - \left(\lambda + \frac{1}{\lambda} \right) X + 1 \quad (5.15)$$

Noting $\mu = \lambda + \frac{1}{\lambda}$ the recurrence relationship for the sequence U in case the error is null is derived:

$$\forall n \in \llbracket 1, N - 2 \rrbracket, \quad U_{n+2} - \mu U_{n+1} + U_n = 0 \quad (5.16)$$

Or, in a better way:

$$\forall n \in \llbracket 1, N - 2 \rrbracket, \quad (U_{n+2} + U_n) - \mu U_{n+1} = 0 \tag{5.17}$$

Equations (5.16) and (5.17) can also be understood as convolution product between a symmetric three term long sequence and the displacement field. An estimate $\hat{\mu}$ of μ can be obtained by solving the least square problem of equation (5.18) :

$$\begin{cases} (\alpha, \beta, \alpha) = \operatorname{argmin} \{ \| U * (a, b, c) \|_2, \| (a, b, c) \|_2 = 1, c = a \} \\ \hat{\mu} = -\frac{\beta}{\alpha} \end{cases} \tag{5.18}$$

Estimates for the pair of propagation constants are then obtained as:

$$\left(\hat{\lambda}, \frac{1}{\hat{\lambda}} \right) = \left(\frac{\hat{\mu} + \sqrt{\hat{\mu}^2 - 4}}{2}, \frac{\hat{\mu} - \sqrt{\hat{\mu}^2 - 4}}{2} \right) \tag{5.19}$$

In equation (5.20) the convolution product is put in matrix form similarly to equation (5.11):

$$U * (a, b, a) = H_1(U) \begin{bmatrix} a \\ b \end{bmatrix} = \begin{pmatrix} U_3 + U_1 & U_2 \\ U_4 + U_2 & U_3 \\ \vdots & \vdots \\ U_{N-1} + U_{N-3} & U_{N-2} \\ U_N + U_{N-2} & U_{N-1} \end{pmatrix} \begin{bmatrix} a \\ b \end{bmatrix} \tag{5.20}$$

Equation (5.21) introduces a new matrix A_1 :

$$A_1 = \begin{pmatrix} 2 & 0 \\ 0 & 1 \end{pmatrix} \tag{5.21}$$

which accounts for the fact that:

$$\| (a, b, a) \|_2^2 = \begin{bmatrix} a \\ b \end{bmatrix}^* A_1 \begin{bmatrix} a \\ b \end{bmatrix} \tag{5.22}$$

The system of equation (5.18) is then rewritten in the form of equation (5.23):

$$\begin{cases} \begin{bmatrix} \alpha \\ \beta \end{bmatrix} = \operatorname{argmin} \{ x^* H_1^*(U) H_1(U) x, x^* A_1 x = 1 \} \\ \hat{\mu} = -\frac{\beta}{\alpha} \end{cases} \tag{5.23}$$

A solution can be obtained by finding the eigenvector associated to the smallest eigenvalue of the generalized eigenvalue problem:

$$(H_1^*(U) H_1(U)) x = \rho A_1 x \tag{5.24}$$

5.1.3 General 1D formulation

Now, the general case is considered. The displacement field is comprised of multiple plane waves and their reflections. It takes the form:

$$U(x) = \sum_{p=1}^{n_w} A_p e^{-ik_p x} + B_p e^{ik_p x} \quad (5.25)$$

Consequently, the general form for $(U_n)_{n \in \llbracket 1, N \rrbracket}$ the sequence of measurements is:

$$\begin{cases} U_n = \sum_{p=1}^{n_w} (A_p \lambda_p^n + B_p \lambda_p^{-n}) + \epsilon_n \\ \forall p \in \llbracket 1, n_w \rrbracket, \lambda_p = e^{-ik_p L} \end{cases} \quad (5.26)$$

Since it is a sum of geometric sequences, its characteristic polynomial is:

$$P_U = \prod_{p=1}^{n_w} (X - \lambda_p) \left(X - \frac{1}{\lambda_p} \right) \quad (5.27)$$

Because the propagation constants come in pairs $(\lambda_p, \frac{1}{\lambda_p})$, P_U is a palindromic polynomial of even degree. This means it is of the form:

$$\begin{cases} P_U = \sum_{p=0}^{2n_w} a_p X^p \\ \forall p \in \llbracket 0, 2n_w \rrbracket, a_{2n_w-p} = a_p \end{cases} \quad (5.28)$$

Therefore P_U can be rewritten as:

$$P_U = a_{n_w} X^{n_w} + \sum_{p=0}^{n_w-1} a_p (X^p + X^{2n_w-p}) \quad (5.29)$$

The corresponding recurrence relationship for the sequence U is then:

$$\forall n \in \llbracket 1, N - 2n_w \rrbracket, \quad a_{n_w} U_{n+n_w} + \sum_{p=0}^{n_w-1} a_p (U_{n+p} + U_{n+2n_w-p}) = 0 \quad (5.30)$$

As in the previous two cases, an estimate of the coefficients a_p is obtained by solving a least square problem. This least square problem comes from

understanding equation (5.30) as a convolution product. Two matrix families are introduced. First the family A_{n_w} :

$$A_{n_w} = \begin{pmatrix} 2 & 0 & \dots & 0 \\ 0 & 2 & \dots & 0 \\ \vdots & \dots & 2 & \vdots \\ 0 & \dots & \dots & 1 \end{pmatrix} \tag{5.31}$$

For all natural integers A_{n_w} is an $(n_w + 1) \times (n_w + 1)$ diagonal matrix. The first n_w diagonal terms are equal to 2 while the last one is equal to 1. Like for A_1 introduced in equation (5.21) this can be understood as weighing in the least-squares problem introduced to account for the fact that most coefficients appear two times in the recurrence relationship of equation (5.30). The second family of matrices to be introduced is the family $H_{n_w}(U)$ that represents the matrix form of the convolution product of a symmetric sequence of $2n_w + 1$ terms with the sequence of measurements:

$$H_{n_w}(U) = \begin{pmatrix} U_{2n_w+1} + U_1 & U_{2n_w} + U_2 & \dots & U_{n_w+2} + U_{n_w} & U_{n_w+1} \\ U_{2n_w+2} + U_2 & U_{2n_w+1} + U_3 & \dots & U_{n_w+3} + U_{n_w+1} & U_{n_w+2} \\ \vdots & \vdots & \dots & \vdots & \vdots \\ U_{N-1} + U_{N-2n_w-1} & U_{N-2} + U_{N-2n_w} & \dots & U_{N-n_w} + U_{N-n_w-2} & U_{N-n_w-1} \\ U_N + U_{N-2n_w} & U_{N-1} + U_{N-2n_w+1} & \dots & U_{N-n_w+1} + U_{N-n_w-1} & U_{N-n_w} \end{pmatrix} \tag{5.32}$$

Finally, by finding the smallest eigenvalue of (5.33), the coefficients of the P_U are given by the associated eigenvector.

$$(H_{n_w}^*(U)H_{n_w}(U))x = \rho A_{n_w}x \tag{5.33}$$

The propagation constants' estimates are then obtained by finding the roots of the polynomial P_U .

5.1.4 Palindromic transform

Due to numerical issues the solutions of $P_U(X) = 0$ may violate the relationship between the pairs of propagation constants $(\lambda, \frac{1}{\lambda})$. To prevent this, a transformation of P_U is performed. First, a rational fraction Q is introduced in equation (5.34):

$$Q(X) = \frac{P_U(X)}{X^{n_w}} = a_{n_w} + \sum_{p=0}^{n_w-1} a_p (X^{n_w-p} + X^{p-n_w}) \tag{5.34}$$

The change of variables $Y = X + \frac{1}{X}$ is then performed for Q . This yields a polynomial R of degree n_w whose roots are $\mu_i = \left(\lambda_i + \frac{1}{\lambda_i}\right)$. After finding the

roots μ_i of R , the pairs of propagation constants are obtained using equation (5.35) :

$$\left(\lambda_i, \frac{1}{\lambda_i}\right) = \left(\frac{\mu_i + \sqrt{\mu_i^2 - 4}}{2}, \frac{\mu_i - \sqrt{\mu_i^2 - 4}}{2}\right) \quad (5.35)$$

This process is similar to the transformation of quadratic palindromic eigenvalue problems that appear in optimal control theory and for the 1D WFEM [214].

5.1.5 Number of waves

Before determining what the propagation constants and wavenumbers are, it is necessary to know how many waves are present in the wavefield. That number may be known *a priori* using known physical or numerical properties of the phenomenon generating the signal. When that is not the case, that number may be determined by using a stability diagram as in [210] but an alternative method is proposed here. Indeed, the number of waves n_w can be determined by looking at the rank of the matrix $H_n(U)$. As long as $n_w \leq n$ the rank of $H_n(U)$ is equal to n_w . Practically, the rank of the matrix $H_n(U)$ is determined by looking at its singular values, as the rank is equal to the number of non-zero singular values. Because of numerical precision and experimental error, singular values below a certain threshold should be considered null. Procedures for appropriate truncation criteria can be found in [164, 73]. In general the truncation value S_t should at least verify $S_t \geq \max(\alpha S_{max}, \frac{S_{max}}{nr})$ with α the numerical precision, nr the signal to noise ratio and S_{max} the largest singular value of $H_n(U)$.

5.2 The 2D inverse convolution method

This section deals with the 2D version of INCOME. In subsection 5.2.1 the 2D version of INCOME is intuitively derived using the convolution framework and partially justified by comparison to the 2D Wave Finite Element Method. Finally, subsection 5.3 details how to extract the proper K-Space corresponding to a given convolution operator.

5.2.1 General version of the 2D case

The 1D version of the proposed method works by finding a (symmetric) convolution kernel that results in a null sequence when multiplied with a sequence of (periodically spaced) measurements. An intuitive way to extend the method to the 2D case would be to search for a 2D symmetric convolution

kernel that would do the same with a 2D sequence of measurements. This introduces two issues. Firstly, is it possible to mathematically justify this approach? Secondly, what would be the size of such a convolution kernel and which among the many forms of 2D symmetry should it have? Both questions are partially answered when looking at the 2D (WFEM) when written as the explicit assembly of a 2D periodic medium from identical unit cells [28, 4]:

$$\begin{aligned}
F_{r,s} = & (D_{11} + D_{22} + D_{33} + D_{44})\Psi_{r,s} + (D_{13} + D_{24})\Psi_{r,s+1} + (D_{12} + D_{34})\Psi_{r+1,s} \\
& + (D_{31} + D_{42})\Psi_{r,s-1} + (D_{21} + D_{43})\Psi_{r-1,s} \\
& + D_{14}\Psi_{r+1,s+1} + D_{23}\Psi_{r-1,s+1} + D_{32}\Psi_{r+1,s-1} + D_{41}\Psi_{r-1,s-1}
\end{aligned} \tag{5.36}$$

In equation (5.36), setting all external forces $F_{r,s}$ to zero and applying the Floquet-Bloch theorem leads to the the classical form of the 2D WFEM. Another way of approaching equation (5.36) is to consider it as a convolution product between a 2D sequence of vectors (representing structural displacements) and a 2D sequence of matrices (representing the partial differential equation governing the periodic medium). When no forces are present, this convolution product should result in a null sequence. This validates the general concept proposed to extend the present method to the 2D case and specifies the size, shape and level of symmetry of the generic 2D convolution kernel, S , used for the retrieval of a single wave. A representation of this kernel is provided in equation (5.37) by using tables:

$$\begin{array}{|c|c|c|} \hline S_{1,3} & S_{2,3} & S_{3,3} \\ \hline S_{1,2} & S_{2,2} & S_{3,2} \\ \hline S_{1,1} & S_{2,1} & S_{3,1} \\ \hline \end{array} = \begin{array}{|c|c|c|} \hline e & c & d \\ \hline b & a & b \\ \hline d & c & e \\ \hline \end{array} \tag{5.37}$$

The symmetries of equation (5.37) mimic those of equation (5.36) and can also be linked to the Hermitian symmetry of the k-space:

$$\forall (i, j) \in \llbracket 1, 4 \rrbracket^2, \quad D_{ij} = D_{ji}^T \tag{5.38}$$

Assuming only one wave type is present in a sequence of 2D (periodically spaced) perfect measurements $(U_{i,j})_{(i,j) \in \llbracket 1, N \rrbracket \times \llbracket 1, M \rrbracket}$, there exists a 2D convolution operator S in the form of equation (5.37) such that:

$$V = U * S = 0 \tag{5.39}$$

Or, in a explicit form:

$$\forall (p, q) \in \llbracket 1, N - 3 \rrbracket^2, \quad V_{p,q} = \sum_{(i,j) \in \llbracket 1, 3 \rrbracket^2} S_{i,j} U_{p+3-i, q+3-j} = 0 \tag{5.40}$$

Similarly to the 1D case, it is possible to capture more waves by taking the convolution product of several single wave operators. For two waves, the general

form is as follows:

$$R = S_1 * S_2 = \begin{array}{|c|c|c|c|c|} \hline R_{1,5} & R_{2,5} & R_{3,5} & R_{4,5} & R_{5,5} \\ \hline R_{1,4} & R_{2,4} & R_{3,4} & R_{4,4} & R_{5,4} \\ \hline R_{1,3} & R_{2,3} & R_{3,3} & R_{4,3} & R_{5,3} \\ \hline R_{1,2} & R_{2,2} & R_{3,2} & R_{4,2} & R_{5,2} \\ \hline R_{1,1} & R_{2,1} & R_{3,1} & R_{4,1} & R_{5,1} \\ \hline \end{array} = \begin{array}{|c|c|c|c|c|} \hline m & j & g & i & l \\ \hline k & e & c & d & h \\ \hline f & b & a & b & f \\ \hline h & d & c & e & k \\ \hline l & i & g & j & m \\ \hline \end{array} \quad (5.41)$$

The coefficients of the 2D convolution kernels can be determined via linear least-squares optimization that results in an eigenvalue problem. The process is similar to the 1D case and is detailed for the generic one wave kernel. First, the matrix $J_1(U)$ is introduced in equation (5.42):

$$J_1(U) = \begin{pmatrix} U_{2,2} & U_{3,2} + U_{1,2} & U_{2,3} + U_{2,1} & U_{3,3} + U_{1,1} & U_{3,1} + U_{1,3} \\ U_{3,2} & U_{4,2} + U_{2,2} & U_{3,3} + U_{3,1} & U_{4,3} + U_{2,1} & U_{4,1} + U_{4,3} \\ \vdots & \vdots & \vdots & \vdots & \vdots \\ U_{i,j} & U_{i+1,j} + U_{i-1,j} & U_{i,j+1} + U_{i,j-1} & U_{i+1,j+1} + U_{i-1,j-1} & U_{i+1,j-1} + U_{i-1,j+1} \\ \vdots & \vdots & \vdots & \vdots & \vdots \\ U_{N-1,M-1} & U_{N,M-1} + U_{N-2,M-1} & U_{N-1,M} + U_{N-1,M-2} & U_{N,M} + U_{N-2,M-2} & U_{N,M-2} + U_{N-2,M} \end{pmatrix} \quad (5.42)$$

The matrix B_1 representing the norm of the 2D convolution sequence S as a function of the coefficients vector is then introduced:

$$B_1 = \begin{pmatrix} 1 & 0 & 0 & 0 & 0 \\ 0 & 2 & 0 & 0 & 0 \\ 0 & 0 & 2 & 0 & 0 \\ 0 & 0 & 0 & 2 & 0 \\ 0 & 0 & 0 & 0 & 2 \end{pmatrix} \quad (5.43)$$

Finally, the vector of convolution coefficients $[a, b, c, d, e]^T$ can be obtained by solving the Hermitian eigenvalue problem:

$$(J_1^*(U)J_1(U))x = \rho B_1 x \quad (5.44)$$

The coefficients' vector is the eigenvector for the smallest eigenvalue ρ of equation (5.44). This process can easily be generalized to the 2 waves convolution kernel.

5.2.2 Extracting wavenumbers and k-space

This subsection describes how wavenumbers and k-space can be extracted from the knowledge of the convolution kernel of the sequence. The process can be compared to wavenumbers computations in the 2D WFEM framework. Let L_x and L_y be the step size between measurements in the x and y direction on the grid and S the convolution kernel determined in the previous part. A pair of

wavenumbers (k_x, k_y) and its associated pair of propagation constants (λ_x, λ_y) are introduced. They are linked by the relation:

$$\begin{cases} \lambda_x = e^{-ik_x L_x} \\ \lambda_y = e^{-ik_y L_y} \end{cases} \quad (5.45)$$

We introduce the infinite 2D sequence $V(k_x, k_y)$ corresponding to the sampling of the displacement field of a plane wave with wavenumbers (k_x, k_y) on the regular grid.

$$\forall(n, m) \in \mathbb{Z}^2, \quad V_{n,m} = \lambda_x^n \lambda_y^m \quad (5.46)$$

The pair of wavenumbers (k_x, k_y) is said to be part of the extended K-Space K^e if and only if $V(k_x, k_y) * S = 0$. In case S is the generic one wave kernel of equation (5.37), this condition is explicitly developed:

$$a + b \left(\lambda_x + \frac{1}{\lambda_x} \right) + c \left(\lambda_y + \frac{1}{\lambda_y} \right) + d \left(\frac{\lambda_x}{\lambda_y} + \frac{\lambda_y}{\lambda_x} \right) + e \left(\lambda_x \lambda_y + \frac{1}{\lambda_x \lambda_y} \right) = 0 \quad (5.47)$$

Equation (5.47) can be understood as scalar form of the direct 2D WFEM. As such, it shares the same features. Namely, it can be reduced to a polynomial if either λ_x or λ_y (resp. k_x or k_y) is fixed. Solution for the other variable will be found and the pairs will belong to the extended K-space K^e . However these solutions do not have much meaning as it is likely their directions of propagation and directions of decay do not coincide. Forcing this to happen leads to the definition of the proper K-Space K^p . A pair of wavenumbers (k_x, k_y) belongs to K^p if and only if:

$$\exists k \in \mathbb{C}, \exists \theta \in \mathbb{R}, k_x = k \cos(\theta), k_y = k \sin(\theta), V(k_x, k_y) * S = 0 \quad (5.48)$$

With that supplementary constraint the direction of propagation and decay are forced to coincide with each other and are given by the angle θ . In case $\theta = 0 \bmod \frac{\pi}{2}$, solving equation (5.47) reduces to finding the roots of a palindromic polynomial as in the 1D case. To solve for other angles a continuation method is used whereby the angle θ is the parameter. The proper K-Space K^p can then be retrieved.

5.3 Experimental considerations

This section details some considerations related to the use of INCOME within an experimental (noisy) context. In subsection 5.3.1 a modification is brought to the formulation that enables to weigh the convolution residuals. Formulas based on coherence data are proposed for the weights and a two step estimation that

discards the worst data is proposed. The proposed enhancements help improve the accuracy of INCOME when measurements are noisy, the measurement grid is distorted or when there are sources in the measurement area. In subsection 5.3.2 several alternative forms of 2D convolution kernels are proposed. These forms enable a reduction of the number of parameters to estimate by accounting for additional wave propagation symmetries and by drawing analogies with Finite-Difference modeling. When appropriately used, these should also help improve the accuracy of INCOME.

5.3.1 Weighted residuals and two step estimates

In section we assume that periodic sampling of a wave field has been achieved using e.g. a laser vibrometer. In that case, not only the displacement U but also the coherence C should be available. We start by considering a 1D case with only one wave and its reflection. The sequence of measurements is thus $(U_n)_{n \in \llbracket 1, N \rrbracket}$ and the corresponding coherence data is similarly referred to as $(C_n)_{n \in \llbracket 1, N \rrbracket}$. The original formulation of INCOME works by minimizing the coefficients $(a, b) \in \mathbb{C}^2$ that minimize the norm of the residual sequence R defined as the convolution product between U and (a, b, a) :

$$\begin{cases} R = U * (a, b, a) \\ \forall i \in \llbracket 1, N - 2 \rrbracket, R_i = a(U_{i+2} + U_i) + bU_{i+1} \end{cases} \quad (5.49)$$

The norm of the sequence R being defined as:

$$\| R \|_2^2 = \sum |R_i|^2 \quad (5.50)$$

While this works well in ideal cases with little noise present and no source in the measurement area, this behaviour could be problematic when these conditions are not met. Firstly, $|R_i|$, scales with the norm of the displacements U_i, U_{i+1}, U_{i+2} which means that at equal relative error points with higher displacement amplitude have a higher influence on the obtained convolution kernel. In case the excitation source is present on the measurement area, this would results in the points having the most influence being ones that violate the free-wave assumption embedded inside INCOME. A second problem with equation (5.50) is that it does not exploit the presence of the coherence data and treats all measurements as if they are equally accurate. Both problems can be dealt with by introducing weights w_i for the residual creating a new sequence S such that:

$$\forall i \in \llbracket 1, N - 2 \rrbracket, S_i = w_i R_i \quad (5.51)$$

In matrix form this can be recast as $S = WR$ with W a diagonal matrix containing the weights as diagonal elements:

$$\begin{bmatrix} S_1 \\ S_2 \\ \vdots \\ S_{N-2} \end{bmatrix} = \begin{pmatrix} w_1 & 0 & \dots & 0 \\ 0 & w_2 & \dots & 0 \\ \vdots & \dots & \ddots & \vdots \\ 0 & \dots & \dots & w_{N-2} \end{pmatrix} \begin{bmatrix} R_1 \\ R_2 \\ \vdots \\ R_{N-2} \end{bmatrix} \quad (5.52)$$

The optimization problem should then be changed to minimizing the norm of S instead of that of R which practically is done by working $H_1^w(U) = WH_1(U)$ instead of $H_1(U)$ in equation (5.24).

We now propose a first family of weights, $(w_n^e)_{n \in \llbracket 1, N-2 \rrbracket}$, that ensures that residuals no longer scale with the magnitude of the local displacements:

$$w_i^e = \frac{1}{\sqrt{|U_i|^2 + |U_{i+1}|^2 + |U_{i+2}|^2}} \quad (5.53)$$

It should be used when the excitation source (e.g. a shaker) is inside the measurement field. A second family of weights, $(w_n^c)_{n \in \llbracket 1, N-2 \rrbracket}$, that exploits the coherence data is also proposed:

$$w_i^c = \sqrt{C_{i+1} \frac{C_i |U_i| + C_{i+2} |U_{i+2}|}{|U_i| + |U_{i+2}|}} \quad (5.54)$$

The formula of equation (5.54) is derived by taking the geometric mean of a confidence indicator created for each term of the matrix $H_1(U)$. Indeed the residual R_i is defined as:

$$\forall i \in \llbracket 1, N-2 \rrbracket, R_i = a(U_{i+2} + U_i) + bU_{i+1} \quad (5.55)$$

Since a multiplies $(U_{i+2} + U_i)$ and b U_{i+1} . It is necessary to assess how much certainty we have about both terms. For the term U_{i+1} , its coherence C_{i+1} is directly used as a proxy for that level of certainty (with 1 meaning absolute certainty and 0 complete uncertainty). For the other term $(U_{i+2} + U_i)$ and b U_{i+1} things are not as straightforward as it is obtained as a sum. We therefore chose a weighted average between the coherences of its two terms. The weights of this average are chosen as the respective amplitudes of each term ($|U_i|$ and $|U_{i+2}|$). This choice reflects the fact that if $U_{i+2} \ll U_i$, the accuracy of $U_{i+2} + U_i$ would only depend solely on the accuracy of U_i (and conversely if the situation were to be reversed). This explains the appearance of the term $\frac{C_i |U_i| + C_{i+2} |U_{i+2}|}{|U_i| + |U_{i+2}|}$ in equation (5.54). The square root comes from taking the geometric average of both the confidence indicators used for both U_{i+1} and $(U_{i+2} + U_i)$.

In order to take advantage of both categories of weights, w^e and w^c , a two step estimation process for the optimal coefficients (a, b) is proposed. A first pair of coefficients (a_1, b_1) is determined by using INCOME with the w^e weights. The corresponding weighted residual sequence $S = W^e(U * (a_1, b_1, a_1))$ is then computed. The worst ten percent of the data is then filtered out when determining the second estimates. This is done by introducing a new sequence $(\delta_n)_{n \in \llbracket 1, N-2 \rrbracket}$ such that:

$$\begin{cases} \delta_i = 1 \text{ if } |S_i| \leq S_{max} \\ \delta_i = 0 \text{ if } |S_i| > S_{max} \end{cases} \quad (5.56)$$

With S_{max} the 90th percentile of the absolute values of S . The second estimate is then formed by using INCOME with the weights $(w_i^e \delta_i)_{i \in \llbracket 1, N-2 \rrbracket}$. Though the proposed weighing and two step estimation strategies were discussed for the simplest formulation of INCOME, they can be easily extended to the general 1D case and to the various 2D scenarios.

5.3.2 Alternative shapes for 2D convolution kernels

In this subsection, the use of alternative convolution kernels is discussed. The aim here is to make the 2D version of INCOME more robust by limiting the number of parameters to be estimated. This can be done in tow ways. Firstly, by accounting for 2D wave propagation symmetries in the formulation. Secondly by drawing analogy with finite difference stencils (see [109]) and INCOME convolution kernels, new convolution kernels can be proposed for specific type of structures.

General 2D convolution kernels derived for different symmetries

In this section we propose 2D convolution kernels that go beyond equations (5.37) and (5.41) that only account for the most general central symmetry of the K-Space. We start with different convolution kernels accounting for one wave type. For "orthotropic" wave propagation, e.g. corresponding to elliptic differential equations, equation (5.57) is proposed:

$$\begin{array}{|c|c|c|} \hline S_{1,3} & S_{2,3} & S_{3,3} \\ \hline S_{1,2} & S_{2,2} & S_{3,2} \\ \hline S_{1,1} & S_{2,1} & S_{3,1} \\ \hline \end{array} = \begin{array}{|c|c|c|} \hline d & c & d \\ \hline b & a & b \\ \hline d & c & d \\ \hline \end{array} \quad (5.57)$$

While the for isotropic wave propagation cases such as the Helmholtz equation (5.58) is appropriate:

$$\begin{array}{|c|c|c|} \hline S_{1,3} & S_{2,3} & S_{3,3} \\ \hline S_{1,2} & S_{2,2} & S_{3,2} \\ \hline S_{1,1} & S_{2,1} & S_{3,1} \\ \hline \end{array} = \begin{array}{|c|c|c|} \hline c & b & c \\ \hline b & a & b \\ \hline c & b & c \\ \hline \end{array} \quad (5.58)$$

In both equations (5.57) and (5.58) symmetries mirroring those of the k-space are introduced in the convolution kernel in order to reduce the number of independent coefficients to be estimated. This strategy can be extended for the case of multiple waves by taking the product of several one-wave convolution kernels. In the case of 2-waves convolution kernels the following form is proposed for "orthotropic" wave propagation:

$$\begin{array}{|c|c|c|c|c|} \hline R_{1,5} & R_{2,5} & R_{3,5} & R_{4,5} & R_{5,5} \\ \hline R_{1,4} & R_{2,4} & R_{3,4} & R_{4,4} & R_{5,4} \\ \hline R_{1,3} & R_{2,3} & R_{3,3} & R_{4,3} & R_{5,3} \\ \hline R_{1,2} & R_{2,2} & R_{3,2} & R_{4,2} & R_{5,2} \\ \hline R_{1,1} & R_{2,1} & R_{3,1} & R_{4,1} & R_{5,1} \\ \hline \end{array} = \begin{array}{|c|c|c|c|c|} \hline i & g & f & g & i \\ \hline h & d & c & d & h \\ \hline e & b & a & b & e \\ \hline h & d & c & d & h \\ \hline i & g & f & g & i \\ \hline \end{array} \quad (5.59)$$

While wave propagation in highly symmetric media (not necessarily isotopic) can be captured by the kernel of equation (5.60)

$$\begin{array}{|c|c|c|c|c|} \hline R_{1,5} & R_{2,5} & R_{3,5} & R_{4,5} & R_{5,5} \\ \hline R_{1,4} & R_{2,4} & R_{3,4} & R_{4,4} & R_{5,4} \\ \hline R_{1,3} & R_{2,3} & R_{3,3} & R_{4,3} & R_{5,3} \\ \hline R_{1,2} & R_{2,2} & R_{3,2} & R_{4,2} & R_{5,2} \\ \hline R_{1,1} & R_{2,1} & R_{3,1} & R_{4,1} & R_{5,1} \\ \hline \end{array} = \begin{array}{|c|c|c|c|c|} \hline f & e & d & e & f \\ \hline e & c & b & c & e \\ \hline d & b & a & b & d \\ \hline e & c & b & c & e \\ \hline f & e & d & e & f \\ \hline \end{array} \quad (5.60)$$

Convolution kernels derived by analogy with finite difference methods

In this paragraph, simplified convolution kernels for 2D wave propagation are proposed. These kernels are derived by taking inspiration from finite difference schemes [109] on regular grids that have been successfully used to model acoustic waves and the vibration of plates [72, 100, 148, 209, 52]. By using second order accurate central differences, the following convolution kernel is obtained for the Helmholtz equation:

$$\begin{array}{|c|c|c|} \hline S_{1,3} & S_{2,3} & S_{3,3} \\ \hline S_{1,2} & S_{2,2} & S_{3,2} \\ \hline S_{1,1} & S_{2,1} & S_{3,1} \\ \hline \end{array} = \begin{array}{|c|c|c|} \hline 0 & b & 0 \\ \hline b & a & b \\ \hline 0 & b & 0 \\ \hline \end{array} \quad (5.61)$$

For wave propagation in thin isotropic thin plates satisfying Kirchhoff–Love plate theory assumptions (5.62) can be used:

$$\begin{array}{ccccc} R_{1,5} & R_{2,5} & R_{3,5} & R_{4,5} & R_{5,5} \\ R_{1,4} & R_{2,4} & R_{3,4} & R_{4,4} & R_{5,4} \\ R_{1,3} & R_{2,3} & R_{3,3} & R_{4,3} & R_{5,3} \\ R_{1,2} & R_{2,2} & R_{3,2} & R_{4,2} & R_{5,2} \\ R_{1,1} & R_{2,1} & R_{3,1} & R_{4,1} & R_{5,1} \end{array} = \begin{array}{ccccc} 0 & 0 & b & 0 & 0 \\ 0 & 2b & -8b & 2b & 0 \\ b & -8b & a & -8b & b \\ 0 & 2b & -8b & 2b & 0 \\ 0 & 0 & b & 0 & 0 \end{array} \quad (5.62)$$

While wave propagation in highly symmetric plate type structures (e.g. sandwich structures with regular hexagonal cores) can be dealt with using the kernel of equation (5.63):

$$\begin{array}{ccccc} R_{1,5} & R_{2,5} & R_{3,5} & R_{4,5} & R_{5,5} \\ R_{1,4} & R_{2,4} & R_{3,4} & R_{4,4} & R_{5,4} \\ R_{1,3} & R_{2,3} & R_{3,3} & R_{4,3} & R_{5,3} \\ R_{1,2} & R_{2,2} & R_{3,2} & R_{4,2} & R_{5,2} \\ R_{1,1} & R_{2,1} & R_{3,1} & R_{4,1} & R_{5,1} \end{array} = \begin{array}{ccccc} 0 & 0 & d & 0 & 0 \\ 0 & c & b & c & 0 \\ d & b & a & b & d \\ 0 & c & b & c & 0 \\ 0 & 0 & d & 0 & 0 \end{array} \quad (5.63)$$

Finally, for orthotropic plate type structure (e.g. some composite plates and sandwich structures) this stencil is recommended:

$$\begin{array}{ccccc} R_{1,5} & R_{2,5} & R_{3,5} & R_{4,5} & R_{5,5} \\ R_{1,4} & R_{2,4} & R_{3,4} & R_{4,4} & R_{5,4} \\ R_{1,3} & R_{2,3} & R_{3,3} & R_{4,3} & R_{5,3} \\ R_{1,2} & R_{2,2} & R_{3,2} & R_{4,2} & R_{5,2} \\ R_{1,1} & R_{2,1} & R_{3,1} & R_{4,1} & R_{5,1} \end{array} = \begin{array}{ccccc} 0 & 0 & f & 0 & 0 \\ 0 & d & c & d & 0 \\ e & b & a & b & e \\ 0 & d & c & d & 0 \\ 0 & 0 & f & 0 & 0 \end{array} \quad (5.64)$$

Naturally, it would be possible to produce more complex stencils/convolution kernels using higher order accuracy schemes but the proposed stencils should be sufficient for most NVH-related applications.

5.3.3 Using data from different origins

This subsection describes how to increase the accuracy of INCOME based wavenumber extraction by using data from different sources. This is based on the fact that joint estimations can be obtained by concatenation of the modified Hankel matrix that is characteristic of INCOME (see equations (5.20), (5.32) and (5.42)). This matrix will be noted as $H(U)$ irrespective of the number waves of that one try to estimate or whether one is dealing with a 1D or 2D problem.

In case one were to perform several measurements on the same structure or a different structure leading to, e.g., three sequences of measurements U , V and

One can perform a joint wavenumber extraction using all the data available by concatenating all three matrices:

$$H = \begin{pmatrix} H(U) \\ H(V) \\ H(W) \end{pmatrix} \tag{5.65}$$

This leads to the matrix H of equation (5.65) which can then be used as any of its three constituents in order to determine the coefficients of a palindromic polynomial.

Another more subtle possibility for data augmentation concerns the case where measurements are carried out on a given frequency band. In that case the measurement sequence U is a smooth function of the circular frequency ω and we note it $U(\omega)$. For a frequency ω_0 we have:

$$U(\omega_0 + \delta_\omega) = U(\omega_0) + \delta_\omega \frac{dU}{d\omega}(\omega_0) + o(\delta_\omega) \tag{5.66}$$

That is as long as δ_ω is small, $U(\omega_0)$ and $U(\omega_0 + \delta_\omega)$ should be almost identical thus one should be able to use them in order to improve the quality of the estimates of the wavenumbers/K-Space at the frequency ω_0 as outlined in equation (5.65). It should also be noted that the first order effects related to the term $\delta_\omega \frac{dU}{d\omega}(\omega_0)$ will not introduce bias in the final results as long as one samples symmetrically around ω_0 , e.g. $(U(\omega_0 - \delta_\omega), U(\omega_0), U(\omega_0 + \delta_\omega))$. Thus, bias should only appear due to second (and higher even orders) effects. By ensuring δ_ω is small enough one can safely augment their data set and the accuracy of the final wavenumber estimates.

5.4 Numerical validation and benchmarks

In this section we benchmark INCOME, the ESPRIT algorithm and the IWC on a 1D case. Next the performance of INCOME and the IWC are compared on two 2D cases. All the cases treated are numerical and noiseless, hence, this is mostly a test of the ability of these methods to retrieve exact or quasi-exact wavenumber estimates under perfect conditions. Experimental validations are carried out in section 5.5.

5.4.1 Analytical Euler-Bernoulli Beam

In this subsection, INCOME, the ESPRIT algorithm and the IWC are used in order to retrieve the dispersion curves of a cantilever Euler-Bernoulli beam of

length L loaded at its end. The system of equations verified by the deflection of the beam $f(\omega, x)$ is given in equation (5.67):

$$\begin{cases} EI \frac{\partial^4 f}{\partial x^4} - \omega^2 \mu f = 0 \\ f(\omega, 0) = 0, \quad \frac{\partial f}{\partial x}(\omega, 0) = 0 \\ \frac{\partial^2 f}{\partial x^2}(\omega, L) = 0, \quad -EI \frac{\partial^3 f}{\partial x^3}(\omega, L) = F \end{cases} \quad (5.67)$$

This enables analytical computation of the forced response and the dispersion relationship:

$$k^4 = \frac{\mu}{EI} \omega^2 \quad (5.68)$$

The dispersion relation of equation (5.68) describes two pairs of waves. For each pair one wave propagates in the positive direction while the other propagates in the opposite direction. Additionally, one of these pairs corresponds to strongly evanescent waves which are barely observable. For this application, the values of F , μ and L are set to 1 while the product EI is set to $1 + 0.08i$. Additionally, the signal sampling period dl is chosen equal to $\frac{L}{100} = 0.01$, hence, there are 101 samples. The three aforementioned wavenumber extraction methods are applied to the displacement fields of equation (5.67) and the obtained wavenumbers are compared to the analytical solutions of equation (5.68) in Figure 5.2. To get a better view of the error introduced by each of the methods compared to the analytical solution the relative error is presented for both propagating and evanescent waves in the case of INCOME and of the ESPRIT algorithm while only the error for the propagative wave is displayed in the case of the IWC as it only returns one wavenumber. As expected, both INCOME and the ESPRIT algorithm achieve close to numerical precision accuracy while the IWC do not get below 10% relative error in the proposed frequency range. This is because both INCOME and the ESPRIT algorithm are exact methods for the 1D case while the IWC is an approximation and only works well at higher frequencies where the number of wavelengths present in the displacement field is high and that it is almost monochromatic.

5.4.2 Helmholtz Equation

In this subsection, the 2D INCOME, the IWD and the IWC are applied to a solution of the 2D Helmholtz equation with the aim of retrieving its parameter k . The equation and its parameter are defined in equation (5.69):

$$\nabla^2 f + k^2 f = 0 \quad (5.69)$$

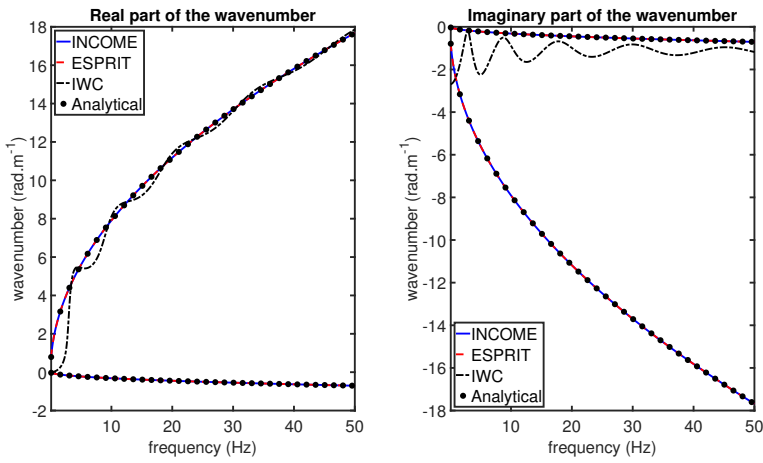


Figure 5.2: Comparison of the wavenumbers obtained with INCOME, the ESPRIT algorithm and the IWC for an Euler-Bernoulli beam

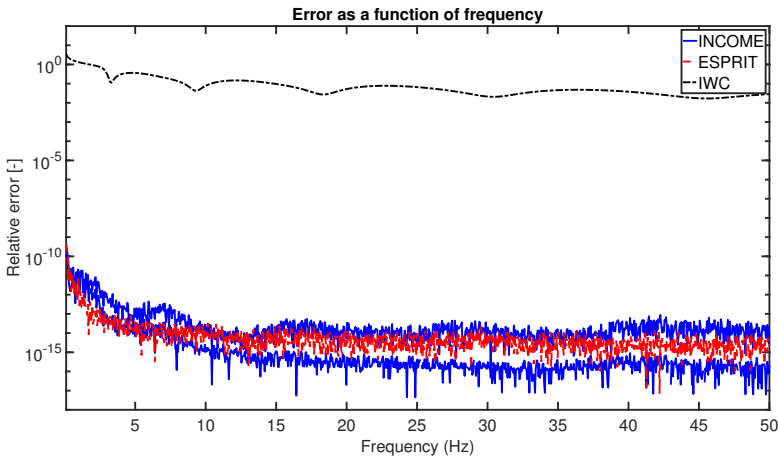


Figure 5.3: Comparison of the accuracy of wavenumbers retrieved with INCOME, the ESPRIT algorithm and the IWC for an Euler-Bernoulli beam

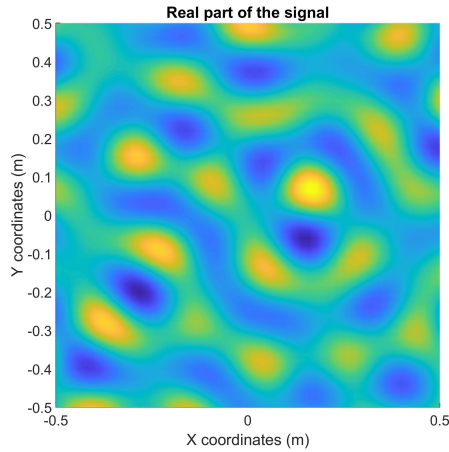


Figure 5.4: Randomly generated solution of the Helmholtz equation

To generate a valid random solution of equation (5.69) punctual sources of random amplitudes, phases and positions are generated outside of the domain of interest. The solution within the domain is then computed analytically since the Green's function of the equation is known and given in equation (5.70):

$$G(x, y) = \frac{i}{4} H_0^{(1)} \left(k \sqrt{x^2 + y^2} \right) \quad (5.70)$$

Where $H_0^{(1)}$ is a Hankel function of the first kind. In view of applying INCOME, the value of k is chosen equal to 30. The sampling domain is a 1 by 1 square centered around the origin and the sampling period dl is chosen equal to 0.02 in both directions hence the sampling grid is 51 by 51 square grid. A realization of this process is presented in Figure 5.4. Given the additional symmetries of the Helmholtz equation, the INCOME is used with a convolution kernel S of the form of equation (5.71).

$$\begin{bmatrix} S_{1,3} & S_{2,3} & S_{3,3} \\ S_{1,2} & S_{2,2} & S_{3,2} \\ S_{1,1} & S_{2,1} & S_{3,1} \end{bmatrix} = \begin{bmatrix} c & b & c \\ b & a & b \\ c & b & c \end{bmatrix} \quad (5.71)$$

The general accuracy and computation time for INCOME, IWC (in the x direction) and the IWD with 15 wave propagation directions are compared in Table 5.1. It can be seen that INCOME is both the fastest and the most accurate method for this case. The IWC also performs pretty well and generally achieves accuracy comparable to that of the IWD while only requiring a fraction

| Method | INCOME | IWD | IWC |
|----------------------|-----------------------|-----------------------|-----------------------|
| Relative error [-] | $5,63 \times 10^{-8}$ | $1,25 \times 10^{-3}$ | 2.34×10^{-3} |
| Computation time (s) | $1,48 \times 10^{-3}$ | 18.1 | 9.51×10^{-2} |

Table 5.1: Accuracy and CPU of wavenumber retrieval for INCOME, the IWD and the IWC

of its CPU time. Noteworthy, convergence is not guaranteed for either the IWC and IWD as they rely on nonlinear optimization. In particular, for the IWC, accuracy may drop significantly for some of the wavefields generated if the random wave front are mostly parallel to the x axis while the IWD is more consistent in the final error obtained. On the other, for the IWD, it is not guaranteed that increasing the number of plane waves in the field decomposition will result in higher accuracy estimates while it certainly will increase the CPU time. This issue exemplify why the IWC has been more popular than the IWD despite the latter being generally more robust and accurate. The codes and functions used to perform these comparison are available in Appendix C.

5.4.3 Orthotropic Plate

In this subsection, the 2D INCOME, and the IWC are applied to the displacement field of a strongly orthotropic thin plate whose material properties correspond to a laminate studied in [211]. The reason why the IWD is not compared is because it does not seem to converge in a reasonable CPU time which is likely due to its high number of parameters and the fact that they have different *dimensions*. The considered plate has length of $0.5m$ a width of $0.5m$ and a thickness of $5mm$. Its material properties are given in Tables 5.2, 5.3 and 5.4. In order to obtain the (frequency dependent) displacement field on which INCOME and the IWC are used, the plate is modeled in ANSYS APDL 17.0 using SHELL181 elements which are based on Mindlin-Reissner plate theory. The mesh is chosen to be a regular 101 by 101 grid. Once the mass and stiffness matrices are extracted, an hysteretic damping η of 5% is added to the model.

| Property | Density | E_x | E_y | E_z |
|----------|--------------------------|---------|--------|---------|
| Value | 7850 kg.m^{-3} | 2.1 GPa | 21 GPa | 210 GPa |

Table 5.2: Density and Young Moduli of the studied plate

First the frequency forced response of the plate with free boundary conditions for a point force excitation at the top right corner is computed on the $[0, 600]$ Hz frequency range. The dispersion curves in the main sampling directions

| Property | G_{xy} | G_{yz} | G_{xz} | η |
|----------|-----------|-----------|-----------|--------|
| Value | 3.033 Gpa | 30.33 Gpa | 2.625 GPa | 0.05 |

Table 5.3: Shear Moduli of the studied plate

| Property | ν_{xy} | ν_{yz} | ν_{xz} |
|----------|------------|------------|------------|
| Value | 0.095 | 0.095 | 0.03 |

Table 5.4: Poisson's ratios of the plate material

are extracted using both the 2D INCOME and the IWC. Additionally, the corresponding curves are computed using the Shift-Cell Operator Method [47] with 5 Lagrange \mathcal{Q}_1 elements in the thickness of the plate. The results from all three methods are compared in Figure 5.5. As can be seen, there is excellent agreement between INCOME and the Shift-Cell Operator method for both the real and imaginary parts of the wavenumber, while the IWC only provides a qualitative approximation of the wavenumber's real part. As a second step, the k-space at 600 Hz is computed with all three methods for the propagating waves. The k-spaces obtained with INCOME and the Shift-Cell Operator method are compared in Figure 5.6. As can be seen in Figure 5.6, the K-Spaces obtained via the Shift-Cell Operator method and INCOME are indistinguishable. The IWC on the other hand, fails to produce a coherent K-space as shown in Figure 5.7. The failure of both IWC and the IWD to provide accurate wavenumber

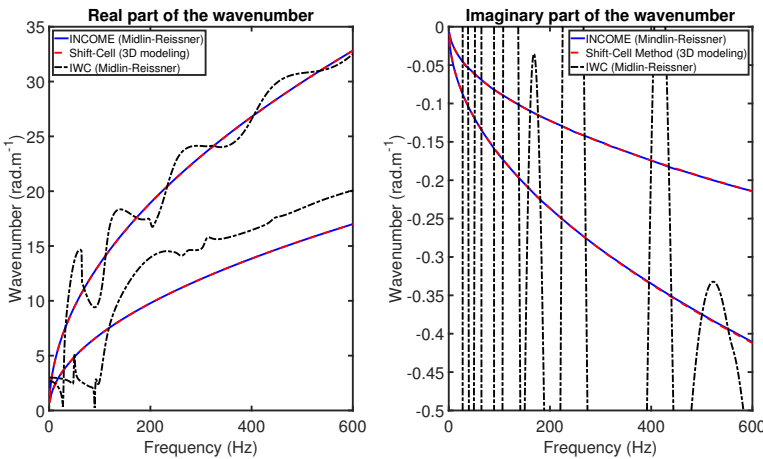


Figure 5.5: Comparison of dispersion curves obtained via INCOME, the Shift Cell Operator method and the IWC

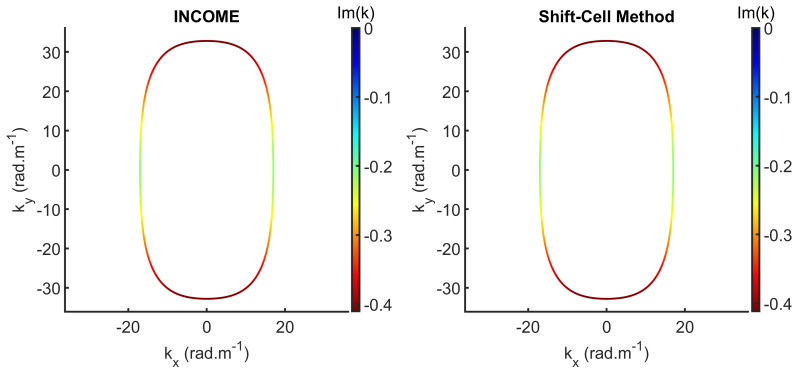


Figure 5.6: Comparison of the K-Spaces at 600 Hz obtained via INCOME and the Shift Cell Operator method

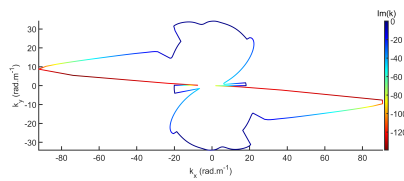


Figure 5.7: K-Space at 600 Hz computed with the IWC

and k-space estimates demonstrates the potential of the proposed method.

5.5 Experimental applications

In Section 5.4, INCOME was benchmarked against the IWC and the IWD in noiseless, numerical cases. In all three proposed examples, INCOME outperformed the other two methods. Nonetheless, the introduction of experimental issues such as, an imperfectly periodic sampling grid, measurement noise and the presence of sources within the sampled displacement field. These doubts are put to rest in this section which is organized as follows. In Subsection 5.5.1 INCOME is applied to a 1D aluminum beam with constrained viscoelastic



Figure 5.8: Experimental setup for the aluminum beam with a constrained viscoelastic layer

layer. It is subsequently applied to a locally resonant metamaterial that was previously studied in [187] in subsection 5.5.2 and to a rubber panel in Subsection 5.5.3.

5.5.1 Beam with constrained viscoelastic layer

Herein we consider an aluminum beam with an uncharacterized viscoelastic layer. Clamped-Free boundary conditions are applied to the beam. It is excited with a shaker and the displacement field in the 0-5kHz regions is measured with a laser Doppler vibrometer. The beam is 11 cm long and 89 equally spaced measurement points are used. The experimental setup is shown in Figure 5.8. Since there is no reference, 4 methods are used in order to extract the dispersion curves. Mc Daniel's method with the Euler-Bernoulli hypothesis, INCOME, the IWC and the ESPRIT algorithm. The retrieved dispersion curves are shown in Figure 5.9. As expected, good agreement for both the real and imaginary parts of the wavenumber is obtained between INCOME, the ESPRIT algorithm and Mc Daniel methods while the IWC only manages to roughly approximate the real part of the wavenumber. In terms of robustness, the IWC performs the best

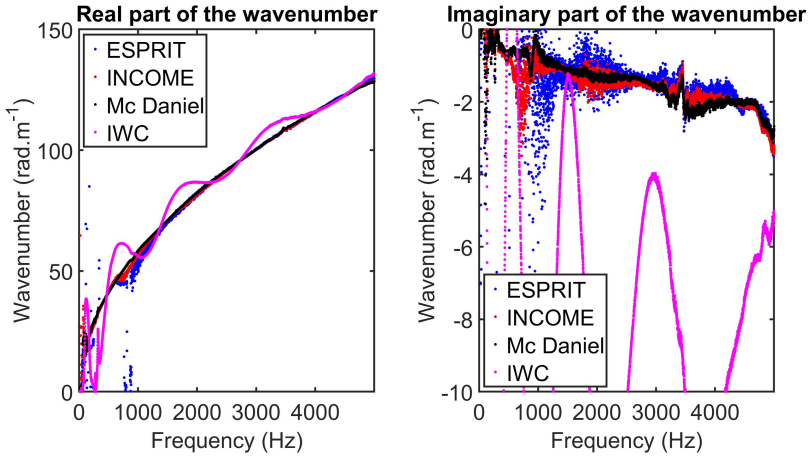


Figure 5.9: Experimental dispersion curves of the aluminum beam retrieved with the ESPRIT algorithm (blue) INCOME (red), the Mc Daniel method (black) and the IWC (magenta).

as it has low point to point variance. It is followed by the IWC, INCOME and finally, the ESPRIT algorithm which is only slightly edged out by INCOME. For practical purpose however, the robustness of the IWC is irrelevant in the present case as it does not provide accurate results.

While there are no references, it would stand to reason that the Mc Daniel's method is the most accurate (here) as it relies on an exact expression of an ideal displacement field that is fitted on to the experimental data. Convergence is ensured using analytically derived gradients and Hessian matrix as well as the proposed optimization algorithm of Chapter 4 with a continuation method between frequencies. Taking Mc Daniel's method as the reference, INCOME and the ESPRIT algorithm achieve similar levels of accuracy though INCOME is slightly more accurate. Lastly the IWC performs last in this department. In terms of required computation time INCOME, the ESPRIT algorithm and the IWC manage to complete the wave number extraction of the full 6375 considered frequencies in a matter of seconds, while a few minutes are required for Mc Daniel's method.

The present results demonstrate that INCOME can be used in a 1D wavenumber extraction context even though other methods perform equally well or better depending on the evaluation criteria used. The advantages of both INCOME and the ESPRIT algorithm in such a context is that unlike methods based on nonlinear optimization, they do not require a 'well chosen' starting point in order to ensure convergence/the accuracy of the final results. They are

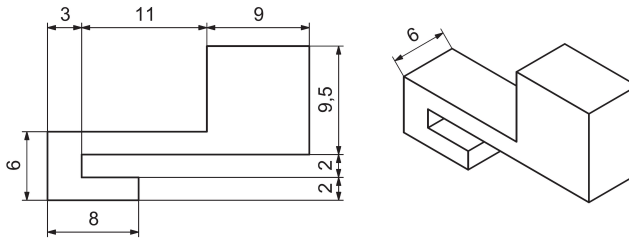


Figure 5.10: Geometry of the locally resonant add-ons. Dimensions in mm

also considerably faster. In practice, they can also be used to provide a sensible starting point for nonlinear methods when a single displacement field is considered.

5.5.2 2D Locally resonant metamaterial

In this subsection INCOME is employed in order to retrieve the dispersion curves of a locally resonant metamaterial comprised of a 1mm thick host aluminum plate with locally resonant PMMA add-on. The add-ons are placed on a square grid. The resulting periodic pattern is such that an irreducible unit cell is of dimensions 3 cm by 3 cm. The Young's moduli, Poisson's ratios, density and hysteretic damping of both aluminum and PMMA are given in Table 5.5. Additionally, the dimensions of the locally resonant add-ons are

| Material | Young's modulus | Poisson's ratio | Density | Damping |
|----------|-----------------|-----------------|--------------------------|----------------------|
| Aluminum | 69 GPa | 0.33 | 2697 kg.m^{-3} | 2.8×10^{-3} |
| PMMA | 4.85 GPa | 0.31 | 1188 kg.m^{-3} | 5×10^{-2} |

Table 5.5: Material parameters for the host structure (aluminum) and the resonant add-ons (PMMA)

given in Figure 5.10 taken from the original paper [187]. In order to measure the dispersion curves, A 60 cm by 60 cm panel comprised of 20 by 20 UCs is excited with a shaker. 'Free-Free' boundary conditions are approximated by suspending the panel as shown in Figure 5.11. The resulting displacement field is measured using a laser Doppler vibrometer on a regular 41 by 41 grid. The measurement spacing is 1.5 cm in both directions and is equal to half the length/width of UC. As can be seen, the shaker is exciting the panel in the middle of the measurement field thus the underlying assumption of INCOME and the IWD are violated. In order to compensate for this, INCOME is

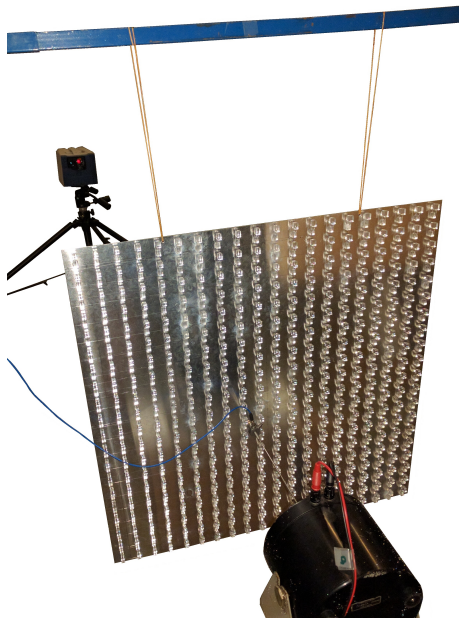


Figure 5.11: Experimental setup for the locally resonant metamaterial

used with most of the enhancements presented in section 5.3. Specifically, the two step estimation strategy with coherence based residual weighting is used. Additionally, the simplified convolution kernel of equation (5.64) is used as the considered metamaterial is a plate-type structure. Finally, the cross-frequency data enrichment described in Subsection 5.3.3 is performed with a centered 3 Hz window. The retrieved dispersion curves and k-spaces are compared to those obtained numerically using the Shift-Cell Operator method with the nominal material property values.

As can be observed in Figure 5.12, there is good agreement between the retrieved and theoretical dispersion curves. Nonetheless, a few differences are present. Firstly, the extrema of the real and imaginary parts are shifted in frequency which suggests that the resonance frequency of the add-ons may have been underestimated. This could be due to deviation in terms of material properties or related to the manufacturing process (e.g. geometric tolerances). The second noticeable difference is that peak spatial attenuation is consistently higher in the numerical dispersion curves which could be explained by an underestimation of the damping or by variability effects (all physical resonant add-ons are slightly different).

Lastly the k-space at 1150 Hz where flexural waves can propagate in the x

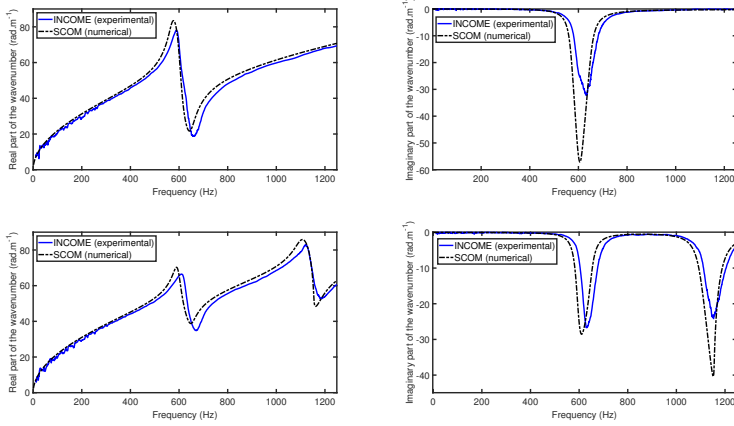


Figure 5.12: Comparison of the experimental and theoretical dispersion curves in the x (top) and y (bottom) directions.

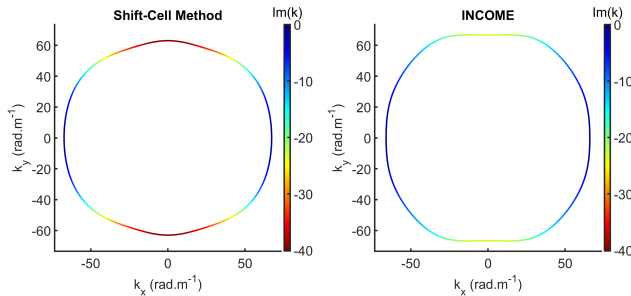


Figure 5.13: Comparison of the k-spaces at 1150 Hz obtained using INCOME on experimental data and the shift-cell operator method

direction but not in the 'y' direction (partial band gap) is obtained using both INCOME and the shift cell operator method. Logically, the differences observed in the dispersion curves persist as there is less attenuation in the experimental k-space and that the wavenumber values are also different. Additionally, the experimental k-space appears to be less directive than the theoretical one.

5.5.3 Rubber Panel

In this subsection, INCOME is applied to a rubber panel of unknown material properties in order to identify its dispersion characteristics. The panel is 49.2 cm long by 49.2 cm wide and 6.5 mm thick. In order to measure its dispersion curves the panel is excited with a shaker and the displacement field is measured with a laser Doppler vibrometer on a regular 48 by 48 grid square grid with a 1cm spacing. 'Free-Free' boundary conditions are approximated by suspending the panel as shown in Figure 5.14.

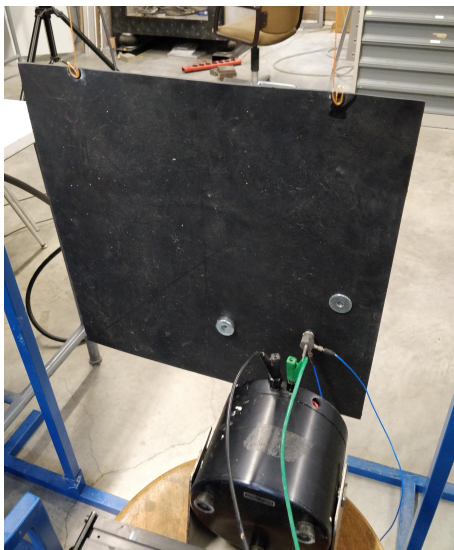


Figure 5.14: Experimental setup for the rubber panel

As can be seen in Figure 5.14, the shaker is exciting the panel in the middle of the measurement field thus the underlying assumption of INCOME and the IWD are violated. In order to compensate for this, INCOME is used with most of the enhancements presented in section 5.3. Specifically, the two step estimation strategy with coherence based residual weighting is used. Additionally, the simplified convolution kernel of equation (5.63) is used as the considered structure is an homogeneous plate. Finally, the cross-frequency data enrichment described in Subsection 5.3.3 is performed with a centered 2 Hz window. The retrieved dispersion curves are presented in Figure 5.15. They appear relatively smooth and will be used to estimates the frequency dependent

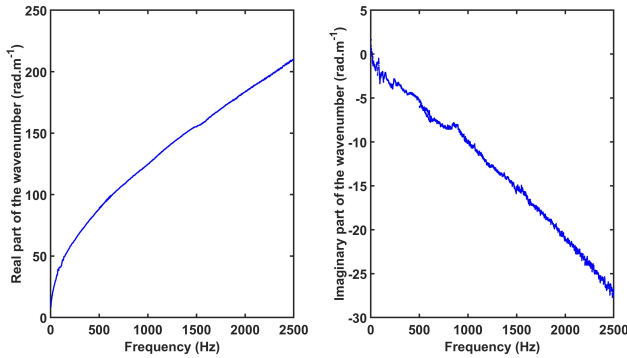


Figure 5.15: Dispersion curves of the rubber panel retrieved with INCOME

material properties of the rubber sample by combining Kirchhoff–Love plate theory with a parametric viscoelastic model in a curve fitting algorithm.

5.6 Conclusions and perspectives

In this chapter, a method for one-dimensional and two-dimensional wavenumber extraction is presented. Based on a convolution framework, the method requires periodic sampling of the signal of interest to produce a convolution kernel that describes its wavenumbers, or K-Space. The core of INCOME is very similar to the Prony series method but takes advantage of a convolution framework to encode wave propagation symmetries and reach the 2D case. The main conclusions and contributions of the chapter can be summarised as follows:

- The INCOME method relies on solving small linear problems and is exact in both 1D and 2D cases. The wording "exact" refers here to the propagation scheme adopted for the inverse algorithm. Precisely, a given propagation model is fitted to the input data with consistency. The INCOME method is also mathematically robust and its numerical implementation easy to handle.
- In the 2D case, all properties of the K-Space are retrieved together in a coherent manner and INCOME was shown to successfully identify the wave heading (directivity) and the spatial attenuation. This is the most advantageous property of INCOME and it is achieved by making periodic sampling of the input mandatory.

- The proposed method draws inspiration from the WFEM framework [125, 143, 82, 16, 67, 92], and can be considered an inverse WFEM approach. The periodicity requirement for INCOME and the use of recurrence relationships make the formulation comprehensive for WFEM practitioners. The literature belonging to the WFEM being rich, one could expect bridges to be created between the direct WFEM and the INCOME.

Finally, the accuracy of the proposed method was demonstrated in both 1D and 2D scenarios and it was shown to be sufficiently noise resistant to compete with the most robust methods of the literature when the structure studied allow for their use. Several perspectives are identified for the method:

- Damage detection and source detection. Specifically, the analogy developed in equation (5.36) suggest that the residual obtained by taking the convolution product of the identified kernel with the experimental displacement field should reveal the presence of singularities (damage, excitation source) in the measured displacement field. The relevance of this idea is further reinforced in section 5.3.2 where the use of convolution kernels based on finite difference approximation was suggested. This introduces parallels between INCOME and the Force Analysis Technique [113, 2, 65] (FAT). A technique that leverage finite difference models of structures with experimental data in order to detect input forces.
- The aforementioned similarities between INCOME and the FAT suggest that most data preprocessing techniques developed for the FAT can be carried over to INCOME and increase its robustness.
- K-spaces obtained via INCOME could also be used with plate and sandwich structures theories to predict the sound transmission loss of samples from purely structural measurements [208]. Finiteness effects could be accounted for via wavenumber windowing techniques [161, 192] or more accurately by SEA-like energy methods [212].
- Another interesting perspective would be to apply INCOME to the computations of "all complex dispersion curves" for which wavenumbers and frequencies can be simultaneously complex [79]. In order to estimates such dispersion characteristic with INCOME the classical processing of time domain data should be modified such that a discrete Laplace transform is used instead of a discrete Fourier transform. For the former transform to yield accurate results, special attention should be paid to the excitation method and properties (e.g. hammer, shaker, etc) which in turn would impact the way the displacement fields are measured (e.g. accelerometers, laser vibrometer, high-speed camera, etc...).

- Lastly, because INCOME can provide accurate wavenumber estimates at very low CPU time. The method could be used to speed up potentially more robust but computationally expensive methods based on non-linear fits of the displacement field. Developing an improved version of the IWD [40, 169] could make sense in such a context.

Chapter 6

A rational Krylov subspace method for sound transmissions loss computation with the Shift Cell Method

Part of this Chapter has been published as [30]: "R.F. Boukadia, E. Deckers, C. Claeys, M. Ichchou, W. Desmet. A rational Krylov subspace method for the unit cell modeling of 2D infinite periodic media. In: *Proceedings of ISMA 2020 - International Conference on Noise and Vibration Engineering and USD 2020 - International Conference on Uncertainty in Structural Dynamics*, pages 1915-1924 ,Leuven, Belgium, September 2020."

In this chapter a novel model order reduction technique for diffuse field sound transmission loss (STL) evaluation within the Shift-Cell Operator Method (SCOM) framework is presented. Firstly, a method for the computation of the STL in the SCOM framework is derived by adapting the Hybrid-WFEM method [203, 57] to the SCOM framework. This development is motivated by the fact that incident plane waves can be made to look like constant pressure fields in the SCOM framework which enables the use of a moment matching based model order reduction (MOR) scheme to reduce the structural part of the sound transmission problem. While both MOR schemes [102, 216, 62, 103]

and methods for STL computations [42, 155, 203, 57, 156] have been developed within the WFEM framework, the available MOR techniques were created for the computation of free-waves and rely on simple mode-based projection methods which generally are less accurate than their moment-matching based counterparts [119, 101, 22]. This difference in accuracy comes from the fact that moment-matching based reduction techniques include information about loads and coupling directly in their formulations while modal methods are more suited to obtain a general idea of the response for any load and will only represent the system accurately near its poles. Unfortunately, plane-wave with different wavenumbers/incidence angles do not look the same within the WFEM framework. Therefore, a moment matching based MOR scheme would not be efficient in that context which justifies the proposed modeling strategy. The rest of the chapter is organized as follows. In Section 6.1 a quick reminder of the SCOM's properties is given and the adaptation of the Hybrid-WFEM to the SCOM framework is also described. In Section 6.2 a multiparameter moment-matching process for computations in the SCOM framework is presented and a MOR scheme exploiting this technique is detailed. Numerical examples are presented in Section 6.3. The proposed modeling strategy is first validated on a simple homogeneous plate, its potential is subsequently illustrated on a complex locally resonant waveguide. Finally Section 6.4 summarizes the main conclusions.

6.1 Hybrid coupling with the shift cell operator method

In this section, the new method for STL computations in the SCOM framework is presented. First, a small reminder of the SCOM's basic properties is given in Subsection 6.1.1 which facilitates the introduction of the fluid-structure coupling described in Subsection 6.1.2.

6.1.1 Reminder: Basic properties of the shift-cell method

This subsection presents some of the basic properties of the shift-cell operator method, some of which were described in Section 2.4. In order to keep things simple, a 1D modeling scenario is presented though the reasoning easily extends to 2D and 3D cases.

The shift cell operator method uses a modified FEM formulation in which the displacement field is modulated by plane a wave. That is, a normal FE model solves a partial differential equation involving a function f of a spatial variable x

and a time variable t , the shift-cell method allows to solve the partial differential equation from a function g such that:

$$f(x, t) = e^{-ikx}g(x, t), \quad (6.1)$$

for any complex wavenumber k . Contrary to what one may think, the matrices resulting from this discretization do not have a complicated dependency in k . Instead the discretized equations of motion take the following form in the 1D case:

$$(K - ikL + k^2H)U + C\frac{dU}{dt} + M\frac{d^2U}{dt^2} = F. \quad (6.2)$$

With K , M and C the classical FEM stiffness, mass and damping matrices and L and H additional matrices that encode the wavenumber modulation. An important change however happens in the load vector F as it has to be computed by applying an inverse modulation to the load distribution i.e. if $l(x)$ is used for a normal FE discretization then $p(x) = l(x)e^{ikx}$ must be used for the shift cell discretization. Noteworthy, choosing $k = 0$ renders the shift-cell discretization identical to classical FEM. Another interesting property is the following: Assuming one wants to compute the response to a load distribution of the form $l(x) = l_0e^{-ik_0x}$ then one could equal k to k_0 and the vector of forces F would be computed for a load distribution $p(x) = l(x)e^{ikx} = l_0$. The load now look like a constant force but its spatial oscillations are accounted for by a polynomial dependence in k_0 carried by the matrices L and H . This second property is leveraged in the rest of the chapter to make the coupling matrices between acoustic plane waves and a structure modeled using the shift cell operator method (quasi) wavenumber invariant. This invariance in turn enables the use of the multiparameter moment matching algorithm described in Section 6.2.

6.1.2 Sound transmission loss computation with shift cell method

This subsection describes how to modify the Hybrid-WFEM method [203, 57] and apply it to the Shift-Cell Operator Method framework to compute the sound transmission loss of a periodic structure excited by an incident plane wave. The idea is to couple an infinite 2D periodic structure occupying the region space $0 \leq z \leq h$ to two semi-infinite acoustic domains corresponding to the regions of space $z < 0$ and $z > h$. An incident acoustic field p_i is present in the half-space $z < 0$ which by fluid-structure coupling leads to a structural response, a reflected pressure field p_r , and a transmitted field p_t in the half-space $z > h$. In order to simplify the equations, the assumption that the structure considered is weakly periodic is made. This means higher order modes in the

reflected and transmitted pressure fields caused by periodic diffraction can be ignored. Thus, the acoustic fields in both half spaces take the respective forms:

$$\begin{cases} p_- = p_i e^{-i(k_x x + k_y y + k_z z)} + p_r e^{-i(k_x x + k_y y - k_z z)} \\ p_+ = p_t e^{-i(k_x x + k_y y + k_z z)} \end{cases} \quad (6.3)$$

The fluid-structure coupling equations are given in equation (6.4) and are valid on Γ_- , the $z = 0$ plane and Γ_+ , the $z = h$ plane:

$$\begin{cases} \frac{1}{\rho_f} \frac{\partial p}{\partial n} + \frac{\partial^2 u}{\partial t^2} \cdot \vec{n} = 0 \\ \sigma \cdot \vec{n} + p \vec{n} = 0 \end{cases} \quad (6.4)$$

In equation (6.4), ρ_f is the fluid's density, u the structural displacement, σ the stress tensor, p the fluid's pressure and \vec{n} , the outward normal of the solid. The first line of the equation expresses the continuity of the normal acceleration while the second lines specifies how the fluid's pressure acts as a force on the solid (Neumann boundary condition). As such, the first equation gives rise to two matrices K_{ff} and M_{fs} while the second equation only gives rise to a single coupling matrix K_{sf} and can be interpreted as a boundary condition. The weak form corresponding to each matrix when discretized for the Shift-Cell-Operator Method are given in equation (6.5):

$$\begin{cases} K_{ff} \leftrightarrow \frac{1}{\rho_f} \iint w_f^* \frac{\partial p}{\partial n} e^{i(k_x x + k_y y)} \\ M_{fs} \leftrightarrow \iint w_f^* \frac{\partial^2 v}{\partial t^2} \cdot \vec{n} \\ K_{sf} \leftrightarrow \iint (w_s \vec{n}) p e^{i(k_x x + k_y y)} \end{cases} \quad (6.5)$$

The shape functions for v and the usual FEM shape functions are identical to the test functions w_s while the shape functions for the pressure p are chosen according to equation (6.3). Finally the test functions w_f are chosen as the product of the pressure shape functions with $e^{i(k_x x + k_y y)}$. With these choices, the terms in $e^{i(k_x x + k_y y)}$ vanish from both the pressure and the solid shape functions such that the matrices depend only of k_z . Specifically, M_{fs} scales with $e^{i k_z z_0}$ (z_0 being the z coordinate of the interface) and K_{sf} with $e^{-i k_z z_0}$. Additionally, $K_{sf} = M_{fs}^H$ with the H exponent indicating the Hermitian transpose. Because of these properties, the subspace spanned by the columns of K_{fs} is independent of the wavenumbers k_x , k_y and k_z . This property still holds when higher order acoustics modes are added to the transmitted and reflected fields. The coupled

system can now be considered and takes the following form (in the frequency domain):

$$\begin{bmatrix} D_{ss} & K_{sf} \\ -\omega^2 M_{sf} & K_{ff} \end{bmatrix} \begin{bmatrix} U \\ p \end{bmatrix} = \begin{bmatrix} 0 \\ F_p \end{bmatrix} \quad (6.6)$$

With U the vector of structural displacements, p the vector of pressure displacements (plane wave coefficients) and D_{ss} the dynamic stiffness matrix of the structure in the SCOM framework (see Section 2.4):

$$D_{ss} = K + i\omega C - \omega^2 M - ik_x L_x - ik_y L_y + k_x^2 H_{xx} + k_y^2 H_{yy} + k_x k_y H_{xy} \quad (6.7)$$

The transmission loss $\tau(k_x, k_y, k_z, \omega)$ is computed by applying periodic boundary conditions on the structural part of equation (6.6) and imposing the value of the incident pressure p_i . After solving the system the transmission loss is obtained:

$$\tau(k_x, k_y, k_z, \omega) = \frac{|p_t|^2}{|p_i|^2} \quad (6.8)$$

The diffuse field transmission loss $\tau_d(\omega)$ can be computed by averaging the transmission loss $\tau(k_x, k_y, k_z, \omega)$ for acoustic wave coming from all incident directions. The detailed process can be found in [42, 155, 31] and was detailed in subsection 4.6.4

6.2 Model Order Reduction Scheme

This section details the model order reduction scheme used in section 6.3. First, the multiparameter moment matching method underlying the proposed MOR scheme is described in subsection 6.2.1. The full algorithm of the proposed MOR scheme is then detailed in subsection 6.2.2.

6.2.1 Multiparameter moment matching

The proposed MOR method is based on the moment matching concept which seeks to match the transfer function of the full order model (FOM) by replicating the first terms of its power series around an expansion point (see equation (6.10)). Herein, this method is applied to the structural part of the Hybrid-Shift-Cell modeling of the transmission reflection problem and can be considered a particular case of the technique presented in [68]. The starting point is the discretized equation of motion obtained via the shift-cell operator method:

$$(K + sC + s^2 M - ik_x L_x - ik_y L_y + k_x^2 H_{xx} + k_y^2 H_{yy} + k_x k_y H_{xy})U = F \quad (6.9)$$

In equation (6.9) s is the Laplace variable for the time domain, k_x and k_y are the wavenumbers of the shift-cell operator method, U is the structural displacement matrix and F a matrix whose columns span the subspace of inputs. A development of U into a multiparameter series is realized at the $(0, 0, 0)$ expansion point:

$$U = \sum_{(p,q,r) \in \mathbb{N}^3} U_{p,q,r} k_x^p k_y^q s^r \quad (6.10)$$

In order to compute the moments $U_{p,q,r}$ a recurrence relationship is established between them. First, equation (6.9) is rewritten in a more practical form:

$$[I_n + K^{-1}(sC + s^2M - ik_x L_x - ik_y L_y + k_x^2 H_{xx} + k_y^2 H_{yy} + k_x k_y H_{xy})]U = (K^{-1}F) \quad (6.11)$$

Finally, by replacing U with the series of equation (6.10), the following recurrence relationship is obtained for its moments:

$$\begin{aligned} U_{p,q,r} = & K^{-1}(iL_x U_{p-1,q,r} + iL_y U_{p,q-1,r} - CU_{p,q,r-1} \\ & - H_{xx} U_{p-2,q,r} - H_{yy} U_{p,q-2,r} - MU_{p,q,r-2} - H_{xy} U_{p-1,q-1,r}) \end{aligned} \quad (6.12)$$

with the initial condition:

$$U_{0,0,0} = K^{-1}F. \quad (6.13)$$

This makes it possible to match the moments of U in a classical manner. Because of the multiple parameters, the number of moments of order n , moments for which $p + q + r = n$, is equal to:

$$m_0 = \frac{(n+1)(n+2)}{2}, \quad (6.14)$$

while the number of moments of orders inferior or equal to n is:

$$m_1 = \frac{n^3 + 6n^2 + 11n + 6}{6} \quad (6.15)$$

Thus, the growth is polynomial which is acceptable. However, matching the moments of U as per equation (6.12) may not be numerically stable as the moments of the system are computed explicitly without any orthogonalisation process [69]. An implicit and stable moment matching process is proposed in [19] but it would change the vector growth rate from $O(n^3)$ to $O(7^n)$. As such, its computational cost becomes prohibitive before instabilities appear in the proposed algorithm. It should also be noted that the above method can be applied to compute moments around another expansion point (k_x^0, k_y^0, s_0) by replacing (k_x, k_y, s) with $(k_x^0 + k_x, k_y^0 + k_y, s_0 + s)$. Hence, numerical stability issues can also be mitigated by working with multiple expansion points.

6.2.2 MOR strategy

The proposed MOR strategy works by producing a projection basis $P \in \mathbb{C}^n$ that spans the subspace of the moments of the displacement matrix at one or several expansion points. From the matrix P the ROM's matrices and reduced loads are produced via Galerkin projection:

$$\left\{ \begin{array}{l} K^r = P^H K P \\ C^r = P^H C P \\ M^r = P^H M P \\ L_x^r = P^H L_x P \\ L_y^r = P^H L_y P \\ H_{xx}^r = P^H H_{xx} P \\ H_{xy}^r = P^H H_{xy} P \\ H_{yy}^r = P^H H_{yy} P \\ F_r = P^H F \end{array} \right. \quad (6.16)$$

The assessment of the quality of the ROM is done via residuals as defined in equation (6.17) which avoids the direct computation of the FOM response:

$$\left\{ \begin{array}{l} U_r = (K^r + sC^r + s^2M^r - ik_x L_x^r - ik_y L_y^r + k_x^2 H_{xx}^r + k_y^2 H_{yy}^r + k_x k_y H_{xy}^r)^{-1} (F_r) \\ F_a = (K + sC + s^2M - ik_x L_x - ik_y L_y + k_x^2 H_{xx} + k_y^2 H_{yy} + k_x k_y H_{xy})(P U_r) \\ res(k_x, k_y, s) = \frac{\|F_a - F\|}{\|F\|} \end{array} \right. \quad (6.17)$$

The proposed algorithm iteratively produces ROMs of higher dimensions by increasing the number of moments matched and expansion points until a ROM of sufficient quality is generated. In practice, this is achieved if the residuals of all points of a validation set \mathcal{V}_0 are below a threshold ϵ . Both \mathcal{V}_0 and ϵ must be supplied by the user in addition to a decay rate $\alpha < 1$. The details of when and where new expansion points are generated are the following. At each iteration, the expansion order at all expansion points is increased. Then, a

ROM is produced and an error criterion r^j is computed as per equation (6.18):

$$\begin{cases} r_a^j = \frac{1}{|\mathcal{V}_0|} \sum_{p \in \mathcal{V}_0} res(p) \\ r_m^j = \max\{res(p), p \in \mathcal{V}_0\} \\ r^j = \sqrt{r_m^j r_a^j} \end{cases} \quad (6.18)$$

If $r^j \geq \alpha r^{j-1}$ a new expansion point is created at the point of maximal residual. Otherwise, the iterative process continues normally with increasing the order of active expansion points. The algorithm stops when $r_m^j \leq \epsilon$.

6.3 Numerical Results

In this section, the proposed modeling technique and model order reduction scheme are applied to two examples. First, the proposed modeling strategy is compared to the Hybrid-WFEM method and validated in subsection 6.3.1. It is then applied to the full 3D FEM modeling of a doubly stiffened panel previously studied in [78, 33] via asymptotic homogenisation. The computation in this chapter are carried out with the speed of sound in the air c_0 set to 342.21 m.s^{-1} and the density of air ρ_0 set to 1.2041 kg.m^{-3} .

6.3.1 Validation Case

In this subsection, both the new hybrid variant and the proposed MOR scheme are applied to a 3mm thick homogeneous aluminum plate and compared to the classical Hybrid-WFEM modeling. All numerical methods, including the WFEM and the Shift-Cell Operator Method, are implemented on Matlab. The UC of the plate is modeled using classical 3D Lagrange $Q1$ elements with 10 perfectly cubic elements in the thickness of the plate. For the MOR scheme the frequency range $[0\text{Hz}, 10000\text{Hz}]$ is considered with a maximal residual value ϵ chosen equal to 10^{-4} . After application of the periodic or Floquet-Bloch boundary conditions the original model has 32dofs. Using the proposed MOR scheme a 4 dofs model is obtained. For the diffuse field computations, 3000 polar angles are used with only 1 azimuthal angle owing to the fact that the critical frequency is within the frequency range of interest and that the structure is isotropic. The diffuse field transmission loss obtained via both methods are presented in Figure 6.1. Both methods are in perfect agreement which validates the implementation of the Hybrid Shift-Cell and the proposed MOR scheme.

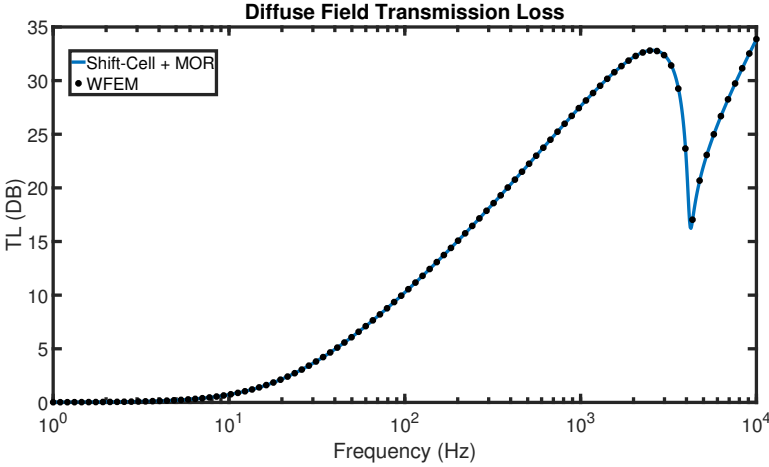


Figure 6.1: Diffuse field transmission loss of the aluminum plate

6.3.2 Doubly stiffened plate

In this subsection, the novel Hybrid-Shift-Cell modeling of Section 6.1 is combined to the MOR scheme of Section 6.2 to analyse a doubly stiffened panel. The panel was first introduced in [78, 33] and studied via asymptotic homogenization because of the high material property contrast between its stiffeners (Aluminum) and base panel (Perspex/PPMA) given in Table 6.1. This contrast leads to the appearance of full and partial resonant band-gaps for

| Material | Density ($kg.m^{-3}$) | Young Modulus (GPa) | Poisson coefficient | Damping ratio |
|----------|----------------------------|----------------------------|------------------------|------------------|
| Aluminum | 2700 | 69 | 0.3 | 0.0025 |
| Perspex | 1200 | 3 | 0.37 | 0.05 |

Table 6.1: Material properties of aluminum and Perspex in the model of [33]

flexural and torsional waves generated by local modes of the stiffened structure. For our study, the main reason this case is considered is the fact that while the structure possesses resonant band-gaps, the resonant part of the structure is also its radiating part. As such, its sound insulation properties should be non trivial. For the diffuse field computations, 500 polar angles are used with 9 azimuthal angles (since the structure is highly symmetric). Both the Shift-Cell Operator Method and of the Hybrid coupling are implemented on Matlab with standard 3D quadratic Serendipity Elements. The mesh of the structural part is presented in Figure 6.2 and the corresponding full order model (FOM) consists of 57915

dofs. The proposed MOR scheme is applied to the FOM for with maximal

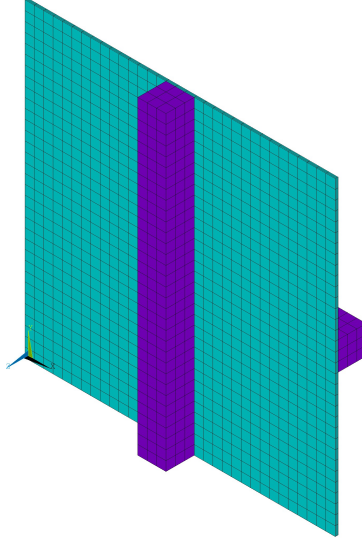


Figure 6.2: Mesh of the unit cell of the doubly stiffened panel. Aluminum is purple and Perspex is green

residual ϵ of 10^{-3} on the $[0Hz, 1000Hz]$ frequency range. More precisely, the set for which we want the ROM to be accurate is:

$$\mathcal{V} = \left\{ (\omega, k_x, k_y) \in [0, 2\pi f_{max}] \mathbb{R}^2, k_x^2 + k_y^2 \leq \frac{\omega^2}{c_0^2} \right\} \quad (6.19)$$

with $f_{max} = 1000$ Hz. The corresponding, discrete validation set \mathcal{V}_0 used in the MOR scheme to evaluate the accuracy of the ROM is obtained by generating 71000 random points of via uniform statistical distribution on \mathcal{V} . The performance of the proposed MOR strategy is detailed in Table 6.2. Using

| Model | Reduction time (s) | Model size | matrix inversion time (s) |
|-------|--------------------|------------|---------------------------|
| FOM | NA | 57915 | 2.56×10^1 |
| ROM | 8087 | 364 | 7.68×10^{-3} |

Table 6.2: Performance of the proposed model order scheme

the proposed MOR, a reduced order model of 364 dofs is produced using 3 expansion points. This reduction brings the time required for a matrix-vector inversion from 25 seconds to 7 milliseconds. The time required to produce the ROM however is of about 2 hours. This is not a major problem because 4.5

millions matrix inversions are required in order to compute the diffuse field STL of the structure every 1 Hertz. These computations would take more than 5 months using the FOM but were performed in 9 hours using the ROM. The resulting diffuse field transmission loss and absorption are presented in Figure 6.3. Unexpectedly, the multiple STL peaks do coincide with the predicted

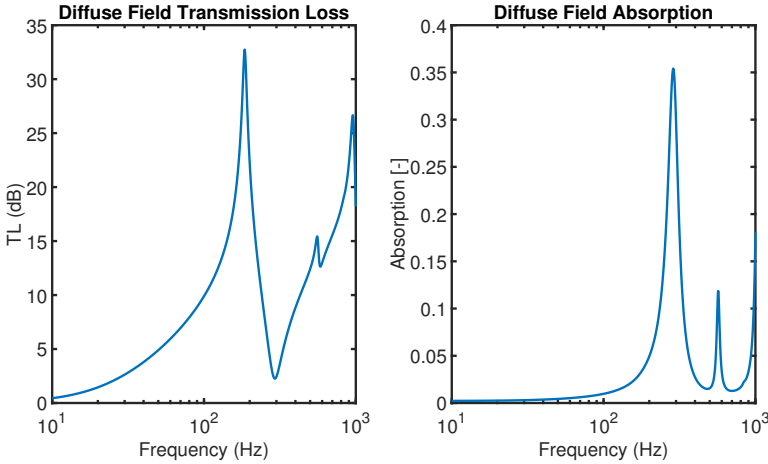


Figure 6.3: Transmission loss and absorption of the doubly stiffened panel

resonance frequencies at 170, 470 and 921 Hz [33]. This shows that the STL of the structure does increase inside the resonant band-gaps despite the fact that it is the radiating part of the structure that is supposed to resonate. However, the STL peaks are followed by STL minima at which absorption levels are rather high given the respective damping of PMMA and Perspex. This might be explained by the conjunction of the resonance mechanism with the dissipative properties of Perspex, effectively focusing vibration energy in the dissipative part of the structure.

6.4 Conclusions and perspectives

In this chapter a reduced order modeling strategy was presented for diffuse field STL computations in the SCOM framework was presented. The main contributions of the Chapter are the following:

- A novel method enabling the evaluation of the sound transmission loss in the SCOM framework was developed by adapting the Hybrid-WFEM [203, 57] method.
- A model order reduction scheme based on a moment-matching technique was developed and was shown to result in substantial reduction in computation time.

Though results obtained are promising the proposed MOR scheme could still be improved. The main possible areas of improvement are listed below:

- The method used to compute the moments in subsection 6.2.1 is not numerically stable [69, 19] which may lead to the production of reduced order models of suboptimal size [122]. This issue could be addressed by developing orthogonalization algorithms for the computation taking inspiration from the work done in [122] on the second order Arnoldi algorithm [14, 13] and the work of Slone et al. [177, 168, 167] on the asymptotic waveform evaluation [159, 41, 39].
- Similarly, the algorithm 6.2.2 was proposed as a first try but is not necessarily optimal. Many different schemes can be found in the literature even for single parameter systems [190, 206, 154].

Chapter 7

Conclusions and perspectives

The vibroacoustics of periodic structures and metamaterials is a rich topic that has been the focus of many PhD thesis and several research projects in the past decades. Among those were the Marie Curie Initial Training Network VIPER project (GA 675441) and the DENORMS cost action (CA 15125) both of which have recently ended. For both projects, consolidating the research surrounding periodic structures and metamaterials and sparking collaborations within the scientific community were important goals which to a large extent have been fulfilled. As an Early Stage Researcher of the VIPER project, my assigned research topic was "Vibroacoustics and structural dynamics of periodic structures". In principle, this topic covered most of the research space defined by the VIBroacoustics of PERiodic media project. A project which involved 11 other PhD students, all of them having very specific research topics (e.g. "Periodic viscoelastic add-ons"). In that context, I decided to orient my work toward methodological aspects and design tool as these could be useful in most practical and phenomenological aspects of the project while not being tied to any of them. My areas of choice were optimization, model order reduction and characterization which are now part of this manuscript's title. Section 7.1 details my contributions to these areas of research while Section 7.2 discusses possible follow-ups to the work done during this thesis and research directions related to its broader theme.

7.1 Main contributions of the thesis

The main contributions of the work produced during this PhD are summarized below:

In Chapter 3 a novel model order reduction strategy for the unit cell modeling of 1D periodic structures in the WFEM framework was presented and compared to the previous methods of the literature. The proposed strategy builds upon the inner dof reduction of [48, 102, 216] and the interface reduction of [60, 62]. The main contributions of the Chapter can be summarized as follows:

- The Craig-Bampton model order reduction scheme used in [216] was expanded to tackle models including hysteretic and generalized damping as well as frequency dependent material properties.
- A faster and more complete sampling strategy has been developed to replace the one used in [60]. These simultaneous gains are achieved by relying on the inverse WFEM formulation instead of the direct one as the former is usually faster than the latter.
- A better control of the dofs/accuracy trade off is achieved in the proposed interface reduction strategy by the use of an SVD based orthogonalization scheme instead of QR-based one. This can result in much faster ROMs as the complexity of the WFEM eigenvalue problem scales with the third power of the number of interface dofs.

In Chapter 4, a framework for the unit cell based optimization of periodic structures and waveguides was presented and applied to several numerical examples. The main contributions of chapter are summarized below:

- Firstly, efficient formulae for first and second order derivatives of most quantities that can be computed in the WFEM framework were derived using an intrusive methodology.
- A second order optimization algorithm based on the sequential quadratic programming paradigm [25] was proposed to exploit the aforementioned derivatives to their fullest. The proposed algorithm combines an ellipsoidal trust-region method [157, 54, 115] with a line search method used when the objective function is convex. This combination, solves issues related to step length, variable scaling, and saddle points that are encountered when using first order optimization techniques. It also address the sometime slow convergence of trust-regions methods when switching from regions of mixed curvatures to ones where the objective function is convex.

- The optimization framework obtained by combining the aforementioned contributions allows for the modeling of loads and boundary conditions during the optimization process which are important when considering applications with finite metamaterials [202, 182, 153, 207, 170].

In Chapter 5, a novel methodology for one-dimensional and two-dimensional wavenumber extraction was presented. Based on a convolution framework, the proposed method requires periodic sampling of the signal of interest to produce a convolution kernel that describes its wavenumbers, or K-Space. The core of INCOME is similar to the Prony series method but takes advantage of a convolution framework to encode wave propagation symmetries and reach the 2D case. The accuracy of INCOME was demonstrated in both 1D and 2D scenarios and it was shown to be sufficiently noise resistant to compete with the most robust methods of the literature when the structures studied allow for their use. The contributions of Chapter 5 can be summarized as follows:

- The INCOME method relies on solving small linear problems and is exact in both 1D and 2D cases. The wording "exact" refers here to the propagation scheme adopted for the inverse algorithm. Precisely, a given propagation model is fitted to the input data with consistency. The INCOME method is also mathematically robust and its numerical implementation easy to handle.
- In the 2D case, all properties of the K-Space are retrieved together in a coherent manner and INCOME was shown to successfully identify the wave heading (directivity) and the spatial attenuation. This is the most advantageous property of INCOME and it is achieved by making periodic sampling of the input mandatory.
- The proposed method draws inspiration from the WFEM framework [125, 143, 82, 16, 67, 92], and can be considered an inverse WFEM approach. The periodicity requirement for INCOME and the use of recurrence relationships make the formulation comprehensive for WFEM practitioners. The literature belonging to the WFEM being rich, one could expect bridges to be created between the direct WFEM and the INCOME.

In Chapter 6, a new reduced order modeling strategy for diffuse field sound transmission loss computations in the Shift Cell Operator Method framework was presented and validated. The main contributions of the chapter are the following:

- A novel method enabling the evaluation of the sound transmission loss in the Shift-Cell Operator Method framework was developed by adapting the

Hybrid-WFEM [203, 57] method. The main advantage of this formulation is that the structural loads corresponding to acoustic plane waves appear wavenumber invariant.

- Using the aforementioned invariance as a starting point, a multiparameter moment matching process whereby the forced wavenumbers and frequency are the parameters was derived. It was subsequently combined with a rational Krylov subspace method to produce a new model order reduction scheme. The proposed reduced order modeling strategy was validated on a simple example and applied to a complex 3D metaplate model where a speed up by three orders of magnitude was demonstrated.

7.2 Future work and perspectives

The work presented during this thesis has many direct and indirect follow-ups that can be conceptualized at different time scales and levels of details. Some of them are presented below:

From a short term perspective, the model order reduction strategy developed in Chapter 3 could be extended to cover parametric models [15, 51, 68, 20] allowing both material properties and geometry to vary. The resulting technique could be used in conjunction with the framework developed in Chapter 4 in order to produce optimal designs.

The optimization algorithm proposed in Chapter 4 could be improved by using a low dimensional representation of the hessian matrix when the objective function has many parameters. A practical implementation of this program could be realized by adapting conjugate gradient methods [180, 46] while using an adjoint-adjoint framework [81, 94] for the computation of second order derivatives. This would avoid forming the full hessian matrix and enable fast second order shape optimization.

Regarding Chapter 5, the follow-ups are straightforward. The similarities between INCOME and the Force Analysis Technique [113, 2, 65] should be leveraged. This would allow an easy extension of the method to source and damage detection. The preprocessing techniques used for the Force Analysis Technique should also be used to increase the robustness of INCOME. This is in fact already a work in progress. INCOME could also provide a good starting point for wavenumber extraction techniques relying on nonlinear least square fits such as Mc Daniel's method or an extended IWD method. This is of interest because such methods tend to be more robust than their linear counterparts. Lastly, wavenumber extraction in axisymmetric and curved media could also be considered.

Similarly, the methods developed in Chapter 6 could be extended to

axisymmetric structures by using a cylindrical coordinates based FEM/SCOM formulation [63, 87] and Bessel/Hankel functions to represent the acoustic field. Also, improvements to the numerical stability of the proposed multiparameter moment matching process could be made by developing a proper orthogonalization strategy for the computation of the moments. The work of Slone et al, with the asymptotic waveform evaluation should serve as an example [177, 168, 167].

From a top level perspective, most numerical tools enabling the study and designs of linear deterministic periodic structures and metamaterials have been developed and disseminated thus a shift in research priorities towards aspects related to manufacturing, characterization, industrial applications and maintenance is expected. Regarding the last domain, damage detection strategies exploiting insights gained through a wave propagation prism (see e.g. [59]) seem to be a promising area of research. The development of such strategies could be accelerated by the time domain friendly model order reduction scheme for dynamical systems containing periodic sub components as the power of (real time) virtual sensing [188, 106, 107] could be leveraged to track changes in the scattering properties of sub-components of these systems and possibly detect the apparition of defects as well as their types and severity.

As previously implied, the development of numerical design tools for periodic media is still lacking in two areas. The first one concerns the development of numerical methods for the study of nonlinear wave-propagation in periodic structures and vibroacoustic systems. Some work has been done semi-analytically (e.g. via homogenization methods) or analytically [98, 90, 1, 9] but attempts at creating a nonlinear WFEM have so far been limited to its inverse formulation and only in basic cases [37]. Similarly, wave propagation in random (statistically periodic) media has not yet been studied efficiently through numerical approaches. On the other hand many analytical developments have been made [189, 200, 146] since the topic is of importance in theoretical physics [74, 23, 133]. In both cases, the use of perturbation theory within the existing numerical frameworks should provide first insights.

Appendix A

General Codes

In this chapter general purpose matlab function codes are given

A.1 Normalizing all columns of a matrix

```
1 function [ M2 ] = normalize_columns( M )
2 N = sqrt(sum(abs((M.^2))));
3 N(N==0)=1;
4 M2=bsxfun(@rdivide,M,N);
5 end
```

A.2 Create a sparse diagonal matrix from a vector

```
1 function [ diag ] = sparsediag( vec )
2 %sparsediag Build a sparse diagonal matrix form a vector
3 t=length(vec);
4 diag=spdiags(vec(:),0,t,t);
5 end
```

A.3 QR-based Orthogonalization

```

1 function [P] = Gram_Schmidtt_Orthogonalization(M)
2 %Gram_Schmidtt_Orthogonalization Applies the Gram-Schmidtt process to M
3 % This function returns a projection basis obtained by applying a stable
4 % Gram-Schmidtt algorithm orthogonalization algorithm with 2-step
5 % orthogonalization and a deflation tolerance This function is mainly
6 % used to produce orthogonal projection basis
7
8 [n,m]=size(M);
9 P=zeros(n,m);
10 nvect=0;
11 epsilon=1.490116119384766e-08;
12 reorth_tol=0.707106781186548;
13 M=normalize_columns(M);
14
15
16 for i=1:m
17     v=M(:,i);
18     %Stable Ortohogonalization (vector by vector. See https://en.wikipedia.org/wiki/Gram%E2%80%93Schmidt\_process
19     for j=1:nvect
20         v=v-P(:,j)*(P(:,j)'\*v);
21     end
22     nv=norm(v);
23
24     %The vector is either added, re-orthogonalized or rejected
25     if(nv>=reorth_tol) %the vector is really far from the current subspace
26         v=v/nv;
27         nvect=nvect+1;
28         P(:,nvect)=v;
29
30     elseif(reorth_tol>nv)&&(nv>epsilon)%the vector is close from the
31         %correct subspace but acceptably far.
32         %reorthogonalization
33         for j=1:nvect
34             v=v-P(:,j)*(P(:,j)'\*v);
35         end
36         v=v/norm(v);
37         nvect=nvect+1;
38         P(:,nvect)=v;
39     else% the vector is too close to the current subsapce we don't add it
40         %do nothing
41     end
42 end
43 P=P(:,1:nvect);

```

```
44  
45 end
```

A.4 SVD-based Orthogonalization

```
1 function [P] = SVD_Orthogonalization(M,epsilon)  
2 %SVD_Orthogonalization Retrurns an orthogonal matrix that approximateely  
3 %sapsns the same subsapce as M  
4 % The quality of the apporximation is controled by epsilon values  
5 % between  
6 % 10-4 and 10-6 arerecommended  
7 [P,S,~]=svd(M,'econ');  
8 S=diag(S);  
9 rank=max(epsilon_rank(S,epsilon),ceil(effective_rank(S)));  
10 P=P(:,1:rank);  
11 end  
12  
13 function [ rank ] = epsilon_rank( S , epsilon)  
14 %rank_percent Compute the singular values that needs to be kept.  
15 % The estimation is basd on the sum of the ignored singular values  
16 % against the global sumation  
17 sigma=0;  
18 T=sum(S);  
19 i=0;  
20  
21 while((T-sigma)/T>epsilon)  
22     i=i+1;  
23     sigma=sigma+S(i);  
24 end  
25 rank=i;  
26 end  
27  
28 function [ erank ] = effective_rank( S )  
29 %effective_rank : Computes the effective rank of a matrix from it's  
30 % singular values vector S  
31 % See: O. Roy and M. Vetterli, 'The effective rank: A measure of  
32 % effective dimensionality, '2007 15th European Signal Processing  
33 % Conference, Poznan, 2007, pp. 606–610.  
34 p=S/sum(S);  
35 dist=-p.*log(p);  
erank=exp(sum(dist));  
end
```

A.5 Solving a quadratic eigenvalue problem

```

1 function [ V,D ] = quadeigs( A0,A1,A2,nval)
2 %quadeigs Solve a general quadratic eigenvalue problem with no regards for
3 %its structure.
4 [p,q]=size(A0);
5 if(issparse(A0))
6     0=sparse(p,q);
7     I=norm(A0(:))*speye(p,q)/sqrt(q);
8 else
9     0=zeros(p,q);
10    I=norm(A0(:))*eye(q)/sqrt(q);
11 end
12 A=[A0,0;0,-I];
13 B=[A1,A2;I,0];
14 %solving the eigenvalue problem
15 [V,D]=eigs(A,B,2*nval,'sm');
16 V=V(1:p,1:(2*nval));
17 D=diag(D);
18 end

```

A.6 Solving a Hermitian quadratic eigenvalue problem

```

1 function [ V,D ] = quad_hermitian_eigs( K,C,M,nval)
2 %quad_hermitian_eigs : Solve quadratic hermitian eigen value problem
3 %conserving the hermitian structure through second companion form of the
4 %quadratic eigenvalue problem.
5 [p,q]=size(K);
6 if(issparse(K))
7     0=sparse(p,q);
8 else
9     0=zeros(p,q);
10 end
11 A=[-K, 0 ; 0 M];
12 B=[C, M ; M, 0];
13 %Solving the eigenvalue problem
14 [V,D]=eigs(A,B,2*nval,'sm');
15 V=V(1:p,1:(2*nval));
16 D=diag(D);
17 end

```

Appendix B

1D WFEM Code Snippets

In this chapter, Matlab code snippets related to the 1D WFEM are proposed. These codes are not optimized or fully general and are meant as a starting point for new WFEM user to build from.

B.1 Classical 1D WFEM implementation

```
1 function [Lambda,PHI] = WFEM1D_Classic( K,M,C,QL,QR,QI,omega)
2 %WFEM1D_Classic Classical 1D WFEM formulation
3 % Classical 1D WFEM formulation with the linearization of: Fan, Y., Zhou
   , C. W., Laine, J. P., Ichchou, M. & Li, L. Model reduction schemes
   for the wave and finite element method using the free modes of a unit
   cell.
4 % Comput. Struct. 197, 42–57 (2018).
5
6 %Step 1 building the (condensed) dynamic stiffness matrix
7 if isempty(QI)% if no internal degree of freedom no condensation
8     D=K+1i*omega*C-(omega^2)*M;
9
10 else% condense the inner dofs
11     G=K+1i*omega*C-(omega^2)*M;
12
13     Qm=[QL,QR];%master dofs
14     Qs=QI;%slave dofs
15
16     Gmm=G(Qm,Qm);
17     Gms=G(Qm,Qs);
```



```

18     Gsm=G(Qs,Qm);
19     Gss=G(Qs,Qs);
20     D=Gmm-full(Gms/Gss)*Gsm;
21 end
22
23 % Step2 setting up the eigenvalue problem of Zhong's formulation
24 DLL=D(QL,QL);
25 DLR=D(QL,QR);
26 DRL=D(QR,QL);
27 DRR=D(QR,QR);
28
29 A0=DRL;
30 A1=DLL+DRR;
31 A2=DLR;
32
33 [PHI,Lambda] = quadeig(A0,A1,A2);
34 end
35
36 function [ V,D ] = quadeig( A0,A1,A2 )
37 %quadeig Solve the quadratique eigen value Problem
38
39 [p,q]=size(A0);
40 O=zeros(p,q);
41 I=norm(A0(:))*eye(q)/sqrt(q);
42 A=[A0,0;0,-I];
43 B=[A1,A2;I,0];
44
45 [V,D]=eig(A,B);
46 V=V(1:p,1:(2*q));
47 D=diag(D);
48 end

```

B.2 Zhong's formulation with an iterative solver

```

1 function [Lambda,PHI] = WFEM1D_Zhong( K,M,C,QL,QR,QI,omega,nwaves)
2 %WFEM1D_Zhong 1D WFEM formulation compatible with an iterative solver.
3 % WFEM with a structure preservinf linearization coming from control
4 % theory often refered to as Zhong's method. It is assumed that the
5 % matrices dofs have been reordered in the QL,QR,QI order with matching
6 % dofs ordering for QL and QR.
7 % For theoretical details see: Huang, T.-M., Lin, W.-W. & Qian, J.
8 % Structure-Preserving Algorithms for Palindromic Quadratic Eigenvalue
9 % Problems Arising from Vibration of Fast Trains. SIAM J. Matrix Anal.

```

```

10 % Appl. 30, 1566–1592 (2009).
11
12 %Step 1 building the (condensed) dynamic stiffness matrix
13 if isempty(QI)% if no internal degrees of freedom no condensation
14     D=K+li*omega*C-(omega^2)*M;
15
16 else% condense the inner dofs
17     G=K+li*omega*C-(omega^2)*M;
18
19     Qm=[QL,QR];%master dofs
20     Qs=QI;%slave dofs
21
22     Gmm=G(Qm,Qm);
23     Gms=G(Qm,Qs);
24     Gsm=G(Qs,Qm);
25     Gss=G(Qs,Qs);
26     D=Gmm-full(Gms/Gss)*Gsm;
27 end
28
29 % Step2 setting up the eigenvalue problem of Zhong's formulation
30 DLL=D(QL,QL);
31 DLR=D(QL,QR);
32 DRL=D(QR,QL);
33 DRR=D(QR,QR);
34
35 A=DRL-DLR;
36 B=DLL+DRR;
37 n=length(A);
38 if (issparse(A))%if the original matrices are sparse we ensure the assembled
39     matrix are too.
40     O=sparse(n,n);
41 else
42     O=zeros(n,n);
43 end
44 P=[A,B;-B,A];
45 Q=[O,-DRL;DLR,O];
46
47 opts.p = 5*nwaves+2;%Handpicked number of Lanczos basis vectors. This
48     seems to work most of the time unlike matlabs defaults
49 [Z,Nu]=eigs(P,Q,2*nwaves,'sm',opts);% Nu= (lambda + 1/lambda)
50
51 %Step 3 Post processing of the eigenvalues and eigenvectors to match the
52 %original palindromic eigenvalue problem.
53 Nu=diag(Nu);

```

```
54 [~,perm]=sort(abs(Nu),'ascend');
55 Nu=Nu(perm);
56 Nu(abs(Nu)==Inf)=Inf;
57 Nu(abs(Nu)<eps)=0;
58 Z=normalize_columns(Z(:,perm));
59
60 % Since all eigenvalues come in pair we average the value for each pair.
61 pair1=2*(1:nwaves);
62 pair2=pair1-1;
63
64 % Split back each double value into the corresponding 2 propagation
65 % constants
66 Nu=(Nu(pair1)+Nu(pair2))/2;
67 indexNuInf=(abs(Nu)==Inf);
68 Lambda1=(Nu+sqrt(Nu.^2-4))/2;
69 Lambda1(indexNuInf)=0;
70
71 Lambda2=(Nu-sqrt(Nu.^2-4))/2;
72 Lambda2(indexNuInf)=Inf;
73
74 %Separating the eigenvector pairs
75 Z1=Z(:,pair1);
76 Z2=Z(:,pair2);
77
78
79 %Post processing of the eigenvalues and eigenvectors
80 t=1:n;
81 b=n+(1:n);
82
83 %First group of eigenvalues/eigenvectors
84 I=ones(1,nwaves);;
85 I=sparseddiag(I);
86 L2=sparseddiag(Lambda2);
87
88 PHI1=Z1(t,:)*I + Z1(b,:)*L2;
89 PHI1=normalize_columns(PHI1);
90
91 %Second group of eigenvalues/eigenvectors
92 I=ones(1,nwaves);;
93 I=sparseddiag(I);
94 L1=sparseddiag(Lambda1);
95
96 PHI2=Z2(t,:)*I + Z2(b,:)*L1;
97 PHI2=normalize_columns(PHI2);
98
99 PHI=[PHI1,PHI2];
```

```

100 Lambda=[Lambda1,Lambda2];
101 end

```

B.3 An improved version of the MOR scheme of Droz et al

```

1 function [Kred,Mred,Cred,QL_red,QR_red,QI2,PROJ_LR] = MOR_Droz2014(K,M,C,
2   QL,QR,QI,L,fmax,n_cutonfind,maxImk)
3 %MOR_DROZ2014 An implementation of a MOR technique for 1D UC analysis
4 % This function implements the paper: 'A reduced formulation for the
5 % free-wave propagation analysis in composite structures'
6 % https://doi.org/10.1016/j.compstruct.2014.03.017
7
8 %QL: left interface dofs vector
9 %QR: right interface dofs vector
10 %QI inner dofs vector
11 %L length of the structure in the direction of propagation
12 %Step 1: Determine the cut on frequencies.
13 cut_on_frequencies=get_cut_on_frequencies(K,M,QL,QR,QI,fmax,n_cutonfind);
14 lmin=exp(-L*maxImk);
15 nc=length(cut_on_frequencies);
16 nwaves=(nc+8)*2;% some overdimensioning because the number of propagating
17   waves can vary ———> bangaps
18 n=length(QR);
19 %Step 2: Use the WFEM Method to build the snapshot matrix
20 Phi_Collection=zeros(n,nwaves*nc);
21 count=0;
22 for i=1:nc
23   omega=2*pi*cut_on_frequencies(i);
24   [lambdas, phi] = WFEM_1D_Zhong(K,M,C,QL,QR,QI,omega,nwaves);
25   index=find((abs(lambdas)>=lmin)&(abs(lambdas)<=1));
26   ni=length(index);
27   Phi_Collection(:,(count+1):(count+ni))=phi(:,index);
28   count=count+ni;
29 end
30 Phi_Collection=Phi_Collection(:,1:count);
31
32 %Step 3: Creation of the local interface projection basis via a QR like
33 %algorithm
34 Phi_Collection=[real(Phi_Collection),imag(Phi_Collection)];
35 Proj=Gram_Schmidt_Orthogonalization(Phi_Collection);

```

```

36
37 % Building the reduced order model
38
39 %Size of different matrices
40 nbKeep=size(Proj,2);
41 sizePhi=size(Proj,1);
42 sizeQI=length(QI);
43
44 %Dof structure for the reduced UC
45 QL_red=1:nbKeep;
46 QR_red=(nbKeep+1):(2*nbKeep);
47 QI2=(2*nbKeep+1):(2*nbKeep+sizeQI);
48
49 % Building the Final projection matrix
50 PROJ_LR=zeros(2*sizePhi+sizeQI,2*nbKeep+sizeQI);
51 PROJ_LR(GeoMesh.QL,QL_red)=Proj;
52 PROJ_LR(GeoMesh.QR,QR_red)=Proj;
53 PROJ_LR(QI,QI2)=eye(sizeQI);
54
55 %Obtaineing the reduced order matrices
56 Kred=symetrize(PROJ_LR.*K*PROJ_LR);
57 Mred=symetrize(PROJ_LR.*M*PROJ_LR);
58 Cred=symetrize(PROJ_LR.*C*PROJ_LR);
59
60 end
61 %% Auxiliary functions
62 function [cut_on_frequencies]= get_cut_on_frequencies(K,M,QL,QR,QI,fmax,
        n_cutonfind)
63
64 QL0=[QL,QI];
65 QR_tild=QL;
66 QL_tild=1:length(QL0);
67 QR0=QR;
68
69
70 n=length(QL_tild);
71 if(issparse(K))
72     KLambda=spalloc(n,n,nz(K));
73     MLambda=spalloc(n,n,nz(M));
74 else
75     KLambda=zeros(n);
76     MLambda=zeros(n);
77 end
78
79 %Applying Floquet–Bloch Boundary conditions for \lambda=1 i.e. k=0
80 KLambda(QR_tild,QL_tild)=KLambda(QR_tild,QL_tild)+ K(QR0,QL0);

```

```

81 | KLambda(QL_tild,QL_tild)=KLambda(QL_tild,QL_tild)+ K(QL0,QL0);
82 | KLambda(QR_tild,QR_tild)=KLambda(QR_tild,QR_tild)+ K(QR0,QR0);
83 | KLambda(QL_tild,QR_tild)=KLambda(QL_tild,QR_tild)+ K(QL0,QR0);
84 |
85 | KLambda=symetrize(KLambda);
86 |
87 | MLambda(QR_tild,QL_tild)=MLambda(QR_tild,QL_tild)+ M(QR0,QL0);
88 | MLambda(QL_tild,QL_tild)=MLambda(QL_tild,QL_tild)+ M(QL0,QL0);
89 | MLambda(QR_tild,QR_tild)=MLambda(QR_tild,QR_tild)+ M(QR0,QR0);
90 | MLambda(QL_tild,QR_tild)=MLambda(QL_tild,QR_tild)+ M(QL0,QR0);
91 |
92 | MLambda=symetrize(MLambda);
93 | Omega2=eigs(KLambda,MLambda,n_cutonfind,'sm');
94 | cut_on_frequencies=sqrt(Omega2)/(2*pi);
95 |
96 | %Filtering unwanted frequencies & cleaning the array
97 | cut_on_frequencies=real(cut_on_frequencies);% we keep only the real part
98 | cut_on_frequencies(cut_on_frequencies<10)=0; % we put back to zero the
    |     frequencies that should be there
99 | cut_on_frequencies=unique(cut_on_frequencies);%values appearing multiple
    |     times are put back to one appearance.
100 | cut_on_frequencies=cut_on_frequencies(cut_on_frequencies<=fmax);%
    |     frequencies higher than fmax are removed because we are not interested
    |     in them
101 | end

```

B.4 Basic Craig-Bampton MOR scheme implementation for inner dofs reduction

```

1 | function [ Kred, Mred,QI_red,Proj] =Craig_Bampton_MOR( K,M,QL,QR,QI, fmax,
    |     nf,nval)
2 | %Craig_Bampton_MOR Craig Bampton MOR for 1D unit cell modeling
3 |
4 |
5 | %K is the stiffness matrix it can be complex (hysteretic damping)
6 | %M is the mass matrix. It should be real
7 | %QL vector of the left interface dofs indexes
8 | %QR vector of the right interface dofs indexes
9 | %QI vector of the inner dofs indexes.
10 | %It is assumed that the matrices has been reordered such that [QL,QR,QI]
    |     is equal to 1:n with n the total number of dofs of the UC's matrices
11 |
12 | %Check on the frequency sampling factor. It should be higher than 2

```

```
13 if (nf<2)
14     nf=2;
15 end
16
17 %Extracting the relevant submatrices
18 Qbd=[QL,QR];%vector of all the boundary degrees of freedom
19 kii=K(QI,QI);
20 mii=M(QI,QI);
21 kib=K(QI,Qbd);
22
23 % Computation of the clamped interface modes
24 [Vec,Omega2]=eigs(kii,mii,nval,'sm');
25
26 %Sorting of the eigenfrequency and modes shapes
27 [Omega2,index]=sort(diag(Omega2));
28 Freqs=sqrt(Omega2)/2/pi;
29 Vec=Vec(:,index);
30
31 if(isreal(kii))%no hysteretic damping the eigenvectors are real
32     Vec=normalize_columns(Vec);
33 else% hysteretic damping is present. A real basis for the mode shapes
34     subspaces is built
35     Vec=Gram_Schmidt_Orthogonalization([real(Vec),imag(Vec)]);
36 end
37 %Selection of the mode shapes corresponding to frequencies higher than nf*
38     fmax
39 index_keep= abs(Freqs)<nf*fmax;
40 PhiISele=Vec(:,index_keep);
41 nb_modes=size(PhiISele,2);
42
43 %Computation of clamped static modes
44 PhiBd=full(real(kii)\real(kib));
45
46 %Building of the projection matrix
47 Proj=[eye(nddl_bound) zeros(nddl_bound,nb_modes);
48     PhiBd PhiISele];
49
50 %Projection of the mass and stiffness matrices
51 Kred=Proj.'*K*Proj;
52 Mred=Proj.'*M*Proj;
53
54 %Building the index of interior modes for the reduced model
55 ndofs_boundaries=length(Qbd);
56 QI_red=(ndofs_boundaries+1):(ndofs_boundaries+nb_modes);
57 end
```

Appendix C

Wavenumber extraction code snippets

C.1 The 1D ESPRIT algorithm

In this section, an implementation of the 1D ESPRIT algorithm [163] assuming the number of waves is known is implemented in Matlab.

```
1 function [K] = ESPRIT_HRWA(Y,Order)
2 %ESPRIT_HRWA Applies the ESPRIT algorithm to 1D Wavenumber extraction
3 % See:
4 % P. Margerit, A. Lebee, J. F. Caron, and X. Boutillon, 'High
5 % Resolution Wavenumber Analysis (HRWA) for the mechanical
6 % characterisation of viscoelastic beams',
7 % J. Sound Vib., vol. 433, pp. 198–211, 2018.
8
9 N=length(Y);
10 k=floor(N/2);
11 R=N-k;
12 H=zeros(R,k);
13 index=1:R;
14 for i=1:k
15     H(:,i)=Y(index);
16     index=index+1;
17 end
18 [W,~,~]=svd(H, 'econ');
```



```

19
20
21 I=speye(R-1,R-1);
22 O=sparse(R-1,1);
23 A1=[I,0];
24 A2=[0,I];
25
26 Wp=W(:,1:Order);
27 Wp1=A1*Wp;
28 Wp2=A2*Wp;
29
30 F=lsqminnorm(Wp1,Wp2);
31
32 Lambda=eig(F);
33 K=1i*log(Lambda);
34
35 end

```

C.2 A modified 1D ESPRIT algorithm

In this section a version of the 1D ESPRIT algorithm modified in order to account for the forward-backward 1D wave propagation symmetry is presented.

```

1 function [K] = ESPRIT_HRWA_R(Y,Order)
2 %ESPRIT_HRWA_R Applies the ESPRIT algorithm to 1D Wavenumber extraction
3 %with a few personal modification
4 % See:
5 % P. Margerit, A. Lebee, J. F. Caron, and X. Boutillon, 'High
6 % Resolution Wavenumber Analysis (HRWA) for the mechanical
7 % characterisation of viscoelastic beams',
8 % J. Sound Vib., vol. 433, pp. 198–211, 2018.
9 % Modifiacations:
10 % 1) Space symetrization by introducing f(-t) when building the
11 % invariant space
12
13 N=length(Y);
14 k=floor(N/2);
15 R=N-k;
16 Y2=Y(N:-1:1);
17
18 H=zeros(R,2*k);
19 index=1:R;
20
21 for i=1:k

```

```

19     H(:,2*i-1)=Y(index);
20     H(:,2*i)=Y2(index);
21     index=index+1;
22 end
23 [W,~,~]=svd(H, 'econ' );
24
25
26 I=speye(R-1,R-1);
27 O=sparse(R-1,1);
28 A1=[I,0];
29 A2=[0,I];
30
31 Wp=W(:,1:Order);
32 Wp1=A1*Wp;
33 Wp2=A2*Wp;
34 F=lsqminnorm(Wp1,Wp2);
35
36 Lambda=eig(F);
37 K=1i*log(Lambda);
38 end

```

C.3 A basic implementation of the 1D IWC

```

1 function [k,fval,exitflag] = IWC_1D(x,y,kr0,ki0)
2 %IWC 1D Summary of this function goes here
3 % Detailed explanation goes here
4 y=y/norm(y);
5 a = [];
6 b = [];
7 Aeq = [];
8 beq = [];
9 lb = [];
10 ub = [];
11 nonlcon = [];
12 options = optimoptions('fmincon','FunctionTolerance',10^-8,'
    OptimalityTolerance',10^-8,'MaxIterations',10^6,'
    MaxFunctionEvaluations',10^9,'Display','off');
13 x0=[kr0,ki0];
14 f=@(p)f0(x,y,p(1),p(2));
15 [kf,fval,exitflag]= fmincon(f,x0,a,b,Aeq,beq,lb,ub,nonlcon,options);
16 k=kf(1)+1i*kf(2);
17 end
18 function err=f0(x,y,kr,ki)

```

```

19 exp_fun=exp(-1i*(kr+1i*ki)*x);
20 exp_fun=exp_fun/norm(exp_fun);
21 err=-abs(exp_fun'*y)^2;
22 end

```

C.4 A basic implementation of the 2D IWC

```

1 function [k,fval,exitflag] = IWC_2D(theta,x,y,z,kr0,ki0)
2 %IWC_2D Summary of this function goes here
3 % Detailed explanation goes here
4 z=z/norm(z);
5 a = [];
6 b = [];
7 Aeq = [];
8 beq = [];
9 lb = [];
10 ub = [];
11 nonlcon = [];
12 options = optimoptions('fmincon','FunctionTolerance',10^-8,'
    OptimalityTolerance',10^-8,'MaxIterations',10^6,'
    MaxFunctionEvaluations',10^9,'Display','off');
13 x0=[kr0,ki0];
14 f=@(p)f0(x,y,z,theta,p(1),p(2));
15 [k,fval,exitflag]= fmincon(f,x0,a,b,Aeq,beq,lb,ub,nonlcon,options);
16 k=k(1)+1i*k(2);
17 end
18 function err=f0(x,y,z,theta,kr,ki)
19 exp_fun=exp(-1i*(kr+1i*ki)*(x*cos(theta)+y*sin(theta)));
20 exp_fun=exp_fun/norm(exp_fun);
21 err=-abs(exp_fun'*z);
22 end

```

C.5 A basic implementation of the IWD

```

1 function [k,Amplitudespr,Amplitudespi,Amplitudesnr,Amplitudesni,fval,
    exitflag] = IWD_H1W(XY,Z,Directions,k0,Amplitudespr0,Amplitudespi0,
    Amplitudesnr0,Amplitudesni0)
2 %IWD_H1W : Inverse Wave decomposition used for wavenumber extraction
3
4 n=length(Amplitudespr0);

```

```

5
6 Z=Z/norm(Z);
7 a = [];
8 b = [];
9 Aeq = [];
10 beq = [];options = optimoptions('fmincon','FunctionTolerance',10^-8,'
    OptimalityTolerance',10^-8,'MaxIterations',10^6,'
    MaxFunctionEvaluations',10^9,'Display','off');
11 lb = [];
12 ub = [];
13 nonlcon = [];
14 options = optimoptions('fmincon','FunctionTolerance',10^-8,'
    OptimalityTolerance',10^-8,'MaxIterations',10^6,'
    MaxFunctionEvaluations',10^9,'Display','off');
15 p0=[real(k0),imag(k0),Amplitudespr0,Amplitudespi0,Amplitudesnr0,
    Amplitudesni0];
16
17 i1=3:(n+2);
18 i2=n+i1;
19 i3=n+i2;
20 i4=n+i3;
21 f=@(p)f0(XY,Z,Directions,p(1),p(2),p(i1),p(i2),p(i3),p(i4),n);
22
23 [p,fval,exitflag]= fmincon(f,p0,a,b,Aeq,beq,lb,ub,nonlcon,options);
24 k=p(1)+1i*p(2);
25
26 Amplitudespr=p(i1);
27 Amplitudespi=p(i2);
28 Amplitudesnr=p(i3);
29 Amplitudesni=p(i4);
30 end
31
32 function err=f0(XY,Z,Directions,kr,ki,Amplitudespr,Amplitudespi,
    Amplitudesnr,Amplitudesni,n)
33
34 k=ones(1,n)*(kr+1i*ki);
35
36 x=XY*Directions;
37 u=exp(-1i*k.*x);
38 v=exp(1i*k.*x);
39
40 Amplitudesp=Amplitudespr(:).'+1i*Amplitudespi(:).';
41 Amplitudesn=Amplitudesnr(:).'+1i*Amplitudesni(:).';
42 Uapp=sum(u.*Amplitudesp + v.*Amplitudesn,2);
43 Uapp=Uapp/norm(Uapp);
44 err=-abs(Uapp'*Z)^2;

```

45 | end

C.6 A 1D INCOME code for 2 wavetypes

```

1  function [K,coeffs] = WaveNumberExtraction1D2W(X,n)
2  %WaveNumberExtraction1D2W Summary of this function goes here
3  % Detailed explanation goes here
4  s=length(X);
5  ind=(2*n+1):(s-2*n);
6
7  %Creation of the three columns of teh modified Hankel Matrix
8  X0=X(ind);
9  X1=X(ind+n)+X(ind-n);
10 X2=X(ind+2*n)+X(ind-2*n);
11
12 %Assembly of the modified hankel matrix
13 R=[X0(:),X1(:),X2(:)];
14
15 %Obtention of the convolution kernel's coefficients
16 coeffs=SVD(R);
17
18 %Determining the propagation constants using the palindromic
    transformation
19 Pcoeffs=[coeffs(3),coeffs(2),coeffs(1)-2*coeffs(3)];
20 Eta=roots(Pcoeffs);
21 Lambda=[(Eta+sqrt(Eta.^2-4))/2;(Eta-sqrt(Eta.^2-4))/2];
22
23 %The pseudo wavenumber is obtained by taking the logarithm it need to be
24 %divided by the sampling length in order to be a true wavenumber
25 K=1i*log(Lambda)/n;
26 end
27
28
29 function [coeffs]=SVD(H)
30 W=diag([1,2,2]);
31 [V,D]=eig(H'*H,W);
32 D=diag(D);
33 [~,ind]=sort(D);
34 coeffs=V(:,ind(1));
35 end

```

C.7 The Mc Daniel method for Euler-Bernoulli beams

```

1 function [err,gradient,hessian] = errFunctionBernoulli(y,x,L,kr1,ki1,apr1,
2   api1,anr1,ani1,apr2,api2,anr2,ani2)
3 %UNTITLED3 Summary of this function goes here
4 %errFunction2Waves Summary of this function goes here
5 % Detailed explanation goes here
6 if (nargout==1)
7   xm=L-x;
8   u1=exp(-li*(kr1+li*ki1)*x);
9   u2=exp(-li*(ki1-li*kr1)*x);
10  v1=exp(-li*(kr1+li*ki1)*xm);
11  v2=exp(-li*(ki1-li*kr1)*xm);
12  f=(apr1+li*api1)*u1 +(anr1+li*ani1)*v1 +(apr2+li*api2)*u2 +(anr2+li*
13    ani2)*v2;
14  diff=f-y;
15  err=diff'*diff;
16 elseif (nargout==2)
17   xm=L-x;
18   u1=exp(-li*(kr1+li*ki1)*x);
19   u2=exp(-li*(ki1-li*kr1)*x);
20   v1=exp(-li*(kr1+li*ki1)*xm);
21   v2=exp(-li*(ki1-li*kr1)*xm);
22   f=(apr1+li*api1)*u1 +(anr1+li*ani1)*v1 +(apr2+li*api2)*u2 +(anr2+li*
23     ani2)*v2;
24   diff=f-y;
25   err=diff'*diff;
26   %calcul du gradient
27   gradient=zeros(10,1);
28   %Onde 1
29   df_dkr1= -li*(apr1+li*api1)*x.*u1 -li*(anr1+li*ani1)*xm.*v1 -(apr2+li
30     *api2)*x.*u2 -(anr2+li*ani2)*xm.*v2;
31   df_dki1= (apr1+li*api1)*x.*u1 +(anr1+li*ani1)*xm.*v1 -li*(apr2+li*
32     api2)*x.*u2 -li*(anr2+li*ani2)*xm.*v2;
33   df_dapr1= u1;
34   df_dapi1= li*u1;
35   df_danr1= v1;
36   df_dani1= li*v1;
37   %Onde 2
38   df_dapr2= u2;
39   df_dapi2= li*u2;
40   df_danr2= v2;

```

```

38     df_dani2= li*v2;
39
40     gradient(1)=2*real(df_dkr1'*diff);
41     gradient(2)=2*real(df_dkil'*diff);
42     gradient(3)=2*real(df_dapr1'*diff);
43     gradient(4)=2*real(df_dapil'*diff);
44     gradient(5)=2*real(df_danr1'*diff);
45     gradient(6)=2*real(df_dani1'*diff);
46     gradient(7)=2*real(df_dapr2'*diff);
47     gradient(8)=2*real(df_dapi2'*diff);
48     gradient(9)=2*real(df_danr2'*diff);
49     gradient(10)=2*real(df_dani2'*diff);
50 elseif (nargout==3)
51     xm=L-x;
52     u1=exp(-li*(kr1+li*kil)*x);
53     u2=exp(-li*(kil-li*kr1)*x);
54     v1=exp(-li*(kr1+li*kil)*xm);
55     v2=exp(-li*(kil-li*kr1)*xm);
56     f=(apr1+li*apil)*u1 +(anr1+li*anil)*v1 +(apr2+li*api2)*u2 +(anr2+li*
        ani2)*v2;
57     diff=f-y;
58     err=diff'*diff;
59     %calcul du gradient
60
61     gradient=zeros(10,1);
62     %Onde 1
63     df_dkr1= -li*(apr1+li*apil)*x.*u1 -li*(anr1+li*anil)*xm.*v1 -(apr2+li
        *api2)*x.*u2 -(anr2+li*ani2)*xm.*v2;
64     df_dkil= (apr1+li*apil)*x.*u1 +(anr1+li*anil)*xm.*v1 -li*(apr2+li*
        api2)*x.*u2 -li*(anr2+li*ani2)*xm.*v2;
65     df_dapr1= u1;
66     df_dapil= li*u1;
67     df_danr1= v1;
68     df_dani1= li*v1;
69     %Onde 2
70     df_dapr2= u2;
71     df_dapi2= li*u2;
72     df_danr2= v2;
73     df_dani2= li*v2;
74
75     gradient(1)=2*real(df_dkr1'*diff);
76     gradient(2)=2*real(df_dkil'*diff);
77     gradient(3)=2*real(df_dapr1'*diff);
78     gradient(4)=2*real(df_dapil'*diff);
79     gradient(5)=2*real(df_danr1'*diff);
80     gradient(6)=2*real(df_dani1'*diff);

```

```

81 gradient(7)=2*real(df_dapr2'*diff);
82 gradient(8)=2*real(df_dapi2'*diff);
83 gradient(9)=2*real(df_danr2'*diff);
84 gradient(10)=2*real(df_dani2'*diff);
85
86
87 % Hessian
88 hessian=zeros(10,10);
89 x2=x.^2;
90 xm2=xm.^2;
91
92 %Premiere Onde
93 %kr1
94 d2f_dkr_dkr= -(apr1+li*api1)*x2.*u1 -(anr1+li*ani1)*xm2.*v1 + (apr2
    +li*api2)*x2.*u2 + (anr2+li*ani2)*xm2.*v2;
95 d2f_dkr_dki=-li*(apr1+li*api1)*x2.*u1 -li*(anr1+li*ani1)*xm2.*v1 +li*(
    apr2+li*api2)*x2.*u2 +li*(anr2+li*ani2)*xm2.*v2;
96 d2f_dkr_dapr1= -li*x.*u1;
97 d2f_dkr_dapi1= 1*x.*u1;
98 d2f_dkr_danr1= -li*xm.*v1;
99 d2f_dkr_dani1= 1*xm.*v1;
100 %premiere onde kil
101 d2f_dki_dki= (apr1+li*api1)*x2.*u1 + (anr1+li*ani1)*xm2.*v1 - (apr2+li
    *api2)*x2.*u2 - (anr2+li*ani2)*xm2.*v2;
102 d2f_dki_dapr1= x.*u1;
103 d2f_dki_dapi1= 1i*x.*u1;
104 d2f_dki_danr1= xm.*v1;
105 d2f_dki_dani1= 1i*xm.*v1;
106 %Deuxieme Onde
107 %kr2
108 d2f_dkr_dapr2= -x.*u2;
109 d2f_dkr_dapi2= -li*x.*u2;
110 d2f_dkr_danr2= -xm.*v2;
111 d2f_dkr_dani2= -li*xm.*v2;
112 %ki2
113 d2f_dki_dapr2= -li*x.*u2;
114 d2f_dki_dapi2= x.*u2;
115 d2f_dki_danr2= -li*xm.*v2;
116 d2f_dki_dani2= xm.*v2;
117
118 %Hessienne
119 %Ligne 1
120 hessian(1,1)=2*real(diff'*d2f_dkr_dkr + df_dkr1'*df_dkr1);
121 hessian(1,2)=2*real(diff'*d2f_dkr_dki + df_dki1'*df_dkr1);
122 hessian(1,3)=2*real(diff'*d2f_dkr_dapr1 + df_dapr1'*df_dkr1);
123 hessian(1,4)=2*real(diff'*d2f_dkr_dapi1 + df_dapi1'*df_dkr1);

```



```
124 hessian(1,5)=2*real(diff'*d2f_dkr_danr1 + df_danr1'*df_dkr1);
125 hessian(1,6)=2*real(diff'*d2f_dkr_dani1 + df_dani1'*df_dkr1);
126 hessian(1,7)=2*real(diff'*d2f_dkr_dapr2 + df_dapr2'*df_dkr1);
127 hessian(1,8)=2*real(diff'*d2f_dkr_dapi2 + df_dapi2'*df_dkr1);
128 hessian(1,9)=2*real(diff'*d2f_dkr_danr2 + df_danr2'*df_dkr1);
129 hessian(1,10)=2*real(diff'*d2f_dkr_dani2 + df_dani2'*df_dkr1);
130 %Ligne 2
131 hessian(2,2)=2*real(diff'*d2f_dki_dki + df_dki1'*df_dki1);
132 hessian(2,3)=2*real(diff'*d2f_dki_dapr1 + df_dapr1'*df_dki1);
133 hessian(2,4)=2*real(diff'*d2f_dki_dapi1 + df_dapi1'*df_dki1);
134 hessian(2,5)=2*real(diff'*d2f_dki_danr1 + df_danr1'*df_dki1);
135 hessian(2,6)=2*real(diff'*d2f_dki_dani1 + df_dani1'*df_dki1);
136 hessian(2,7)=2*real(diff'*d2f_dki_dapr2 + df_dapr2'*df_dki1);
137 hessian(2,8)=2*real(diff'*d2f_dki_dapi2 + df_dapi2'*df_dki1);
138 hessian(2,9)=2*real(diff'*d2f_dki_danr2 + df_danr2'*df_dki1);
139 hessian(2,10)=2*real(diff'*d2f_dki_dani2 + df_dani2'*df_dki1);
140 %Ligne 3
141 hessian(3,3)=2*real(df_dapr1'*df_dapr1);
142 hessian(3,4)=2*real(df_dapi1'*df_dapr1);
143 hessian(3,5)=2*real(df_danr1'*df_dapr1);
144 hessian(3,6)=2*real(df_dani1'*df_dapr1);
145 hessian(3,7)=2*real(df_dapr2'*df_dapr1);
146 hessian(3,8)=2*real(df_dapi2'*df_dapr1);
147 hessian(3,9)=2*real(df_danr2'*df_dapr1);
148 hessian(3,10)=2*real(df_dani2'*df_dapr1);
149 %Ligne 4
150 hessian(4,4)=2*real(df_dapi1'*df_dapi1);
151 hessian(4,5)=2*real(df_danr1'*df_dapi1);
152 hessian(4,6)=2*real(df_dani1'*df_dapi1);
153 hessian(4,7)=2*real(df_dapr2'*df_dapi1);
154 hessian(4,8)=2*real(df_dapi2'*df_dapi1);
155 hessian(4,9)=2*real(df_danr2'*df_dapi1);
156 hessian(4,10)=2*real(df_dani2'*df_dapi1);
157 %Ligne 5
158 hessian(5,5)=2*real(df_danr1'*df_danr1);
159 hessian(5,6)=2*real(df_dani1'*df_danr1);
160 hessian(5,7)=2*real(df_dapr2'*df_danr1);
161 hessian(5,8)=2*real(df_dapi2'*df_danr1);
162 hessian(5,9)=2*real(df_danr2'*df_danr1);
163 hessian(5,10)=2*real(df_dani2'*df_danr1);
164 %Ligne 6
165 hessian(6,6)=2*real(df_dani1'*df_dani1);
166 hessian(6,7)=2*real(df_dapr2'*df_dani1);
167 hessian(6,8)=2*real(df_dapi2'*df_dani1);
168 hessian(6,9)=2*real(df_danr2'*df_dani1);
169 hessian(6,10)=2*real(df_dani2'*df_dani1);
```

```

170 %Ligne 7
171 hessian(7,7)=2*real(df_dapr2'*df_dapr2);
172 hessian(7,8)=2*real(df_dapi2'*df_dapr2);
173 hessian(7,9)=2*real(df_danr2'*df_dapr2);
174 hessian(7,10)=2*real(df_dani2'*df_dapr2);
175 %Ligne 8
176 hessian(8,8)=2*real(df_dapi2'*df_dapi2);
177 hessian(8,9)=2*real(df_danr2'*df_dapi2);
178 hessian(8,10)=2*real(df_dani2'*df_dapi2);
179 %Ligne 9
180 hessian(9,9)=2*real(df_danr2'*df_danr2);
181 hessian(9,10)=2*real(df_dani2'*df_danr2);
182 %Ligne 10
183 hessian(10,10)=2*real(df_danr2'*df_danr2);
184
185 %Symetrisation
186 hessian=hessian+hessian'-diag(diag(hessian));
187
188 end

```

C.8 A 2D INCOME code for quasi-isotropic wave propagation with 1 wavetype

```

1 function [K,coeffs] = WaveNumberExtraction2DHighSymmetry1W(X,nxy)
2 %WaveNumberExtraction2DHighSymmetry1W Summary of this function goes here
3 % Detailed explanation goes here
4 [n,m]=size(X);
5 indX0=(nxy+1):(n-nxy);
6 indY0=(nxy+1):(m-nxy);
7
8 %Creation of the three columns of teh modified Hankel Matrix
9 XV=X(indX0-nxy,indY0)+X(indX0+nxy,indY0)+X(indX0,indY0-nxy)+X(indX0,indY0+
10 nxy);
11 XD=X(indX0-nxy,indY0-nxy)+X(indX0+nxy,indY0+nxy)+X(indX0-nxy,indY0+nxy)+X(
12 indX0+nxy,indY0-nxy);
13 X0=X(indX0,indY0);
14
15 %Assembly of the modified hankel matrix
16 R=[XV(:),XD(:),X0(:)];
17
18 %Obtention of the convolution kernel's coefficients
19 coeffs=SVD(R);

```

```

19 %Determining the propagation constant in the x/y direction (they are
    identical since this case has high symmetry)
20 Eta=-(coeffs(3)+2*coeffs(1))/(2*coeffs(2)+coeffs(1));
21 Lambda=[(Eta+sqrt(Eta.^2-4))/2;(Eta-sqrt(Eta.^2-4))/2];
22
23 %The pseudo wavenumber is obtained by taking the logarithm it need to be
24 %divided by the sampling length in order to be a true wavenumber
25 K=1i*log(Lambda)/nxy;
26 end
27
28 function [coeffs]=SVD(H)
29 W=diag([4,4,1]);
30 [V,D]=eig(H'*H,W);
31 D=diag(D);
32 [~,ind]=sort(D);
33 coeffs=V(:,ind(1));
34 end

```

C.9 Palindromic Transform

In this section an implementation of the palindromic transform of subsection 5.1.4. It produces a matrix M of size $n + 1$ such that:

$$\begin{bmatrix} p_{2n} \\ p_{2n-1} \\ \vdots \\ p_n \end{bmatrix} = \begin{pmatrix} M_{1,1} & M_{1,2} & \dots & M_{1,n+1} \\ M_{2,1} & M_{2,2} & \dots & M_{2,n+1} \\ \vdots & \vdots & \ddots & \vdots \\ M_{n+1,1} & M_{n+1,2} & \dots & M_{n+1,n+1} \end{pmatrix} \begin{bmatrix} r_n \\ r_{n-1} \\ \vdots \\ r_0 \end{bmatrix} \quad (\text{C.1})$$

With p_i the i^{th} coefficient of the palindromic polynomial P and r_j the j^{th} coefficient of its reduced polynomial R .

```

1 function [M]=palindromic_transform_matrix(maxOrder)
2 M=zeros(maxOrder+1);
3
4 for orderc=0:maxOrder
5     i=maxOrder+1-orderc;
6     Nsteps=0;
7     ordercoeff=orderc;
8     while ordercoeff>=0
9         j=maxOrder+1-ordercoeff;
10        M(j,i)=nchoosek(orderc,Nsteps);
11        ordercoeff=ordercoeff-2;
12        Nsteps=Nsteps+1;

```

```

13     end
14 end
15
16 end

```

C.10 Comparison of the accuracy of different methods for an analytical Euler-Bernoulli beam

```

1 %% Euler-Bernoulli beam
2 clear all
3 clc
4 np=101;%number of measurement points
5 nf=1000;
6 nfp=50;
7 EI=1+0.08*1i;%value of EI
8 mu=1;%Value of mu lineic mass
9 L=1;%Length of the beam
10 alpha=sqrt(mu/EI);%k=alpha*sqrt(omega);
11 x=linspace(0,L,np);%cordinate of measurement points
12 mf=0.1;%maximal frequeny
13 Mf=50;%minimal frequeny
14 frequency=linspace(mf,Mf,nf);
15 frequencyp=linspace(mf,Mf,nfp);
16 F=1;%Force applied on the beam
17 dl=L/(np-1);
18
19 %% Computing the frequency forced response of the beam
20 Y=zeros(nf,np);
21 k_analytic=zeros(nf,4);
22 for i=1:nf
23     k=alpha*sqrt(2*pi*frequency(i));%wavenumber as a function of frequency
24     kv=[1i*k,-k,-1i*k,k];
25     k_analytic(i,:)=fliplr(kv);
26     %Determine wave amplitude form boundary conditions
27     M=zeros(4);
28     M(1,:)=1;
29     M(2,:)=kv;
30     M(3,:)=exp(kv*L).*kv.^2;
31     M(4,:)=exp(kv*L).*kv.^3;
32     V=[0;0;0;-F/EI];
33     A=M\V;

```

```

34     %Build the displacement vector for the ith frequency
35     for j=1:4
36         Y(i,:)=Y(i,:)+A(j)*exp(kv(j)*x);
37     end
38 end
39 %% Wavenumber extraction
40 K_income=zeros(nf,4);
41 K_esprit=zeros(nf,4);
42 k_iwc=zeros(nf,1);
43 for i=1:nf
44     Y0=Y(i,:);
45     K_income(i,:)=WaveNumberExtraction1D2W(Y0,10)/dl;
46     K_esprit(i,:)=ESPRIT_HRWA(Y0,4)/dl;
47     k_iwc(i)=IWC_1D(x(:),Y0(:),real(k_iwc(i)),imag(k_iwc(i)));
48     if (i<nf)
49         k_iwc(i+1)=k_iwc(i);
50     end
51 end
52 k_iwc=-k_iwc;
53 %%
54 K_income= wavetracking(K_income,frequency,0);
55 K_esprit= wavetracking(K_esprit,frequency,0);
56
57 coherence=(K_income'*k_analytic);
58 [~,ind]=max(real(coherence));
59 k_income=K_income(:,ind);
60
61 coherence=(K_esprit'*k_analytic);
62 [~,ind]=max(real(coherence));
63 k_esprit=K_esprit(:,ind);
64
65 indp=1:30:nf;
66 figure(1)
67 subplot(1,2,1)
68 h(1:2)=plot(frequency,real(k_income(:,[1,2])), 'b-', 'LineWidth',4);
69 hold on
70 h(3:4)=plot(frequency,real(k_esprit(:,[1,2])), 'r-', 'LineWidth',4);
71 h(5)=plot(frequency,real(k_iwc), 'k-', 'LineWidth',4);
72 h(6:7)=plot(frequency(indp),real(k_analytic(indp,[1,2])), 'k.', 'MarkerSize'
73             ,30);
74 title('Real part of the wavenumber')
75 xlim([mf,Mf])
76 xlabel('Frequency (Hz)')
77 ylabel('Wavenumber (rad.m^{-1})')
78 lgd = legend(h([1,3,5,6]), 'INCOME', 'ESPRIT', 'IWC', 'Analytical');
lgd.Location='northwest';

```

```

79
80
81 subplot(1,2,2)
82 g(1:2)=plot(frequency,imag(k_income(:,[1,2])), 'b-', 'LineWidth',4);
83 hold on
84 g(3:4)=plot(frequency,imag(k_esprit(:,[1,2])), 'r—', 'LineWidth',4);
85 g(5)=plot(frequency,imag(k_iwc), 'k-.', 'LineWidth',4);
86 g(6:7)=plot(frequency(indp),imag(k_analytic(indp,[1,2])), 'k.', 'MarkerSize'
      ,30);
87 title('Imaginary part of the wavenumber')
88 xlim([mf,Mf])
89 xlabel('Frequency (Hz)')
90 ylabel('Wavenumber (rad.m{-1})')
91 lgd = legend(g([1,3,5,6]), 'INCOME', 'ESPRIT', 'IWC', 'Analytical');
92 lgd.Location='southwest';
93
94
95 figure(2)
96 win(1:2)=semilogy(frequency,abs((k_income(:,[1,2])—k_analytic(:,[1,2]))./
      k_analytic(:,[1,2])), 'b-');
97 hold on
98 win(3:4)=semilogy(frequency,abs((k_esprit(:,[1,2])—k_analytic(:,[1,2]))./
      k_analytic(:,[1,2])), 'r—');
99 win(5)=semilogy(frequency,abs((k_iwc—k_analytic(:,1))./k_analytic(:,1)), 'k
      -.'');
100 xlabel('Frequency (Hz)')
101 ylabel('Relative error [-]')
102 title('Error as a function of frequency')
103 xlim([mf,Mf])
104 lgd = legend(win([1,3,5]), 'INCOME', 'ESPRIT', 'IWC');
105
106 %%
107 function Kt= wavetracking(K,f,fc)
108 n=size(K,1)—1;
109
110 for i=1:n
111     iref=i;
112     while(abs((K(iref,1)—K(iref,2))/K(iref,1))<0.03)
113         iref=iref—1;
114     end
115     Ki=K(iref,:);
116     Kip=perms(K(i+1,:));
117
118     if(f(i)<fc)
119         R=sum(abs(real(Kip—Ki)).^2,2);
120     else

```

```

121     R=sum(abs(Kip-Ki).^2,2);
122     end
123     [~,ind]=min(R);
124     K(i+1,:)=Kip(ind(1),:);
125 end
126 Kt=K;
127 end

```

C.11 Comparison of the accuracy of different methods for the Helmholtz equation

```

1  %% Wavenumber etxratcion for Helmholtz Equation
2  clear all
3  clc
4  addpath('..\')
5  %% Definition of the domain of sampling
6  np=51;
7  dl=1/(np-1);
8  X=linspace(-0.5,0.5,np);
9  Y=linspace(-0.5,0.5,np);
10 [X,Y]=meshgrid(X,Y);
11 %% Coordinates and amplitudes of the sources (phase will be random in the
    simulation)
12 ns=30;
13 Rs=0.9+3*rand(1,ns);%distance of the source from the origin
14 Ts=2*pi*rand(1,ns); %polar andgles of the sources in poolar cordiante
15
16 As=exp(2*1i*pi*rand(1,ns)).*rand(1,ns)/4; %Random amplitudes and phases of
    the sources
17 Xs=Rs.*cos(Ts);% abccissas of the sources
18 Ys=Rs.*sin(Ts);% ordinates of the sources
19 %% Detarministic field
20 k=30;% wavenumber value in the Helmholtz equation
21 Zd=zeros(np,np);
22 for i=1:ns
23     Ri=sqrt((X-Xs(i)).^2+(Y-Ys(i)).^2);
24     Zd=Zd+As(i)*besselh(0,k*Ri);
25 end
26 %% Ploting the deterministic field
27 figure(1)
28 surf(X,Y,real(Zd));
29 title('Real part of the wavefield');
30 shading interp

```

```

31 axis equal
32 xlabel('X coordinates (m)')
33 ylabel('Y coordinates (m)')
34 view(2)
35 colormap hot
36 %% Application of INCOME to 2D wavenumber extraction deterministic case
37 tic
38 k1=WaveNumberExtraction2DHighSymmetry1W(Zd,1);
39 t_income=toc;
40 k1=k1/dl;
41 res_income=min(abs((k+k1)/k));
42 noise_level=0.1;
43 %% Application of the IWD
44 na=15;
45 angles=pi*(0:(na-1))/na;
46 Directions=zeros(2,na);
47 for i=1:na
48     Directions(:,i)=[cos(angles(i));sin(angles(i))];
49 end
50 XY=[X(:),Y(:)];
51 Amplitudespr0=(rand(1,na)-0.5)*rand(1);
52 Amplitudesnr0=(rand(1,na)-0.5)*rand(1);
53 Amplitudespi0=(rand(1,na)-0.5)*rand(1);
54 Amplitudesni0=(rand(1,na)-0.5)*rand(1);
55 tic
56 [k_iwd,~,~,~,fval,exitflag] = IWD_H1W(XY,Zd(:),Directions,0,
    Amplitudespr0,Amplitudespi0,Amplitudesnr0,Amplitudesni0);
57 t_iwd=toc;
58 res_iwd=min(abs(k_iwd-k),abs(k_iwd+k))/k;
59 %% Application of the IWC
60 tic
61 [k_iwc,fval,exitflag] = IWC_2D(0,X(:),Y(:),Zd(:),0,0);
62 t_iwc=toc;
63 res_iwc=min(abs(k_iwc+k),abs(k_iwc-k))/k;

```


Appendix D

Some Proofs and analytical formulas

D.1 Coherent system of derivatives for eigenvalues and eigenvectors

The aim of this subsection is to determine how equation of the form:

$$XA = B \tag{D.1}$$

Should be solved in the context of eigenvector derivatives computations. Indeed, equations (B.5) and (B.9) can be used to evaluate the derivatives of the eigenvector. However, because the matrix function is singular when λ is an eigenvalue, an infinite number of solutions exists. This subsection shows that solving according to equation (D.2) produces a coherent set of derivatives.

$$\left\{ \begin{array}{l} \left(U_i(p) \left| \frac{\partial U_i(p)}{\partial p_k} \right. \right) = 0 \\ \left(U_i(p) \left| \frac{\partial^2 U_i(p)}{\partial p_k \partial p_l} \right. \right) = -\Re \left(\left(\frac{\partial U_i(p)}{\partial p_k} \left| \frac{\partial U_i(p)}{\partial p_l} \right. \right) \right) \end{array} \right. \tag{D.2}$$

In what follows, it is assumed that the derivatives are computed for $p = 0$ and that they are C^2 functions of the eigenvalue λ_i and the eigenvectors U_i . We start by normalizing the eigenvector function. That is, we use $\frac{1}{\|U_i(p)\|} U_i(p)$ instead of $U_i(p)$. Since eigenvectors are defined up to a multiplicative constant

this function is still an eigenvector function. Moreover it is also C^2 since U_i cannot be equal to zero (eigenvectors are non-trivial solutions). In what follows we still note this new function $U_i(p)$.

$$\forall p \in \mathbb{R}^m, \|U_i(p)\| = 1 \tag{D.3}$$

Taking the first order derivative of equation (D.3) yields

$$\forall p \in \mathbb{R}^m, \Re \left(\frac{\partial U_i}{\partial p_k} \middle| U_i \right) = \Re \left(U_i \middle| \frac{\partial U_i}{\partial p_k} \right) = 0 \tag{D.4}$$

Considering the second order derivatives leads to:

$$\forall p \in \mathbb{R}^m, \Re \left(U_i(p) \middle| \frac{\partial^2 U_i(p)}{\partial p_k \partial p_l} \right) = -\Re \left(\frac{\partial U_i(p)}{\partial p_k} \middle| \frac{\partial U_i(p)}{\partial p_l} \right) \tag{D.5}$$

Equations (D.4) and (D.5) are only true for the imaginary parts because the $(\cdot | \cdot)$ is an hermitian inner product. Therefore we still have to show that the imaginary part of the concerned inner products can be chosen equal to 0. Equation (D.4) can be rewritten for $p = 0$ as:

$$\frac{\partial U_i}{\partial p_k}(0) = j\alpha_k U_i(0) + Q_k \tag{D.6}$$

With

$$\forall k \in \llbracket 1, m \rrbracket, \alpha_k \in \mathbb{R}, (U_i(0) | Q_k) = 0, j^2 = -1 \tag{D.7}$$

The eigenvector function R defined by equation (D.8) is considered:

$$\forall p, \in \mathbb{R}^m, R_i(p) = U_i(p)e^{-j(\alpha|p)} \tag{D.8}$$

The function R is also a normalized eigenvector function since $|e^{-j(\alpha|p)}| = 1$ hence, it satisfies equations (D.4) and (D.5). Taking the first order derivatives of R leads to:

$$\frac{\partial R_i}{\partial p_k} = \left(\frac{\partial U_i}{\partial p_k} - j\alpha_k U_i \right) e^{-j(\alpha|p)} \tag{D.9}$$

Therefore:

$$\begin{cases} R(0) = U_i(0)e^{-j(\alpha|0)} = U_i(0) \\ \frac{\partial R_i}{\partial p_k}(0) = Q_k e^{-j(\alpha|0)} = Q_k \\ \text{Hence, } \left(R(0) \middle| \frac{\partial R_i}{\partial p_k}(0) \right) = 0 \end{cases} \tag{D.10}$$

The first condition of equation (D.2) is verified by the eigenvector function R_i but not necessarily the second one. It follows that:

$$\begin{cases} \frac{\partial^2 R_i}{\partial p_k \partial p_l}(0) = (\beta_{k,l} + j\gamma_{k,l}) U_i(0) + W_{k,l} \\ \forall (k,l) \in \llbracket 1, m \rrbracket^2, (\beta_{k,l}, \gamma_{k,l}) \in \mathbb{R}^2, (R_i(0)|W_{k,l}) = 0 \end{cases} \quad (\text{D.11})$$

It should be noted that by Schwartz theorem $\beta_{k,l} = \beta_{l,k}$. The same holds true for $\gamma_{k,l}$ and $W_{k,l}$. The m by m matrix H is defined such that $H_{k,l} = \frac{\gamma_{k,l}}{2}$. H is real symmetric. We can now define the normalized eigenvector function S by:

$$\forall p \in \mathbb{R}^m, S_i(p) = R_i(p) e^{-jp^T H p} \quad (\text{D.12})$$

Let $(\nu_k)_{k \in \llbracket 1, m \rrbracket}$ be the canonical basis of \mathbb{R}^m . We have:

$$\begin{cases} S_i(p) = R_i(p) e^{-jp^T H p} \\ \frac{\partial S_i}{\partial p_k} = \left(\frac{\partial R_i}{\partial p_k} - 2j (\nu_k^T H p) R_i \right) e^{-jp^T H p} \\ \frac{\partial^2 S_i}{\partial p_l \partial p_k} = \left[-2j (\nu_l^T H p) \left(\frac{\partial R_i}{\partial p_k} - 2j (\nu_k^T H p) R_i \right) \dots \right. \\ \quad \left. + \left(\frac{\partial^2 R_i}{\partial p_l \partial p_k} - 2j (\nu_k^T H \nu_l) R_i - 2j (\nu_k^T H p) \frac{\partial R_i}{\partial p_l} \right) \right] e^{-jp^T H p} \end{cases} \quad (\text{D.13})$$

Evaluating these expressions at $p = 0$ yields:

$$\begin{cases} S_i(0) = R_i(0) \\ \frac{\partial^2 S_i}{\partial p_k} (0) = \frac{\partial R_i}{\partial p_k} (0) \\ \frac{\partial^2 S_i}{\partial p_l \partial p_k} (0) = \frac{\partial^2 R_i}{\partial p_l \partial p_k} (0) - 2j H_{k,l} R_i(0) = \beta_{k,l} R_i(0) + W_{k,l} \end{cases} \quad (\text{D.14})$$

Hence the eigenvector function S_i satisfies all the conditions of equation (D.2). This proves that the formulas produce a coherent system of eigenvector derivatives.

D.2 Derivatives of the wave stiffness matrix

This section details computation of the derivatives of the wave stiffness matrix in equations:

$$\begin{cases} W_{11} = \Psi^+ \\ W_{12} = \Psi^- \Lambda^N \\ W_{21} = D_{RL} \Psi^+ \Lambda^{N-1} + D_{RR} \Psi^+ \Lambda^N \\ W_{22} = D_{RL} \Psi^- \Lambda + D_{RR} \Psi^- \end{cases} \quad (\text{D.15})$$

The derivatives of W_{11} are trivial but that of the other submatrices are developed:

$$\frac{\partial W_{12}}{\partial p_k} = \frac{\partial \Psi^-}{\partial p_k} \Lambda^N + N \Psi^- \frac{\partial \Lambda}{\partial p_k} \Lambda^{N-1} \quad (\text{D.16})$$

$$\begin{aligned} \frac{\partial^2 W_{12}}{\partial p_k \partial p_l} &= \frac{\partial^2 \Psi^-}{\partial p_k \partial p_l} \Lambda^N + N \left(\frac{\partial \Psi^-}{\partial p_k} \frac{\partial \Lambda}{\partial p_l} + \frac{\partial \Psi^-}{\partial p_l} \frac{\partial \Lambda}{\partial p_k} + \Psi^- \frac{\partial^2 \Lambda}{\partial p_k \partial p_l} \right) \Lambda^{N-1} \\ &\quad + N(N-1) \Psi^- \frac{\partial \Lambda}{\partial p_k} \frac{\partial \Lambda}{\partial p_l} \Lambda^{N-2} \end{aligned} \quad (\text{D.17})$$

$$\begin{aligned} \frac{\partial W_{21}}{\partial p_k} &= \left(\frac{\partial D_{RL}}{\partial p_k} \Psi^+ + D_{RL} \frac{\partial \Psi^+}{\partial p_k} \right) \Lambda^{N-1} + (N-1) D_{RL} \Psi^+ \frac{\partial \Lambda}{\partial p_k} \Lambda^{N-2} \\ &\quad + \left(\frac{\partial D_{RR}}{\partial p_k} \Psi^+ + D_{RR} \frac{\partial \Psi^+}{\partial p_k} \right) \Lambda^N + N D_{RR} \Psi^+ \frac{\partial \Lambda}{\partial p_k} \Lambda^N \end{aligned} \quad (\text{D.18})$$

$$\begin{aligned}
\frac{\partial^2 W_{21}}{\partial p_k \partial p_l} &= \left(\frac{\partial^2 D_{RL}}{\partial p_k \partial p_l} \Psi^+ + \frac{\partial D_{RL}}{\partial p_k} \frac{\partial \Psi^+}{\partial p_l} + \frac{\partial D_{RL}}{\partial p_l} \frac{\partial \Psi^+}{\partial p_k} + D_{RL} \frac{\partial^2 \Psi^+}{\partial p_k \partial p_l} \right) \Lambda^{N-1} \\
&+ (N-1) \left[\left(\frac{\partial D_{RL}}{\partial p_k} \Psi^+ + D_{RL} \frac{\partial \Psi^+}{\partial p_k} \right) \frac{\partial \Lambda}{\partial p_l} + \left(\frac{\partial D_{RL}}{\partial p_l} \Psi^+ + D_{RL} \frac{\partial \Psi^+}{\partial p_l} \right) \frac{\partial \Lambda}{\partial p_k} + D_{RL} \Psi \frac{\partial^2 \Lambda}{\partial p_k \partial p_l} \right] \Lambda^{N-2} \\
&+ (N-1)(N-2) D_{RL} \Psi^+ \frac{\partial \Lambda}{\partial p_k} \frac{\partial \Lambda}{\partial p_l} \Lambda^{N-3} \\
&+ \left(\frac{\partial^2 D_{RR}}{\partial p_k \partial p_l} \Psi^+ + \frac{\partial D_{RR}}{\partial p_k} \frac{\partial \Psi^+}{\partial p_l} + \frac{\partial D_{RR}}{\partial p_l} \frac{\partial \Psi^+}{\partial p_k} + D_{RR} \frac{\partial^2 \Psi^+}{\partial p_k \partial p_l} \right) \Lambda^N \\
&+ N \left[\left(\frac{\partial D_{RR}}{\partial p_k} \Psi^+ + D_{RR} \frac{\partial \Psi^+}{\partial p_k} \right) \frac{\partial \Lambda}{\partial p_l} + \left(\frac{\partial D_{RR}}{\partial p_l} \Psi^+ + D_{RR} \frac{\partial \Psi^+}{\partial p_l} \right) \frac{\partial \Lambda}{\partial p_k} + D_{RR} \Psi \frac{\partial^2 \Lambda}{\partial p_k \partial p_l} \right] \Lambda^{N-1} \\
&+ N(N-1) D_{RR} \Psi^+ \frac{\partial \Lambda}{\partial p_k} \frac{\partial \Lambda}{\partial p_l} \Lambda^{N-2}
\end{aligned} \tag{D.19}$$

$$\frac{\partial W_{22}}{\partial p_k} = \left(\frac{\partial D_{RL}}{\partial p_k} \Psi^- + D_{RL} \frac{\partial \Psi^-}{\partial p_k} \right) \Lambda + D_{RL} \Psi^- \frac{\partial \Lambda}{\partial p_k} + \frac{\partial D_{RR}}{\partial p_k} \Psi^- + D_{RR} \frac{\partial \Psi^-}{\partial p_k} \tag{D.20}$$

$$\begin{aligned}
\frac{\partial^2 W_{22}}{\partial p_k \partial p_l} &= \left(\frac{\partial^2 D_{RL}}{\partial p_k \partial p_l} \Psi^- + \frac{\partial D_{RL}}{\partial p_k} \frac{\partial \Psi^-}{\partial p_l} + \frac{\partial D_{RL}}{\partial p_l} \frac{\partial \Psi^-}{\partial p_k} + D_{RL} \frac{\partial^2 \Psi^-}{\partial p_k \partial p_l} \right) \Lambda \\
&+ \left(\frac{\partial D_{RL}}{\partial p_k} \Psi^- + D_{RL} \frac{\partial \Psi^-}{\partial p_k} \right) \frac{\partial \Lambda}{\partial p_l} + \left(\frac{\partial D_{RL}}{\partial p_l} \Psi^- + D_{RL} \frac{\partial \Psi^-}{\partial p_l} \right) \frac{\partial \Lambda}{\partial p_k} \\
&+ D_{RL} \Psi^- \frac{\partial^2 \Lambda}{\partial p_k \partial p_l} \\
&+ \frac{\partial^2 D_{RR}}{\partial p_k \partial p_l} \Psi^- + \frac{\partial D_{RR}}{\partial p_k} \frac{\partial \Psi^-}{\partial p_l} + \frac{\partial D_{RR}}{\partial p_l} \frac{\partial \Psi^-}{\partial p_k} + D_{RR} \frac{\partial^2 \Psi^-}{\partial p_k \partial p_l}
\end{aligned} \tag{D.21}$$

D.3 Derivatives of the displacement field

$$\begin{aligned}
\frac{\partial V_i}{\partial p_k} &= \frac{\partial \Psi^+}{\partial p_k} \Lambda^i q^+ + i \Psi^+ \frac{\partial \Lambda}{\partial p_k} \Lambda^{i-1} q^+ + \Psi^+ \Lambda^i \frac{\partial q^+}{\partial p_k} + \frac{\partial \Psi^-}{\partial p_k} \Lambda^{N-i} q^- \\
&+ (N-i) \Psi^- \frac{\partial \Lambda}{\partial p_k} \Lambda^{N-i-1} q^- + \Psi^- \Lambda^{N-i} \frac{\partial q^-}{\partial p_k}
\end{aligned} \tag{D.22}$$

$$\begin{aligned}
\frac{\partial^2 V_i}{\partial p_k \partial p_l} &= \frac{\partial^2 \Psi^+}{\partial p_k} \Lambda^i q^+ + \Psi^+ \Lambda^i \frac{\partial^2 q^+}{\partial p_k \partial p_l} + \frac{\partial \Psi^+}{\partial p_k} \Lambda^i \frac{\partial q^+}{\partial p_l} + \frac{\partial \Psi^+}{\partial p_l} \Lambda^i \frac{\partial q^+}{\partial p_k} \\
&+ i \left(\frac{\partial \Psi^+}{\partial p_k} \frac{\partial \Lambda}{\partial p_l} \Lambda^{i-1} q^+ + \frac{\partial \Psi^+}{\partial p_l} \frac{\partial \Lambda}{\partial p_k} \Lambda^{i-1} q^+ + \right. \\
&+ \left. \Psi^+ \frac{\partial \Lambda}{\partial p_k} \Lambda^{i-1} \frac{\partial q^+}{\partial p_l} + \Psi^+ \frac{\partial \Lambda}{\partial p_l} \Lambda^{i-1} \frac{\partial q^+}{\partial p_k} \right) \\
&+ i(i-1) \Psi^+ \frac{\partial \Lambda}{\partial p_k} \frac{\partial \Lambda}{\partial p_l} \Lambda^{i-2} q^+ \\
&+ \frac{\partial^2 \Psi^-}{\partial p_k} \Lambda^{N-i} q^- + \Psi^- \Lambda^{N-i} \frac{\partial^2 q^-}{\partial p_k \partial p_l} + \frac{\partial \Psi^-}{\partial p_k} \Lambda^{N-i} \frac{\partial q^-}{\partial p_l} + \frac{\partial \Psi^-}{\partial p_l} \Lambda^{N-i} \frac{\partial q^-}{\partial p_k} \\
&+ (N-i) \left(\frac{\partial \Psi^-}{\partial p_k} \frac{\partial \Lambda}{\partial p_l} \Lambda^{N-i-1} q^- + \frac{\partial \Psi^-}{\partial p_l} \frac{\partial \Lambda}{\partial p_k} \Lambda^{N-i-1} q^- \right. \\
&+ \left. \Psi^- \frac{\partial \Lambda}{\partial p_k} \Lambda^{N-i-1} \frac{\partial q^-}{\partial p_l} + \Psi^- \frac{\partial \Lambda}{\partial p_l} \Lambda^{N-i-1} \frac{\partial q^-}{\partial p_k} \right) \\
&+ (N-i-1)(N-i-2) \Psi^- \frac{\partial \Lambda}{\partial p_k} \frac{\partial \Lambda}{\partial p_l} \Lambda^{N-i-2} q^-
\end{aligned} \tag{D.23}$$

Bibliography

- [1] ABEDIN-NASAB, M. H., BASTAWROUS, M. V., AND HUSSEIN, M. I. Explicit dispersion relation for strongly nonlinear flexural waves using the homotopy analysis method. *Nonlinear Dynamics* 99, 1 (2020), 737–752.
- [2] ABLITZER, F., PÉZERAT, C., LASCOUR, B., AND BROCAIL, J. Identification of the flexural stiffness parameters of an orthotropic plate from the local dynamic equilibrium without a priori knowledge of the principal directions. *Journal of Sound and Vibration* 404 (2017), 31–46.
- [3] AHMAD, Z. A. B., VIVAR-PEREZ, J. M., AND GABBERT, U. Semi-analytical finite element method for modeling of lamb wave propagation. *CEAS Aeronautical Journal* 4, 1 (2013), 21–33.
- [4] AKROUT, S. *Comportement dynamique déterministe et large bande des structures guidées*. PhD thesis, École Centrale de Lyon, 2005.
- [5] AMSALLEM, D., AND FARHAT, C. Interpolation Method for Adapting Reduced-Order Models and Application to Aeroelasticity. *AIAA Journal* 46, 7 (jul 2008), 1803–1813.
- [6] AMSALLEM, D., AND FARHAT, C. An Online Method for Interpolating Linear Parametric Reduced-Order Models. *SIAM Journal on Scientific Computing* 33, 5 (2011), 2169–2198.
- [7] ANDREASSEN, E., CHANG, H. R., RUZZENE, M., AND JENSEN, J. S. Optimization of directional elastic energy propagation. *Journal of Sound and Vibration* 379 (2016), 53–70.
- [8] ANDREASSEN, E., MANKTELOW, K., AND RUZZENE, M. Directional bending wave propagation in periodically perforated plates. *Journal of Sound and Vibration* 335 (2015), 187–203.
- [9] ANDRIANOV, I. V., DANISHEVSKYY, V., AND AWREJCWICZ, J. *Linear and Nonlinear Waves in Microstructured Solids*. CRC Press, mar 2021.

- [10] ASHARI, A., AND STEPHEN, N. On wave propagation in repetitive structures: Two forms of transfer matrix. *Journal of Sound and Vibration* 439 (2019), 99–112.
- [11] ASRIH, K., VERMAUT, M., NAETS, F., AND DESMET, W. Topology optimization of a high-speed cutting mechanism. In *Proceedings of ISMA2018-USD2018* (2018), pp. 2567–2576.
- [12] BADEAU, R., DAVID, B., AND RICHARD, G. A new perturbation analysis for signal enumeration in rotational invariance techniques. *IEEE Transactions on Signal Processing* 54, 2 (2006), 450–458.
- [13] BAI, Z., AND LI, R.-C. Structure-Preserving Model Reduction Using a Krylov Subspace Projection Formulation. *Communications in Mathematical Sciences* 3, 2 (2005), 179–199.
- [14] BAI, Z., AND SU, Y. SOAR: A Second-order Arnoldi Method for the Solution of the Quadratic Eigenvalue Problem. *SIAM Journal on Matrix Analysis and Applications* 26, 3 (jan 2005), 640–659.
- [15] BALMÈS, E. Parametric families of reduced finite element models. Theory and applications. *Mechanical Systems and Signal Processing* 10, 4 (1996), 381–394.
- [16] BARDELL, N. S., AND MEAD, D. J. Free vibration of an orthogonally stiffened cylindrical shell, part I: Discrete line simple supports. *Journal of Sound and Vibration* 134, 1 (1989), 29–54.
- [17] BELI, D., MENCIK, J., AND ARRUDA, J. R. F. A projection-based model reduction strategy for the wave and vibration analysis of rotating periodic structures. *Computational Mechanics* 62, 6 (2018), 1511–1528.
- [18] BENMEDDOUR, F., TREYSSÈDE, F., AND LAGUERRE, L. Numerical modeling of guided wave interaction with non-axisymmetric cracks in elastic cylinders. *International Journal of Solids and Structures* 48, 5 (2011), 764–774.
- [19] BENNER, P., AND FENG, L. A Robust Algorithm for Parametric Model Order Reduction Based on Implicit Moment Matching. *Reduced Order Methods for Modeling and Computational Reduction* (2014), 159–185.
- [20] BENNER, P., GUGERCIN, S., AND WILLCOX, K. A Survey of Projection-Based Model Reduction Methods for Parametric Dynamical Systems. *SIAM Review* 57, 4 (2015), 483–531.

- [21] BERTHAUT, J., ICHCHOU, M. N., AND JEZEQUEL, L. K-space identification of apparent structural behaviour. *Journal of Sound and Vibration* 280, 3-5 (2005), 1125–1131.
- [22] BESSELINK, B., TABAK, U., LUTOWSKA, A., VAN DE WOUW, N., NIJMEIJER, H., RIXEN, D. J., HOCHSTENBACH, M. E., AND SCHILDERS, W. H. A comparison of model reduction techniques from structural dynamics, numerical mathematics and systems and control. *Journal of Sound and Vibration* 332, 19 (2013), 4403–4422.
- [23] BLAUNSTEIN, N. Theoretical aspects of wave propagation in random media based on quantum and statistical field theory. *Progress In Electromagnetics Research* 47 (2004), 135–191.
- [24] BLOCH, F. Über die Quantenmechanik der Elektronen in Kristallgittern. *Zeitschrift für Physik* 52, 7 (1929), 555–600.
- [25] BOGGS, P. T., AND TOLLE, J. W. Sequential Quadratic Programming. *Acta Numerica* 4 (jan 1995), 1–51.
- [26] BOTTOU, L., CURTIS, F. E., AND NOCEDAL, J. Optimization methods for large-scale machine learning. *SIAM Review* 60, 2 (2018), 223–311.
- [27] BOUCHOUCHA, F., ICHCHOU, M. N., AND HADDAR, M. Stochastic wave finite element method in uncertain elastic media through the second order perturbation. *Journal of Applied Mechanics and Technical Physics* 58, 2 (2017), 362–370.
- [28] BOUKADIA, R. F. *Projet VIPER: modélisation de structures périodiques dans le cadre d'applications vibroacoustiques*. Master thesis, École Centrale de Lyon, 2016.
- [29] BOUKADIA, R. F., CLAEYS, C., DROZ, C., ICHCHOU, M., AND DECKERS, E. Model order reduction in unit cell modeling and its application to complex structures. In *Proceedings of ISMA2018-USD2018* (Leuven, 2018).
- [30] BOUKADIA, R. F., DECKERS, E., CLAEYS, C., ICHCHOU, M., AND DESMET, W. A rational Krylov subspace method for the unit cell modeling of 2D infinite periodic media. In *Proceedings of ISMA 2020 - International Conference on Noise and Vibration Engineering and USD 2020 - International Conference on Uncertainty in Structural Dynamics* (2020), pp. 1915–1924.
- [31] BOUKADIA, R. F., DECKERS, E., CLAEYS, C., ICHCHOU, M., AND DESMET, W. A wave-based optimization framework for 1D and 2D

- periodic structures. *Mechanical Systems and Signal Processing* 139 (2020), 106603.
- [32] BOUKADIA, R. F., DROZ, C., ICHCHOU, M. N., AND DESMET, W. A Bloch wave reduction scheme for ultrafast band diagram and dynamic response computation in periodic structures. *Finite Elements in Analysis and Design* (2018).
- [33] BOUTIN, C., FOSSAT, P., DROZ, C., AND ICHCHOU, M. Dynamics of ribbed plates with inner resonance: Analytical homogenized models and experimental validation. *European Journal of Mechanics, A/Solids* 79, June 2019 (2020), 103838.
- [34] BRILLOUIN, L. *Wave propagation in periodic structures : Electric filters and crystal lattices.*, second ed. Dover publications, New York, 1953.
- [35] BROWN, A. L., AND VAN KAMP, I. WHO environmental noise guidelines for the European region: A systematic review of transport noise interventions and their impacts on health. *International Journal of Environmental Research and Public Health* 14, 8 (2017), 1–44.
- [36] CAI, Y., AND QIAN, J. On Some Inverse Eigenvalue Problems of Quadratic Palindromic Systems.
- [37] CAMPANA, M. A., OUISSE, M., SADOULET-REBOUL, E., RUZZENE, M., NEILD, S., AND SCARPA, F. Impact of non-linear resonators in periodic structures using a perturbation approach. *Mechanical Systems and Signal Processing* 135 (2020), 106408.
- [38] CARRIERE, R., AND MOSES, R. L. High resolution radar target modeling using a modified Prony estimator. *IEEE Transactions on Antennas and Propagation* 40, 1 (jan 1992), 13–18.
- [39] CELIK, M. *Asymptotic Waveform Evaluation*. Springer US, Boston, MA, 2002, pp. 119–152.
- [40] CHARDON, G., LEBLANC, A., AND DAUDET, L. Plate impulse response spatial interpolation with sub-Nyquist sampling. *Journal of Sound and Vibration* 330, 23 (2011), 5678–5689.
- [41] CHIPROUT, E., AND NAKHLA, M. S. *Asymptotic waveform Evaluation*. Springer US, Boston, MA, 1994, pp. 15–39.
- [42] CHRISTEN, J.-L., ICHCHOU, M., ZINE, A., AND TROCLET, B. Wave Finite Element Formulation of the Acoustic Transmission Through Complex Infinite Plates. *Acta Acustica united with Acustica* 102, 6 (2016), 984–991.

- [43] CLAEYS, C., ROCHA DE MELO FILHO, N. G., VAN BELLE, L., DECKERS, E., AND DESMET, W. Design and validation of metamaterials for multiple structural stop bands in waveguides. *Extreme Mechanics Letters* 12 (2017), 7–22.
- [44] COATLÉVEN, J. *Analyse mathématique et numérique de quelques problèmes d'ondes en milieu périodique*. PhD thesis, École Polytechnique, 2011.
- [45] COATLÉVEN, J., AND JOLY, P. Operator factorization for multiple-scattering problems and an application to periodic media. *Communications in Computational Physics* 11, 2 (2012), 303–318.
- [46] COLEMAN, T. F., AND VERMA, A. A preconditioned conjugate gradient approach to linear equality constrained minimization. *Computational Optimization and Applications* 20, 1 (2001), 61–72.
- [47] COLLET, M., OUISSE, M., RUZZENE, M., AND ICHCHOU, M. Floquet–Bloch decomposition for the computation of dispersion of two-dimensional periodic, damped mechanical systems. *International Journal of Solids and Structures* 48, 20 (oct 2011), 2837–2848.
- [48] COTONI, V., LANGLEY, R. S., AND SHORTER, P. J. A statistical energy analysis subsystem formulation using finite element and periodic structure theory. *Journal of Sound and Vibration* 318, 4-5 (2008), 1077–1108.
- [49] CRAIG, R. R., AND BAMPTON, M. C. C. Coupling of substructures for dynamic analyses. *AIAA Journal* 6, 7 (jul 1968), 1313–1319.
- [50] DAMLJANOVIĆ, V., AND WEAVER, R. L. Forced response of a cylindrical waveguide with simulation of the wavenumber extraction problem. *The Journal of the Acoustical Society of America* 115, 4 (2004), 1582–1591.
- [51] DANIEL, L., SIONG, O. C., CHAY, L. S., LEE, K. H., AND WHITE, J. A multiparameter moment-matching model-reduction approach for generating geometrically parameterized interconnect performance models. *IEEE Transactions on Computer-Aided Design of Integrated Circuits and Systems* 23, 5 (2004), 678–693.
- [52] DASTOUR, H., AND LIAO, W. A fourth-order optimal finite difference scheme for the Helmholtz equation with PML. *Computers and Mathematics with Applications* 78, 6 (2019), 2147–2165.
- [53] DATTA, S. K., BRATTON, R. L., CHAKRABORTY, T., AND SHAH, A. H. Wave propagation in laminated composite plates. *Journal of the Acoustical Society of America* 83, 6 (1988), 2020–2026.

- [54] DAUPHIN, Y., PASCANU, R., GULCEHRE, C., CHO, K., GANGULI, S., AND BENGIO, Y. Identifying and attacking the saddle point problem in high-dimensional non-convex optimization. 1–9.
- [55] DAUPHIN, Y. N., DE VRIES, H., AND BENGIO, Y. Equilibrated adaptive learning rates for non-convex optimization. *Advances in Neural Information Processing Systems 2015-Janua* (2015), 1504–1512.
- [56] DE MELO FILHO, N. G., CLAEYS, C., DECKERS, E., AND DESMET, W. Realisation of a thermoformed vibro-acoustic metamaterial for increased STL in acoustic resonance driven environments. *Applied Acoustics 156* (2019), 78–82.
- [57] DECKERS, E., JONCKHEERE, S., VAN BELLE, L., CLAEYS, C., AND DESMET, W. Prediction of transmission, reflection and absorption coefficients of periodic structures using a hybrid Wave Based – Finite Element unit cell method. *Journal of Computational Physics 356* (2018), 282–302.
- [58] DENIS, V., AND MENCIK, J. M. A wave-based optimization approach of curved joints for improved defect detection in waveguide assemblies. *Journal of Sound and Vibration 465* (2020), 115003.
- [59] DROZ, C., BOUKADIA, R., DECKERS, E., AND DESMET, W. Sub-Wavelength Damage Detectability Assessment in Periodic Assemblies Using a Bloch Modelling Framework. In *XI International Conference on Structural Dynamics* (2020), pp. 870–877.
- [60] DROZ, C., LAINÉ, J. P., ICHCHOU, M. N., AND INQUIÉTÉ, G. A reduced formulation for the free-wave propagation analysis in composite structures. *Composite Structures 113*, 1 (2014), 134–144.
- [61] DROZ, C., ROBIN, O., ICHCHOU, M., AND ATALLA, N. Improving sound transmission loss at ring frequency of a curved panel using tunable 3D-printed small-scale resonators. *The Journal of the Acoustical Society of America 145*, 1 (2019), EL72–EL78.
- [62] DROZ, C., ZHOU, C., ICHCHOU, M. N., AND LAINÉ, J. P. A hybrid wave-mode formulation for the vibro-acoustic analysis of 2D periodic structures. *Journal of Sound and Vibration 363* (2016), 285–302.
- [63] DUDA, P. Finite element method formulation in polar coordinates for transient heat conduction problems. *Journal of Thermal Science 25*, 2 (2016), 188–194.

- [64] DUHAMEL, D., MACE, B. R., AND BRENNAN, M. J. Finite element analysis of the vibrations of waveguides and periodic structures. *Journal of Sound and Vibration* 294, 1-2 (2006), 205–220.
- [65] EGE, K., ROOZEN, N. B., LECLÈRE, Q., AND RINALDI, R. G. Assessment of the apparent bending stiffness and damping of multilayer plates; modelling and experiment. *Journal of Sound and Vibration* 426 (2018), 129–149.
- [66] ERRICO, F., ICHCHOU, M., FRANCO, F., DE ROSA, S., BAREILLE, O., AND DROZ, C. Schemes for the sound transmission of flat, curved and axisymmetric structures excited by aerodynamic and acoustic sources. *Journal of Sound and Vibration* 456 (2019), 221–238.
- [67] FAN, Y., COLLET, M., ICHCHOU, M., LI, L., BAREILLE, O., AND DIMITRIJEVIC, Z. Energy flow prediction in built-up structures through a hybrid finite element/wave and finite element approach. *Mechanical Systems and Signal Processing* 66-67 (2016), 137–158.
- [68] FARLE, O., HILL, V., INGELSTROM, P., AND DYCZIJ-EDLINGER, R. Multi-parameter polynomial order reduction of linear finite element models. *Mathematical and Computer Modelling of Dynamical Systems* 14, 5 (2008), 421–434.
- [69] FELDMANN, P., AND FREUND, R. W. Efficient Linear Circuit Analysis by Padé Approximation via the Lanczos Process. *IEEE Transactions on Computer-Aided Design of Integrated Circuits and Systems* 14, 5 (1995), 639–649.
- [70] FENG, S., AND HALTERMAN, K. Coherent perfect absorption in epsilon-near-zero metamaterials. *Physical Review B - Condensed Matter and Materials Physics* 86, 16 (2012), 10–15.
- [71] FEPPON, F. *Optimisation topologique de systèmes multiphysiques*. Theses, Université Paris-Saclay, 2019.
- [72] FIELDING, L. M., VILLAÇA, S. F., AND GARCIA, L. F. Energetic finite differences with arbitrary meshes applied to plate-bending problems. *Applied Mathematical Modelling* 21, 11 (1997), 691–698.
- [73] FISHLER, E., AND POOR, H. V. Estimation of the number of sources in unbalanced arrays via information theoretic criteria. *IEEE Transactions on Signal Processing* 53, 9 (2005), 3543–3553.
- [74] FLATTE, S. Calculations of wave propagation through statistical random media, with and without a waveguide. *Optics Express* 10, 16 (2002), 777.

- [75] FLISS, S. *Analyse mathématique et numérique de problèmes de propagation des ondes dans des milieux périodiques infinis localement perturbés*. PhD thesis, École Polytechnique, 2010.
- [76] FLOQUET, G. Sur les équations différentielles linéaires à coefficients périodiques. *Annales scientifiques de l'École Normale Supérieure 2e série*, (1883), 47–88.
- [77] FOSSAT, P., BOUTIN, C., AND ICHCHOU, M. Homogenized bending model of a periodic ribbed plate with inner resonance. *Procedia Engineering 199* (2017), 1435–1440.
- [78] FOSSAT, P., BOUTIN, C., AND ICHCHOU, M. Dynamics of periodic ribbed plates with inner resonance: Analytical homogenized model and dispersion features. *International Journal of Solids and Structures 152-153* (2018), 85–103.
- [79] FRAZIER, M. J., AND HUSSEIN, M. I. Théorème de Bloch généralisé pour les métamatériaux visqueux : dispersion et propriétés effectives fondées sur les fréquences et nombres d'onde simultanément complexes. *Comptes Rendus Physique 17*, 5 (2016), 565–577.
- [80] FRISWELL, M. I., AND ADHIKARI, S. Derivatives of complex eigenvectors using Nelson's method. *AIAA Journal 38*, January (2000), 2355–2357.
- [81] GIANNAKOGLU, K. C., AND PAPADIMITRIOU, D. I. Adjoint Methods for Gradient – and Hessian – Based Aerodynamic Shape Optimization. *Evolutionary Methods for Design, Optimization and Control* (2007).
- [82] GRAS, T., HAMDI, M. A., BEN TAHAR, M., TANNEAU, O., AND BEAUBATIE, L. On a coupling between the Finite Element (FE) and the Wave Finite Element (WFE) method to study the effect of a local heterogeneity within a railway track. *Journal of Sound and Vibration 429* (2018), 45–62.
- [83] GUYAN, R. J. Reduction of stiffness and mass matrices. *AIAA Journal 3*, 2 (feb 1965), 380–380.
- [84] HAMMER, M. S., SWINBURN, T. K., AND NEITZEL, R. L. Environmental noise pollution in the United States: Developing an effective public health response. *Environmental Health Perspectives 122*, 2 (2014), 115–119.
- [85] HEDAYATRASAA, S., ABHARY, K., UDDIN, M., AND NG, C. T. Optimum design of phononic crystal perforated plate structures for widest bandgap of fundamental guided wave modes and maximized in-plane stiffness. *Journal of the Mechanics and Physics of Solids 89* (2016), 31–58.

- [86] HEDAYATRASA, S., KERSEMANS, M., ABHARY, K., UDDIN, M., GUEST, J. K., AND VAN PAEPEGEM, W. Maximizing bandgap width and in-plane stiffness of porous phononic plates for tailoring flexural guided waves: Topology optimization and experimental validation. *Mechanics of Materials* 105 (2017), 188–203.
- [87] HEYLIGER, P. R. Simple cylindrical and spherical finite elements. *International Journal for Numerical Methods in Engineering* 112, 13 (2017), 2174–2182.
- [88] HOUGH, P. D., AND VAVASIS, S. A. Complete orthogonal decomposition for weighted least squares. *SIAM Journal on Matrix Analysis and Applications* 18, 2 (1997), 369–392.
- [89] HUANG, T.-M., LIN, W.-W., AND QIAN, J. Structure-Preserving Algorithms for Palindromic Quadratic Eigenvalue Problems Arising from Vibration of Fast Trains. *SIAM Journal on Matrix Analysis and Applications* 30, 4 (2009), 1566–1592.
- [90] HUSSEIN, M. I., AND KHAJEHTOURIAN, R. Nonlinear Bloch waves and balance between hardening and softening dispersion. *Proceedings of the Royal Society A: Mathematical, Physical and Engineering Sciences* 474, 2217 (2018).
- [91] IBRAHIM, A. M., MAREI, M. I., MEKHAMER, S. F., AND MANSOUR, M. M. An artificial neural network based protection approach using total least square estimation of signal parameters via the rotational invariance technique for flexible AC transmission system compensated transmission lines. *Electric Power Components and Systems* 39, 1 (2011), 64–79.
- [92] ICHCHOU, M. N., AKROUT, S., AND MENCIK, J. M. Guided waves group and energy velocities via finite elements. *Journal of Sound and Vibration* 305, 4-5 (2007), 931–944.
- [93] ICHCHOU, M. N., BOUCHOUCHA, F., BEN SOUF, M. A., DESSOMBZ, O., AND HADDAR, M. Stochastic wave finite element for random periodic media through first-order perturbation. *Computer Methods in Applied Mechanics and Engineering* 200, 41-44 (2011), 2805–2813.
- [94] ITO, S.-I., MATSUDA, T., AND MIYATAKE, Y. Adjoint-based exact Hessian computation. *BIT Numerical Mathematics* (2021).
- [95] JOLY, P., LI, J., AND FLISS, S. Exact Boundary Conditions for Periodic Waveguides Containing a Local Perturbation. *Commun. Comput. Phys* 1, 6 (2006), 945–973.

- [96] JUNYI, L., AND BALINT, D. S. An inverse method to determine the dispersion curves of periodic structures based on wave superposition. *Journal of Sound and Vibration* 350 (2015), 41–72.
- [97] KAHN, M. H. Effect of the numerical rank of the coefficient matrix on the performance of the Kumaresan-Tufts Prony method. *Chemometrics and Intelligent Laboratory Systems* 16, 1 (1992), 17–23.
- [98] KHAJEHTOURIAN, R., AND HUSSEIN, M. I. Dispersion characteristics of a nonlinear elastic metamaterial. *AIP Advances* 4, 12 (2014).
- [99] KHELIF, A., CHOUJAA, A., DJAFARI-ROUHANI, B., WILM, M., BALLANDRAS, S., AND LAUDE, V. Trapping and guiding of acoustic waves by defect modes in a full-band-gap ultrasonic crystal. *Physical Review B - Condensed Matter and Materials Physics* 68, 21 (2003), 1–4.
- [100] KOCATÜRK, T., AND ALTINTAS, G. Determination of the steady state response of viscoelastically point-supported rectangular specially orthotropic plates by an energy-based finite difference method. *Journal of Sound and Vibration* 267, 5 (2003), 1143–1156.
- [101] KOUTSOVASILIS, P., AND BEITELSCHMIDT, M. Comparison of model reduction techniques for large mechanical systems : AA study on an elastic rod. *Multibody System Dynamics* 20, 2 (2008), 111–128.
- [102] KRATTIGER, D., AND HUSSEIN, M. I. Bloch mode synthesis: Ultrafast methodology for elastic band-structure calculations. *Physical Review E - Statistical, Nonlinear, and Soft Matter Physics* 90, 6 (2014), 1–10.
- [103] KRATTIGER, D., AND HUSSEIN, M. I. Generalized Bloch mode synthesis for accelerated calculation of elastic band structures. *Journal of Computational Physics* 357 (2018), 183–205.
- [104] KRYLOV, A. De la résolution numérique de l'équation servant à déterminer dans des questions de mécanique appliquée les fréquences de petites oscillations des systèmes matériels. *Uspekhi Mat. Nauk* 65, 3(393) (2010), 201–202.
- [105] KUDELA, P., RADZIEŃSKI, M., AND OSTACHOWICZ, W. Identification of cracks in thin-walled structures by means of wavenumber filtering. *Mechanical Systems and Signal Processing* 50-51 (2015), 456–466.
- [106] KULLAA, J. Bayesian virtual sensing in structural dynamics. *Mechanical Systems and Signal Processing* 115 (2019), 497–513.

- [107] KULLAA, J. Robust damage detection in the time domain using Bayesian virtual sensing with noise reduction and environmental effect elimination capabilities. *Journal of Sound and Vibration* 473 (2020), 115232.
- [108] KUMARESAN, R., AND TUFTS, D. W. Estimating the Parameters of Exponentially Damped Sinusoids and Pole-Zero Modeling in Noise. *IEEE Transactions on Acoustics, Speech, and Signal Processing* 30, 6 (1982), 833–840.
- [109] LANGTANGEN, H. P., AND LINGE, S. *Finite Difference Computing with PDEs*, vol. 16 of *Texts in Computational Science and Engineering*. Springer International Publishing, Cham, 2017.
- [110] LARKIN, P. J. Basic Principles. In *Infrared and Raman Spectroscopy*. Elsevier, 2018, pp. 7–28.
- [111] LARKIN, P. J. *Illustrated IR and Raman Spectra Demonstrating Important Functional Groups*. 2018.
- [112] LARSON, M. G., AND BENGTSON, F. *The Finite Element Method: Theory, Implementation, and Applications*, vol. 10 of *Texts in Computational Science and Engineering*. Springer Berlin Heidelberg, Berlin, Heidelberg, 2013.
- [113] LECLÈRE, Q., ABLITZER, F., AND PÉZERAT, C. Practical implementation of the corrected force analysis technique to identify the structural parameter and load distributions. *Journal of Sound and Vibration* 351 (2015), 106–118.
- [114] LEE, Y. P., RHEE, J. Y., YOO, Y. J., AND KIM, K. W. *Metamaterials for Perfect Absorption*, vol. 236 of *Springer Series in Materials Science*. Springer Singapore, Singapore, 2016.
- [115] LEFEBVRE, T., DE BELIE, F., AND CREVECOEUR, G. A Radial Basis Function based Optimization Algorithm with Regular Simplex set geometry in Ellipsoidal Trust-Regions.
- [116] LI, L., HU, Y., AND WANG, X. Harmonic response calculation of viscoelastic structures using classical normal modes: An iterative method. *Computers and Structures* 133 (2014), 39–50.
- [117] LI, W., LIU, Y., YANG, G., HUANG, C., AND LIU, Q. H. Preprocessing for characteristic mode tracking based on the correlation. *International Journal of Numerical Modelling: Electronic Networks, Devices and Fields* 33, 6 (2020), 1–7.

- [118] LIANG, J., XU, Y., BAO, C., QUAN, Y., AND JI, H. Barzilai–Borwein-based adaptive learning rate for deep learning. *Pattern Recognition Letters* 128 (2019), 197–203.
- [119] LIAO, B.-S., BAI, Z., AND GAO, W. The important modes of subsystems: A moment-matching approach. *International Journal for Numerical Methods in Engineering* 70, 13 (jun 2007), 1581–1597.
- [120] LIAPOUNOV, A. M. Problème général de la stabilité du mouvement. *Annales de la faculté des sciences de Toulouse* 2, 9 (1903), 203–474.
- [121] LIU, Z., RUMPLER, R., AND FENG, L. Broadband locally resonant metamaterial sandwich plate for improved noise insulation in the coincidence region. *Composite Structures* 200, April (2018), 165–172.
- [122] LU, D., SU, Y., AND BAI, Z. Stability analysis of the two-level orthogonal Arnoldi procedure. *SIAM Journal on Matrix Analysis and Applications* 37, 1 (2016), 195–214.
- [123] LU, J., TANG, J., APLEY, D. W., ZHAN, Z., AND CHEN, W. A mode tracking method in modal metamodeling for structures with clustered eigenvalues. *Computer Methods in Applied Mechanics and Engineering* 369 (2020), 113174.
- [124] LUDICK, D. J., TONDER, J. V., AND JAKOBUS, U. A hybrid tracking algorithm for characteristic mode analysis. *Proceedings - 2014 International Conference on Electromagnetics in Advanced Applications, ICEAA 2014* (2014), 455–458.
- [125] MACE, B. R., AND MANCONI, E. Modelling wave propagation in two-dimensional structures using finite element analysis. *Journal of Sound and Vibration* 318, 4-5 (2008), 884–902.
- [126] MACKEY, D. S., MACKEY, N., MEHL, C., AND MEHRMANN, V. Numerical methods for palindromic eigenvalue problems: Computing the anti-triangular Schur form. *Numerical Linear Algebra with Applications* 16, 1 (2009), 63–86.
- [127] MAGLIACANO, D., ASHANI, S., OUISSE, M., DECKERS, E., PETRONE, G., DESMET, W., AND DE ROSA, S. Formulation and validation of the shift cell technique for acoustic applications of poro-elastic materials described by the Biot theory. *Mechanical Systems and Signal Processing* 147 (2021), 107089.
- [128] MANCONI, E., SOROKIN, S., AND GARZIERA, R. Wave propagation in pipes with helical patterns. *COMPADYN 2017 - Proceedings of the*

- 6th International Conference on Computational Methods in Structural Dynamics and Earthquake Engineering 1* (2017), 529–536.
- [129] MANCONI, E., SOROKIN, S., AND GARZIERA, R. Wave propagation in polar periodic structures using Floquet theory and finite element analysis. *COMPADYN Proceedings 2* (2019), 3448–3456.
- [130] MARCHETTI, F., ROOZEN, N. B., SEGERS, J., EGE, K., KERSEMANS, M., AND LECLÈRE, Q. Experimental methodology to assess the dynamic equivalent stiffness properties of elliptical orthotropic plates. *Journal of Sound and Vibration 495* (2021), 115897.
- [131] MARGERIT, P., LEBÉE, A., CARON, J. F., AND BOUTILLON, X. High Resolution Wavenumber Analysis (HRWA) for the mechanical characterisation of viscoelastic beams. *Journal of Sound and Vibration 433* (2018), 198–211.
- [132] MARGERIT, P., LEBÉE, A., CARON, J. F., EGE, K., AND BOUTILLON, X. The High-Resolution Wavevector Analysis for the characterization of the dynamic response of composite plates. *Journal of Sound and Vibration 458* (2019), 177–196.
- [133] MARTINI, A., MARCHI, L., FRANCESCHETTI, M., AND MASSA, A. Stochastic ray propagation in stratified random lattices-Comparative assessment of two mathematical approaches. *Progress In Electromagnetics Research 71* (2007), 159–171.
- [134] MAURIN, F., CLAEYS, C., DECKERS, E., AND DESMET, W. Probability that a band-gap extremum is located on the irreducible Brillouin-zone contour for the 17 different plane crystallographic lattices. *International Journal of Solids and Structures 135* (2018), 26–36.
- [135] MAURIN, F., CLAEYS, C., VAN BELLE, L., AND DESMET, W. Bloch theorem with revised boundary conditions applied to glide, screw and rotational symmetric structures. *Computer Methods in Applied Mechanics and Engineering 318* (2017), 497–513.
- [136] MCCOMBS, J. R., AND STATHOPOULOS, A. Iterative Validation of Eigensolvers: A Scheme for Improving the Reliability of Hermitian Eigenvalue Solvers. *SIAM Journal on Scientific Computing 28*, 6 (jan 2006), 2337–2358.
- [137] MCDANIEL, J. G., DUPONT, P., AND SALVINO, L. A wave approach to estimating frequency-dependent damping under transient loading. *Journal of Sound and Vibration 231*, 2 (2000), 433–449.

- [138] MCDANIEL, J. G., AND SHEPARD, W. S. Estimation of structural wave numbers from spatially sparse response measurements. *The Journal of the Acoustical Society of America* 108, 4 (2002), 1674–1682.
- [139] MEAD, D. J. Free wave propagation in periodically supported, infinite beams. *Journal of Sound and Vibration* 11, 2 (1970), 181–197.
- [140] MEAD, D. J. Vibration Response and Wave Propagation in Periodic Structures. *Journal of Engineering for Industry* 93, 3 (aug 1971), 783.
- [141] MEAD, D. J. A general theory of harmonic wave propagation in linear periodic systems with multiple coupling. *Journal of Sound and Vibration* 27, 2 (1973), 235–260.
- [142] MEAD, D. J. Wave propagation and natural modes in periodic systems: II. Multi-coupled systems, with and without damping. *Journal of Sound and Vibration* 40, 1 (1975), 19–39.
- [143] MEAD, D. J. The forced vibration of one-dimensional multi-coupled periodic structures: An application to finite element analysis. *Journal of Sound and Vibration* 319, 1-2 (2009), 282–304.
- [144] MENCİK, J. M. On the low- and mid-frequency forced response of elastic structures using wave finite elements with one-dimensional propagation. *Computers and Structures* 88, 11-12 (2010), 674–689.
- [145] MENCİK, J. M., AND ICHCHOU, M. N. Multi-mode propagation and diffusion in structures through finite elements. *European Journal of Mechanics, A/Solids* 24, 5 (2005), 877–898.
- [146] MEZZANI, F., REZAEI, A. S., AND CARCATERRA, A. Periodic and Random Long-Range Interactions in Metamaterials. In *Proceedings of MEDYNA2020, 3rd Euro-Mediterranean Conference on Structural Dynamics and Vibroacoustics* (Napoli, 2020), pp. 17–20.
- [147] MITROU, G., FERGUSON, N., AND RENNO, J. Wave transmission through two-dimensional structures by the hybrid FE/WFE approach. *Journal of Sound and Vibration* 389 (2017), 484–501.
- [148] MORENO-GARCÍA, P., LOPES, H., AND ARAÚJO DOS SANTOS, J. V. Application of higher order finite differences to damage localization in laminated composite plates. *Composite Structures* 156 (2016), 385–392.
- [149] MÜNZEL, T., SØRENSEN, M., GORI, T., SCHMIDT, F. P., RAO, X., BROOK, J., CHEN, L. C., BROOK, R. D., AND RAJAGOPALAN, S. Environmental stressors and cardio-metabolic disease: Part I—epidemiologic evidence supporting a role for noise and air pollution and

- effects of mitigation strategies. *European Heart Journal* 38, 8 (2017), 550–556.
- [150] NELSON, R. B. Simplified calculation of eigenvector derivatives. *AIAA Journal* 14, 9 (1976), 1201–1205.
- [151] NOCEDAL, J., AND WRIGHT, S. *Numerical optimization, series in operations research and financial engineering*. 2006.
- [152] OÑATE, E. *Structural Analysis with the Finite Element Method*, vol. 1 of *Lecture Notes on Numerical Methods in Engineering and Sciences*. Springer Netherlands, Dordrecht, 2009.
- [153] PAL, R. K., SCHAEFFER, M., AND RUZZENE, M. Helical edge states and topological phase transitions in phononic systems using bi-layered lattices. *Journal of Applied Physics* 119, 8 (2016).
- [154] PANAGIOTOPOULOS, D., DECKERS, E., AND DESMET, W. Krylov subspaces recycling based model order reduction for acoustic BEM systems and an error estimator. *Computer Methods in Applied Mechanics and Engineering* 359 (2020), 112755.
- [155] PARRINELLO, A., AND GHIRINGHELLI, G. L. Transfer matrix representation for periodic planar media. *Journal of Sound and Vibration* 371 (2016), 196–209.
- [156] PARRINELLO, A., GHIRINGHELLI, G. L., AND ATALLA, N. Generalized Transfer Matrix Method for periodic planar media. *Journal of Sound and Vibration* 464 (2020), 114993.
- [157] PASCANU, R., DAUPHIN, Y. N., GANGULI, S., AND BENGIO, Y. On the saddle point problem for non-convex optimization.
- [158] PENG, W., AND NADARAJAH, S. Truncated-Newton Method with Adjoint-based Hessian-vector Product for Aerodynamic Shape Optimization Problems. In *AIAA Scitech 2020 Forum* (Reston, Virginia, jan 2020), American Institute of Aeronautics and Astronautics.
- [159] PILLAGE, L., AND ROHRER, R. Asymptotic waveform evaluation for timing analysis. *IEEE Transactions on Computer-Aided Design of Integrated Circuits and Systems* 9, 4 (apr 1990), 352–366.
- [160] RAMZI, L., CHIKHAOUI, K., BOUAZIZI, M.-L., AND BISHARAT, A. Robust 2D-Spatial Fourier Transform Identification of Wavenumber-Space Characteristics of a Composite Plate. In *Design and Modeling of Mechanical Systems - IV* (Cham, 2020), N. Aifaoui, Z. Affi, M. S. Abbes,

- L. Walha, M. Haddar, L. Romdhane, A. Benamara, M. Chouchane, and F. Chaari, Eds., Springer International Publishing, pp. 271–281.
- [161] RHAZI, D., AND ATALLA, N. A simple method to account for size effects in the transfer matrix method. *The Journal of the Acoustical Society of America* 127, 2 (2010), EL30–EL36.
- [162] ROGGE, M. D., AND JOHNSTON, P. H. Wavenumber imaging for damage detection and measurement. *AIP Conference Proceedings* 1430, 31 (2012), 761–768.
- [163] ROY, A., PAULRAJ, A., AND KAILATH, T. Estimation of Signal Parameters Via Rotational Invariance Techniques-Esprit. *Proceedings - IEEE Military Communications Conference* (1986).
- [164] ROY, O., AND VETTERLI, M. The effective rank: A measure of effective dimensionality. *European Signal Processing Conference, Eusipco* (2007), 606–610.
- [165] ROY, R., AND KAILATH, T. ESPRIT-estimation of signal parameters via rotational invariance techniques. *IEEE Transactions on Acoustics, Speech, and Signal Processing* 37, 7 (jul 1989), 984–995.
- [166] ROY, R., PAULRAJ, A., AND KAILATH, T. ESPRIT—A subspace rotation approach to estimation of parameters of cisoids in noise. *IEEE Transactions on Acoustics, Speech, and Signal Processing* 34, 5 (oct 1986), 1340–1342.
- [167] RUMPLER, R. Padé approximants for multivariate reduced order models. In *Proceedings of MEDYNA2020, 3rd Euro-Mediterranean Conference on Structural Dynamics and Vibroacoustics* (Napoli, 2020).
- [168] RUMPLER, R., AND GÖRANSSON, P. An assessment of two popular Padé-based approaches for fast frequency sweeps of time-harmonic finite element problems. *Proceedings of Meetings on Acoustics* 30, 1 (2017).
- [169] RUZEK, M., GUYADER, J.-L., AND PEZERAT, C. Model selection for the equation of motion. In *Proceedings of MEDYNA2013, 1st Euro-Mediterranean Conference on Structural Dynamics and Vibroacoustics* (Marrakech, 2013), pp. 154–157.
- [170] SANGIULIANO, L., DECKERS, E., AND CLAEYS, C. Control of edge modes in finite vibro-acoustic resonant metamaterials. In *Proceedings of ISMA2018-USD2018* (2018).

- [171] SEIDLER, A. L., HEGEWALD, J., SCHUBERT, M., WEIHOFEN, V. M., WAGNER, M., DRÖGE, P., SWART, E., ZEEB, H., AND SEIDLER, A. The effect of aircraft, road, and railway traffic noise on stroke - results of a case-control study based on secondary data. *Noise and Health* 20, 95 (2018), 152–161.
- [172] SEPEHRI, S., JAFARI, H., MASHHADI, M. M., YAZDI, M. R. H., AND FAKHRABADI, M. M. S. Study of tunable locally resonant metamaterials: Effects of spider-web and snowflake hierarchies. *International Journal of Solids and Structures* 204-205 (2020), 81–95.
- [173] SHAH, A., AND DATTA, S. Harmonic waves in a periodically laminated medium. *International Journal of Solids and Structures* 18, 5 (1982), 397–410.
- [174] SHI, S., CHEN, C., AND PRATHER, D. W. Plane-wave expansion method for calculating band structure of photonic crystal slabs with perfectly matched layers. *J. Opt. Soc. Am. A* 21, 9 (sep 2004), 1769–1775.
- [175] SINGH, K. V., AND RAM, Y. M. Transcendental Eigenvalue Problem and Its Applications. *AIAA Journal* 40, 7 (jul 2002), 1402–1407.
- [176] SINGH, R. P., DROZ, C., ICHCHOU, M., FRANCO, F., BAREILLE, O., AND DE ROSA, S. Stochastic wave finite element quadratic formulation for periodic media: 1D and 2D. *Mechanical Systems and Signal Processing* 136 (2020), 106431.
- [177] SLONE, R. D., LEE, R., AND LEE, J. F. Well-Conditioned Asymptotic Waveform Evaluation for Finite Elements. *IEEE Transactions on Antennas and Propagation* 51, 9 (2003), 2442–2447.
- [178] SOROKIN, S., MANCONI, E., LEDET, L., AND GARZIERA, R. Wave propagation in helically orthotropic elastic cylindrical shells and lattices. *International Journal of Solids and Structures* 170 (2019), 11–21.
- [179] STANSFELD, S. A., AND MATHESON, M. P. Noise pollution: Non-auditory effects on health. *British Medical Bulletin* 68 (2003), 243–257.
- [180] STEIHAUG, T. The Conjugate Gradient Method and Trust Regions in Large Scale Optimization. *SIAM Journal on Numerical Analysis* 20, 3 (jun 1983), 626–637.
- [181] SUGINO, C., RUZZENE, M., AND ERTURK, A. Merging mechanical and electromechanical bandgaps in locally resonant metamaterials and metastructures. *Journal of the Mechanics and Physics of Solids* 116 (2018), 323–333.

- [182] SÜSSTRUNK, R., AND HUBER, S. D. Observation of phononic helical edge states in a mechanical topological insulator. *Science (New York, N.Y.)* 349, 6243 (jul 2015), 47–50.
- [183] TANG, J., NI, W. M., AND WANG, W. L. Eigensolutions sensitivity for quadratic eigenproblems. *Journal of Sound and Vibration* 196, 2 (1996), 179–188.
- [184] TREYSSÈDE, F. Elastic waves in helical waveguides. *Wave Motion* 45, 4 (2008), 457–470.
- [185] TUFANO, G. *k-space analysis of complex large-scale periodic structures*. PhD thesis, École Centrale de Lyon, 2020.
- [186] TUFANO, G., ERRICO, F., ROBIN, O., DROZ, C., ICHCHOU, M., PLUYMERS, B., DESMET, W., AND ATALLA, N. K-space analysis of complex large-scale meta-structures using the Inhomogeneous Wave Correlation method. *Mechanical Systems and Signal Processing* 135 (2020), 106407.
- [187] VAN BELLE, L., CLAEYS, C., DECKERS, E., AND DESMET, W. On the impact of damping on the dispersion curves of a locally resonant metamaterial: Modelling and experimental validation. *Journal of Sound and Vibration* 409 (2017), 1–23.
- [188] VAN DE WALLE, A., NAETS, F., AND DESMET, W. Virtual microphone sensing through vibro-acoustic modelling and Kalman filtering. *Mechanical Systems and Signal Processing* 104 (2018), 120–133.
- [189] VAN DER BAAN, M. Acoustic wave propagation in one-dimensional random media: The wave localization approach. *Geophysical Journal International* 145, 3 (2001), 631–646.
- [190] VAN OPHEM, S., ATAK, O., DECKERS, E., AND DESMET, W. Stable model order reduction for time-domain exterior vibro-acoustic finite element simulations. *Computer Methods in Applied Mechanics and Engineering* 325 (2017), 240–264.
- [191] VIE, J.-L. *Second-order derivatives for shape optimization with a level-set method*. Theses, Université Paris-Est, 2016.
- [192] VILLOT, M., GUIGOU, C., GAGLIARDINI, L., AND GAGLIARDINI, L. Predicting the acoustical radiation of finite size multi-layered structures by applying spatial windowing on infinite structures. *Journal of Sound and Vibration* 245, 3 (2001), 433–455.

- [193] VINYALS, O., AND POVEY, D. Krylov subspace descent for deep learning. *Journal of Machine Learning Research* 22, 2 (2012), 1261–1268.
- [194] VLACHAS, K., TATSIS, K., AGATHOS, K., BRINK, A., AND CHATZI, E. A physics-based, local POD basis approach for multi-parametric reduced order models. In *Proceedings of ISMA 2020 - International Conference on Noise and Vibration Engineering and USD 2020 - International Conference on Uncertainty in Structural Dynamics* (2020), pp. 1925–1936.
- [195] VLACHAS, K., TATSIS, K., AGATHOS, K., BRINK, A. R., AND CHATZI, E. A local basis approximation approach for nonlinear parametric model order reduction. *Journal of Sound and Vibration* 502 (jun 2021), 116055.
- [196] WAAS, G. Earth vibration effects and abatement for military facilities: report 3: analysis method for footing vibrations through layered media. Tech. rep., Vicksburg, Miss., 1972.
- [197] WAKI, Y., MACE, B. R., AND BRENNAN, M. J. Numerical issues concerning the wave and finite element method for free and forced vibrations of waveguides. *Journal of Sound and Vibration* 327, 1-2 (2009), 92–108.
- [198] WANG, X., LUO, X., ZHAO, H., AND HUANG, Z. Acoustic perfect absorption and broadband insulation achieved by double-zero metamaterials. *Applied Physics Letters* 112, 2 (2018).
- [199] WIGNER, E. P. The unreasonable effectiveness of mathematics in the natural sciences. In *Mathematics and Science*. World Scientific, 1990, pp. 291–306.
- [200] WILLIS, J. R. Transmission and reflection at the boundary of a random two-component composite. *Proceedings of the Royal Society A: Mathematical, Physical and Engineering Sciences* 476, 2235 (2020).
- [201] WORLD HEALTH ORGANIZATION REGIONAL OFFICE FOR EUROPE. Environmental Noise Guidelines for the European Region (2018). Tech. rep., World Health Organization Regional Office for Europe, Copenhagen, 2018.
- [202] XIAO, M., ZHANG, Z. Q., AND CHAN, C. T. Surface impedance and bulk band geometric phases in one-dimensional systems. *Physical Review X* 4, 2 (2014), 1–12.
- [203] YANG, Y., MACE, B. R., AND KINGAN, M. J. Prediction of sound transmission through, and radiation from, panels using a wave and finite element method. *The Journal of the Acoustical Society of America* 141, 4 (2017), 2452–2460.

- [204] YANG, Y., MACE, B. R., AND KINGAN, M. J. Wave and finite element method for predicting sound transmission through finite multi-layered structures with fluid layers. *Computers and Structures* 204 (2018), 20–30.
- [205] YANG, Z. B., RADZIENSKI, M., KUDELA, P., AND OSTACHOWICZ, W. Scale-wavenumber domain filtering method for curvature modal damage detection. *Composite Structures* 154 (2016), 396–409.
- [206] YOGARATHINAM, A., KAUR, J., AND CHAUDHURI, N. R. A New H-IRKA Approach for Model Reduction with Explicit Modal Preservation: Application on Grids with Renewable Penetration. *IEEE Transactions on Control Systems Technology* 27, 2 (2019), 880–888.
- [207] ZAK, J. Berrys phase for energy bands in solids. *Physical Review Letters* 62, 23 (1989), 2747–2750.
- [208] ZERGOUNE, Z. Z. *Meso-Macro Approach for Modeling the Acoustic Transmission Through Sandwich Panels*. PhD thesis, École Centrale de Lyon, 2016.
- [209] ZHANG, H., WANG, C. M., CHALLAMEL, N., AND ZHANG, Y. P. Uncovering the finite difference model equivalent to Hencky bar-net model for axisymmetric bending of circular and annular plates. *Applied Mathematical Modelling* 61 (2018), 300–315.
- [210] ZHANG, J., REYNDERS, E., DE ROECK, G., AND LOMBAERT, G. Model updating of periodic structures based on free wave characteristics. *Journal of Sound and Vibration* 442 (2019), 281–307.
- [211] ZHENG, S., YIFENG, Z., XIAO, P., AND QIUSHI, L. Equivalent model of thin-walled orthotropic composite plates with straight segments using variational asymptotic method. *Composite Structures* 259, October 2020 (2021), 113229.
- [212] ZHONG, Q., CHEN, H., AND LE BOT, A. Radiative energy transfer model for finite anisotropic plates. *Journal of Sound and Vibration* 497 (2021), 115947.
- [213] ZHONG, S., MA, Y., AND HE, S. Perfect absorption in ultrathin anisotropic ϵ -near-zero metamaterials. *Applied Physics Letters* 105, 2 (2014).
- [214] ZHONG, W. X., AND WILLIAMS, F. W. On the Direct Solution of Wave-Propagation for Repetitive Structures. *Journal of Sound and Vibration* 181, 3 (1995), 485–501.

- [215] ZHONG, W. X., AND ZHONG, X. X. Computational structural mechanics. Optimal control and semi-analytical method for PDE. *Computers and Structures* 37, 6 (1990), 993–1004.
- [216] ZHOU, C. W., LAINÉ, J. P., ICHCHOU, M. N., AND ZINE, A. M. Multi-scale modelling for two-dimensional periodic structures using a combined mode/wave based approach. *Computers and Structures* 154 (2015), 145–162.
- [217] ZHOU, M., ZHONG, W., AND WILLIAMS, F. W. Wave propagation in substructural chain-type structures excited by harmonic forces. *International Journal of Mechanical Sciences* 35, 11 (1993), 953–964.
- [218] ZOHDI, T. I. *A Finite Element Primer for Beginners*. SpringerBriefs in Applied Sciences and Technology. Springer International Publishing, Cham, 2015.

Curriculum Vitae

Régis Fabien Boukadia

Personal data

Date of Birth: 12 Sptember 1990 in Lyon, France.

Nationality: French

Email: regis.boukadia@gmail.com

Education

2017-2021 PhD Student

KU Leuven, Departement of Mechanical Engineering,
Noise & Vibration Research Group.

École Centrale de Lyon, LTDS,
Vibro-Acoustics and Complex Media Research Group

2011-2016 Joint MSc in Engineering Sciences - specializations: Vibroacoustics, Aeronautics and Consulting

École Centrale de Lyon & University Claude Bernard Lyon 1
Master's Thesis: "Modeling of periodic structures for vibroacoustics applications".

2009-2011 Preparatory Classes

Lycée Aux Lazaristes,
MP-I: Mathematics, Physics, Computer Science

2008-2009 Preparatory Classes

Lycée Aux Lazaristes,
MPSI: Mathematics, Physics, Engineering Sciences

Grants and awards

2017 3-year Marie Skłodowska-Curie ITN grant in the VIPER project

List of publications

Articles in refereed journals

- R.F. Boukadia, C. Claeys, C. Droz, M. Ichchou, W. Desmet, E. Deckers. An INverse CONvolution MEmethod for wavenumber extraction (INCOME): formulations and applications. *Journal of Sound and Vibration*, Manuscript in revision, 2021.
- C. Droz, R. Boukadia, W. Desmet. A multi-scale model order reduction scheme for transient modelling of periodic structures. *Journal of Sound and Vibration*, Manuscript submitted for publication, 2021.
- R.F. Boukadia, E. Deckers, C. Claeys, M. Ichchou, W. Desmet. A wave-based optimization framework for 1D and 2D periodic structures. *Mechanical Systems And Signal Processing*, 139:106603, May 2020.
- S. Ahsani, R. Boukadia, C. Droz, C. Claeys, E. Deckers, W. Desmet. Diffusion based homogenization method for 1D wave propagation. *Mechanical Systems And Signal Processing*, 136:106515, February 2020.
- R. Boukadia, C. Droz, M. Ichchou, W. Desmet. A Bloch wave reduction scheme for ultrafast band diagram and dynamic response computation in periodic structures, *Finite Elements In Analysis And Design*, 148, 1-12, September 2018.
- C. Droz, Z. Zergoune, R. Boukadia, O. Bareille, M.N. Ichchou. Vibro-acoustic optimisation of sandwich panels using the wave/finite element method. *Composite Structures*, 156, 108-114, November 2016.

Academic book chapters

- L. Van Belle, L. Sangiuliano, N.G. Rocha de Melo Filho, M. Clasing Villanueva, R.F. Boukadia, S. Ahsani, F. Alves Pires, Z. Zhang, C. Claeys, E. Deckers, B. Pluymers, W. Desmet. Vibro-Acoustic Metamaterials for Improved Interior NVH Performance in Vehicles. In: *Future Interior Concepts*, pages 31-51, Springer, August 2020.

Articles in conference proceedings

- R.F. Boukadia, L. Sangiuliano, C. Claeys, M. Ichchou; W. Desmet, E. Deckers. Vibration damping of flexible rotating rings using simple and double modes tuned vibration absorbers. Submitted to *Metamaterials 2021*.
- F. Qu, L. Van Belle, R. Boukadia, E. Deckers, W. Desmet. Comparison between wave finite element and shift cell operator method for calculating dispersion diagrams of periodic metamaterial structures. Submitted to *Metamaterials 2021*.
- C. Droz, R.F. Boukadia, E. Deckers, W. Desmet. Sub-wavelength damage detectability assessment in periodic assemblies using a Bloch modelling framework. In: *Proceedings of the International Conference on Structural Dynamic , EUROODYN*, pages 870-877, Athens, Greece, November 2020.
- R.F. Boukadia, E. Deckers, C. Claeys, M. Ichchou, W. Desmet. A rational Krylov subspace method for the unit cell modeling of 2D infinite periodic media. In: *Proceedings of ISMA 2020 - International Conference on Noise and Vibration Engineering and USD 2020 - International Conference on Uncertainty in Structural Dynamics*, pages 1915-1924 ,Leuven, Belgium, September 2020.
- S. Ahsani, R.F. Boukadia, C. Droz, T.G. Zielinski, L. Jankowski, C. Claeys, W. Desmet, E. Deckers. On the potential of meta-poro-elastic systems with mass inclusions to achieve broadband near-perfect absorption coefficient. In: *Proceedings of ISMA 2020 - International Conference on Noise and Vibration Engineering and USD 2020 - International Conference on Uncertainty in Structural Dynamics*, pages 2463-2472 ,Leuven, Belgium, September 2020.
- R.F. Boukadia, E. Deckers, C. Claeys, M. Ichchou, W. Desmet. A convolution based wavenumber extraction method. In: *Proceedings of*

MEDYNA2020, the 3rd Euro-Mediterranean Conference on Structural Dynamics and Vibroacoustics, pages, Naples, Italy, February 2020.

- R.F. Boukadia, E. Deckers, C. Claeys, M. Ichchou, W. Desmet. A Wave-Based Methodology for the Optimization of Finite1D Metamaterials. In: *Proceedings of SMART2019*, pages 1066-1075, Paris, France, 2019.
- R.F. Boukadia, C. Claeys, C. Droz, M. Ichchou, E. Deckers. Model order reduction in unit cell modeling and its application to complex structures. In: *Proceedings of ISMA 2018 - International Conference on Noise and Vibration Engineering and USD 2018 - International Conference on Uncertainty in Structural Dynamics*, pages 4663-4678, Leuven, Belgium, 2018.
- S. Ahsani, R.F. Boukadia, C. Droz, C. Claeys, E. Deckers. Diffusion based homogenization method for one dimensional locally resonant system. In: *Proceedings of ISMA 2018 - International Conference on Noise and Vibration Engineering and USD 2018 - International Conference on Uncertainty in Structural Dynamics*, pages 4637-4652, Leuven, Belgium, 2018.
- T. Bourgana, R.F. Boukadia, S. Jonckheere, C. Claeys, G. Chevallier, M. Ouisse, E. Deckers. Inverse characterization method of viscoelastic materials using dispersion analysis. In: *Proceedings of ISMA 2018 - International Conference on Noise and Vibration Engineering and USD 2018 - International Conference on Uncertainty in Structural Dynamics*, pages 4691-4706, Leuven, Belgium, 2018.
- C. Droz, R.F. Boukadia, M. Ichchou, W. Desmet. Diffusion-based design of locally resonant sub-systems using a reduced wave finite element framework. In: *Proceedings of ISMA 2018 - International Conference on Noise and Vibration Engineering and USD 2018 - International Conference on Uncertainty in Structural Dynamics*, pages 3071-3084, Leuven, Belgium, 2018.

Conference abstracts/posters

- R.F. Boukadia, L. Van Belle, C. Claeys, E. Deckers, M. Ichchou, W. Desmet. Vibration based material characterisation. Presented at the Flanders Make Scientific Conference, Online, February 2021.
- L. Van Belle, R.F. Boukadia, C. Claeys, E. Deckers, W. Desmet. Measuring dispersion curves for vibro-acoustic metamaterials. Presented at the DENORMS Action Final event, Coimbra, Portugal, February 2020.

- C. Droz, R. Boukadia, M. Ichchou, W. Desmet. Wave conversion in sandwich structures: reduced wave/FE modelling for fast dispersion-based optimization. In: *International Conference on Composite Structures*, Abstract No. 81. Presented at the ICCS, CNAME, Paris, France, September 2017.

FACULTY OF ENGINEERING SCIENCE
DEPARTMENT OF MECHANICAL ENGINEERING
NOISE AND VIBRATION RESEARCH GROUP

Celestijnenlaan 300 box 2420

B-3001 Leuven

regis.boukadia@kuleuven.be

<https://www.mech.kuleuven.be/en/mod>

